3D Printed Gas Dynamic Virtual Nozzles for X-Ray Laser Sample Delivery and Optical Characterization of Microjets and Microdroplets.

by

Reza Nazari

A Dissertation Presented in Partial Fulfillment
of the Requirements for the Degree
Doctor of Philosophy

Approved October 2020 by the
Graduate Supervisory Committee:

Ronald Adrian, Co-Chair
Richard Kirian, Co-Chair
Marcus Herrmann
Patrick Phelan
Uwe Weierstall

ARIZONA STATE UNIVERSITY

December 2020

ABSTRACT

Gas Dynamic Virtual Nozzles (GDVN) produce microscopic flow-focused liquid jets and are widely used for sample delivery in serial femtosecond crystallography (SFX) and time-resolved solution scattering. Recently, 2-photon polymerization (2PP) made it possible to produce 3D-printed GDVNs with submicron printing resolution. Comparing with hand- fabricated nozzles, reproducibility, and less developing effort, and similarity of the performance of different 3D printed nozzles are among the advantages of using 3D printing techniques to develop GDVN's. Submicron printing resolution also makes it possible to easily improve GDVN performance by optimizing the design of nozzles. In this study, 3D printed nozzles were developed to achieve low liquid and gas flow rates and high liquid jet velocities. A double-pulsed nanosecond laser imaging system was used to perform Particle Tracking Velocimetry (PTV) in order to determine jet velocities and assess jet stability/reproducibility. The testing results of pure water jets focused with He sheath gas showed that some designs can easily achieve stable liquid jets with velocities of more than 80 m/s, with pure water flowing at 3 microliters/min, and helium sheath gas flowing at less than 5 mg/min respectively. A numerical simulation pipeline was also used to characterize the performance of different 3D printed GDVNs. The results highlight the potential of making reproducible GDVNs with minimum fabrication effort, that can meet the requirements of present and future SFX and time-resolved solution scattering research.

This dissertation is dedicated to my dear mom, whose sacrificial care for me made it possible for me to complete this work, and to my dear sister.

ACKNOWLEDGMENTS

I would like to thank my advisors, Professor Ronald Adrian and Professor Richard Kirian, for the guidance and wisdom they have provided me over the years.

I would also like to thank the following people for their invaluable contributions: Garrett Nelson for his contributions towards GDVNs (Gas Dynamics Virtual Nozzles), 3D printing and injection. Sahba Zaare, Roberto Alvarez, Konstantinos Karpos, Dr. Joe Chen, Stella Lisova, Hao Hu, Trent Engelman and Caleb Madsen for their helps towards printing, developing and assembling GDVNs, setting up the test station and maintaining it to keep it up and running for different experiments, and also for their help in the data collection; Adil Ansari for his contributions towards the numerical simulations as we closely worked together to come up with the best possible numerical simulation pipeline; Austin Echelmeier, Sahir Gandhi, Mukul Sonker, Jorvani Cruz Villareal, Sebastian Quintana, Diandra Doppler, Dayhiun Kim, Mohammad Towshif Rabbani, Dr. Max wiedorn, for their contributions towards 3D printing and the collaborative projects to help with several X-ray Free Electron Laser (XFEL) experiments; Sankar Raju and Lars Paulsen for working closely with us to provide 3D printed sheet jet sample delivery devices; All the collaborators that gave me the opportunity to help them with their experiments by providing them the novel 3D printed sample delivery devices, such as Professor Martin Trebbin, Professor Andrew Martin, Professor Rousseu, Dr. Andy Aquila, Dr. Dan Deponte, Dr. Mark hunter, Dr. Ray Sierra; and finally Professor John Spence, Professor Petra Fromme, Professor Reymond Fromme, Professor Brenda Hogue, Professor Kevin Schmidt, Professor Uwe Weierstall, Professor Alexandra Ros, Professor Martin Trebbin, Professor Marcus Herrmann, and Professor Patrick Phelan for their invaluable advice at different stages of my PhD research.

TABLE OF CONTENTS

Page

LIST OF TABLES viii

LIST OF FIGURES ix

CHAPTER

1 INTRODUCTION 1

1.1 Liquid Jet Requirements for Serial X-ray Diffraction Measurements. 2

1.2 Nanodroplet Requirements for Single-particle Imaging 4

1.3 Structure of the Dissertation........ 6

1.4 Results of the Dissertation 9

2 PHYSICS OF GDVN LIQUID MICROJET AND MICRODROPLET PRODUCTION 11

2.1 An Overview of the Geometry of a GDVN 11

2.2 Physics of Different Operating Regimes of GDVNs 11

2.3 Global and Local Instability, Absolute and Convective Instability of Flow Focusing Jets 13

2.3.1 Global and Local Instabilities in Spatially Developing Flows 16

2.3.2 Absolute and Convective Instabilities in Spatially Developing Flows........ 16

2.4 Droplet Formation and Droplet and Estimation of Droplet Diameters 16

2.4.1 Different Methods of Producing Micron-sized and Submicron-sized Droplets 17

2.5 Theoretical Estimation of Droplet Diameters Resulting From Breakup of Rayleigh Jets 18

3 3D PRINTING OF GAS-DYNAMIC VIRTUAL NOZZLES AND OPTICAL CHARACTERIZATION OF HIGH-SPEED MICROJETS 20

3.1 Abstract 20

3.2 Introduction 20

3.3 Overview of Gas-dynamic Virtual Nozzles 22

  3.3.1 Basic Principles of Flow-focused Liquid Microjet Formation . 22

  3.3.2 Nozzle Design Goals 23

  3.3.3 Asymmetric Nozzles for Fast Jets 24

3.4 Nozzle Fabrication and Assembly 26

  3.4.1 3d Printing With 2-photon Polymerization 26

3.5 Procedures for Quantifying GDVN Performance 29

  3.5.1 Overview of Nozzle Testing Station 29

  3.5.2 Image Processing and Analysis 31

3.6 Results of Nozzle Testing 33

  3.6.1 Sheath Gas Flow Rates and Pressures 34

  3.6.2 Jet Velocities 34

  3.6.3 Jet Lengths 37

  3.6.4 Jet Diameters 37

  3.6.5 Jet Deviation Angles 38

  3.6.6 Jet Performance and Reproducibility 38

  3.6.7 Droplet Diameters 38

  3.6.8 Estimation of Internal Nozzle Gas Pressure 39

  3.6.9 Sheath Gas Reynolds Numbers 42

3.7 Discussion and Conclusions 44

3.8 Acknowledgements 45

3.9 Disclosures 45

4 NUMERICAL AND EXPERIMENTAL INVESTIGATION OF THE EFFECT OF DIFFERENT GEOMETRICAL PARAMETERS ON THREE-DIMENSIONAL PRINTED GAS DYNAMICS VIRTUAL NOZZLES . . . 46
4.1 Abstract 46
4.2 Introduction 47
4.3 Theory 48
4.3.1 Navier-Stokes Equations 48
4.3.2 Volume of Fluid Method 49
4.3.3 Numerics 51
4.3.4 Surface Tension 64
4.4 Mesh Independence and Grid Convergence Index Study 65
4.4.1 Cylinder-Collapse 66
4.5 Test Case for Investigation of a Bell-shaped Nozzle Design and a Cone-shaped Nozzle Design. 69
4.5.1 The Difference Between Bell-shaped and Cone-shaped Nozzles 69
4.5.2 Designing and Developing 3d Printed Gdvns With the Bell-shaped and the Cone-shaped Gas Flow Field Geometry 69
4.5.3 Developing the 3d Half Geometry for the Cone-shaped and the Bell-shaped Nozzles 70
4.5.4 Test Case for Experimental Testing and Numerical Simulation 71
4.5.5 Runs 72
4.5.6 Testing and Image Analysis 73
4.5.7 Results of the 3D Simulations and Comparison of the Results With the Experimental Testing Results 74

4.5.8 Contours and Figures From the Numerical Simulation Results 75
4.6 Three-dimensional Numerical Simulation of a Widely Used 3D Printed Nozzle 76
4.7 Conclusion 77
5 3D PRINTED GAS DYNAMIC VIRTUAL NOZZLES ALONG WITH LIQUID AND GAS FLOW RATE MANIPULATION SYSTEM TO SYNCHRONIZE DROPLETS WITH THE XFEL PULSES 109
5.1 Abstract 109
5.2 Introduction 109
5.3 Current Efforts and the Project Progress 112
5.3.1 Results 113
6 MISCELLANEOUS PROJECTS 115
6.1 Array of Nozzles 115
6.2 Integration of Nozzle Designs With Mixer Designs 115
6.3 Integration of Nozzle With T-junction 116
6.4 Double Focusing Nozzles 117
REFERENCES 122

APPENDIX

A SUPPLEMENTARY INFORMATION 131

LIST OF TABLES

Table Page

4.1 Average Pressure Values f Inside the Domain With Three Different AMR Levels. The Value h Indicates the Finest Resolution at the Interface After AMR. 68

A.1 Some of the XFEL Experiments of Which Reza Nazari Had contribution. 135

A.2 Geometrical Parameters of the Designs With 100 μm Inner Diameter Liquid Line. 146

LIST OF FIGURES

Figure Page

2.1 A Picture of an Operating GDVN. 12

2.2 Regimes of Global and Local Instabilities. 15

3.1 A Picture of an Operating GDVN. 22

3.2 Design Dimensions of Design 1 in Micrometers. 25

3.3 Drawing of the Nozzle Design 2 (Dimensions Are in Micrometers). 26

3.4 An Assembled 3d Printed Nozzle. 28

3.5 SEM Images of a Nozzle From Design 2. Only Half of the Nozzle Was Printed in Order to Reveal the Internal Structure. 29

3.6 Schematic of the Test Station. Helium Gas Drives the Liquid Jet and the Pressure and Mass Flow Rate Are Monitored Upstream of the Glass Capillary That Leads to the Nozzle. an HPLC Pump Drives the Liquid (Water) and a Flowmeter Measures Its Volumetric Flow Rate. Nitrogen Gas and Isopropanol Are Used to Clean and Dry Nozzles, Particularly When Running Samples Other Than Water. the Nozzle Is Located in a Small Chamber at ∼1 mbar Pressure. a Pulsed ∼100 ns Laser Provides Brightfield Illumination for the High-frame-rate Camera, and Electronic Delay System Allows for Doublets of Images. 31

3.7 Illustration of Image Processing Steps. (a) Raw Image Before Processing Steps. (B) Binary Image After Background Subtraction and Thresholding. (C) Perimeter of Extracted Jet Region. (D) Pair of Extracted Droplet Series Separated in Time by 550 ns. the Droplet Colors Indicate Matching Droplets in the Image Pair. 33

3.8 He Pressure at the Inlet of the Gas Capillary Versus Helium Flow Rate for a Nozzle of Design 1, Showing That the Liquid Flow Does Not Effect the Gas Flow in the Measurements. 34

3.9 (a) Plots of Jet Velocity Versus Helium Flow Rate for Different Liquid (Water) Flow Rates for 5 Different Nozzles From Design 1 and (B) 5 Different Nozzles From Design 2. (C) Plots of Jet Length Versus Helium Flow Rate for Different Liquid (Water) Flow Rates for 5 Different Nozzles From Design 1 and (D) 5 Different Nozzles From Design 2. Symbol Colors Distinguish Liquid Flow Rates, While Symbol Shapes Distinguish Different Nozzles. 35

3.10 (a) Jet Diameter Versus Helium Flow Rate for Different Liquid (Water) Flow Rates for 5 Different Nozzles From Design 1 and (B) 5 Different Nozzles From Design 2. (C) Jet Angle Versus Helium Flow Rate for Different Liquid (Water) Flow Rates for 5 Different Nozzles From Design 1 and (D) 5 Different Nozzles From Design 2. Symbol Colors Distinguish Liquid Flow Rates, While Symbol Shapes Distinguish Different Nozzles. 36

3.11 (a) Jet Diameter Versus Helium Flow Rate for Different Liquid (Water) Flow Rates for a Nozzle From Design 2. (B) Median Droplet Diameter Versus Helium Flow Rate for Different Liquid (Water) Flow Rates for a Nozzle From Design 2. (C) Median Droplet Diameter Versus Calculated Jet Diameter for a Nozzle From Design 2. (D) Plot of Estimated Pressure Inside the Nozzle Versus Liquid Jet Reynolds Number for 5 Nozzles From Design 1 Under Different Operating Conditions. 40

3.12 (a) Plot of Liquid Jet Weber Number Versus Liquid Jet Reynolds Number for 5 Nozzles From Design 1 Under Different Operating Conditions. (B) Plot of Liquid Jet Reynolds Number Versus Helium Flow Rate for 5 Nozzles From Design 1 Under Different Operating Conditions, (C) Plot of Liquid Jet Weber Number Versus Helium Flow Rate for 5 Nozzles From Design 1. (D) Plot of Calculated Sheath Gas Reynolds Number Versus Helium Flow Rate for 5 Nozzles From Design 1 Under Different Operating Conditions. Symbol Colors Distinguish Liquid Flow Rates, While Symbol Shapes Distinguish Different Nozzles 43
4.1 Left: Potential Description of a True Interface, Center: Discrete Cellular Representation of Volume of Fluid, Right: Discrete and Piece-wise Representation of Continuous Interface Showing Planar Distribution of Fluid Fractions. 50
4.2 A Visualization of a Parent Hexahedral Cell Connected to an Adaptively Refined Neighboring Cell. 52
4.3 A Visualization of Iso-face in an Interface Cell. 59
4.4 Left: a Visualization of a Face in an Interface Cell Shows $a_f\left(\tau\right)$ Highlighted With Dotted Shading. The Brown Shaded Patch Shows $a_f(T)$ and Combined With the Green Patch Shows $a_f(T+\delta T)$. Center: $a_f\left(\tau\right)$ Visualized in Second Interval. Right: the Integral $\int_t^{t+\delta T} a_f\left(\tau\right) d\tau$ Can Be Visualized as a Polyhedron Extruded With Variable $a_f(\tau)$ Varying for Each Infinitesimal Cross Sections. 63

4.5 The Final Condition of the Cylinder Collapse Test Case for Grid Resolution Independency Study. The Left Picture Corresponds to One AMR (Adaptive Mesh Refinement) Level (Coarsest Mesh Resolution in the Vicinity of the Liquid-gas Interface), the Middle Picture Corresponds to Two AMR (Medium Mesh Resolution in the Vicinity of the Liquid-gas Interface) Levels, and the Right Picture Corresponds to Three AMR Levels (Fine Mesh Resolution in the Vicinity of the Liquid-gas Interface). 67

4.6 The Initial Condition of the Cylinder Collapse Test Case for Grid Resolution Independency Study (Left Picture), and the Final Condition of the Cylinder Collapse Test Case for Grid Resolution Independency Study With 1 AMR Level (Right Picture). 68

4.7 Cylinder Collapse for GCI Analysis to Study the Grid Resolution Independency of the Results. It Starts From Time 0 Till Time 12 μ *Sec* With 3 μ*Sec* Interval. The Left Pictures Correspond to the Coarsest Mesh Resolution at the Interface With 1 AMR Level, the Middle Pictures Correspond to the Medium Mesh Resolution With 2 AMR Levels, and the Right Pictures Correspond to the Fine Mesh Resolution at the Interface With 3 AMR Levels. 79

4.8 Cylinder Collapse for GCI Analysis to Study the Grid Resolution Independency of the Results. It Starts From Time 14 Till Time 26 μ *Sec* With 4 μSec Interval.the Left Pictures Correspond to the Coarsest Mesh Resolution at the Interface With 1 AMR Level, the Middle Pictures Correspond to the Medium Mesh Resolution With 2 AMR Levels, and the Right Pictures Correspond to the Fine Mesh Resolution at the Interface With 3 AMR Levels. 80
4.9 Schematic of a GDVN With Bell-shaped Geometry for Gas Flow Field (a), and Schematic of a GDVN With Cone-shaped Geometry for Gas Flow Field (B). 81
4.10 Design of the bell-shaped 3D printed GDVN cut into half. 81
4.11 Geometrical Parameters of a Cross-section of the Cone-shaped and Bell-shaped 3D Printed GDVNs. 82
4.12 Picture of the 3d Printed GDVN With Bell-shaped Gas Flow Field Geometry (Upper Picture) and Picture of the 3D Printed GDVN With Cone-shaped Gas Flow Field Geometry (Lower Picture). 83
4.13 Computational Flow Field for the GDVN With Bell-shaped Geometry for Gas Flow Field. Blue Surface Is the Surface of Symmetry. 84
4.14 Computational Flow Field Region for the GDVN With Cone-shaped Geometry for Gas Flow Field. 84
4.15 Complete Flow Field Region for the Bell-shaped Nozzle Numerical Simulation. 85
4.16 A Visualization of Simple Domain Decomposition. 85
4.17 A Visualization of Scotch Domain Decomposition. 85

4.18 Speed Variation of Various Methods for a Various Number of Cores. . . . 86
4.19 Experimental Results of Cone-shaped and Bell-shaped Nozzles. 87
4.20 The Jet Length and Diameter for Given Times. The Temporal Resolution Is 1 μS. 88
4.21 Numerical Simulation Results of Cone-shaped and Bell-shaped Nozzles (a), and Experimental Results of Cone-shaped and Bell-shaped Nozzles (B). 88
4.22 Experimental and Cfd Results of Bell-shaped Nozzles (a), and Experimental and Cfd Results of Cone-shaped Nozzles (B). 89
4.23 A Picture From the Numerical Simulation and the Experimental Testing of a Running Jet From the Cone-shaped GDVN Design. 89
4.24 Pressure Values in Pascal for the Gas and Liquid for the Cone-shaped and the Bell-shaped 3D Simulation. 90
4.25 Three AMR Levels for the Cells in the Vicinity of the Liquid-gas Interface for the Bell-shaped Nozzle Design. 90
4.26 Streamlines of the Gas Flow and the Liquid Flow for the 3D Simulation of the Cone-shaped and the Bell-shaped Nozzle Designs. 91
4.27 U Component of the Velocity Magnitude in m/s. This Component of the Velocity Magnitude Is the Component in the Direction of Jet Propagation. 91
4.28 A Cross-section of the Jet and How It Breaks Up Into Droplets for the Bell-shaped Design (Upper Picture) and the Cone-shaped Design (Lower Picture). 92
4.29 Jet Regions in the Cone-shaped and the Bell-shaped Design. 92

4.30 The Jet Regions for a Running Nozzle Along With the Droplets After the Jet Breakup for the Cone-shaped (Lower Picture) and the Bell-shaped (Upper Picture) Designs. 93
4.31 Contours of the Pressure Values (in Pascal) for the Cone-shaped (Lower Picture) and the Bell-shaped (Upper Picture) Designs. 93
4.32 CAD (Computer Aided Design) of the GDVN. 94
4.33 Three-dimensional Flow Region Extracted From the CAD File (Above Picture) and Afterward, Adding a Big Cylinder to It to Account for the Flow Region of the Chamber. 95
4.34 Another Picture of the Entire Flow Field Region. 96
4.35 Complete Flow Region Resulting From Adding the Flow Region in the Chamber to the Region Inside the Nozzle. 96
4.36 The Boundary Condition for Walls. 97
4.37 The Boundary Condition for Sheath Gas Inlet. 97
4.38 Boundary Condition for Water Inlet. 98
4.39 Boundary Condition for Pressure Outlet. 99
4.40 Body of Influence for Mesh Refinement in the Vicinity of the Liquid Jet and the Droplets Inside the Chamber. 100
4.41 The Meshing of the Entire Flow Field. 101
4.42 Liquid Jet Results at Different Time Steps Shown in Red Color for the 3d Simulation Described in Section 4.6. 102
4.43 Liquid Jet Results at Different Time Steps Shown in Red Color for the 3D Simulation Described in Section 4.6. 103

4.44 Liquid Jet Results at Different Time Steps Shown in Red Color for the 3D Simulation Described in Section 4.6. 104
4.45 Liquid Jet Results at Different Time Steps Shown in Red Color for the 3D Simulation Described in Section 4.6, Colored by the Component of Velocity in the Jet Propagation Direction. 105
4.46 Liquid Jet Results at Different Time Steps Shown in Red Color for the 3D Simulation Described in Section 4.6, Colored by the Component of Velocity in the Jet Propagation Direction. 106
4.47 Liquid Jet Results at Different Time Steps Shown in Red Color for the 3D Simulation Described in Section 4.6, Colored by the Component of Velocity in the Jet Propagation Direction. 107
4.48 Liquid Jet Results at Different Time Steps Shown in Red Color for the 3D Simulation Described in Section 4.6, Colored by the Component of Velocity in the Jet Propagation Direction. 108
5.1 Example of Wasted Sample From a Recent XFEL Experiment. 112
5.2 A Single Droplet Being Released From the Nozzle Tip. 114
5.3 Natural Droplet Frequency From a 3D Printed GDVN in Dripping Mode. 114
6.1 A 3D Printed Array of Nozzles Device. 116
6.2 A Picture of a Design of a Mix and Inject Device. In the Picture, the Left Line Is for the Sacrificing Oil, the Middle Line Is for the Sample, and the Right Line Is for the Sheath Gas. 117
6.3 A Picture of a Design of the T-junction With a Nozzle Design. 118
6.4 A Picture of a Design of the Double Focusing GDVN Cut Into Half. . . . 119
6.5 A Picture of a 3D Printed Double Focusing Gdvn Device. 119

Figure Page

6.6 Average Velocity Versus Upstream Helium Gauge Pressure for a DFFN GDVN Liquid Jet Operating in Vacuum Chamber. 120
6.7 Median Jet Length Versus Upstream Helium Flow Rate for a DFFN GDVN Liquid Jet Operating in Vacuum Chamber. 120
6.8 Average Velocity Versus Helium Flow Rate for a DFFN GDVN Liquid Jet Operating in Vacuum Chamber. 121
6.9 Jet Diameter Versus Helium Flow Rate for a DFFN GDVN Liquid Jet Operating in Vacuum Chamber. 121
A.1 A 3D Printed GDVN Operating in an XFEL Experiment at Slac National Laboratory, Stanford, USA. 136
A.2 DILAS Laser Parameters. 138
A.3 Design Dimensions of the A42 Design (Design 42) in Micrometers. 139
A.4 Design Dimensions of Design 53 in Micrometers. 139
A.5 Design Dimensions of the SC30I Design (Design 30) in Micrometers. . . . 140
A.6 The 56 Design; Two Views of the Design. Dimensions Are in Microns. . 140
A.7 Sheet 1 of the 79 Design; 3rd Angle Projection Drawing of the Design. . 141
A.8 Sheet 2 of the 79 Design; 3rd Angle Projection Drawing of the Design. . 142
A.9 Sheet 3 of the 79 Design; Some Projections of the Sections of the Design. 143
A.10 Sheet 4 of the 79 Design; Some Projections of the Sections of the Liquid Capillaries of the Design. 144
A.11 The 175 Design; the Design for 75 μM Liquid Line. Dimensions Are in Microns. 145
A.12 Geometrical Parameters of the 3D Printed Designs. 145
A.13 Integration of a Concentric Mixer With a Nozzle Design (N63). 152

A.14 Schematic of the Dual Image With Dual Pulse Laser Imaging Station Configuration. 153
A.15 Picture From the Oscilloscope Indicating That the Master Clock (Channel 1; Yellow), the DG645 Delay Generator (Channel 2; Light Blue), the DILAS Laser (Channel 3; Purple) and the Photron Fastcam (Channel 4; Green), Are All Synchronized With Respect to Each Other. 154
A.16 Top: Bad Quality Score, Bottom: Acceptable Score. 154
A.17 (Left) Marking the Gas Capillary Line Using a Black Sharpie. (Right): Holding the Nozzle With Tweezers During Capillary Insertion. 155
A.18 (Left): Standalone Nozzle, Figure 3b (Right): Capillaries Inserted Into the Nozzle. Top: Liquid Line, Bottom: Gas Line. 155
A.19 Using a Short/broken Capillary to Apply Epoxy to Nozzle Head. 156
A.20 (Top): Metal Sleeve Glued to Nozzle/capillary, Figure 5b (Bottom): a Visual on the Approximate Amount of Glue Needed at Each End of the Sleeve. 157
A.21 Permission from Optics Express Journal; part 1. 158
A.22 Permission from Optics Express Journal; part 2. 159
A.23 Permission from Optics Express Journal; part 3. 160
A.24 Permission from the AIP Publishing publications; part 1. 161
A.25 Permission from the AIP Publishing publications; part 2. 162
A.26 Permission from the AIP Publishing publications; part 3. 163

Chapter 1

INTRODUCTION

Gas Dynamic Virtual Nozzles (GDVN) produce microscopic flow-focused liquid jets and microdroplets [31], which are widely used for applications in the food industry and the pharmaceutical industry [53, 14, 20]. One of the most important applications of GDVNs to emerge in the last decade is at x-ray free-electron laser (XFEL) facilities where they are used to deliver hydrated biomolecules into an intense micro-focused x-ray beam in order to make ultrafast diffraction measurements. XFELs generate x-ray pulses of ∼10-femtosecond duration (10^{-14} seconds) and with mJ pulse energies, which is more than sufficient to initiate a Coulomb explosion that results in a high-temperature plasma that destroys the liquid jet. Despite the catastrophic destruction of the liquid jet and the protein sample, the x-ray diffraction patterns produced by XFELs can be used to synthesize atomic-resolution electron density maps that are free of damage because the femtosecond-duration x-ray pulses terminate before the atomic motions. This paradigm is known as "diffraction-before-destruction". Data can be recorded at high frequency because the liquid jet recovers prior to the subsequent XFEL pulse, which arrives after approximately 1-10,000 μs. Diffraction-before-destruction was first demonstrated on protein samples in 2009 just after the Linac Coherent Light Source (LCLS) facility at SLAC national lab, the world's first XFEL, began operating [18]. The field that is now known as serial femtosecond crystallography (SFX) has been developing rapidly since 2009, and now routinely enables studies on crystals down to sub-micrometer dimensions, at room temperature, without radiation damage. When XFELs are combined with an excitation scheme such as an optical laser or rapid mixing, dynamics of atomic motion can be observed with a time resolution down to about 10 femtoseconds. Alongside the development of SFX, the techniques of fast solution scattering (FSS) and single-particle imaging (SPI) are being developed in order to circumvent the often critical bottleneck of growing well-ordered protein crystals (for example, it is extremely difficult to crystallize membrane proteins, which are the targets of the majority of pharmaceutical drugs).

1.1 Liquid Jet Requirements for Serial X-ray Diffraction Measurements

A sample delivery apparatus for XFEL serial diffraction measurements must meet several basic requirements. Protein samples must be hydrated, and since the XFEL beam is highly destructive, samples must be replenished after every shot. X-ray pulse repetition rates in the range of 30-120 Hz are usually needed in order to accumulate sufficient data in a reasonable timeframe. The minimum speed of the sample is in principle set by the pulse repetition rate and the extent of the destruction caused by the x-ray pulse, which is typically on the order of 100 μm [81]. The European XFEL facility will produce x-ray pulses at a repetition rate of 4.5 MHz [1] in which case microjet speeds in excess of 100 m/s are required. A typical SFX measurement requires roughly 1 million raw diffraction patterns, and this number should be multiplied by the number of desired timepoints for a time-resolved diffraction study and/or by the number of sample conditions that must be screened (typically five or more conditions). Since large numbers of diffraction patterns are needed, it is critical that sample delivery systems minimize the quantity of protein that is required per diffraction pattern, because highly purified protein samples are often very expensive and time-consuming to make. In addition to minimizing sample wastage, the injection system should maximize the fraction of XFEL pulses that strike a desired target. This “hit fraction” can be very important because XFELs are billion-dollar facilities

---

[1] Data is recorded at a rate of only 2,700 frames per second due to the limited memory and transfer speeds of the x-ray pixel array detector

that can only multiplex a few experiments at any given time, and each experimental team is assigned only a limited time to utilize the source. The composition of protein samples varies significantly from one target to the next; some samples survive in pure water, but many require high concentrations of salts or polymers such as polyethylene glycol to sustain well-ordered microcrystals, or detergents in order to stabilize membrane proteins in solution. Since sample preparation is delicate process, sample delivery systems must be adapted to work with the native sample medium; only in rare circumstances can a sample be modified to suit the delivery system. In most serial diffraction experiments the samples are injected into a vacuum chamber at a pressure of approximately 10^{-8} atmospheres in order to reduce x-ray background scatter from the surrounding gas. The sample delivery devices should in general be designed to produce very little x-ray scatter, which most often limits the thickness of any solid or liquid matter that is placed in the XFEL beam to no more than about 1-100 μm. Helium gas flow rates are typically restricted to approximately 40 mg/min (roughly 0.2 liters/min at STP).

Despite the prevalence of GDVNs in the XFEL field, GDVNs have important limitations and therefore continue to be the subjects of intense research in the XFEL community. One of the greatest drawbacks of a continuous liquid jet is that the vast majority of a protein sample is wasted when operating with the typical x-ray probe of 1-μm diameter and pulse repetition rate of 120 Hz. Jet speeds of approximately 20 m/s are typically required in order to maintain a stable jet, in which case much less than one part in 10,000 of the sample is utilized. Low-speed viscous extrusion injectors [94] are under development and are highly effective at reducing sample wastage, but it is difficult to prepare most protein crystals in an appropriate shear-thinning viscous medium. Sample wastage can also be reduced by placing samples on thin solid support substrates such as polyimide tape, silicon wafers, or graphene, which can be translated between XFEL pulses. Solid supports can be very effective but can also result in sample dehydration if good humidity controls are not in place, and they are not easily adapted to vacuum environments or MHz x-ray repetition rates.

Although there are many effective means of injecting samples into an XFEL beam, liquid microjets produced by GDVNs will likely continue to be favored in at least two highly important measurement regimes: (1) any experiment in which MHz pulse repetition rates are desired, which would include time-resolved studies or large combinatorial screenings of sample conditions, and (2) experiments in which rapid mixing is desired. Liquid microjets naturally move at speeds that are appropriate for MHz XFEL sources, and jet diameters are appropriately sized for mixing experiments that require diffusion timescales in the millisecond regime that is characteristic of many enzymes. The development of MHz mixing measurements can potentially open up a new field of time-resolved rapid-mixing enzymology, which would allow the study of a great variety of biomolecular catalysts.

1.2 Nanodroplet Requirements for Single-particle Imaging

One of the most important goals of XFEL facilities is the development of "single-particle imaging" (SPI), which warrants a discussion that is separate from solution scattering and crystallography experiments. In the case of SPI, individual protein molecules or molecular assemblies such as viruses are delivered to the x-ray beam one-by-one, in a vacuum environment of approximately 10^{-8} atmospheres. An incredibly sparse photon scatter signal is generated from single proteins – a mere $\sim$100 photons per molecule in extreme cases – which demands that the background scatter sources produce even fewer photons. With so few photons per molecule, large datasets of perhaps 10^6 single-particle diffraction patterns or more are required in order to utilize advanced algorithms that construct a structural model that is consistent with the entire dataset. With regard to sample injection, the requirements for SPI are several-fold: (1) isolated bioparticles must be removed from bulk liquid shortly before they enter the vacuum chamber, (2) the initial droplets that contain the particles must be comparable to the size of the particles (diameters of just tens or hundreds of nanometers) in order to avoid aggregation of insoluble solvents and debris in the native liquid, (3) the carrier gas should be helium in order to reduce background scatter associated with air, and (4) upon evaporation of residual liquid a high-density beam of bioparticles must be placed in the 100-nm cross section of the XFEL beam in order to ensure that a significant portion of XFEL pulses yield useful photon scatter.

The delivery of bioparticles to the nano-focused XFEL beam may be carried out by aerodynamic lens stacks or electrodynamic traps, while the production of nanodroplets is typically carried out by electrospray devices. However, GDVNs offer the opportunity to operate with a helium carrier gas and to produce nanodroplets by purely mechanical means, without placing requirements on the conductivity of the protein solution, and without the potential of structural artifacts that may arise due to sample charging. therefore, using aerodynamic lens system [52], [51] along with a flow focused GDVN, as the droplet generation source has been recently used for single particle imaging purpose to study the structure of viruses. For that purpose, production of droplets with the smallest possible sizes are desired. We want to produce sub-micron droplets for protein sample delivery into vacuum for single particle imaging (SPI) research [80], [83]. Moreover, production of more droplets to achieve large particle densities are desirable since it increases x-ray hit rate. In this regard, smaller droplets allow us to increase the initial number density of particles. Tyipical number densities range from 1e11 to 1e15 particles per cm^3 and the number density is sometimes limited by the droplet size when the droplets are too big. Droplets contain viruses and smaller droplets have less content of other contamination substances other than viruses. Therefore, after droplet evaporation, the virus particles are expected to be less contaminated if the droplets are smaller.

1.3 Structure of the Dissertation

Chapter 2 explains the physics of GDVN liquid microjet and microdrop production. It starts with an overview of the geometry of a GDVN in section 2.1.The physics of different operating regimes of GDVNs are explained based on compilation of the previous investigations in the literature in section 2.2. Section 2.3 describes global and local instability, absolute and convective instability of flow focusing jets. Section 2.3 also explains how vega et al. [92] quantified each instability regime by two dimensionless numbers, namely Reynolds number and Weber number (Reynolds number and Weber number are introduced in section A of the Appendix). Section 2.4 of Chapter 2 involves the formation of droplets with diameters in the micron and submicron scale ranges, and it presents different methods of producing micon-sized and submicron-sized droplets that are available in the literature. The last section of Chapter 2, that is section 2.5, represents a classical theoretical technique for estimation of droplet diameters resulting from breakup of Rayleigh jets.

Chapter 3 materials reproduce exactly the published paper "Nazari, R., Zaare, S., Alvarez, R. C., Karpos, K., Engelman, T., Madsen, C., ... Kirian, R. A. (2020). 3D printing of gas-dynamic virtual nozzles and optical characterization of high-speed microjets. Optics Express, 28(15), 21749-21765."[61], with the permission of AIP publishing. This chapter includes content of the paper "Nazari, Reza, et al. "3D printing of gas-dynamic virtual nozzles and optical characterization of high-speed microjets." Optics Express 28.15 (2020): 21749-21765". In this chapter, jet characteristics of the 3D printed GDVNs (Gas Dynamics Virtual Nozzle) from two different designs were studied. Experimental testing of 5 devices from each design was done, and the novel image analysis pipeline assessed jet characteristics of the 3D printed devices under different operating conditions. Moreover, image analysis on droplets has been done and size of the droplets formed after liquid jet breakup, and the size distribution of the droplets are investigated by the novel image analysis pipeline. In the aforementioned paper [61]. The DOI for this paper is: 10.1364/OE.390131 with the following link: https://doi.org/10.1364/oe.390131. For Chapter 3, I worked with multiple authors. I designed and printed all the nozzles, I collected all data, developed the complete image processing pipeline to analyze all data, and wrote almost all of the manuscript. However, I had some help with development and Sahba Zaare, Trent Engelman and Caleb Madsen in the lab developed the hardware. Roberto Alvarez helped with assembling of some of the nozzles.

Chapter 4 involves introducing a computational fluid dynamics (CFD) pipeline to numerically simulate GDVNs. The first section of Chapter 4 involves explaining the theory behind the available open source numerical models that were used for the simulation. Section 4.4.1 explains how to assess an optimum resolution for numerical simulation.

Section 4.5 Compares the numerical simulation results of 3D printed GDVNs from two different designs, with the results from their experimental testings. Moreover, section 4.5 includes the numerical and experimental investigation of the difference in jet characteristics resulting from two different geometries operating under the same conditions. Among the projects that I lead, two projects among several projects that involve numerical simulations are included in section 4.5 and section 4.6. In section 4.5 the effect of cone-shaped and bell-shaped GDVN geometries are investigated. In section 4.6, the complete procedure of the numerical simulation of an existing 3D printed design of a widely-used device is explained. The procedure starts from developing the computational fluid dynamics numerical simulation flow field region from the three-dimensional design, and is followed by developing the mesh from flow field, running the case and post-processing the results. On almost all of the projects that include computational fluid dynamics numerical simulation, Adil Ansari worked closely with me to prepare the report for the theory of the existing numerical simulation models we used, preparing the setup, running the cases and post-processing the results of the numerical simulation. Sahba Zaare, Konstantinos Karpos, and Roberto Alvarez also had a significant contribution in preparing and maintaining the test station, developing and testing some of the 3D printed nozzles.

I also led the research activity for chapter Chapter 5, in terms of introducing the ideas, providing the operating condition ranges for testings and developing an image processing code to accurately assess the droplet generation frequency for periodic droplets that are to be triggered to the laser pulse. Sahba Zaare contributed to helping with the 3D printed nozzles development, development of the test station and the hardware of the imaging system. Konstantinos Karpos contributed to helping with maintaining the imaging test station and capturing the data from the test station, and Roberto Alvarez contributed to helping with nozzle assembling.

Chapter 6 briefly explains several projects and sub-projects that I have contributions during my Ph.D. period. First project is developing array of nozzles to overcome clogging of the GDVNs in XFEL experiments, that is introduced in section 6.1. The next few sections explain integration of the 3D printed GDVN design with several different designs to satisfy the requirements of different XFEL experiments. Among several integrated designs that are mostly results of collaborative work with Professor Alexandra Ros's group, some integrated designs are included in Chapter 6, such as nozzle-mixer integrated design that is introduced in section 6.2,and nozzle-T-Junction integrated design that is introduced in section 6.3.

?? includes some publications that I have contributed to during my Ph.D. period (section A), along with a table of the XFEL experiments the 3D printed devices helped with sample delivery systems (section A.1), introducing some dimensionless numbers that were used in other chapters of the dissertation (section A), some hardware specifications of the microjet test station (section A), some selected drawings of the designs (section A), Setup manual for the double-pulsed PIV imaging configuration (section A), manual for the 3D printed nozzle assembly (section A), operation notes for the Nanoscribe 3D printed device (section A), and obtained permissions for the dissertation (section A).

1.4 Results of the Dissertation

The results of this dissertation is important for the following main reasons:

- It introduces a novel pipeline for the reproducible fabrication of Gas Dynamic Virtual Nozzles by means of two-photon polymerization additive manufacturing technique. These 3D printed devices has been widely used to produce microjets of protein samples that satisfy the requirements of several experiments at the world's most powerful X-Ray laser facilities, such as SLAC national laboratory at Stanford.

- It introduces a novel pipeline of imaging and image analysis based on the particle tracking velocimetry (PTV) technique that can image the microjets and afterward, accurately extract all jet characteristics such as jet velocimetry, jet length, jet deviation angle, and jet jittering. Such high-throughput diagnostic pipelines are highly valuable for the development of new GDVN devices, and they play a vital role in the preparations conducted prior to XFEL experiments.

- It introduces a novel image processing pipeline to accurately assess micron-sized droplets diameters and moreover, to calculate jet diameters beyond the optical resolution of the imaging system.

- It introduces a pipeline to numerically simulate the performance of the GDVNs, that include developing flow field regions from the geometry of GDVNs, building the setup for CFD (computational fluid dynamics) simulation, and processing the results.

Chapter 2

PHYSICS OF GDVN LIQUID MICROJET AND MICRODROPLET PRODUCTION

2.1 An Overview of the Geometry of a GDVN

A picture of an operating GDVN is shown in figure 3.1. As we can see in figure 3.1 [61], the sheath gas focuses the liquid and a micron-sized or submicron-sized liquid jet is achieved. By focusing the liquid with a sheath gas, we can achieve thin liquid jets at lower liquid flow rates than can be achieved with gas-free Rayleigh jets. This results in reduced sample consumption for XFEL experiments, and the use of relatively large-diameter capillaries that enable GDVNs to deliver samples for several hours or days without clogging.

2.2 Physics of Different Operating Regimes of GDVNs

There are two different modes relating to flow focusing jets: the first is the Rayleigh mode [71] in which the droplets form in sizes comparable to the size of the jet diameter, and the second mode is the the Taylor mode [88] in which the droplets are smaller in size than the jet diameter [79]. Generally, liquid jets break up into droplets due to instabilities that originate from interfacial instabilities [30].

Droplet formation can be categorized in two different instability regimes, namely dripping and jetting. In the dripping instability regime, the liquid meniscus breaks up into droplets at the onset of the gas orifice of the nozzle orifice. However, in the jetting mode, droplets form further downstream when the liquid jet breaks up [19]. Jets are formed when the liquid (flow focused fluid) velocity is large enough so that

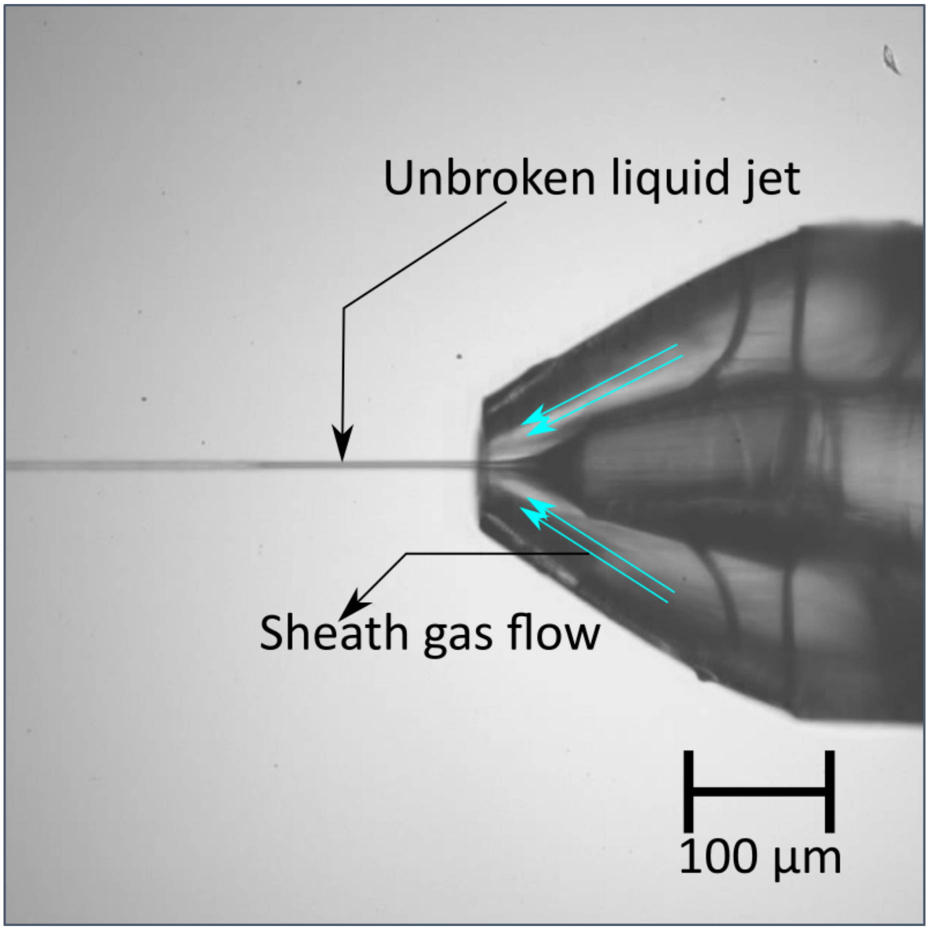

Figure 2.1: A picture of an operating GDVN [61].

inertial forces dominate forces resulting from surface tension at the nozzle tip [91]. The length scales in our study are below the capillary length (defined in section A). Therefore we can neglect the effects of gravity [91]. A third intermediate regime is also observed between dripping and jetting regime, namely intermittent jetting. This regime has been already reported as oscillatory jetting regime by Martínez-Calvo et al. [57]. For a comparatively moderate gas flow rate, jetting regime happens when liquid flow rate is large enough, while dripping regime happens when the flow rate is small enough. Oscillatory jetting is in an intermediate region between dripping and jetting regimes [57]. We characterize the jetting regime as a liquid column that undergoes breaking up into drops as a result of capillary instability waves growth [68], [71].

Transition between dripping to jetting mode corresponds to the transition between convective and absolute instability [59], [90]. Experience showed that dripping-jetting instabilities has hysteresis effect. Hysteresis effect means in the case we are already in jetting mode, the jetting mode sustains even when we lower the gas flow rate beyond the minimum value that is needed to achieve a stable jet. Therefore, the suggestion to have a stable focusing jet is that we start jetting with higher liquid flow rates and afterwards, we lower the liquid flow rate to the desired flow rate value. The reason is that because achieving a stable jet with a higher liquid flow rate value is comparatively easier and after we get a stable jet with a higher liquid flow rate, with lowering the liquid (sample)flow rate, we can take advantage of the Hysteresis effect that helps sustaining the jetting mode.

There is another regime that is observed when the gas flow rate is very high. We have seen in our experiments that by increasing the sheath gas flow rate, we transit from axisymmetric jetting to non-axisymmetric jetting [59]. We also saw in our experiments that there was a maximum gas flow rate threshold to achieve axisymmetric jetting and after that threshold, the jets form the shape of a moving sinusoidal-like shape.

2.3 Global and Local Instability, Absolute and Convective Instability of Flow Focusing Jets

In this section, we briefly demonstrate the concepts of convective/absolute and global/local instabilities. Global and local instability relates to both the jet and also the tapering liquid meniscus [92]. According to Vega et al., there are three regimes, namely steady jetting regime, locally instability regime, and the global instability regime [92].

In the global instability regime, the liquid meniscus is unstable. It is possible to observe the liquid meniscus instability with a good optical system. In the case of local instability regime, the jet is “absolutely” unstable whereas the liquid meniscus is stable. Finally in the case of steady jetting regime, the jet is “convectively” unstable and the meniscus is stable [92], [90].

Vega et al. [92] studied the conditions that result in each of the regimes of steady jetting and local instability regime and global instability regime, and also the conditions that result in transition between the regimes for a flow focusing device that runs water as liquid and has the geometrical specifications of capillary diameter of 200 μm and capillary to orifice distance of 200 μm. They showed their results in terms of different regions in the diagram with liquid jet Reynolds number as the horizontal axis and liquid jet Weber number as the vertical axis in figure 2.2 [92]. For global stability, stability of the liquid meniscus is observed by Vega et al. [92]. The liquid meniscus is defined by the liquid portion placed between the orifice and the end of the liquid line.

Vega et al. [92] stated that there is a threshold for minimum (pure water) liquid flow rate Q_{min} for each value of capillary to orifice distance H, below which the gas focused liquid jet is globally unstable, Moreover, Vega et al. [92] found a minimum critical value of capillary to orifice distance corresponding to each capillary diameter, below which the jet becomes unstable again and a new regime of jet instability, namely “flow burring happens [92]. Some additional studies on flow blurring are also done by Pongvuthithum et al. [69] and Calvo et al. [32].

Viscous effects are added into Rayleigh’s temporal analysis on jet instability by Chandrasekhar [16]. Similar to Chandrasekar [16] that added the effects of the viscosity of the liquid jet to the Rayleigh’s [71] temporal analysis, Leib & Goldstein [49]

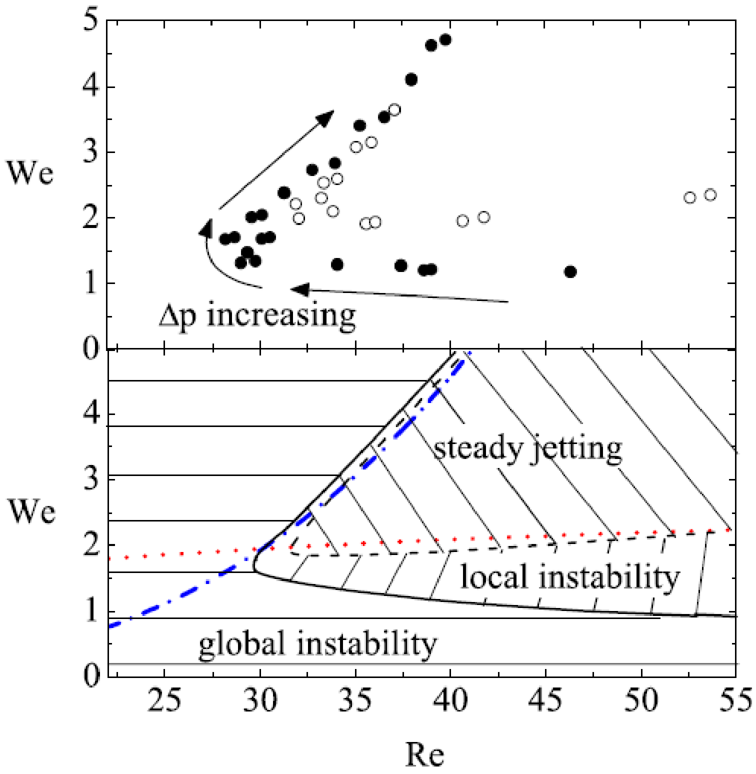

Figure 2.2: Regimes of global and local instabilities [92]. Reproduced from Vega et al. paper [92], with the permission of AIP publishing.

incorporated the viscosity effects to Keller et al. [46] spatial jet instability analysis. However, after Keller et al., Leib & Goldstein [49] showed that for regions with jet Weber numbers of below about three, the jet becomes absolutely unstable and therefore, Keller et al.'s analysis [46] is not valid for these regions. Both Chandrasekar [16] and Leib & Goldstein [49] found that a liquid with a higher viscosity can produce convectively unstable flow focused jets (jetting regime) with wider range of liquid jet Weber numbers since the critical jet Weber number below which convective instability regime transits to absolute instability regime would be lower.

2.3.1 Global and Local Instabilities in Spatially Developing Flows

For global stability, stability of the liquid meniscus is observed by Vega et al. [92] [90] [42]. The liquid meniscus is defined by the liquid portion placed between the orifice and the end of the liquid line. Vega et al. [92] stated that there is a threshold for minimum (pure water) liquid flow rate Q_{min} for each value of capillary to orifice distance H, below which the gas focused liquid jet is globally unstable, Moreover, Vega et al. [92] found a minimum critical value of capillary to orifice distance corresponding to each capillary diameter, below which the jet becomes unstable again and a new regime of jet instability, namely “flow burring happens [92]. Some additional studies on flow blurring are also done by Pongvuthithum et al. [69] and Calvo et al. [32].

2.3.2 Absolute and Convective Instabilities in Spatially Developing Flows

We compare the surface energy with the kinetic energy per unit length. If the relative surface energy dominates the kinetic energy per unit length, absolute instability happens since disturbances can propagate and amplify in both downstream and upstream directions. Otherwise, in the convective instability regime of jets, the disturbances only amplify and propagate in the downstream direction [34].

2.4 Droplet Formation and Droplet and Estimation of Droplet Diameters

Several popular methods for droplet formation will be introduced in this section, and we will explain the reasons for using flow focusing nozzles to produce micron-sized and submicron-sized droplets. Anna et al. observed several modes of droplet breakup [6]. Anna et al. [6] and Vega et al. [92] both confirmed that highly monodisperse droplets result from flow focusing microfluidic nozzles. Anna et al. [6] reported a new breakup mode as the “thread formation” mode that resembles tipstreaming and results in extremely small sub-micron sized droplets [6]. Moreover, Anna et al. [6] characterized the jet thread growth and the maximum jet length as a function of surfactant content and flow variables. According to Vega et al., flow focusing can reach high droplet production rates, up to 10^6 drops/second and also it can produce droplets as small as 500 nm [92].

2.4.1 Different Methods of Producing Micron-sized and Submicron-sized Droplets

He et al. [39] studied electrohydrodynamic jetting for producing submicrometer scale filaments and particles. Basaran et al. [11] also stated that applying an electric field can profoundly affect both dripping and jetting. However, according to Anna et al. [6], particles resulting from electrohydrodynamics jetting are comparatively highly polydisperse. Moreover, imposing electric charge to samples is not desired since it can affect the structure of some biological cells.

According to Anna et al. [6], two principle geometries for production of micro-droplets are so far widely investigated, namely a T-shaped juction [89] and a flow focusing geometry [6]. Flow focusing can reach high droplet production rates, up to 10^6 drops/second and also it can produce droplets as small as 500 nm [92]. Ink jet printers can produce 1000 to 10000 identical drops per second, with droplet sizes ranging from 9.8 to 13.8 μm [11]. Anna et al. [6] and Vega et al. [92] both confirmed that highly monodisperse droplets result from flow focusing microfluidic nozzles. Anna et al. [6] reported a new breakup mode as the “thread formation” mode that resembles tipstreaming and results in extremely small sub-micron sized droplets [6]. Moreover, Anna et al. [6] characterized the jet thread growth and the maximum jet length as a function of surfactant content and flow variables.

Weierstall et al. [95] also used a piezo transducer to vibrate a flow focusing nozzle in order to trigger the droplet breakup into monodispersed sized droplets. Also, Deponte, Weierstall, Spence et al. Triggered the flow focusing nozzle (GDVN) with a piezoelectric actuator and achieved streams of monodisperse droplets of micron and sub-micron size [24].

2.5 Theoretical Estimation of Droplet Diameters Resulting From Breakup of Rayleigh Jets

For nozzle 79 (the design is explained in section A), we compare the jet diameter values for different samples with different viscosities and different surface tensions. That confirms that both surface tension and viscosity does not easily influence the jet diameter, as we can see in formula 2.1 [79].

$$d_1 = \left(\frac{8\rho_l}{\pi^2 \Delta P_g}\right)^{1/4} {Q_l}^{1/2} \tag{2.1}$$

To estimate droplet diameter, we can theoretically estimate for the dominant wavelength of which results in the jet breakup. Temporal instability analysis done by lord Rayleigh [71] demonstrates the ratio of wave-length to diameter for the moderately disturbance leading to the disintegration of the cylindrical jet most rapidly as [71]:

$$\lambda = 4.508 * 2a \tag{2.2}$$

In which λ is the wavelength of the dominant perturbations and a is the jet radius.

However, after Rayleigh that has done temporal instability analysis of liquid jets [71], Keller et al. [46] did some spatial instability analyses on liquid jet breakup. Opposed to the temporal instability analysis, in spatial instability analysis [46], the wavenumber of disturbances K is considered to be complex while the frequency of disturbances σ would be considered to be real.

After Rayleigh [71] and keller et al. [46], Leib & Goldstein [50] has done theoretical instability study for the semi-infhite jet/semi-infinite nozzle configuration instead of the doubly infinite jet. Leib & Goldstein did theoretical investigation on absolute and convective instability regimes without including the effects of viscosity [50]. For capillary or Rayleigh waves, Leib & Goldstein were the first persons who noted the existence of absolute instability.

Chapter 3

3D PRINTING OF GAS-DYNAMIC VIRTUAL NOZZLES AND OPTICAL CHARACTERIZATION OF HIGH-SPEED MICROJETS

3.1 Abstract

Gas Dynamic Virtual Nozzles (GDVNs) produce microscopic flow-focused liquid jets and droplets and play an important role at X-ray free-electron laser (XFEL) facilities where they are used to steer a stream of hydrated biomolecules into an X-ray focus during diffraction measurements. Highly stable and reproducible microjet and microdroplets are desired, as are flexible fabrication methods that enable integrated mixing microfluidics, droplet triggering mechanisms, laser illumination, and other customized features. In this study, we develop the use of high-resolution 3D nano-printing for the production of monolithic, asymmetric GDVN designs that are difficult to fabricate by other means. We also develop a dual-pulsed nanosecond image acquisition and analysis platform for the characterization of GDVN performance, including jet speed, length, diameter, and directionality, among others. We show that printed GDVNs can form microjets with very high degree of reproducibility, down to sub-micron diameters, and with water jet speeds beyond 170 m/s.

3.2 Introduction

Gas Dynamic Virtual Nozzles (GDVN) produce microscopic flow-focused liquid jets and microdroplets [31] that may be used for applications in the food and pharmaceutical industries. An important application of GDVNs is at X-ray free-electron laser (XFEL) facilities, where they are used to deliver hydrated biomolecules into an intense micro-focused X-ray beam in order to make ultrafast diffraction measurements. XFELs generate X-ray pulses with mJ pulse energies that cause catastrophic destruction of the liquid jet and the protein sample, but the ~10-femtosecond duration (10^{-14} seconds) of the X-ray pulses allows for the formation of atomic-resolution images that are free of damage through the "diffraction-before-destruction" paradigm [63]. High-speed liquid jets allow for high-frequency data collection because the liquid jet recovers prior to the subsequent XFEL pulse [82]. GDVNs are therefore likely to be of great importance to the development of mixing enzymology studies at MHz XFEL facilities, for example [17].

The idea of using GDVNs to produce microjets was first introduced in 1998 [31], and a variety of miniaturized GDVNs were developed for serial femtosecond crystallography [94]. The early methods of hand-fabricating individual GDVNs are tedious and time-consuming, and the resulting nozzle and jet characteristics vary from one GDVN to the next. This prompted efforts to develop automated and reproducible fabrication methods, such as the ceramic micro-injection molded nozzles introduced in 2015 [15]. The application of three-dimensional printing for fabricating GDVNs was also introduced in 2015 [62] and has been under development since then [47]. This paper we further develop the use of 3D nano-printing for the production of asymmetric nozzles that create reproducible flow focusing jets, high-speed jets, and also sub-micrometer jets. The jet characteristics of two different 3D printed devices are quantified, and an all-optical GDVN testing and analysis platform is presented that can measure high-speed jets with diameters less than the resolution of the imaging optics.

3.3 Overview of Gas-dynamic Virtual Nozzles

3.3.1 Basic Principles of Flow-focused Liquid Microjet Formation

An operating GDVN is shown in figure 3.1. A sheath gas indicated by the arrows focuses the liquid into a microjet through pressure- and shear-driven acceleration. By focusing the liquid with a gas rather than a solid orifice, GDVNs can deliver solutions of protein microcrystals through channels of diameter ∼50 μm rather than ∼5 μm, which enables jetting for several hours or days without clogging. Other aspects of GDVN performance that are of great relevance to XFEL studies are the jet diameter, jet length, droplet diameter, and overall stability.

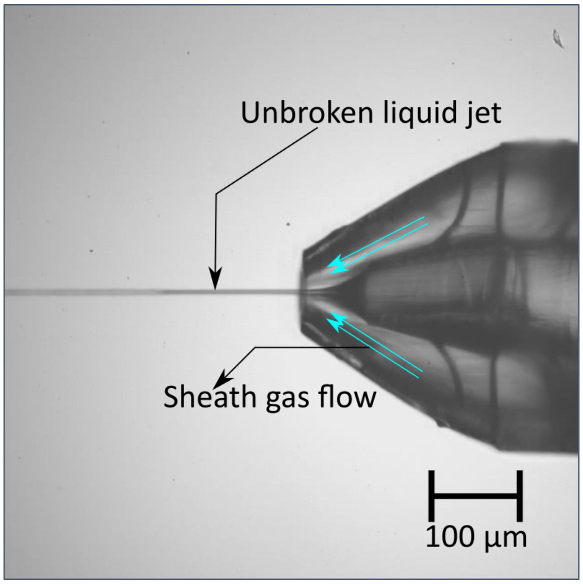

Figure 3.1: A picture of an operating GDVN [61].

There are two primary modes relating to flow focused jets: the first is the Rayleigh mode (Rayleigh 1878) [71] in which droplets form with sizes larger than the jet diameter. In the Rayleigh mode, the liquid jet breaks up into droplets due to instabilities that originate from interfacial instabilities [30]. Surface tension forces and liquid inertia initiate axisymmetric oscillations in the liquid jet. These oscillations grow as they are convected downstream of the liquid jet and finally cause the jet to break up [12]. In the second mode, namely the Taylor mode (Taylor 1963) [88, 79], droplets of sizes comparable to the jet diameter or much smaller than the jet diameter are formed. The Taylor regime, or first-wind-induced regime, can be achieved by increasing the sheath gas flow rate to increase the aerodynamic effects of the sheath gas. This is the appropriate mode of operation when faster jets and smaller droplets are desired.

Droplet formation is often categorized into dripping and jetting instability regimes. In the dripping regime, the liquid meniscus breaks up into droplets at the nozzle orifice and a stable jet is not formed. Stable jets are formed when the liquid (flow-focused fluid) velocity is large enough such that inertial forces dominate surface tension forces at the nozzle tip [91]. Droplets form further downstream and this mechanism determines the length of the liquid jet [19]. The transition between dripping and jetting corresponds to the transition between convective and absolute instability [59, 90]. A hysteresis can be observed in which a jet is sustained even when the gas flow drops below the minimum value that is needed to initiate the jet. In practice, jets containing protein samples cannot be sustained for extended periods when operating in the hysteresis regime. A third regime, known as the first-wind-induced regime, is observed when the gas flow rate is very high, and axisymmetric jetting transitions to non-axisymmetric jetting with sinusoidal oscillations [59].

3.3.2 Nozzle Design Goals

Our primary objectives in the present work are to (1) establish 3D printing methods for monolithic GDVNs that yield highly reproducible jet behaviors, and (2) develop new asymmetric nozzle designs that produce high-speed jets for data collection MHz XFEL sources, as well as sub-micrometer jets for nebulizing protein samples into nanodrops without high voltages as in electrospray devices. Our nozzle designs were inspired by our previous empirical observations in addition to published investigations into the roles of nozzle geometry and fluid properties in the processes of jet and droplet formation [48, 92, 101]. In particular, we employ the design concept proposed by Acero *et. al.* [2] who studied asymmetric nozzles based on hypodermic syringes that produce stable jets in a wide range of operating conditions, including very low liquid flow rates.

Based on these previous studies in the literature, we varied several geometrical parameters in the GDVN design. After testing several prototypes and printing processes, we focused on two designs that can jet in a wide range of operating conditions to satisfy the requirements of XFEL experiments. Details of the two designs and their performance are discussed in the following sections.

3.3.3 Asymmetric Nozzles for Fast Jets

Figure 3.3 shows a 3D printed nozzle design with a liquid channel that terminates with a syringe-like shape. This asymmetric design results in a Couette-type flow field in which a shear-driven liquid stream can accelerate along the surface of the syringe and reduces in size before the free-standing jet is launched from the syringe tip. The increased liquid kinetic energy helps overcome surface tension resistance, and the Couette-type flow field avoids recirculation patterns and related instabilities [2]. By placing the tip of the syringe near to the sheath gas aperture, we exploited empirical observations suggesting that jets formed in the rapid gas expansion region have increased stability at high gas pressures [33]. Our testing results suggest that these combined features allow for increased sheath gas flow rates as well as reduced liquid flow rates, which in turn enables the formation of smaller and/or faster jets (down to sub-μm diameters, and speeds of 170 m/s, in the case of water jets). Although small and/or high-speed jets are not always needed, the increased range of operating conditions increases the possibility of achieving stable jets from samples having complex viscoelastic properties.

Design 1

Our first nozzle design (referred to as “Design 1”) is shown in figure A.5. The upstream end of the nozzle has two circular channels that accept 360 μm OD (outer diameter) glass capillaries that transport the liquid and gas to the nozzle. These capillaries are epoxied in place. The liquid line thickness is varied smoothly throughout the liquid flow field to minimize the possibility of clogging while maintaining a small exit orifice in order to achieve higher jet velocities. Due to the syringe shape, the liquid line tip has an elliptical cross-sectional shape with minor/major axis diameters of 40 μm and 97 μm, respectively. Testing results showed that under certain operating conditions, fast liquid water jets with velocities of higher than 170 m/sec can be produced from this design.

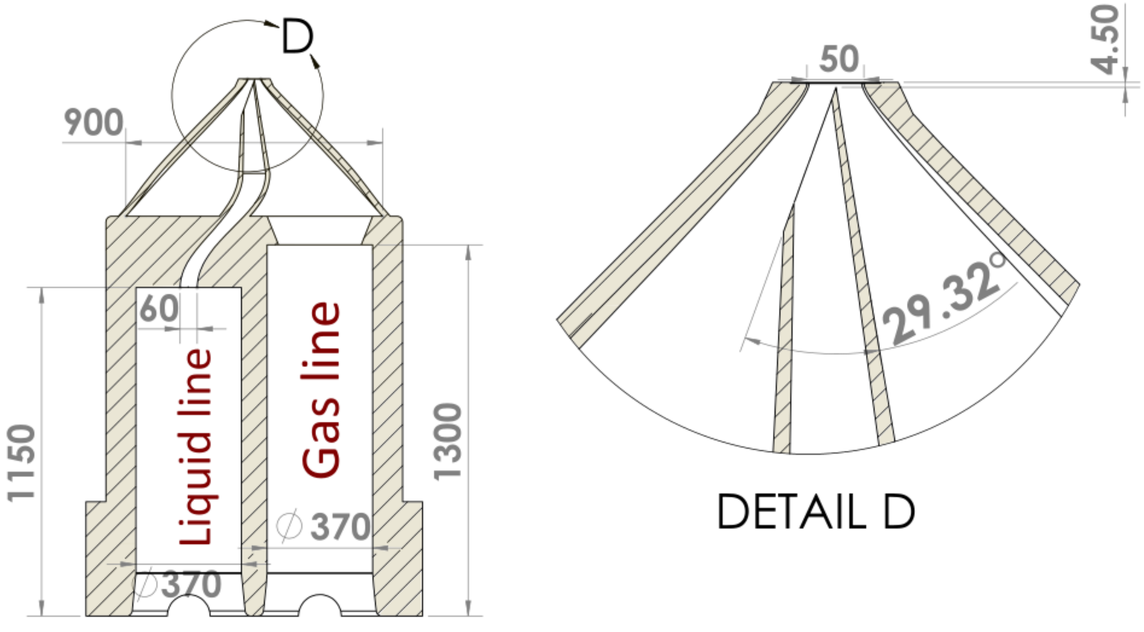

Figure 3.2: Design dimensions of design 1 in micrometers.

Design 2

Design 2, shown in figure 3.3, has a straight liquid channel in order to be more robust against clogging than Design 1. The smaller overall volume of the nozzle also reduces the printing time by roughly 40 minutes. The elliptical cross section of the syringed liquid orifice has minor/major axis diameters of 50 μm and 146 μm, respectively (the eccentricity is larger than Design 1 due to the smaller syringe angle of 20°). The liquid line diameter is smaller than Design 1, and testing results show that a device from this design achieves a maximum water jet velocity of approximately 140 m/s, which is approximately 25% lower than in Design 1.

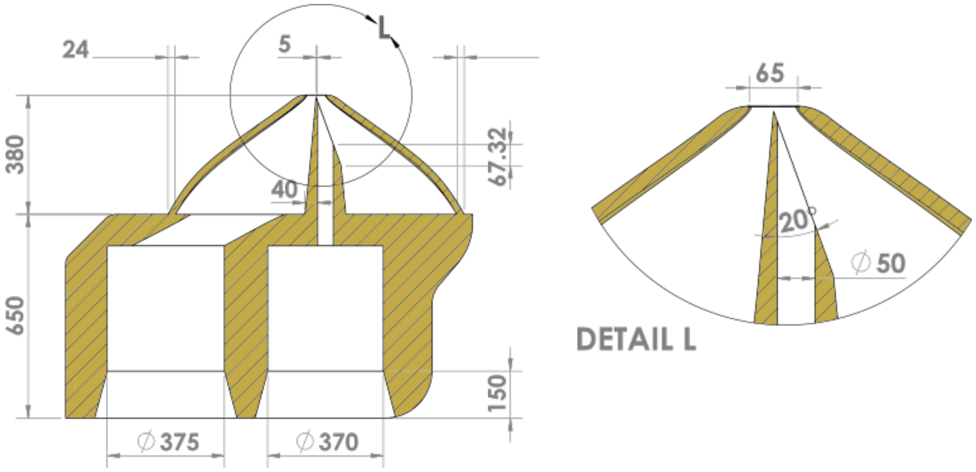

Figure 3.3: Drawing of the nozzle design 2 (dimensions are in micrometers).

3.4 Nozzle Fabrication and Assembly

3.4.1 3d Printing With 2-photon Polymerization

Since the 1990s, the availability of sub-picosecond pulsed lasers enabled broad experimental investigations into two-photon absorption phenomena and related technological applications [36, 45, 67]. Two-photon absorption cross sections increase with the square of the light intensity, which enables higher spatial resolution in laser lithography applications than is achievable with single-photon techniques. In the work presented here, we utilized a Nanoscribe Photonic Professional (GT) laser lithography printer that can achieve ∼200 nm resolution through two-photon polymerization (2PP) direct laser writing. This printer scans an 80 MHz pulsed laser of 780-nm center wavelength, 100 femtosecond pulse duration, and 25KW peak power within a liquid photoresist, which causes rapid polymerization upon exposure. Smaller volumes of up to approximately $300 \times 300 \times 300\ \mu\text{m}^3$ can be printed with rapid-scanning mirrors, whereas larger print volumes utilize the scanning mirrors in conjunction with a 3-axis piezoelectric stage that translate the printed object. Once the laser polymerization stage is completed, the unpolymerized liquid photoresist is washed away during the development process.

Nozzles were composed of IP-S photoresist (Nanoscribe item no. 1907/2006 (REACH)). Depending on the design, each nozzle required 35 minutes to a few hours to print. After printing, the nozzles were developed by placing them in a bath of the developer liquid (MICROCHEM SU-8 developer (CAS Number: 108-65-6)) for 35 minutes followed by Isopropanol for 5 minutes. Following development, the 360 μm OD polyimide-coated fused silica capillaries (Molex) were attached to the liquid and gas inlets with 5-minute epoxy (Hardman double bubble red). Finally, the capillaries were fed through a 1/16-inch OD metal sleeve (IDEX U-115) and epoxied in place in order to mount the nozzles and form a vacuum seal. Figure 3.4 shows an optical image of an assembled nozzle. Figure 3.5 shows SEM (scanning electron microscopy) images of a nozzle from the Design 2 in which only half of the nozzle was printed in order to expose the inner features.

The magnification of the objective lens used in this work was 25× with numerical aperture of 1.4. Nozzles were printed using the “dip in” mode in which the photoresist completely fills the space between the glass substrate and the objective lens. Since the scanning range of the printer with this objective is limited to 200 μm in the horizontal and vertical dimensions (where vertical is defined by the optical axis and horizontal by the plane of the substrate), the nozzle geometry is subdivided into several blocks. The laser polymerizes one block at a time in an orderly manner from bottom to top in such a way that each block is supported by the substrate or the lower block. To prevent floating blocks, cavities with sharp angles of more than about 70 degrees from the vertical are avoided in our designs [54]. The amount of laser overlap, or "stitching", between the blocks was 2 μm for horizontal block walls and 1 μm for vertical block walls. The block walls have an angle of approximately 15° from the vertical in order to minimize multiple exposures by the laser beam. Each block is subdivided into horizontal planes, or "slices", with an inter-slice distance of 1 μm.

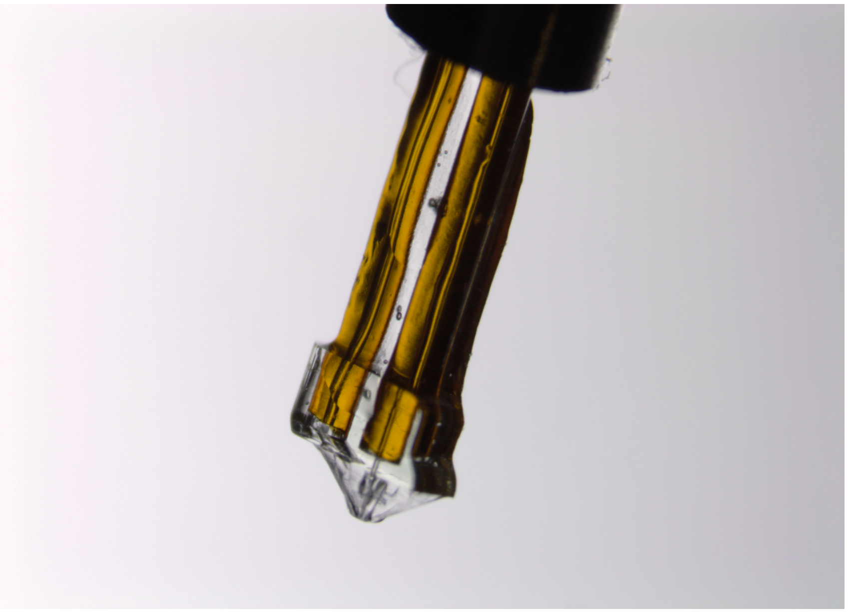

Figure 3.4: An assembled 3D printed nozzle.

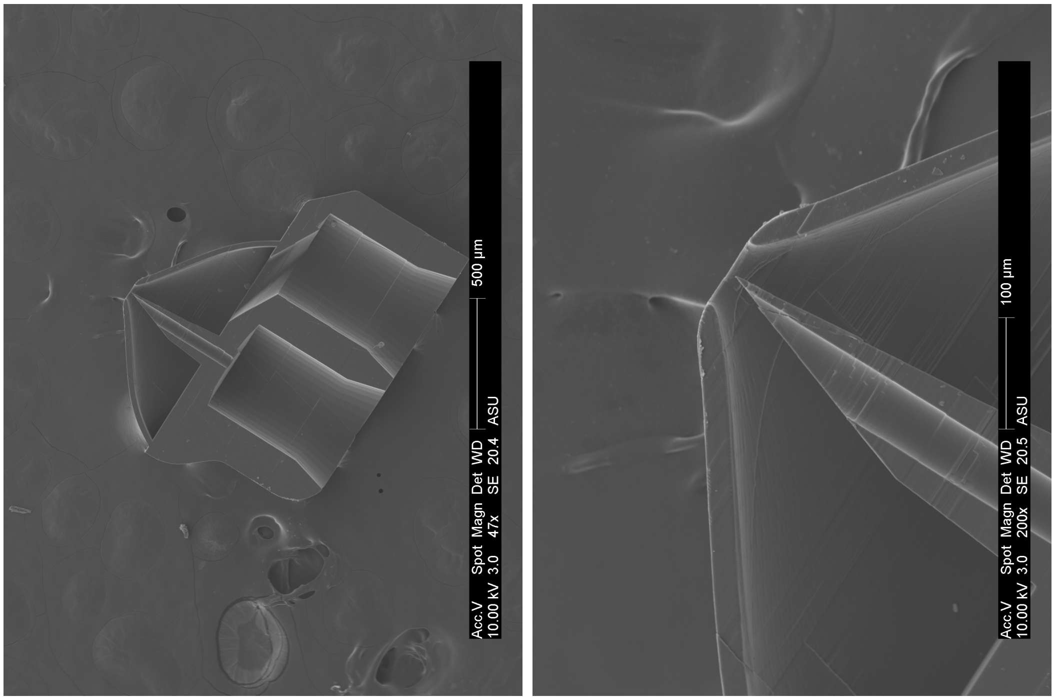

Figure 3.5: SEM images of a nozzle from design 2. Only half of the nozzle was printed in order to reveal the internal structure.

3.5 Procedures for Quantifying GDVN Performance

3.5.1 Overview of Nozzle Testing Station

A schematic of the test station we used to characterize liquid jets is shown in figure 3.6. The station records images of liquid jets while monitoring operational parameters, including upstream sheath gas pressure, upstream liquid pressure, gas flow rate, liquid flow rate, and vacuum pressure. A double-pulsed fiber-coupled 100-ns laser with 633 nm wavelength illuminates the jet, while a high-speed camera and optical lenses gather image data. This system, combined with the image processing methods discussed below, enables accurate statistical quantification of jet characteristics such as jet velocity, jet length, jet diameter, and jet deviation angle, as well as droplet diameters. The data processing scheme described below allows for the accurate determination of sub-μm jet diameters because the calculations are based on observed droplet centroid translations that can be determined with a much better resolution than that of the optical system. This scheme is similar to other super-resolution optical localization microscopy techniques [93].

The test station setup makes it possible to easily run the GDVNs with a controllable sheath gas pressure or mass flow rate and to switch between different gases such as helium and nitrogen. The pressure of the sheath is measured at the inlet of the glass capillary. We typically test GDVNs with helium because the gas composition strongly affects jet behavior, with helium being most favorable, and because XFEL experiments rely on helium due to its low X-ray scattering cross section.

Liquids are supplied to the GDVNs by either high-pressure liquid chromatography (HPLC) pump or pressurized liquid reservoir. The liquid flow rate is measured by volumetric flow sensors. The HPLC pump can supply liquid flow rates with 0.1 μl/min accuracy. A liquid switch with 6 different entrance lines and one exit line allows for rapid switching between sample liquids or a purging gas. After each test, liquid is purged with water and/or isopropanol before purging the liquid with nitrogen gas.

The sealed vacuum chamber consists of a rectangular tube with glass windows and a quick-connect fitting that accepts various types of nozzle mountings. A dry scroll pump is used to evacuate the chamber and typically results in pressures of the order 0.1 mbar. The imaging system consists of a 10X Mitutoyo long working distance objective paired with a variable Navitar 12X UltraZoom magnifying lens, and has a working distance of 3.5 mm. The bright-field illumination source consists of a 400 μm diameter optical fiber that is re-imaged 1:1 to a ~400-μm spot at the focal plane with a single bi-convex lens. At our operational wavelength $\lambda = 633$ nm, the numerical aperture of the objective is NA $= 0.28$, which yields a maximum resolution of $\frac{\lambda}{2*\mathrm{NA}} \approx 1.1\ \mu$m.

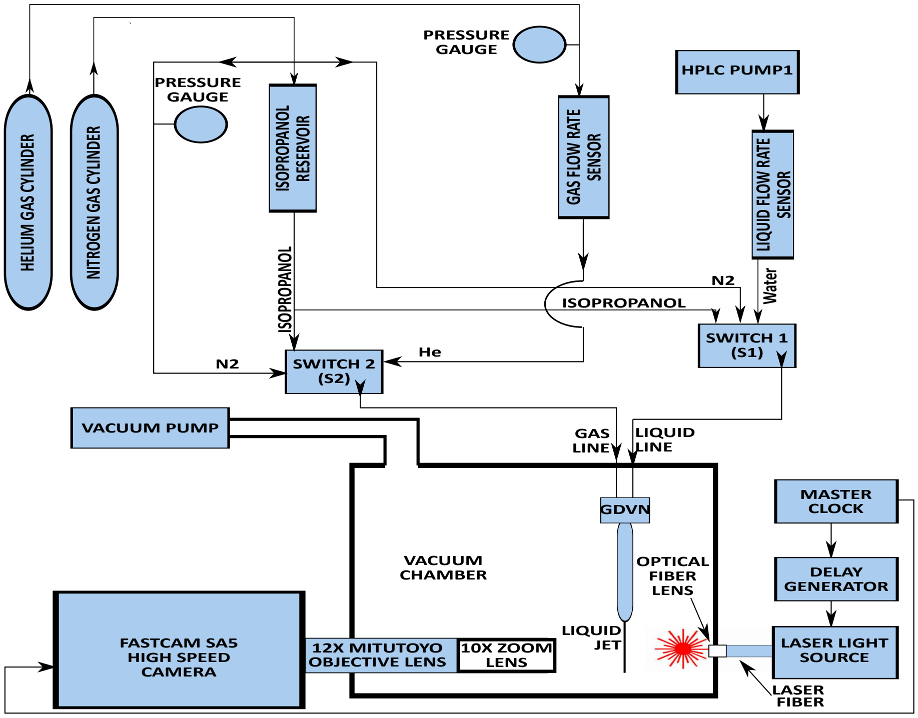

Figure 3.6: Schematic of the test station. Helium gas drives the liquid jet and the pressure and mass flow rate are monitored upstream of the glass capillary that leads to the nozzle. An HPLC pump drives the liquid (water) and a flowmeter measures its volumetric flow rate. Nitrogen gas and IsoPropanol are used to clean and dry nozzles, particularly when running samples other than water. The nozzle is located in a small chamber at ∼1 mbar pressure. A pulsed ∼100 ns laser provides brightfield illumination for the high-frame-rate camera, and electronic delay system allows for doublets of images.

3.5.2 Image Processing and Analysis

To extract the desired jet characteristics from the acquired images, we identified and separated regions in the images corresponding to the jet and droplets. Jet length and jet deviation angles were readily determined from individual images, whereas pairs of 100-ns exposures separated in time by 500 ns were used to quantify droplet speeds through Particle Tracking Velocimetry (PTV) methods [4]. By determining droplet speeds, along with measured liquid flow rates, we were able to determine liquid jet diameters at resolutions better than can be achieved by individual images.

We first subtracted the image backgrounds from the raw images (see figure 3.7(a)) due to the bright-field laser illumination. This step was important because the multimode optical fiber used to illuminate the jet creates a non-uniform background illumination with fluctuations due to coherent speckle. Backgrounds were estimated with a FIJI ImageJ [77] plugin that implements the rolling ball algorithm [84]. For each pixel, the average within a circle of diameter 50 pixels was subtracted from the pixel value in the original image.

After subtracting image background, we converted the resulting 16-bit images to binary images using the IsoData thresholding algorithm [72], which performed best when compared against other algorithms available in FIJI ImageJ. The IsoData technique uses an iterative approach to automatically optimize the threshold selection as long as the image contains an object (jet and droplet regions in our study) and background that have different average gray levels. Figure 3.7(b) shows a binary image after applying IsoData to the image.

From the binary images, droplet and jet regions were identified and extracted using Fiji Imagej plugins with some customization [77, 74, 78]. The binary stack of images were divided into two substacks: the first substack includes only the continuous jet regions before primary breakup, with the droplets removed, while the second substack contains only the droplets that form after the jet breakup. Jet regions were identified as regions in the binary images with size larger than a threshold value and circularity lower than a threshold value. Extracted jet and droplet regions are illustrated in figures 3.7(c) and 3.7(d).

After extracting jet regions, we determined jet deviation angles by fitting an ellipse to each jet region. The angle of the major axis of the ellipse corresponds to the jet deviation angle. Jet lengths were quantified by the smallest rectangle that enclosed each jet region. The length of the rectangle along the jet propagation direction was taken as the jet length, but it is noteworthy that this is an overestimate because diffraction is typically recorded from a point upstream of the droplet breakup region. In practice, the effective length corresponds to the point at which X-ray surface scatter is condensed into a stable streak; i.e. we avoid exposing regions of the jet that have significant surface capillary waves.

Droplet regions were extracted with an open-source macro code that implements Hough circle transforms [70]. Afterwards, a Matlab code was used to implement Particle Tracking Velocimetry [3] of droplets in successive images to determine jet velocities. An example of extracted droplets regions from a pair of frames delayed by 550 ns is shown in figure 3.7(d). By comparing the horizontal center-of-mass coordinates of droplet pairs, and the time delay between pairs of frames, the horizontal velocities of droplets were calculated from the finite difference measurements. For each dataset with a unique set of flow conditions, three different image pairs were used to estimate droplet velocities.

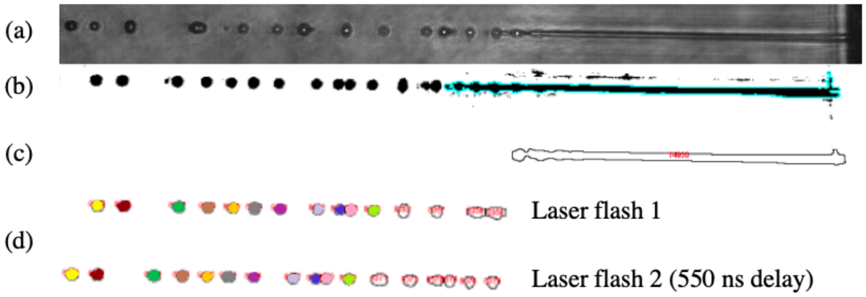

Figure 3.7: Illustration of image processing steps. (a) raw image before processing steps. (b) binary image after background subtraction and thresholding. (c) perimeter of extracted jet region. (d) pair of extracted droplet series separated in time by 550 ns. The droplet colors indicate matching droplets in the image pair.

3.6 Results of Nozzle Testing

We thoroughly tested nozzle designs 1 and 2 with pure water using the data acquisition and analysis procedures described above. In each case, we printed a batch of five nozzles and recorded image pairs at a variety of liquid and gas flow rates, as detailed below.

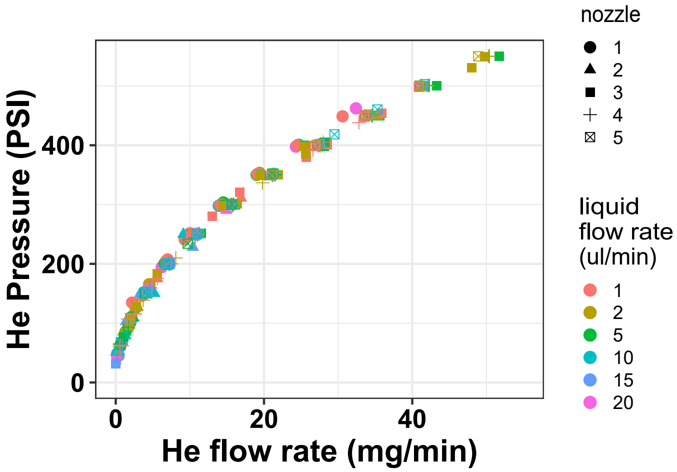

Figure 3.8: He pressure at the inlet of the gas capillary versus Helium flow rate for a nozzle of design 1, showing that the liquid flow does not effect the gas flow in the measurements.

3.6.1 Sheath Gas Flow Rates and Pressures

The helium sheath mass flow rate in a GDVN depends on the inlet pressure along with the pressure head loss in the microcapillaries, and the nozzle aperture size and geometry. Figure 3.8 shows that the liquid flow rate value does not affect the helium mass flow rate, thus we can fully determine the operating condition of the nozzle by considering only the sheath gas mass flow rate and the liquid flow rates for a particular nozzle design.

3.6.2 Jet Velocities

High-speed jets of approximately 80 m/s are required in MHz XFEL serial diffraction because the intense X-ray pulses cause explosions that result in gaps in the jets,

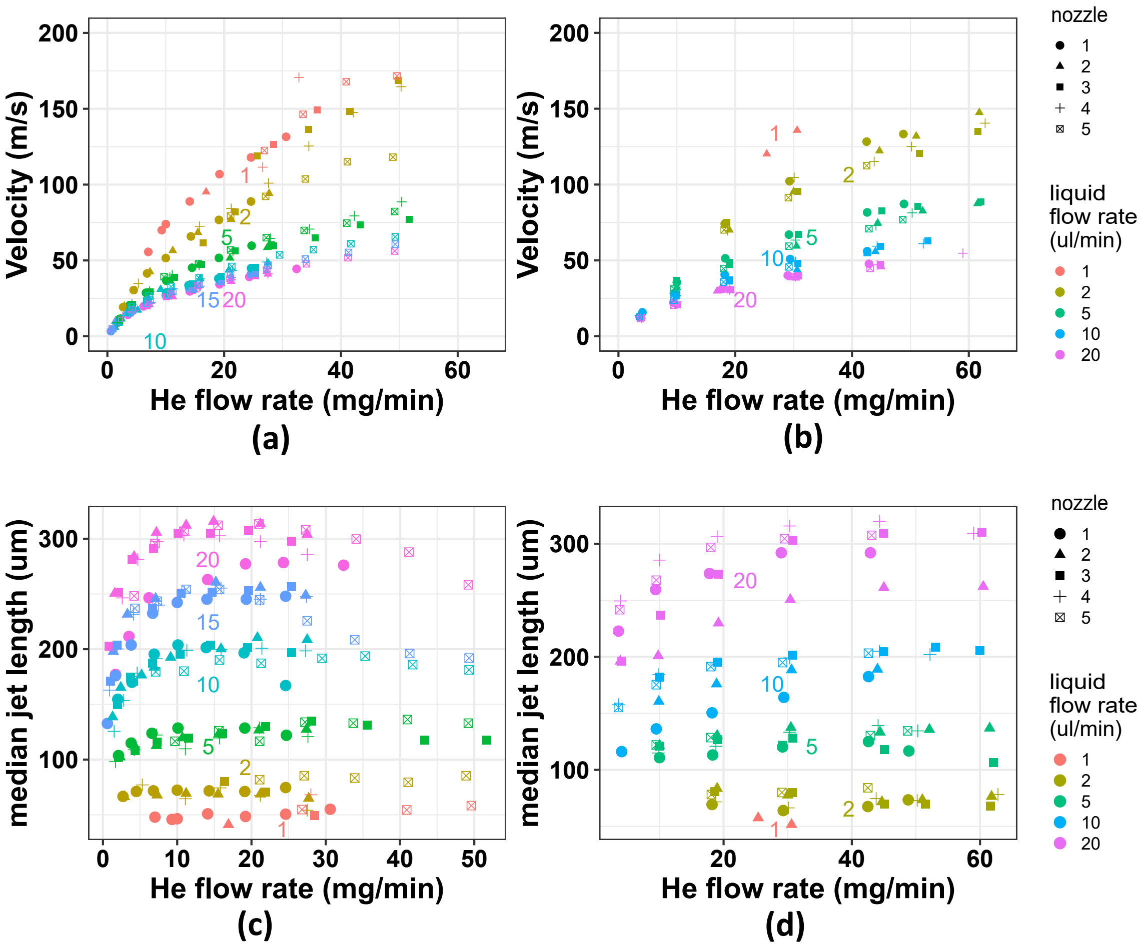

(a) (b) (c) (d)

Figure 3.9: (a) plots of jet velocity versus helium flow rate for different liquid (water) flow rates for 5 different nozzles from design 1 and (b) 5 different nozzles from design 2. (c) plots of jet length versus helium flow rate for different liquid (water) flow rates for 5 different nozzles from design 1 and (d) 5 different nozzles from design 2. Symbol colors distinguish liquid flow rates, while symbol shapes distinguish different nozzles.

and the jets must therefore be fast enough to displace the gap before the subsequent X-ray pulse arrives [96, 97]. Since liquid acceleration is very low beyond the first few hundred micrometers downstream of the orifice, even after breaking up of the jet to droplets [103, 58], the calculated droplet velocities are a good approximation of the jet velocities. Figures 3.9 show the jet velocities estimated by these means for nozzle designs 1 and 2. These figures show that the jet velocity highly depends on liquid and gas flow rates, and it monotonically increases with increasing sheath gas flow rate

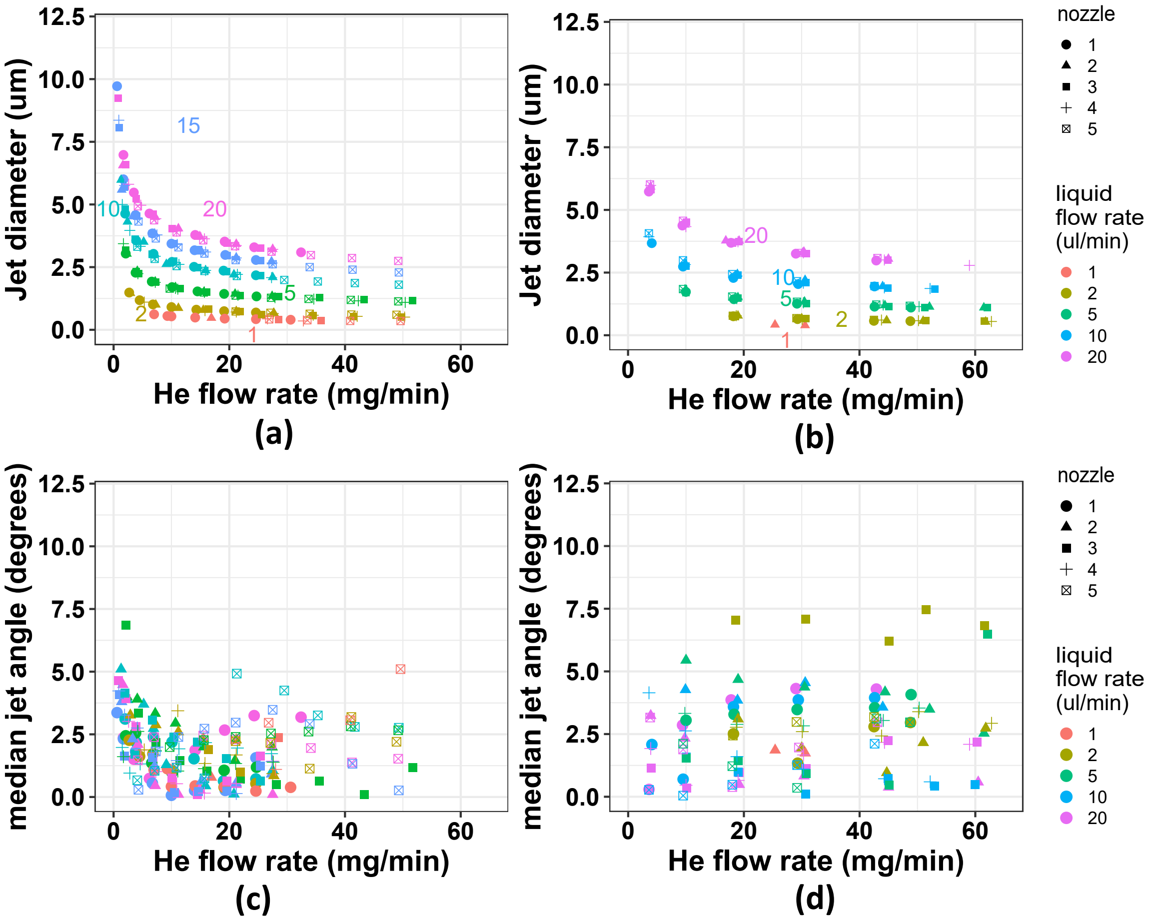

Figure 3.10: (a) jet diameter versus helium flow rate for different liquid (water) flow rates for 5 different nozzles from design 1 and (b) 5 different nozzles from design 2. (c) jet angle versus Helium flow rate for different liquid (water) flow rates for 5 different nozzles from design 1 and (d) 5 different nozzles from design 2. Symbol colors distinguish liquid flow rates, while symbol shapes distinguish different nozzles.

and decreasing liquid flow rate. The fastest jets are achieved when the liquid flow rate is relatively low (below approximately 5 μl/min). By comparing Design 1 with Design 2 in figure 3.9, the observed jet velocities for Design 1 are higher under similar operating conditions, which is most likely because the dimensions of the liquid line tip for Design 1 are smaller. Design 1 achieved maximum jet velocities of approximately 170 m/s, whereas Design 2 achieved maximum jet velocities of approximately 140 m/s. It should be noted that these high-speed jets were less repeatable than jets with speeds closer to 100 m/s, and that further investigations are needed in order to determine the speeds of liquids with higher viscosity and which carry microcrystals.

3.6.3 Jet Lengths

It is important to characterize GDVN jet lengths because the X-ray beam should be located at a distance of approximately 75 μm or more from the nozzle tip in order to avoid additional background scatter from the nozzle material. We can see in almost all cases of figures 3.9, the jet length increases with increasing liquid flow rate. At constant liquid flow rate, the jet length increases with increasing sheath gas flow rate until a maximum value is achieved at approximately 10 mg/min helium, after which the jet length is largely independent of the gas flow rate. Increasing sheath gas flow rates eventually causes a reduction in jet lengths that may be associated with the onset of whipping instabilities [41]. Since in XFEL experiments we almost always run GDVNs with sheath gas flow rates of more than 20 mg/min to be far from the jetting to dripping transition regime, liquid flow rates of roughly 5 μl/min should generally produce jets of sufficient length.

3.6.4 Jet Diameters

Jet diameter is an important characteristic in XFEL experiments because it determines the amount of solution scatter, and also because the size of the gap that is produced when X-rays impact the jet is dependent on the jet diameter [82]. Jet diameters may be determined from jet velocities along with the liquid volumetric flow rate according to the relation $D_j = 2\sqrt{\frac{\pi Q}{v}}$, where v is the jet speed and Q the volumetric liquid flow rate. We can see from figures 3.10 that the estimated jet diameter is mostly dependent on the liquid flow rate for He flow rates of greater than approximately 10 mg/min, while the helium sheath gas flow rate plays the secondary role.

Since we almost always run the GDVNs in the operating conditions of the sheath gas higher than 20 mg/min in XFEL experiments, the liquid flow rate is the dominant factor that affects the jet diameter.

3.6.5 Jet Deviation Angles

Jet deviation angles are important because if a jet emits at a large angle (approximately 10° or more) with respect to the nozzle, the jet may collide with the sidewalls of the vacuum chamber, which causes the formation of ice pillars that grow rapidly as successive droplets freeze on top of the others. These ice pillars may grow at rates of several cm/s and thus can rapidly reach the nozzle orifice and plug the nozzle. Due to the reproducibility of 3D printed nozzles, nearly all jets formed with deviation angles of less than 5°, as shown in figure 3.10.

3.6.6 Jet Performance and Reproducibility

The integrated plots of median jet length 3.9c 3.9d, jet velocity 3.9a 3.9b, calculated jet diameter 3.10a 3.10b and median jet angle 3.10c 3.10d versus He flow rate for five different nozzles from either Design 1 or Design 2 show that different nozzles from a similar design have acceptable performance consistency.

3.6.7 Droplet Diameters

The ratio of jet diameter to droplet diameter is indicative of the mechanism of droplet formation. From the captured droplet images, we can estimate the droplet image diameters from the area A of each droplet image according to the formula $D'_d = 2\sqrt{A/\pi}$. Figures 3.11b and 3.10c show the resulting mean and standard deviations after calculating the droplet image areas of more than 3000 droplets for each flow-rate condition for a nozzle from Design 2 running with pure water. It is evident that there is a linear relationship between droplet image diameters and the jet diameters D_j estimated via the two-flash image analysis results presented in section 3.6.4. The fitted regression line yields the formula

$$D_d = 2.01D_j + 1.95\ \mu\text{m} \tag{3.1}$$

with an R-squared value of 0.98. The non-zero intercept value of 1.95 μm after curve fitting is due to the limited resolution (or “blurring”) of the optical system, which is expected because the images result from the convolution of the focal plane with the point spread function of the optics. The size of the optical point spread function is close to twice the nominal 1.1 μm resolution of our optical system. We confirmed that the 1.95 μm offset was indeed due to the optical system by measuring the jet image diameters D'_j with the same image thresholding scheme, which resulted in the relation $D'_j = 1.03D_j + 1.86\ \mu$m; the offset of 1.86 μm is very similar to that associated with the droplet analysis. We conclude that the actual droplet diameters are related to the actual jet diameters by the relation $D_d = 2.01D_j$, and that this relation holds for all of the observed gas and liquid flow rates. The slope of 2.01 suggests that the Rayleigh instability is the dominant jet breakup mechanism, since it predicts a slope of approximately 1.9 [71].

3.6.8 Estimation of Internal Nozzle Gas Pressure

During the typical operation of a GDVN at an XFEL experiment, gas pressure measurements are made at the inlet of a ∼1-2 m length of capillary, which often results in a poor estimate of the internal nozzle pressure due to the significant pressure drop along the length of the capillary. Estimates of the internal pressure of the nozzle, where the liquid jets are formed, are important because we aim to design nozzles that can withstand the internal pressures with minimal wall thickness (and hence printing

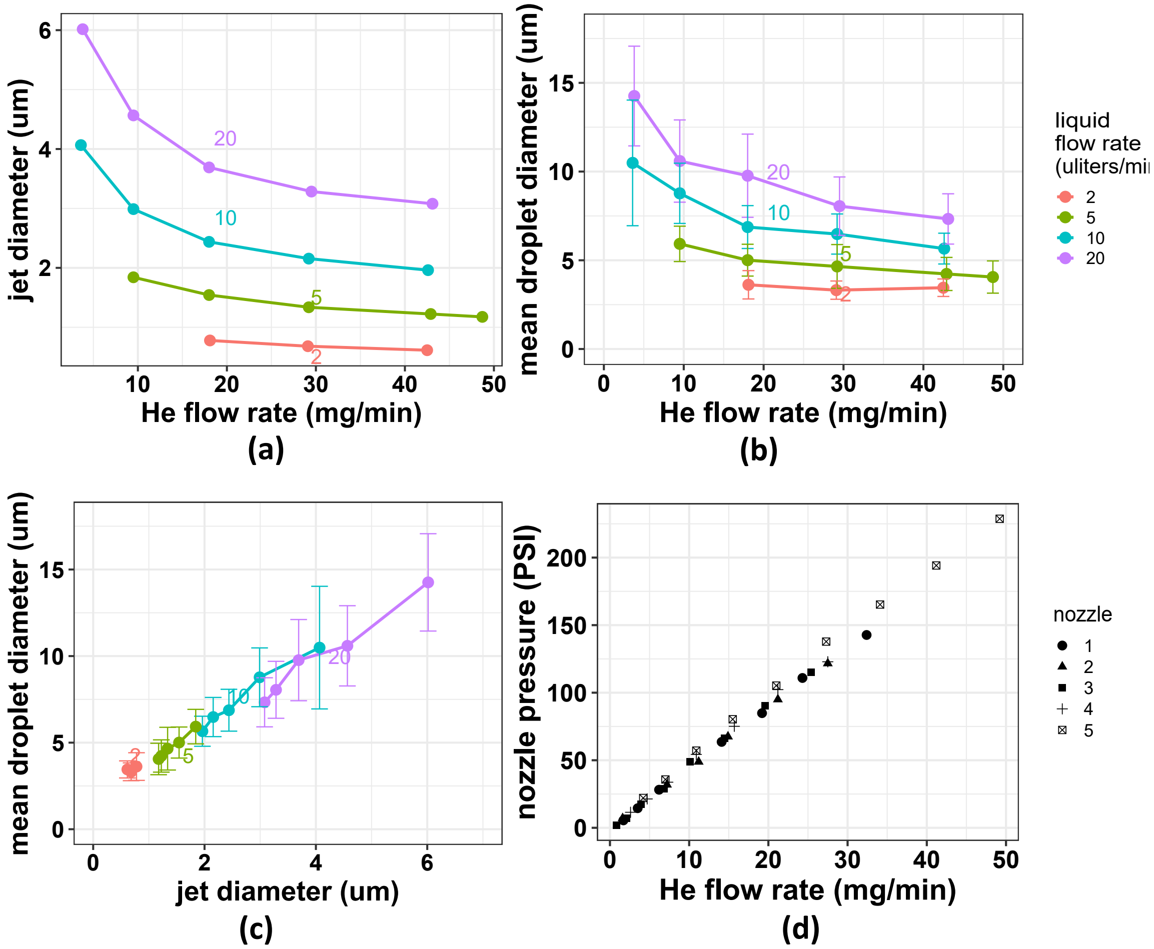

Figure 3.11: (a) jet diameter versus Helium flow rate for different liquid (water) flow rates for a nozzle from design 2. (b) median droplet diameter versus helium flow rate for different liquid (water) flow rates for a nozzle from design 2. (c) median droplet diameter versus calculated jet diameter for a nozzle from design 2. (d) plot of estimated pressure inside the nozzle versus liquid jet Reynolds number for 5 nozzles from design 1 under different operating conditions.

time), and we also wish to relate the characteristics of the liquid jet to the inertial pressure, viscous, and surface-tension forces. Since we do not have a transducer that measures pressure directly within the nozzle, we instead estimate the internal pressure via energy conservation equations.

The Reynolds and Weber numbers are important dimensionless quantities that characterize the regimes of jet and drop formation. The Reynolds number represents the magnitude of inertial forces compared to viscous forces, while the Weber number indicates the relative magnitude of inertial forces to surface tension. We calculate the liquid jet Reynolds and Weber numbers using the following formulas [92]:

$$Re = \frac{\rho Q}{\pi R \mu} \tag{3.2}$$

$$We = \frac{\rho Q^2}{\pi^2 R^3 \sigma} \tag{3.3}$$

where ρ is the liquid density, Q is the volumetric flow rate of the liquid, R is the jet diameter, and σ is the surface tension of the liquid. Measurements were made at a room temperature of 20° C, in which case purified water has the following properties [92]:

$$\begin{aligned} &\rho = 998 \text{ kg/m}^3, \\ &\mu = 10^{-3} \text{ kg/m} \cdot \text{s} \\ &\sigma = 0.072 \text{ N/m}. \end{aligned} \tag{3.4}$$

The liquid jet Reynolds and Weber numbers are plotted for 5 tested nozzles from Design 1 under different operating conditions in figures 3.12a 3.12b 3.12c.

Since we have moderately large values of Reynolds and Weber numbers in almost all operating conditions ($Re \geq 10$ and $We \geq 1$), we can neglect the energy sinks resulting from viscosity and surface tension [92]. Under those conditions, Calvo (1998) [31] justified the following energy conservation equation for cases in which the liquid flow rate is sufficiently large that viscous forces and surface tension may be neglected:

$$\Delta P = \frac{1}{2} \rho v^2 \ . \tag{3.5}$$

Here, ΔP is the pressure drop across the nozzle orifice, ρ is the liquid density, and v is the liquid velocity. Under the aforementioned assumption that the liquid is incompressible and that the external pressure is much smaller than the internal nozzle pressure, we may relate the internal nozzle pressure P to the liquid volumetric flow rate Q and the jet radius R:

$$P = \frac{\rho Q^2}{2\pi^2 R^4} \; . \tag{3.6}$$

Figure 3.11d shows the estimated pressure inside the nozzle, based on equation 3.6. In this plot, we utilized jet diameter measurements made at a liquid flow rate of 20 μl/min. It is evident from figure 3.9a that the trend in jet speed as a function of liquid flow rate at fixed gas flow rate is asymptotic, and approaching the limit of equation 3.6. Since the velocities corresponding to a liquid flow rate of 20 μl/min differ by only ∼10% from those at a flow rate of 15 μl/min, we assume that these pressure estimates are reasonably accurate. We emphasize that this result suggests a simple scheme to estimate internal nozzle pressure: increase the liquid flow rate until the asymptotic behavior of equation 3.5 is observed. Although the increased liquid flow rate is needed to justify calculations based on equation 3.6, figure 3.8 shows that internal pressure is largely independent of liquid flow rate.

3.6.9 Sheath Gas Reynolds Numbers

For future work, it is important to assess instabilities associated with the sheath gas under different operating conditions. For this purpose, we provide the sheath gas Reynolds number:

$$\mathrm{Re}_g = \frac{\rho_g v_g d_g}{\mu_g} \tag{3.7}$$

where v_g is the gas speed, d_g is the diameter of the gas orifice, μ_g is the gas viscosity, and ρ_g is the gas density. Since the (measured) gas mass flow rate is $\dot{m}_g = \rho_g v_g \pi d_g^2/4$, we may instead write the sheath gas Reynolds number as

$$\mathrm{Re}_g = \frac{\rho_g v_g (4A_g)}{\pi \mu_g d_g} = \frac{4\dot{m}_g}{\pi \mu_g d_g} \; . \tag{3.8}$$

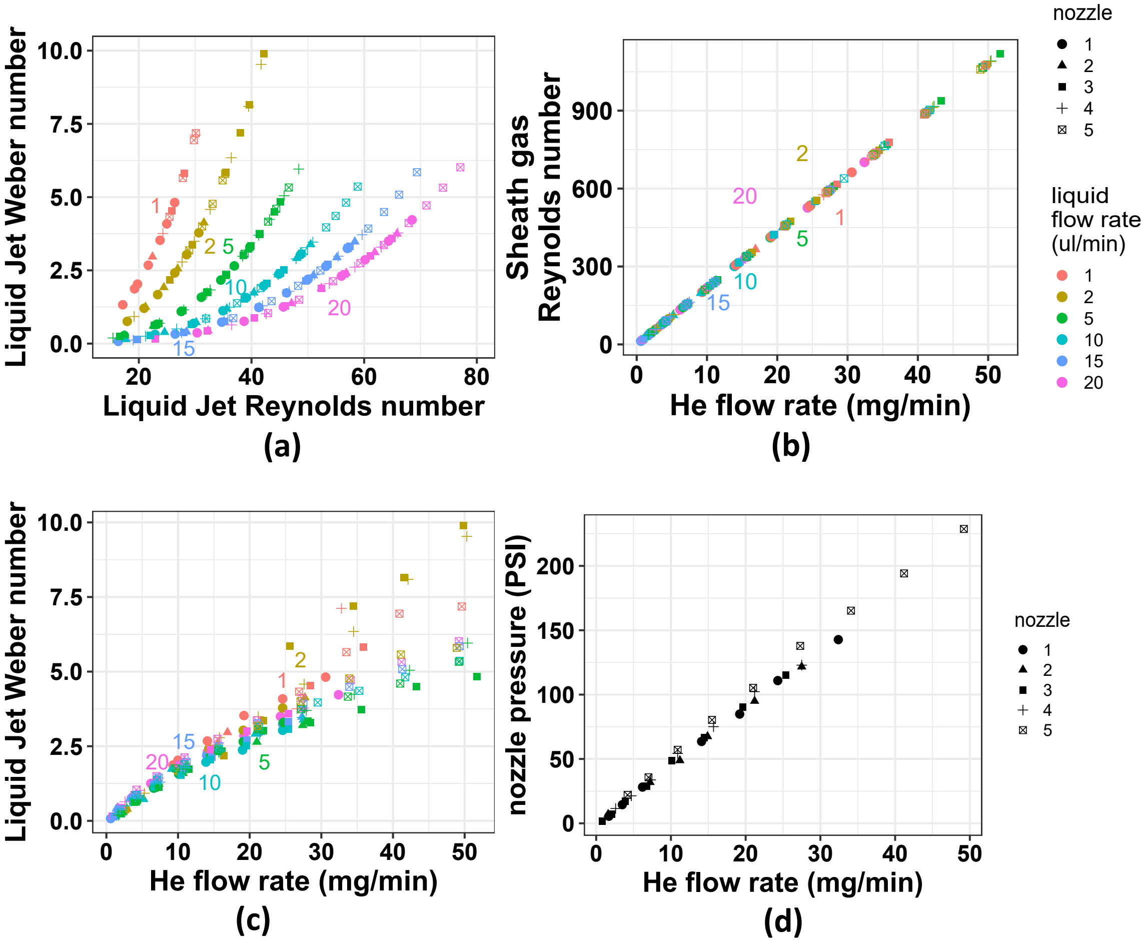

Figure 3.12: (a) plot of liquid jet Weber number versus liquid jet Reynolds number for 5 nozzles from design 1 under different operating conditions. (b) plot of liquid jet Reynolds number versus Helium flow rate for 5 nozzles from design 1 under different operating conditions, (c) plot of liquid jet Weber number versus Helium flow rate for 5 nozzles from design 1. (d) plot of calculated sheath gas Reynolds number versus Helium flow rate for 5 nozzles from design 1 under different operating conditions. Symbol colors distinguish liquid flow rates, while symbol shapes distinguish different nozzles.

The plot of sheath gas Reynolds number versus helium flow rate $\dot{m}$ for the nozzle Design 1 is shown in figure 3.12d, assuming $\mu_g = 1.96 \times 10^{-5}$ Pa·S in all operating conditions. We can see from the plot that $Re < 1000$ in all operating conditions, which suggests that the sheath gas flow is in the laminar regime under those conditions.

3.7 Discussion and Conclusions

We have shown that 3D printed nozzles can yield highly reproducible jet properties, which is of particular importance for XFEL serial diffraction measurements because unpredictable and misbehaved microjets are a common cause of wasted time (or completely failed experiments) at these costly facilities. We utilized an asymmetric nozzle design that would be very difficult to fabricate by other means (e.g. glass forming and injection moulding), and we demonstrated consistent jetting at speeds that are are well in excess of 100 m/s (up to 170 m/s in the data presented here), which is required for data collection at MHz XFEL pulse repetition rates [97, 96]. These designs produced jets at liquid (water) flow rates down to 1 μl/min while maintaining a liquid channel ID of 50 μm or larger, which helps avoid clogging problems. We also observed jet diameters that were consistently below 1 μm (down to 0.325 μm), which is of interest for single-particle imaging experiments, fiber diffraction, or measurements from very small protein nanocrystals. Although these nozzle designs appear to improve the range of jetting conditions (as compared with symmetric designs), systematic studies of the relation between nozzle geometry and liquid jet properties are needed in order to quantitatively identify the most robust designs. The measurement system that we developed in order to characterize the performance of these printed nozzles is capable of determining jet diameters from high-speed jets that are well below the theoretical resolution of the optical system, which we achieved by employing a form of localization microscopy to the translations of droplet image centroids in pairs of images separated in time by 550 ns.

The nozzles presented here have been utilized in multiple XFEL experiments including solution scattering from membrane proteins, single-particle imaging of viruses, and crystallography measurements. 3D printed nozzles of a different form, but made from the same material using the same printing techniques, have been also been utilized in recent MHz crystallography experiments [97, 47]. The systematic jet/droplet characterizations demonstrated here form a foundation for future systematic studies on different liquid samples with varying properties such as viscosity, surface tension, temperature, and particle size.

3.8 Acknowledgements

This work is supported by the BioXFEL Science and Technology Center NSF Award number 1231306.

3.9 Disclosures

The authors declare no conflicts of interest.

Chapter 4

NUMERICAL AND EXPERIMENTAL INVESTIGATION OF THE EFFECT OF DIFFERENT GEOMETRICAL PARAMETERS ON THREE-DIMENSIONAL PRINTED GAS DYNAMICS VIRTUAL NOZZLES

4.1 Abstract

GDVNs (Gas Dynamics Virtual Nozzles) [31] play an important role to satisfy sample delivery requirements of serial femtosecond crystallography and solution scattering experiments [18]. Recently, submicrometer resolution capabilities of two-photon polymerization additive manufacturing techniques [22] made it possible to fabricate reproducible 3D printed devices [62, 47, 61] with few restrictions on the nozzle design geometry. Computational Fluid Dynamics (CFD) techniques are a powerful means to investigate how the properties of microjets and droplets produced by GDVNs relate to geometry and operating conditions, which can help identify optimal GDVN designs for a given purpose. Zahoor et al. [104, 101, 102] used the OpenFOAM open-source Computational Fluid Dynamics code to numerically simulate the operation of an axisymmetric geometry corresponding to 3D printed GDVNs. They also compared the simulations with experimental results. In this investigation, we used a new efficient geometric VOF method called isoAdvector [76] to assess jet characteristics of various 3D printed GDVNs under different operating conditions. The first subject of study was to investigate the difference in jet stability due to difference in gas flow field geometry for two types of gas flow field geometries, namely bell-shaped geometry and the cone-shaped geometry. The numerical simulation results for our test cases showed agreement with the experimental data, with the relative error of

about 10 percent for both the cone-shaped and the bell-shaped test cases.

The median jet length results showed that the numerical simulations results in about 4 percent longer median jet length comparing with the results from experimental testings, for both the cone-shaped and the bell-shaped nozzle geometry. This meaningful difference is observed for the test case with even comparitively very low sheath gas flow rate (6 mg/min) with the very low imposed nonlinearities imposing to the liquid jet.

4.2 Introduction

Thus far, several different approaches have been introduced for numerical modeling of the interface of multiphase flows, such as the front tracking method, the level set method and the volume of fluid method. The most commonly used methods among the interface advection and reconstruction approaches are level sets and volume of fluids [98]. In this investigation, we used a recently developed open source code [76]. This code uses a new method for interface reconstruction and advection, called the isoAdvector method. Comparing the numerical simulation results with the results from experiments, the numerical simulation pipeline was observed to have accurate results with reasonable computational costs.

The first subject of study was to investigate the difference in jet stability due to differet gas flow field geometries. Numerous comparative studies were already done in the rocket propulsion field to investigate how cone-shaped or bell-shaped nozzles can result in different performance of rocket nozzles [87]. Results of the investigations for the bell-shaped and the cone-shaped geometries in macro scales explained that the bell-shaped nozzle designs can often result in comparatively more stable performance under certain conditions. It would also be helpful to study how cone-shaped and bell-shaped geometries in the gas flow field for GDVNs can affect the jet characteristics.

This knowledge can help us to optimize designs for 3D printed devices. In this investigation, we observed that the bell-shaped geometry of the gas flow field in the 3D printed nozzles can increase the stability of the microjets under certain conditions. Bell-shaped gas flow field geometries are observed to result in higher stability in liquid jets. Thus, in certain operating conditions, the gas flow field in the 3D printed nozzles are better to be bell-shaped to increase the jet length and the jet stability.

Another investigation was to numerically simulate the performance of some of our popular 3D printed GDVNs, that have been used in several successful XFEL experiments. The complete pipeline for developing the flow field from the design geometry is illustrated in several figures, and the results of numerical simulations are shown in section 4.6. One of the designs under investigation is design 79 (or design 2 in Chapter 3), with the corresponding drawing shown in figure 3.3.

4.3 Theory

4.3.1 Navier-Stokes Equations

The Navier-Stokes equation describes the temporal evolution of a momentum vector field ($\rho\vec{U}$), which is the product of density (ρ) and velocity ($\vec{U}$):

$$\frac{\partial}{\partial t}\left(\rho\vec{U}\right) + \nabla\cdot\left(\rho\vec{U}\otimes\vec{U}\right) - \nabla\cdot\vec{\sigma_\mu} = -\nabla p + f_\sigma \;. \tag{4.1}$$

The viscous stress (σ_μ) for Newtonian fluids is defined in equation 4.2 and it generalizes the molecular friction on continuum scales on the in terms of viscosity (μ).

$$\vec{\sigma_\mu} = \mu\left(\nabla\vec{U} + \left(\nabla\vec{U}\right)\right) - \frac{2}{3}\mu\vec{I}\left(\nabla\cdot\vec{U}\right) \tag{4.2}$$

The density scalar field is transported along the velocity vector field according to the continuity equation

$$\frac{\partial\rho}{\partial t} + \nabla\cdot\left(\rho\vec{U}\right) = 0 \;. \tag{4.3}$$

Equation of state relates the pressure (p), temperature (T) and density (ρ). Based on ideal gas law, the equation of state is:

$$\frac{p}{\rho RT} = \text{constant} \tag{4.4}$$

Another equation that relates the density to the pressure, based on isentropic gas expansion assumption is:

$$\frac{p}{\rho^{\gamma}} = constant \tag{4.5}$$

The compressibility is defined as:

$$\psi = \frac{\partial \rho}{\partial p} \tag{4.6}$$

With incompressible flow assumption, the mass conservation equation becomes:

$$\nabla \cdot \vec{U} = 0 \tag{4.7}$$

Based on the incompressible flow assumption, equations 4.4, 4.5, 4.6 become irrelevant. Incompressible flow assumption only holds when Mach number is less than $\frac{1}{3}$. The mach number can be defined as:

$$Ma = \frac{|\vec{U}|}{\sqrt{\gamma RT}} \tag{4.8}$$

Moreover, equation 4.1 shows that the surface tension force (f_σ) is in the direction of the normal of the interface. The surface tension value is proportional to the curvature (κ) of the interface.

$$f_\sigma = \sigma \kappa \hat{n} \tag{4.9}$$

σ denotes the surface tension constant. For water, this is equal to $0.07 N/m$, independent of the pressure and temperature of the gas medium.

4.3.2 Volume of Fluid Method

In this paper, the sharp interface (isoAdvector) approach [76] is investigated for interface reconstruction and interface advection. Figure 4.1 describes the immiscible

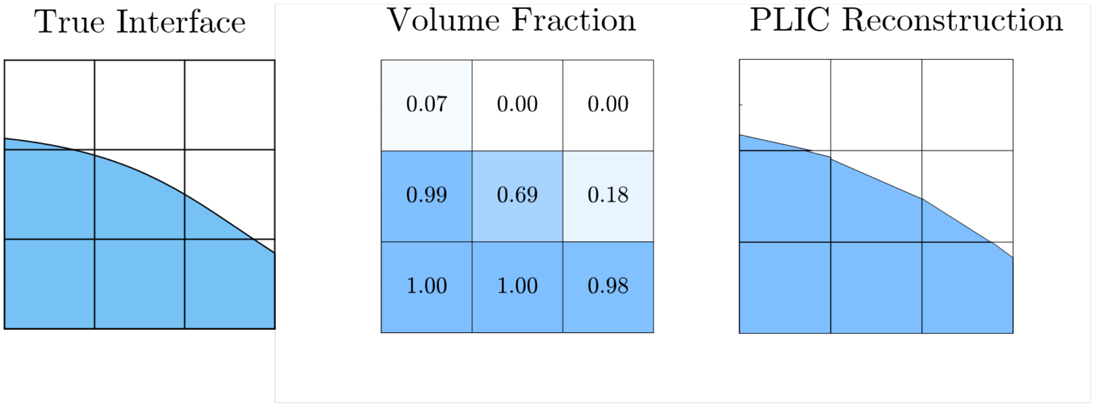

Figure 4.1: Left: potential description of a true interface, center: discrete cellular representation of volume of fluid, right: discrete and piece-wise representation of continuous interface showing planar distribution of fluid fractions [7].

interface whereby a volume fraction α is defined as the fraction of volume occupied by a certain phase within a given cell. A cell with $\alpha = 0$ is completely occupied by gas while a cell with $\alpha = 1$ is completely occupied by liquid. Volume fraction dictates the density and viscosity at the interface according to the linear weighting

$$\rho = \rho_{\text{liquid}}\alpha + \rho_{\text{gas}}(1-\alpha) \tag{4.10}$$

$$\mu = \mu_{\text{liquid}}\alpha + \mu_{\text{gas}}(1-\alpha)\ . \tag{4.11}$$

Assuming there is no evaporation, the α field travels along the velocity field according to the advection equation

$$\frac{D\alpha}{Dt} = \frac{\partial \alpha}{\partial t} + \nabla \cdot (\vec{U}\alpha) = 0\ . \tag{4.12}$$

Numerically this implies that the change in volume fraction in a finite volume is equivalent to a flux of fluid passing through cell faces, according to the divergence theorem:

$$\int_{\Omega_i} \frac{\partial \alpha}{\partial t} dV + \int_{\partial\Omega_i} \alpha\vec{U} \cdot n\ dS = 0\ . \tag{4.13}$$

4.3.3 Numerics

The Finite Volume Method used in OpenFOAM is outlined in the thesis by Jasak et al. [44]. In figure 4.2, $\vec{S}_f$ describes the area-vector of the face connecting the parent and neighbouring cell. The area of the face is given by the magnitude $|\vec{S}_f|$ and the normal vector

$$\hat{n}_f = \frac{\vec{S}_f}{|\vec{S}_f|}\ . \tag{4.14}$$

points outward toward the neighbour cell. $\vec{U}_f$ describes the interpolated velocity vector at center of the face. The flux across a face is given by equation 4.15.

$$\phi_f = \vec{U}_f \cdot \vec{S}_f \tag{4.15}$$

The mesh is stored as a list of points that describe all the available nodes and connectivity matrix that describes the indices of all the nodes that make up the faces. The face is characterized by the equation

$$\vec{S}_f = \frac{1}{2}\sum_{k=1}^{N_v}(\vec{x}_k \times \vec{x}_{k-1}) \tag{4.16}$$

where $\vec{x}_k$ are N_v face vertices ordered in a circular array sequenced by the indices of the connectivity matrix. The face connectivity matrix also contains the index of the normal cell (neighbouring cell) and the anti-normal cell (parent cell). In figure 4.2, T_f is the interpolated value at the face using parent cell value (T_P) and neighbouring cell value (T_N). The hanging nodes are additional constructs generated from mesh refinement of localized cells based on specific field criterion. The vector $\vec{d}$ describes the position of neighbouring cell centroid with respect to the parent cell centroid. Given this mesh geometry described in figure 4.2, the computation of the gradient of T can be done simply by the means of summation of normal area vector ($\vec{S}_f$) multiplied with face-interpolated scalar T_f as described in equation 4.17, using Green's theorem.

$$\frac{1}{|\Omega_i|}\int_{\Omega_i} \nabla T dV = \frac{1}{|\Omega_i|}\int_{\text{face}} T dS \approx \frac{1}{|\Omega_i|}\sum_f \vec{S}_f T_f \tag{4.17}$$

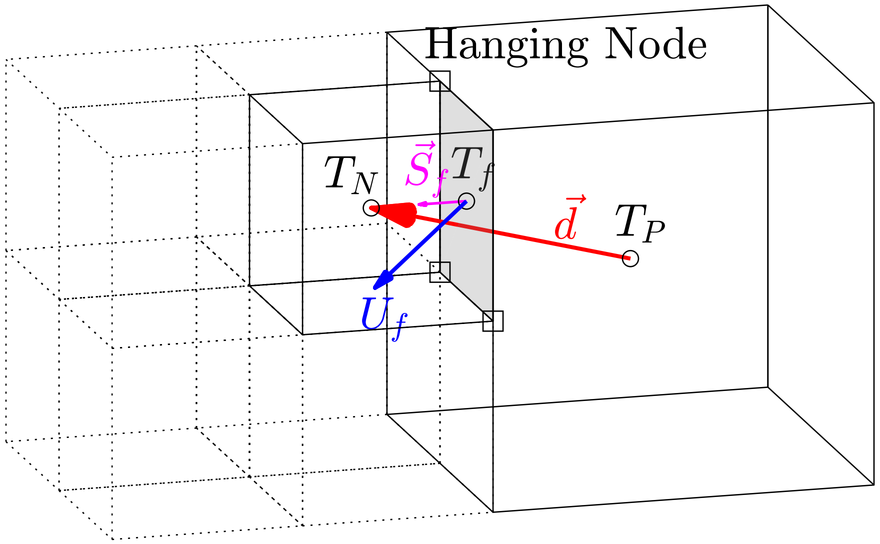

Figure 4.2: A visualization of a parent hexahedral cell connected to an adaptively refined neighboring cell (picture by Adil Ansari).

Ω_i describes the domain inside a cell of index i. Hence the volume of the cell is $|\Omega_i|$. Similarly, gradients of vector can computed for components of the vector fields. Additionally, the divergence of a vector field can be computed using equation 4.18.

$$\frac{1}{V_{cell}} \int_{cell} \nabla \cdot \vec{T}\, dV = \frac{1}{V_{cell}} \int_{face} \vec{T} \cdot d\ S \approx \frac{1}{V_{cell}} \sum_{f} \vec{S}_f \cdot \vec{T}_f \tag{4.18}$$

The computation of divergence and gradients requires the value of vectors and scalars at faces. Even though the values at cell centroid are primarily stored information, the values at face can be obtained by interpolation. The methodology of interpolation, dictates the stability and accuracy of the simulation. The linear interpolation method is formulated as:

$$T_{f,Linear} = \left(1 - \frac{f\bar{N}}{|\vec{d}|}\right) T_N + \frac{f\bar{N}}{|\vec{d}|} T_P \tag{4.19}$$

This method would result in spatial derivatives having an order of accuracy of 2 and is equivalent to central different schemes on uniform grid. However, it lacks numerical stability, especially if cell peclet number (ratio of advective transport to diffusion) is high. A solution is to add artificial numerical diffusion, which is most dominant in upwind scheme. The upwind interpolation scheme to compute the face value is explained in equation 4.20.

$$T_{f,Upwind} = T_N\left(1 - H\left(\vec{U}_f \cdot \hat{n}_f\right)\right) + T_P H\left(\vec{U}_f \cdot \hat{n}_f\right) \tag{4.20}$$

In equation 4.20, $H\left(\vec{U}_f \cdot \hat{n}_f\right)$ is one when $\vec{U}_f \cdot \hat{n}_f$ is positive while $H\left(\vec{U}_f \cdot \hat{n}_f\right)$ is zero when $\vec{U}_f \cdot \hat{n}_f$ is negative. The upwind scheme has the first order of accuracy in space and this scheme imposes artificial numerical diffusion to overcome physical instability. Hence a filter (χ) can be used to implement an appropriate weight based on various factors.

$$T_f = T_{f,Upwind}\left(1 - \chi\right) + T_{f,Linear}\chi \tag{4.21}$$

In equation 4.21, $\chi(r)$ is a function of r which is the gradient ratio. The gradient ratio is computed from equation .

$$r = \frac{2\vec{d} \cdot (\nabla T)_P}{\vec{d} \cdot (\nabla T)_f} - 1 \tag{4.22}$$

And the gradient at face ($(\nabla T)_f$) can be computed as:

$$(\nabla T)_f = \frac{T_P - T_N}{\left|\vec{d}\right|} \tag{4.23}$$

One way to compute the limiter $\chi(r)$ is Van Leer method:

$$\chi(r) = \frac{r + |r|}{1 + |r|} \tag{4.24}$$

Another method to compute the limiter $\chi(r)$ is Linearupwind method, and is an interpolation method available in OpenFOAM. This limiter used for this is named sweby and is shown in equation (4.25).

$$\chi(r) = \max\left(0, \min\left(\beta r, 1\right), \min(\beta, r)\right) \tag{4.25}$$

The value of β can chosen between 1 and 2.

Boundary Conditions

All scalar and vector Fields are physically distributed around cell centroids. The discretization for ascertaining face value requires the knowledge of parent and neighbour centroid values. At the boundaries only one parent cell is available. The lack of information to numerically solve for the flow field parameters can be filled by the knowledge of boundary conditions which are integral part of the partial differential equations. There are two types of boundary conditions, namely Dirichlet and Nuemann . Dirichlet boundary conditions are prescribed values of a given field at the boundary locations. A Nuemann boundary condition involves a known gradient for any given field normal to the direction of the boundary face. In fluid flow simulations, the inlet typically has a prescribed velocity (Dirichlet) and outlet has a prescribed gradient (Nuemann). At walls, due to the no-slip condition, the velocity is prescribed to be zero. This combined with advection and diffusion of momentum leads to a boundary layer near the wall. This is generally true for alpha (α) as well except for the wall boundary condition which is a Nuemann boundary condition and it is dependent on wall contact angle of the liquid. Pressure fields are generally prescribed as Dirichlet at the outlet and Nuemann elsewhere. The specific setup that simulates the boundary conditions in the context of finite volume methods involved ascertaining the boundary face values [13]. For zero-gradient Nuemann condition one can assume that the boundary face value (T_b) is equivalent to parent cell value (T_P) as shown in equation 4.26

$$T_b = T_P \tag{4.26}$$

For Dirichlet boundary conditions, the prescribed value (T_{ref}) is assigned to the boundary face as shown in equation 4.27.

$$T_b = T_{ref} \tag{4.27}$$

Temporal Discretization [25]

The evolution of velocity can be discretized as Equation 4.28 where $\vec{U}^{n+1}$ represent the state of velocity at given point at time $t + \Delta t$, namely the future time-step.

$$\frac{\vec{U}^{n+1} - \vec{U}^{n}}{\Delta t} + \nabla \cdot \left(\vec{U}^{n} \otimes \vec{U}^{n} \right) - \frac{1}{\rho} \nabla \cdot \left(\mu \left(\nabla \vec{U}^{n} + \nabla^{T} \vec{U}^{n} \right) \right) - \frac{1}{\rho} f_{\sigma} = -\frac{1}{\rho} \nabla p^{n+1} \quad (4.28)$$

Equation 4.28 can be decomposed to Equation 4.29 and Equation 4.30 by means of predictor velocity ($\vec{U}^{*}$).

$$\frac{\vec{U}^{*} - \vec{U}^{n}}{\Delta t} + \nabla \cdot \left(\vec{U}^{n} \otimes \vec{U}^{n} \right) - \frac{1}{\rho} \nabla \cdot \left(\mu \left(\nabla \vec{U}^{n} + \nabla^{T} \vec{U}^{n} \right) \right) - \frac{1}{\rho} f_{\sigma} = 0 \quad (4.29)$$

$$\frac{\vec{U}^{n+1} - \vec{U}^{*}}{\Delta t} = -\frac{1}{\rho} \nabla p^{n+1} \quad (4.30)$$

The future time step has a constraint of being divergence free which gives rise to a Poisson system which can be used to recover pressure at future time-step (p^{n+1}).

$$\frac{1}{\Delta t} \nabla \cdot \vec{U}^{n+1} = 0 = \frac{1}{\Delta t} \nabla \cdot \vec{U}^{*} - \nabla \cdot \left(\frac{1}{\rho} \nabla p^{n+1} \right) \quad (4.31)$$

Equation 4.30 can be rearranged to ascertain the future time step.

$$\vec{U}^{n+1} = \vec{U}^{*} - \frac{\Delta t}{\rho} \nabla p^{n+1} \quad (4.32)$$

Equation 4.29, Equation 4.31, Equation 4.32 form temporal loop that is used to integrate incompressible flows in time in a discrete manner. In the context of FVM, the predictor velocity ($\vec{U}^{*}$) is computed in a similar way. The predictor step can be expanded as equation 4.33 which is roughy analogous to Equation 4.29.

$$\begin{aligned} &\frac{\left(\rho_{P}^{n+1} \vec{U}_{P}^{*} \right) - \left(\rho \vec{U} \right)_{P}^{n}}{\Delta t} \left| \Omega_{P} \right| + \sum_{f} \left(\rho_{f} \phi_{f} \right)^{n} \vec{U}_{f}^{*} \\ &= \sum_{f} \mu_{f}^{n+1} \left(\nabla \vec{U} \right)_{f}^{*} \left| \vec{S}_{f} \right| + \nabla \vec{U}_{P}^{n} \cdot \nabla \mu_{P}^{n+1} \left| \Omega_{P} \right| \end{aligned} \quad (4.33)$$

The viscous stress formulation is equivalent to the dicretized version of equation 4.2 under incompressibility conditions. It is important to realize that this momentum step is done after solving for the volume fraction at the future time step (α^{n+1}) and hence scalar fields of density and viscosity is already known. This equation can be simplified such that A_P represents coefficients of $\vec{U}_P^*$ and that are remaining terms are embedded in the operator $\mathcal{H}$.

$$\begin{aligned} A_P &= \frac{\rho_P^{n+1}}{\Delta t} \\ &+ \sum_{f \epsilon \partial\Omega_i} \left(\frac{(\rho_f \phi_f)^n \left(1 + \Theta \varsigma\left(\phi_f\right)(1-\chi)\right)}{2} + \frac{\Theta \mu_f^{n+1} \left|\vec{S}_f\right|}{\left|\vec{d}\right|} \right) \frac{1}{|\Omega_P|} \end{aligned} \tag{4.34}$$

Here Θ is 1 if parent cell is the anti-normal cell and -1 if parent cell is the normal cell in the mesh description. ς operators represents sign function.

$$\begin{aligned} \mathcal{H}\left(\vec{U}^m\right) &= \frac{\left(\rho \vec{U}\right)_P^n}{\Delta t} + \nabla \vec{U}_P^n \cdot \nabla \mu_P^{n+1} \\ &+ \sum_{\forall N} \left(\frac{(\rho_f \phi_f)^n \left(1 - \Theta \varsigma\left(\phi_f\right)(1-\chi)\right)}{2} + \Theta \mu_f^{n+1} \frac{\left|\vec{S}_f\right|}{\left|\vec{d}\right|} \right) \frac{\vec{U}_N^m}{|\Omega_P|} \end{aligned} \tag{4.35}$$

It is important to realize that m is not a temporal time-step marker (n) but rather an iterative step marker, that involves several time step interations between time step n and the next time step. This results is Equation 4.36 which solves for $\vec{U}_P^*$ which is akin to Equation 4.29.

$$\vec{U}_P^* = \frac{\mathcal{H}\left(\vec{U}^m\right)}{A_P} + \frac{(\sigma \kappa \nabla \alpha)^{n+1}}{A_P} \tag{4.36}$$

Equation 4.36 is solved interpolated at face. As the m^{th} iteration is performed within the same time step, $\vec{U}^m$ gets updated. However, A_P remains constant and so does the operator $\mathcal{H}$. This velocity and operator (A_P) can interpolated at face to produce flux relations as the dot product of interpolated face velocity ($\vec{U}_f$) and area vector

$(\vec{S}_f)$ resulting the relation described in Equation 4.37.

$$\phi_f^* = \left(\frac{\mathcal{H}\left(\vec{U}^m\right)}{A_P}\right)_f \cdot \vec{S}_f + \left(\left(\frac{1}{A_P}\right)_f (\sigma\kappa)_f^{n+1} (\nabla\alpha)_f^{n+1}\right) \left|\vec{S}_f\right| \tag{4.37}$$

This equation assists us to get the predictor flux values at each face. The computation of κ is discussed in Section 4.3.4 but it is purely a function of the α scalar field. The intermediate flux values can be used to compute the pressure at cell centroids by solving a non-constant coefficient poison system as described in Equation 4.38 which is analogous to Equation 4.31.

$$\sum_f \left(\frac{1}{A_P}\right)_f (\nabla p)_f^{m+1} = \sum_f \phi_f^* \tag{4.38}$$

Equation 4.38 is solved using various Krylov subspace sparse matrix solvers. Just like Equation 4.32, with the knowledge of pressure (p^{m+1}), once can correct the fluxes.

$$\phi_f^{m+1} = \phi_f^* - A^{-1} \nabla_f^{\perp} p^{m+1} \tag{4.39}$$

The cell center velocity $\vec{U}_P^{m+1}$ can be retrieved from face fluxes as shown in Equation 4.40.

$$\vec{U}_P^{m+1} = \vec{U}_P^* + \left(\frac{1}{A_P}\right) \left(\sum_{f \epsilon \partial\Omega_i} \frac{\left(\vec{S}_f \otimes \vec{S}_f\right)}{\left|\vec{S}_f\right|}\right)^{-1} \cdot \left(\sum_{f \epsilon \partial\Omega_i} \frac{\phi_f^{m+1} - \phi_f^*}{\left(\frac{1}{A_P}\right)_f} \frac{\vec{S}_f}{\left|\vec{S}_f\right|}\right). \tag{4.40}$$

Equation 4.37, 4.38 and 4.39 are cyclical and hence form an mth iteration for the PISO (Pressure-Implicit with Splitting of Operators) loop [23]. Upon the satisfaction of continuity and momentum equation residuals, the loop can be broken before the maximum number of iteration is reached. With this $\vec{U}_P^{n+1}$ is computed to move onto the next time-step where it is treated as the $\vec{U}_P^n$. Crucially, time can be advanced as shown in equation 4.41.

$$t^{n+1} = t^n + \Delta t \tag{4.41}$$

Planar Interface Construction

Advection with planar distribution is known for capturing interface physics more accurately than interface compression (Multidimensional Universal Limiter with Explicit Solution or MULES) methods. In particular, openFOAM contains the isoAdvector solver, which takes advantage of geometric advection [73]. Before the advection, the volume fraction and velocity at current time-step is known. The goal is to compute $\alpha_i(t+\Delta t)$. The cell scalar α_i is described as such:

$$\alpha_i(t) = \frac{1}{|\Omega_i|}\int_{\Omega_i} \alpha\left(\vec{x}, t\right) dV \tag{4.42}$$

Based on equation 4.13, the analytical flux over faces changes the α between time t and $t+\Delta t$ resulting in equation equation 4.43.

$$\alpha_i\left(t+\Delta t\right) = \alpha_i - \frac{1}{|\Omega_i|}\sum_{f \epsilon \partial\Omega_i} \Delta V_f(t) \tag{4.43}$$

Analytical form of the face flux is:

$$\Delta V_f\left(t\right) = \int_t^{t+\Delta t}\int_f \alpha\left(\vec{x}, t\right)\vec{U}\left(\vec{x}, t\right) dS d\tau \tag{4.44}$$

IsoAdvector

This method is also meant for capturing interfaces during the process of advection of volume fraction. The approach is distinct as instead of usage of a algebraic numerical technique, an planar interface is used to describe the interface in cells that are supposed to have an interface. This plane normal of this planar interface can be inferred from values of volume fraction from neighbouring cells. The distance of the plane from the center of the cell enforces the volume fraction of the cell. This planar reconstruction forms the PLIC (Peicewise Linear Interface construction) reconstruction. The planar distribution liquid is used in the advection step i.e. to move the volume fraction field along the velocity field [76].

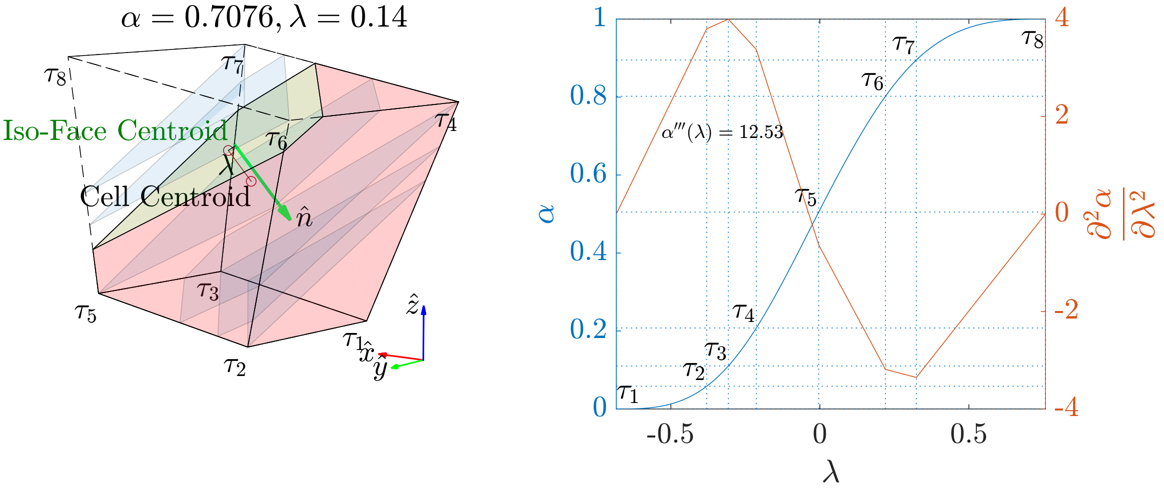

Figure 4.3: A visualization of iso-face in an interface cell (Picture by Adil Ansari).

1. The initial step is to compute the upwind flux of scalar α as ΔV_f which is equivalent to $\alpha_{upwind,f} U_f \cdot \hat{n}_f A_f \Delta t$.

2. With a specified tolerance ϵ marks interface cells where $\epsilon \leq \alpha_i \leq 1 - \epsilon$

3. For each interface cell reconstruct iso-surface by first computing the values of α at vertices. Establish α_v values at cell vertices using weighted interpolation from every connected cell as shown in equation 4.45.

$$\alpha_v = \frac{\sum w_k a_k}{\sum w_k} \tag{4.45}$$

   The weights, w_k can computed as the inverse of distance between vertex v and connected cell k.

4. For every edge where $\alpha_k \leq \alpha_i \leq \alpha_l$ compute

$$\vec{x}_{cut} = \vec{x}_k + \frac{\alpha_i - \alpha_k}{\alpha_l - \alpha_k} \left(\vec{x}_l - \vec{x}_k\right) \tag{4.46}$$

   These cut points can be connected to generate and initial planar distribution.

5. ψ describes the signed distance function which can be used to compute the

interface normal

$$\hat{n}_{S,j} = \frac{\nabla \psi_j}{|\nabla \psi_j|} \tag{4.47}$$

For any cell i in the vicinity of the interface cell j, the distance function scalar can be computed computing perpendicular distances between every interface cell j and vicinity cell i by weighing them based on the dot product of iso-face normal vector ($\hat{n}_{S,j}$) at interface and distance to centroid of interface of cell j.

$$\psi_{ij} = \frac{\sum_j w_{ij} \left(\hat{n}_{S,j} \cdot (\vec{x}_i - \vec{x}_{S,j})\right)}{\sum_j \; w_{ij}} \tag{4.48}$$

The weightage is computed as such:

$$w_{ij} = \frac{|\hat{n}_{S,j} \cdot (\vec{x}_i - \vec{x}_{S,j})|^A}{|\vec{x}_i - \vec{x}_{S,j}|^A} \tag{4.49}$$

The value of A can be between 2 to 25. It does not impact the solution significantly. Once the normal is computed it can replace step 3 and 4. This improvement is outlined in another paper by Roenby et al. [76].

6. It is next to impossible that the planar distribution will represent the expected volume of fraction α_i. As such, we take the normal information and translate in the normal direction such the volume function of lambda gives the appropriate α_i value. Since the volume function is continuous piece-wise sequence of third order polynomials, the volume function can be generated by computing the third derivative for each section as shown in figure 4.3. The number of piece-wise sections is one less than number of vertices in a cell. The interval limits can computed as:

$$\tau_k = \hat{n}_S \cdot (\vec{X}_k - \vec{X}_S) \tag{4.50}$$

Here X_k are the cell vertices and τ_k are values at which plane $\hat{n}_S \cdot \vec{x} = \tau_k$ intersects X_k. $\vec{X}_S$ is the center of the iso-face. Each piece-wise third-derivative can be computed by finding the vector of all the edges intersecting the plane. For all n edges intersecting the plane except for $n = 1$ and n equal to number of intersecting edges:

$$V_n = [\vec{v}_1 sign(\vec{v}_1 \cdot \hat{n}_S), \vec{v}_n sign(\vec{v}_n \cdot \hat{n}_S), \vec{v}_{n+1} sign(\vec{v}_{n+1} \cdot \hat{n}_S)] \tag{4.51}$$

The order of these edges must be counterclockwise on the iso-face from the normal.

7. Once V_n is attained it can be used to compute the third derivative as such:

$$\frac{d^3\alpha(\lambda)}{d\lambda^3} = \frac{1}{V_{cell}} \sum_{n=2}^{N_e-1} \frac{|V_n|}{\prod(V_n \hat{n}_S)} \tag{4.52}$$

In equation 4.52, the denominator inside the summation describes the product of all three elements of the vector $V_n\hat{n}$. N_e is the number edges intersecting the plane between two λ values.

8. Once evaluated, the coefficients of the polynomial can be integrated to ascertain the volume function and compute the root λ that corresponds to α_i.

9. For predicting the iso-face motion (streaming the interface): i. Interpolate the velocity vector $\vec{U}_S$ at point $\vec{x}_S$ which is the center of the iso-face. ii. Compute $U_S = \vec{U}_S \cdot \hat{n}_S$ iii. The new plane can be described as $\hat{n}_S \cdot \vec{x} = \lambda + U_s \Delta t$

10. Compute ΔV_f from new plane for downwind faces. Downwind faces are faces where $\vec{U}_f \cdot \vec{S}_f > 0$. The numerical form of volume fraction flux given in equation 4.44 is given as follows.

$$\Delta V_f(t, \Delta t) \approx \frac{\phi_f(t)}{\left|\vec{S}_f\right|} \int_t^{t+\Delta t} A_f(\tau)\, d\tau \tag{4.53}$$

It is important to realize the face is comprised various vertices $\vec{X}_k$. The time at which a moving planar interface makes any of the vertex co-planar is given by equation 4.54.

$$t_k \approx \; t + \left(\vec{X}_k - \vec{x}_S\right) \cdot \frac{\hat{n}_S}{U_S} \tag{4.54}$$

Since the integral in equation 4.53 is over 3D polygon with sharp bends, the area has to evaluated over multiple piece-wise intervals as shown in equation 4.55.

$$\int_{t}^{t+\Delta t} A_f\left(\tau\right) d\tau = \sum_{k=1}^{M} \int_{\widetilde{t}_k}^{\widetilde{t}_{k+1}} A_f\left(\tau\right) d\tau \tag{4.55}$$

Here $\widetilde{t}_1 = t$ and $\widetilde{t}_M = t + \Delta t$. All intermediate $\widetilde{t}_k$ satisfy the condition that $t < t_k < t + \Delta t$. the submerged area function $(A_f(\tau))$ is a piece-wise function that is continuous and so is its first derivative but its second derivative is discontinuous. As such, $A_f(\tau)$ can integrated in pieces as shown in figure 4.4. The polynomial describing it within a given interval can be computed by equation 4.56.

$$A_f\left(\tau\right) = A_f\left(\widetilde{t}_k\right) + \frac{1}{2} sign\left(U_s\right) \left|\vec{c}_1\left(\tau\right) \times \vec{c}_2\left(\tau\right)\right| \tag{4.56}$$

The goal here is to extract coefficients of τ^0,τ^1 and τ^2 for every peicewise parabolic curve described by equation 4.56 and integrate it analytically across peicewise interval's extrema: $\widetilde{t}_k$ and $\widetilde{t}_{k+1}$. The resultant area is added to ever was achieved from integral of $A_f(\tau)$ across $\widetilde{t}_1$ to $\widetilde{t}_k$ with the same procedure. The vectors $\vec{c}_1\left(\tau\right)$ and $\vec{c}_2\left(\tau\right)$ are diagonal vectors since the the area described in a given interval can only be 3D quadrilateral or 3D triangle. If the interval is triangular, then the vectors $\vec{c}_1\left(\tau\right)$ and $\vec{c}_2\left(\tau\right)$ would be coincident at tail or head.

11. For the upwind face of the cell, the value of ΔV_f can be gathered from downwind faces of neighbouring cells. Once that is done equation 4.43 can be used to compute the new alpha values at $t + \Delta t$.

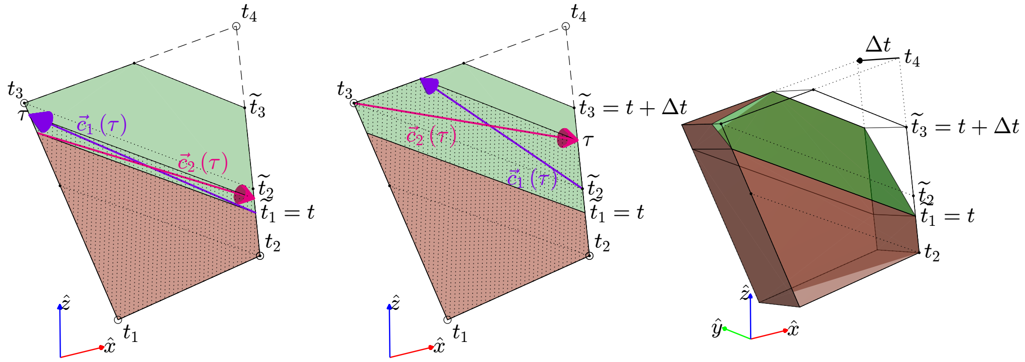

Figure 4.4: Left: a visualization of a face in an interface cell shows $a_f(\tau)$ highlighted with dotted shading. The brown shaded patch shows $a_f(t)$ and combined with the green patch shows $a_f(t + \delta t)$. Center: $a_f(\tau)$ visualized in second interval. Right: the integral $\int_t^{t+\delta t} a_f(\tau)\, d\tau$ can be visualized as a polyhedron extruded with variable $a_f(\tau)$ varying for each infinitesimal cross sections (Picture by Adil Ansari).

12. This process doesn't produce bounded alpha solution i.e. the condition $0 \leq \alpha_i(t + \Delta t) \leq 1$ is not satisfied. Simply snipping the undershoots to 0 and overshoots to 1 would result in lack of conservation of mass and volume fraction. The bounding procedure goes over overfilled cells first and redistributes the surplus by flux weightage. Additionally, the total volume fraction of the flux cannot exceed the precalculated (ϕ) flux at face. This leads us to the follwing equation.

    $$\Delta V_f' = min\left(\phi_f \Delta t, \frac{(\alpha_i - 1)\,\phi_f}{\sum_{k=1}^{N} \phi_k}\right) \tag{4.57}$$

    According to Roenby [73] this process is recursive and repeated for remaining faces if a cell opposing the face fills up. This process is repeated for under-filled cells ($\alpha_i < 0$) by repeated the same procedure on a complimentary field $1 - \alpha_i$.

An important aspect to understand here is that in the isoAlpha reconstruction method, the code goes through steps 1, 2, 3, 4, 6, 7, 8, 9, 10, 11, 12. Step 5 is not used in this method as it is used in another method, namely plicRDF. The procedure in this is to first go through steps 1 to 4 sequentially once. Then steps 5 to 8 are repeated to improve level-set reconstruction. Once the residual threshold is met, steps 9-12 are performed.

4.3.4 Surface Tension

Surface tension forces can be evaluated by ascertaining the interface normal and interface curvature. The analytical form of curvature can be expressed as such:

$$\hat{n} = \frac{\nabla\alpha}{|\nabla\alpha|} \tag{4.58}$$

Computing FVM based gradients of α can result in errors due to sharp sub-grid discontinuity. While most novel approaches use non-gradient approaches to ascertain $\hat{n}$, in youngs PLIC reconstruction [99], the gradient of alpha is employed to compute the normal by smoothing. The analytical form of curvature is given in equation 4.59.

$$\kappa = \nabla \cdot \hat{n} \tag{4.59}$$

Again, FVM methods can be employed to evaluate curvature from interface normal ($\hat{n}_S$), the sharp discontinuity can lead to errors that beget simulation instability. There are many approaches such as height cells to compute the surface tension [40], it is only applicable to cartesian grids [86]. The application for non-cartesian grids requires clipping over several cells which can be computationally expensive. A computationally inexpensive approach to compute the surface tension is to smoothen the α scalar field over pseudo-time ($\Delta\tau$) as shown in equation 4.60.

$$\frac{\alpha^* - \alpha}{\Delta\tau} - \nabla \cdot (\Gamma_\alpha \nabla\alpha) = 0 \tag{4.60}$$

This approach is known as Continuum surface force (CSF). The smoothened scalar (α^*) can be used to compute the curvature as shown in Equation 4.61

$$\kappa = -\nabla \cdot \left(\frac{\nabla\alpha^*}{|\nabla\alpha^*|}\right) = \frac{1}{|\nabla\alpha^*|}\left(\left(\frac{\nabla\alpha^*}{|\nabla\alpha^*|} \cdot \nabla\right)|\nabla\alpha^*| - \nabla \cdot \nabla\alpha^*\right) \tag{4.61}$$

This equation also shows the chain rule decomposition of curvature that is an recommended by Martinez et. al. [56] which seems to produce better results.

4.4 Mesh Independence and Grid Convergence Index Study

To better understand the required mesh resolution for the numerical simulations, we use GCI (grid convergence index) analysis [64] procedure to calculate for the Asymptotic Convergence value. In equations 4.62, 4.63, 4.64, 4.65, 4.66, 4.68. We calculate average pressure value throughout the cubic domain $\overline{p}$ 4.62, grid spacing ratio r having the values of the grid spacing for the coarse mesh h_1 and the grid spacing value for thew fine mesh h_2, values (average value of the pressure throughout the domain) for different grid spacing levels f_1, f_2, f_3. Having grid spacing ratio r and values for different grid spacing levels f_1, f_2, f_3, the value for observed order of convergence (accuracy) p is calculated from equation 4.64. Then, we extrapolate the values of f_1, f_2, f_3 to estimate the Richardson extrapolation value $f_{h=0}$ from equation 4.65. Richardson extrapolation value is obtained from estimating for the value $f_{h=0}$ in the hypothetical case where grid spacing h is zero. From the Equations 4.66, 4.67, GCI (grid convergence index) values for grid levels 1 and 2 GCI_{21}, and GCI for grid levels 2 and 3 GCI_{32} are calculated, inputting the value of 1.25 for constant F_{sec}. Finally, we assess whether the Asymptotic Convergence is near to one 4.68.

$$\bar{p} = \frac{1}{V_{domain} t_{span}} \iiiint p \; d \; V dt \approx \frac{1}{V_{domain} t_{span}} \sum_{n} \left(\Delta t \sum_{i} (p_i \Omega_i) \right) \tag{4.62}$$

$$r = \frac{h_2}{h_1} \tag{4.63}$$

$$p = \frac{\log\left(\frac{f_3 - f_2}{f_2 - f_1}\right)}{\log(r)} \tag{4.64}$$

$$f_{h=0} \approx \; f_1 + \frac{f_1 - f_2}{r^p - 1} \tag{4.65}$$

$$GCI_{21} = F_{sec} \frac{\left| \frac{f_1 - f_2}{f_1} \right|}{r^p - 1} \tag{4.66}$$

$$GCI_{32} = F_{sec} \frac{\left| \frac{f_2 - f_3}{f_2} \right|}{r^p - 1} \tag{4.67}$$

$$\frac{GCI_{i,i+1}}{GCI_{i+1,i+2}} r^p \approx 1 \tag{4.68}$$

4.4.1 Cylinder-Collapse

Our cylinder-collapse test case consists of a cylinder cube with dimensions of 50 μm by 50 μm. The grid is in such a way that each side is subdivided into 20 cells. Consequently, each cell has the size of 50 $\mu m/20 = 2.5$ μm. When we have one level of mesh refinement, the cell size is reduced to 1.25 μm in the refined regions, that are in the vicinity of the liquid-gas interfaces.

The cubic domain is cut into half in the pictures of figures 4.5 4.6 4.5 4.6 4.7 4.8. In pictures of the figures 4.5 4.6 4.7 4.8, the red color red color indicates the cell regions of which the volume fraction of liquid α is one and the blue color is an indication of the cell regions of which the volume fraction of liquid is zero. For the two-level refinement, the cell size is reduced to 2.5 μm / 2^2 that would be 0.625 μm in the finest regions. Finally, for the finest case with three-level mesh refinement, the finest cells have the size of about 2.5 μm / 2^3, that is 0.3125 μm. A picture of the cross-section of the middle of the square region of the cylinder-collapse case for three different mesh resolutions are shown in picture 4.5. Moreover, the two pictures of figure 4.6 show the initial condition of the cylinderCollapse case (left picture), and the final condition of the cylinder collapse case (right picture). The results of the cylinder collapse case for GCI analysis to study the grid resolution independency of the results are shown in figures 4.7 4.7. The cylinder collapse starts from time 0 till time 26 μ *sec* with 3 μsec interval. The left pictures correspond to the coarsest mesh resolution at the interface with 1 AMR level, the middle pictures correspond to the medium mesh resolution with 2 AMR levels, and the right pictures correspond to the fine mesh resolution at the interface with 3 AMR levels. From the figures, we can see that there is no noticeable difference between the results for the middle mesh resolution with 2 AMR

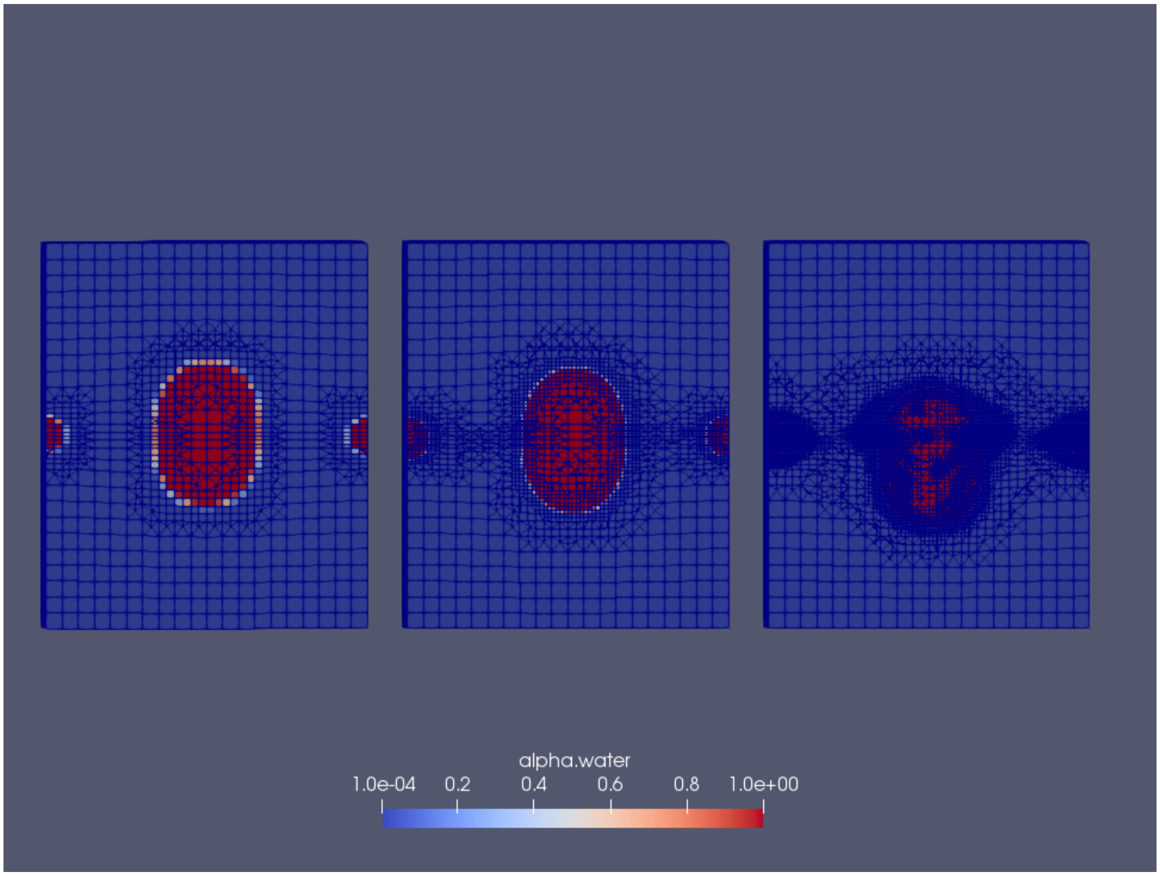

Figure 4.5: The final condition of the cylinder collapse test case for grid resolution independency study. The left picture corresponds to one AMR (adaptive mesh refinement) level (coarsest mesh resolution in the vicinity of the liquid-gas interface), the middle picture corresponds to two AMR levels (medium mesh resolution in the vicinity of the liquid-gas interface), and the right picture corresponds to three AMR levels (fine mesh resolution in the vicinity of the liquid-gas interface).

levels, and the results for the fine mesh resolution with 3 AMR levels. Therefore, we can conclude that the medium mesh resolution and the fine mesh resolution would be fine enough to resolve the interface, and beyond the medium resolution and the fine resolution at the interface, the solution would be mesh-independent and refining mesh, to the levels beyond the medium mesh resolution and the fine mesh resolution of our test case shouldn't noticeably effect the results of the numerical simulation. We also quantitatively investigated the mesh resolution level to be fine enough for the numerical simulation. Following the procedure of 4.62, 4.63, 4.64, 4.65, 4.66, we

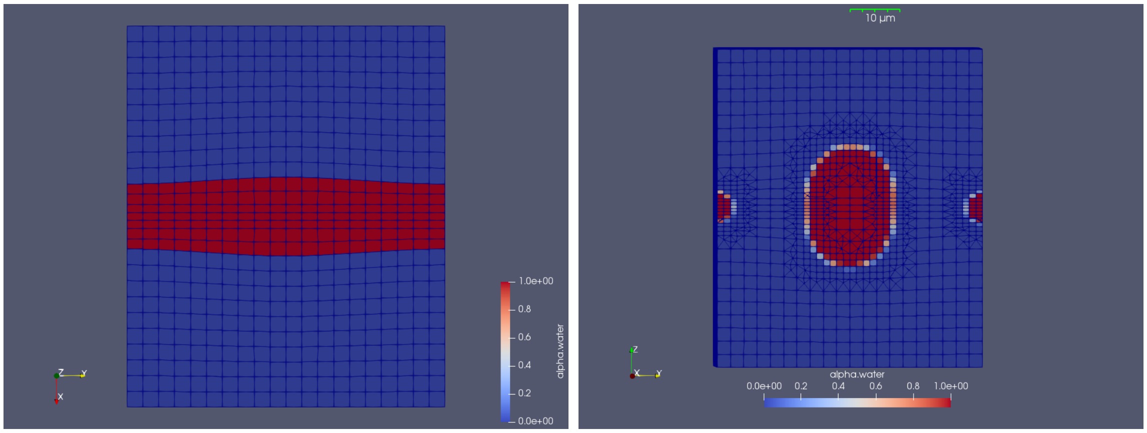

Figure 4.6: The initial condition of the cylinder collapse test case for grid resolution independency study (left picture), and the final condition of the cylinder collapse test case for grid resolution independency study with 1 AMR level (Right Picture).

AMR Grid Level	h (μm)	value (f)
1	1.25	5316.30467
2	0.625	5324.737378
3	0.3125	5328.583019

Table 4.1: Average pressure values f inside the domain with three different AMR levels. The value h indicates the finest resolution at the interface after AMR.

calculate for the average pressure values throughout the cylinder for three different AMR levels that are shown in table 4.4.1 to study grid independence of the PLIC reconstruction method [64]. The results for the studied case are calculated to be:

p = 1.4435

f(h=0) = 5323.9134

$\mathrm{GCI}_{23} = 0.13$

$\mathrm{GCI}_{12} = 0.05$

Asymptotic convergence = 0.9993

The relative error ϵ_r of the results for the coarse mesh resolution $h = 2.5\mu m$ and the medium mesh resolution $h = 1.25\mu m$ is less than 0.1 percent. Therefore, we conclude that even the medium mesh resolution of $1.25\mu m$ is good enough for the interface, and refining mesh beyond that level doesn't have a noticeable effect on the result.

$$\epsilon_r = \frac{f_2 - f_1}{f_1} \tag{4.69}$$

As we can see, the Asymptotic convergence value is 0.9993 and is very near to one. Therefore, we can assume our analysis to be grid independent.

4.5 Test Case for Investigation of a Bell-shaped Nozzle Design and a Cone-shaped Nozzle Design.

4.5.1 The Difference Between Bell-shaped and Cone-shaped Nozzles

3D printed GDVNs from two different designs were developed to study the effect of the cone-shaped or the bell-shaped gas flow field on the GDVN performance. Figure 4.9a illustrates the schematic of the so-called “bell-shaped” gas flow field geometry and figure 4.9b shows the schematic of a gas dynamics virtual nozzles (GDVN) with cone-shaped gas flow field geometry.

4.5.2 Designing and Developing 3d Printed Gdvns With the Bell-shaped and the Cone-shaped Gas Flow Field Geometry

Geomtery for a 3D printed bell-shaped nozzle and also the geometry for the cone-shaped 3D printed nozzle counterpart to the bell-shaped nozzle was made, as shown in figure 4.10. The flow field geometrical parameters, including their dimensional values, are shown in figure 4.11. As an example, the design for the 3D printed bell-shaped nozzle cut into half is shown in figure 4.10. Figure 4.12 shows pictures of the developed and assembled cone-shaped and bell-shaped 3D printed devices based on the design showed in figure 4.10.

4.5.3 Developing the 3d Half Geometry for the Cone-shaped and the Bell-shaped Nozzles

The flow fields for the bell-shaped nozzles and the cone-shaped nozzles were developed analogous to the flow field of the operating 3D printed bell-shaped and cone-shaped GDVNs. For this purpose, Geometrical parameters of a cross-section of the design of the 3D printed GDVN, shown in figure 4.11, is used to develop the flow field for numerical simulations. Consequently, the three-dimensional flow field region for the bell-shaped nozzle, shown in figure 4.13, and and the three-dimensional flow field region for the cone-shaped nozzle, shown in figure 4.14 are developed. The blue surfaces of the figure 4.13 and 4.14 represent the surface of symmetry. Moreover, to come up with the complete flow field region for numerical simulation, a half-large cylinder with diameter of 1600 μm and length of 1100 μm, concentric to the orifice, is attached to the GDVNs for both bell-shaped and cone-shaped flow field regions to account for the chamber. The complete flow field region for the bell-shaped nozzle is shown in figure 4.15. So, for numerical simulations of the cone-shaped and the bell-shaped nozzles, two flow field domains were developed, one for the bell-shaped nozzle and one for the cone-shaped cone-shaped nozzle, shown in figures 4.13 and 4.14. As we can see in the figure, 3D half geometry is made for the flow field domain representation to save computation time, and this is because the cone-shaped and the bell-shaped nozzles are symmetrictrical along the jet propagation axis. Plus, a large half cylinder that is concentric to the gas orifice of the nozzle is attached to the nozzle to account for the chamber, i.e. the flow region that the liquid and the sheath gas enters after they leave the 3D printed nozzle. Diameter of the big half cylinder is 1600 μm and the length of the cylinder is about 1100 μm.

Having the flow field geometrical parameters inside the nozzle for the test cases for the bell-shaped nozzle and the test case for the cone-shaped nozzle, shown in figures 4.10 and 4.11, flow field geometries for numerical simulation of bell-shaped nozzle shown figure 4.13, and the flow field geometry for the numerical simulation of the cone-shaped nozzle shown in figure 4.14, is developed.

4.5.4 Test Case for Experimental Testing and Numerical Simulation

For the test case for both the numerical simulation and experimental testing, the inlet boundary condition for liquid is mass flow rate inlet is 48 $\mu l/min$ and the liquid is pure water, and the Helium sheath gas flow rate is set to be 6 mg/min. The testing results of the numerical simulations are to be compared with the experimental results.

Mesh count of the domain for cone-shaped and the bell-shaped nozzles are about 96000 grid points without adaptive mesh refinement (AMR), and the mesh count for a fully developed jet that experiences 3 AMR levels would become about 400000 for the numerical simulation of the cone-shaped and the bell-shaped nozzles. We need to keep in mind that for 3D simulations, the simulation time would scale 16 times if the mesh resolution was doubled since there are 3 spatial dimensions resulting in 8 times increase, and 1 temporal dimension where a more stringent CFL (Courant–Friedrichs–Lewy) condition leads to 16 times increase [21].

$$C = \Delta t \sum_{i=1}^{n} \frac{u_{x_i}}{\Delta x_i} \tag{4.70}$$

$$Co = \frac{\left|\vec{U}_f \cdot \vec{S}_f\right|}{\vec{d} \cdot \vec{S}_f} \Delta t \tag{4.71}$$

With Adaptive Mesh Refinement (AMR), the assumption is that the resolution is more than enough to capture viscous scales but areas near the interface requires more refinement to capture interface dynamics. As such the refinement only occurs near the interface. This results in the simulation time scaling proportional to 2^3 instead of 2^4. Based on the incompressible flow assumption, the velocity at the nozzle can be computed using mass conservation equation where the mass flux and volume flux is constant from inlet of gas to the orifice. The velocity computed based on our geometry and gas flow rate of 6 mg/min, we ascertain the average velocity to be 286 m/s which is less than 0.3 $Mach$. Therefore, we can conclude that incompressible assumption for the operating condition is valid.

4.5.5 Runs

The domain of the large half-cylinder that accounts for the chamber of the flow field region of the bell-shaped case and the cone-shaped case, is designed to be big enough in such a way that the influence of outlet boundary conditions on the upstream flow would be negligible. Moreover, the 3D simulations are incompressible and they require the mach number to be below 0.3 as a constraint. Anything higher requires a compressible solver as incompressible solvers become unphysical. The compressible solver are numerically stiff, and often result in instability. The mach number is calculated to be under 0.3 for the sheath gas to assume the flow is incompressible.

Parallelization

OpenFOAM codes are based on MPI based multithreading. This ensures its versatility over shared memory as well as distributed memory architectures. The agave HPC facility of Arizona State University, that has been used for running the numerical simulations, is comprised for several 100 nodes with 28 cores. The computational efficiency of the simulations is greatly enhanced when run on a single node. Most of the computations done are on a single node. However, the simulations with highest resolution require a higher number of nodes and as such the computation is done over distributed memory.

The "Simple Method" in OpenFOAM simply does a grid decomposition of the domain and varies the domain boundaries such that the computational load i.e. the number of cells is equivalently distributed. This should not be confused with the SIMPLE algorithm for advancing the fluid simulation. The "Scotch Method" distributes an equal amount of cell count over multiple cores while minimizing the number of cells at the boundary of the domain of each core. As an example, figure 4.16 shows how the computational domain corresponding to the bell-shaped nozzle is decomposed to run on 16 cores be the aforementioned "simple" method, and figure 4.17 shows how the computational domain corresponding to the bell-shaped nozzle is decomposed to run on 16 cores be the aforementioned "scotch" method. The scotch decomposition enables distribution of all the cells in the domain across multiple nodes and cores. The scotch algorithm minimizes the number of contact cells while also minimizing the difference in the number of cells for each processor.

Figure 4.18 shows the Wall clock time in seconds versus iterations for our case to come up with the best possible domain decomposition and parallelization approach for the cone-shaped and the bell-shaped cases. The "scotch" decomposition method with 16 cores has been chosen for running the bell-shaped and the cone-shaped cases.

4.5.6 Testing and Image Analysis

The results for experimental testings for a 3D printed cone-shaped nozzle having the similar geometry as the numerically simulated cone-shaped nozzle, and for a 3D printed bell-shaped nozzle having the similar geometry as the numerically simulated bell-shaped nozzle are shown in figure 4.19. More comprehensive explanation of the results are explained in section 4.5.7.

4.5.7 Results of the 3D Simulations and Comparison of the Results With the Experimental Testing Results

The 3D numerical simulation results of the Jet length versus time, for the time steps between 400 μsec and 1000 μsec, for the cone-shaped and the bell-shaped cases are shown in figure 4.21a. We will consider the results for the time points between 600 μsec and 1000 μsec to make sure the jet is fully developed.

The numerical simulation results for the jet length values for the time steps between 600 μsec and 1000 μsec are shown in figures 4.21a. As We can see from the figure 4.21a, the bell-shaped nozzle operation generally results in the longer liquid jet and consequently more liquid jet stability under the similar operating condition. Quantitatively, the median value for the jet length result of the bell-shaped nozzle (602.1 μm) is about 4 percent longer than the corresponding value for the cone-shaped nozzle (579.5 μm).

The experimental results of testing under similar operating conditions of the 3D printed nozzles with flow field geometrical parameters, one similar with the simulated cone-shaped nozzle, and another similar to the simulated bell-shaped nozzle, are shown in figures 4.21b. Again we can see from figure 4.21b that the bell-shaped nozzles results in the longer liquid jet and consequently more liquid jet stability under the similar operating condition. Quantitatively, the median value for the experimental jet length results of the bell-shaped nozzle (544.3 μm) is about 4 percent longer than the corresponding value for the cone-shaped nozzle (524.8 μm).

Figures 4.22a and 4.22b show the comparison of the experimental results and the numerical simulation results for the cone-shaped nozzle running under similar operating conditions. We can see from figures 4.22a and 4.22b that the jet length values in the numerical simulation results are generally larger than the jet length values in the experimental results, as the median values of the CFD results are bout 10 percent longer than the corresponding values of the experimental results for both cone-shaped and bell-shaped nozzles. This is most likely due to errors in the numerical simulation schemes. Similarly, for the similar operating conditions, figures 4.22a and 4.22b show that the jet length values from the numerical simulation of the bell-shaped nozzle are slightly larger than the experimental testing results, again due to errors in numerical simulation schemes. Moreover, a picture from the numerical simulation and the experimental testing of a running jet for the cone-shaped GDVN design is shown in figure 4.23.

The integrated plots show the CFD results versus the experimental results in figures 4.22a and 4.22b.

Running the Simulation

Moreover, the 3D simulations are incompressible and they require the mach number to be below 0.3 as a constraint. Anything higher requires a compressible solver as incompressible solvers become nonphysical. The compressible solver are numerically stiff, and often result in instability. The mach number is calculated to be under 0.3 for the sheath gas to assume the flow is incompressible.

4.5.8 Contours and Figures From the Numerical Simulation Results

Figure 4.24 shows the pressure contours in Pascal for the 3D simulation of the cone-shaped design and the bell-shaped design.

Streamlines of the flow field are shown in figure 4.26. Recirculation cells can be seen in the pictures of figure 4.26.

three level AMR (adaptive mesh refinement) for the cells in the vicinity of the liquid-gas interface is shown in figure 4.25.

Contours for the Velocity magnitude (in m/s) in the direction of the jet is shown in figure 4.27. 3 AMR (adaptive mesh refinement) levels can be seen for the cells that are in the vicinity of liquid-gas interface.

A cross-section of the jet and how it breaks up to droplets is shown in figure 4.28.

Jet regions for a running nozzle for the cone-shaped and the bell-shaped design is shown in figure 4.29, and the pictures of the jet regions for a running nozzle along with the droplets after the jet breakup for the whole flow field are shown in figures 4.30 for the cone-shaped and the bell-shaped designs.

Contours of the pressure values (in Pascal) are shown in figure 4.31 for the cone-shaped and the bell-shaped designs.

4.6 Three-dimensional Numerical Simulation of a Widely Used 3D Printed Nozzle

In this section, we illustrate how we develop the complete region to numerically simulate the 3D printed GDVNs for design 2 of the paper [61] and the Chapter 3 in three dimensions. Design details can be seen in figure 3.3.

Preparing the Flow Field Setup for the Simulation

First, we extract the liquid flow field and the gas flow field inside the nozzle from the design, shown in figure 4.32. Figure 4.33 shows how we extract the flow field inside the nozzle from the CAD (computer-aided design) file design, that is shown in figure 4.32, by using Ansys SpaceClaim software [8], [9]. Afterward, the flow field regions for the chamber is added by adding a cylinder to the flow field region. This cylinder should be large enough so that the effects of the boundary conditions at the walls of the cylinder on the simulation results would become negligible. Inlet boundary conditions for the liquid and the sheath gas are also implemented. Then, a cylinder is added to account for the region for the chamber, and the complete flow region is formed, that is shown in figure 4.35. Unstructured Hexahedral-dominated Mesh with 9658109 nodes and 26649918 elements 4.41 was created by using Ansys Meshing software.

A cylindrical region with 50 μm diameter concentric to the center of the nozzle orifice was implemented as the body of influence, that is shown in 4.40. In the region inside that cylinder, mesh resolution is high to make sure the mesh resolution is high enough (less than 0.6 μ m) in the regions of the liquid jet and the droplets and their near surroundings, that is shown in figure 4.41. All of the required boundary conditions, including Wall boundary conditions shown in figure 4.36, liquid inlet boundary conditions shown in figure 4.38, the sheath gas inlet boundary condition that shown in figure 4.37, and the pressure outlet boundary conditions, shown in figure 4.39 are also defined in the meshing software.

Simulation Results

The simulation results for the liquid flow rate of about 48 $\frac{\mu\ l}{min}$ and gas flow rate of about 8 $\frac{mg}{min}$ for different time steps are shown in figures 4.42 4.43 4.44 4.45 4.46 4.47 4.48, that also shows how the liquid jet propagates and how it breaks up.

The results of the numerical simulation for the operating condition of 48 $\mu l/min$ of liquid flow rate and 8 mg/min of Helium sheath gas flow rate are shown in the figures below:

4.7 Conclusion

In this section we introduced a pipeline for CFD numerical simulation of a GDVN operation, that can be applied for different designs. Comparing the jet length results of the numerical simulation with the results from the experimental testings showed acceptable agreement. However, numerical simulation results were slightly longer than the corresponding experimental results, due to the errors in the schemes used in the numerical simulations.

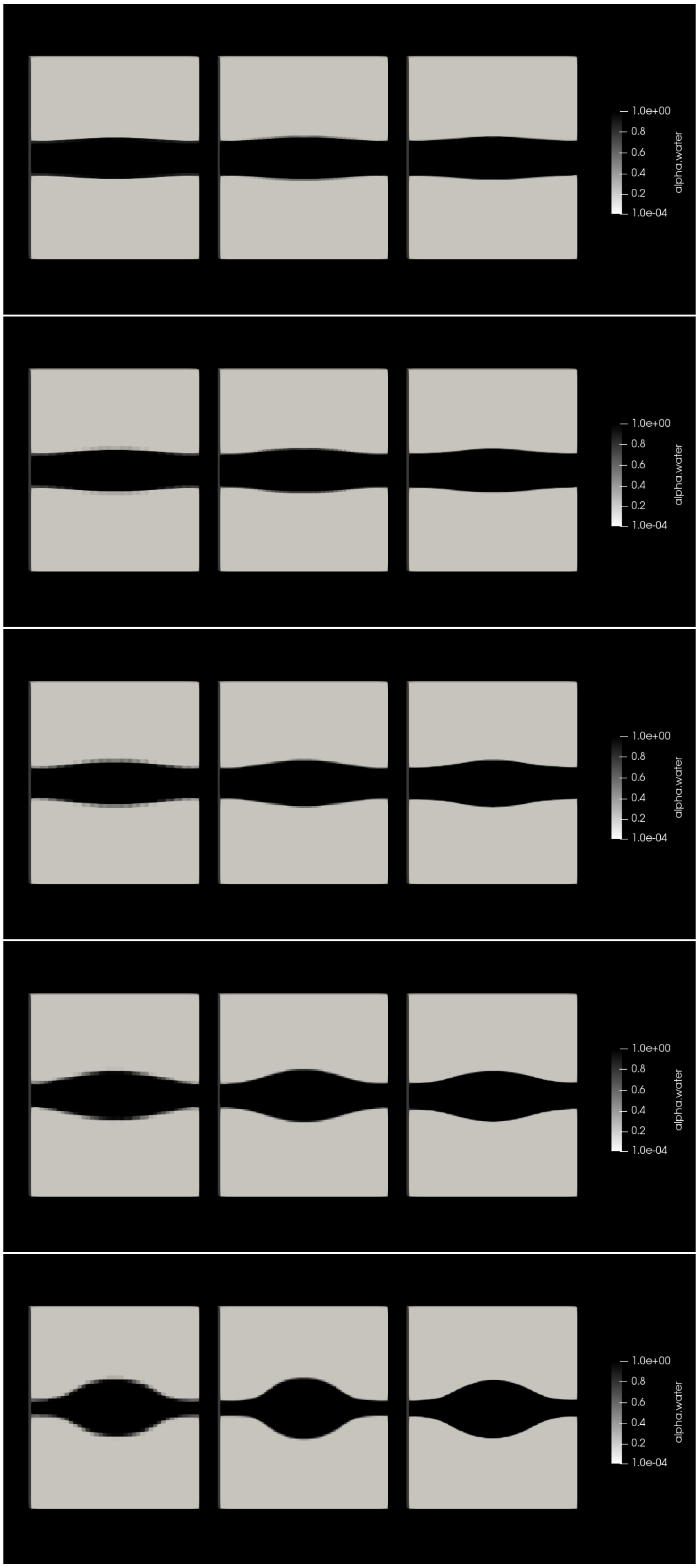

Figure 4.7: Cylinder collapse for GCI analysis to study the grid resolution independency of the results. It starts from time 0 till time 12 μ *sec* with 3 μsec interval. The left pictures correspond to the coarsest mesh resolution at the interface with 1 AMR level, the middle pictures correspond to the medium mesh resolution with 2 AMR levels, and the right pictures correspond to the fine mesh resolution at the interface with 3 AMR levels.

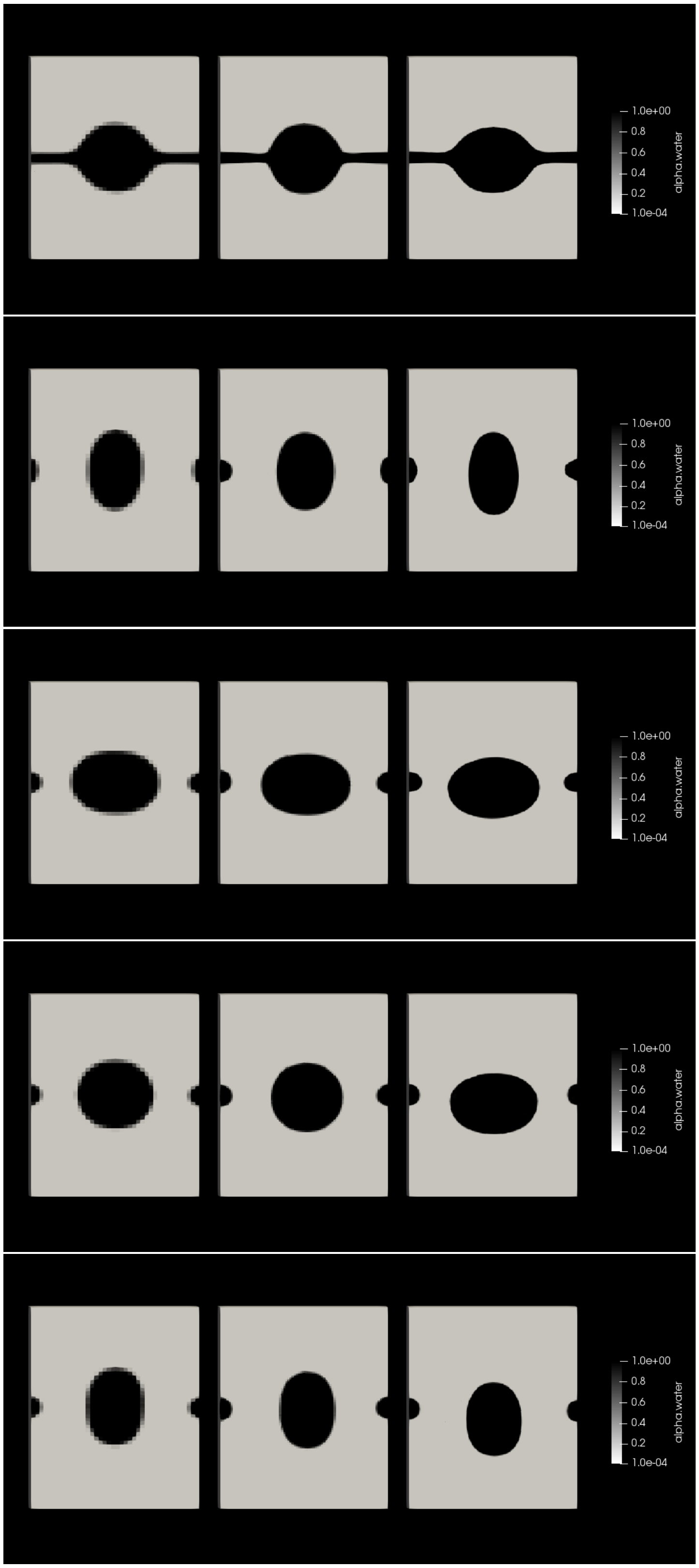

Figure 4.8: Cylinder collapse for GCI analysis to study the grid resolution independency of the results. It starts from time 14 till time 26 μ *sec* with 4 μsec interval.The left pictures correspond to the coarsest mesh resolution at the interface with 1 AMR level, the middle pictures correspond to the medium mesh resolution with 2 AMR levels, and the right pictures correspond to the fine mesh resolution at the interface with 3 AMR levels.

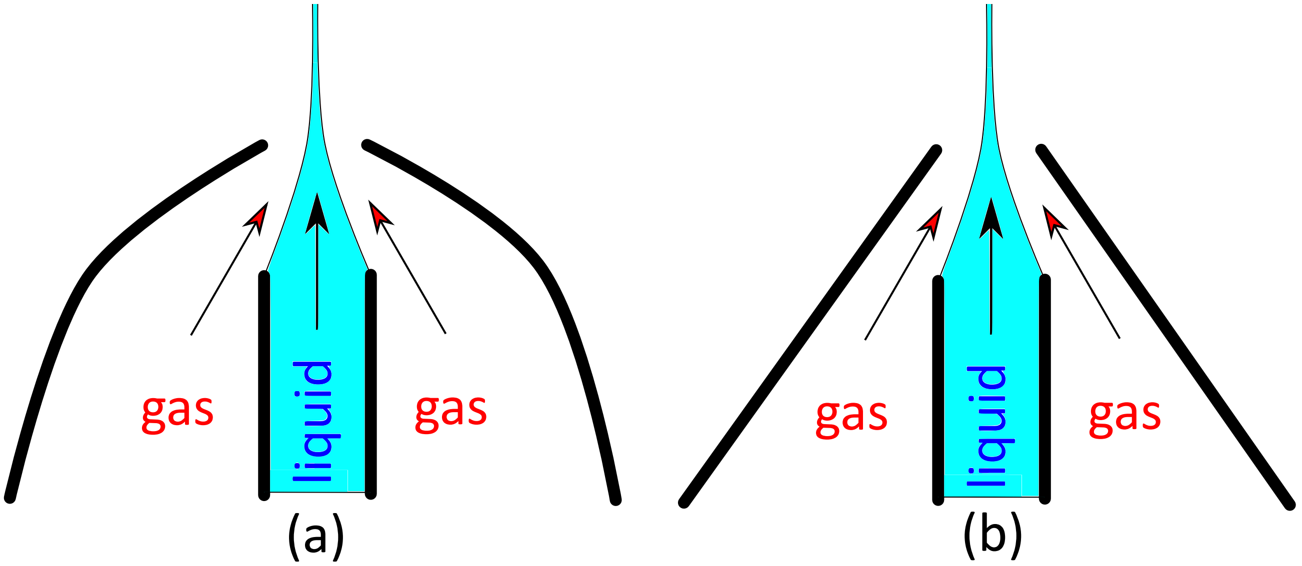

Figure 4.9: Schematic of a GDVN with bell-shaped geometry for gas flow field (a), and schematic of a GDVN with cone-shaped geometry for gas flow field (b).

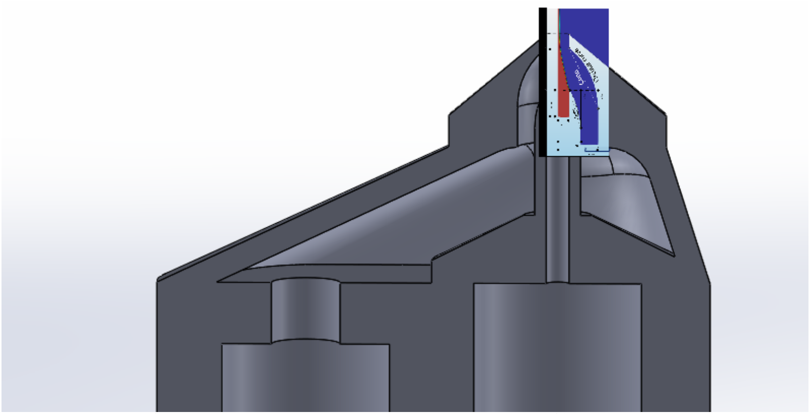

Figure 4.10: Design of the bell-shaped 3D printed GDVN cut into half.

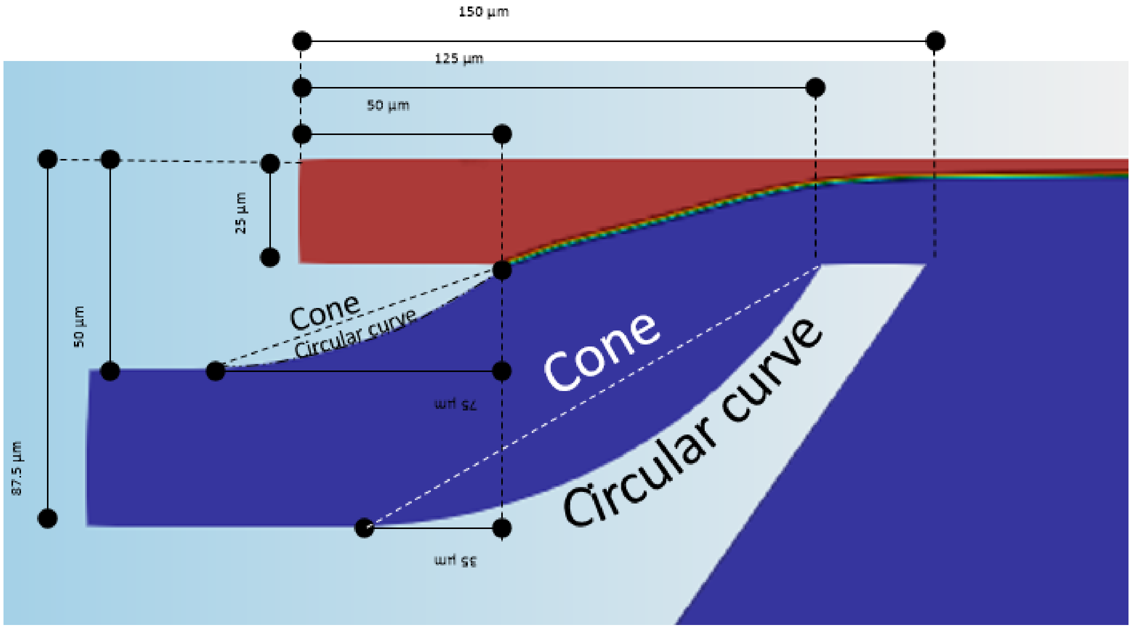

Figure 4.11: Geometrical parameters of a cross-section of the cone-shaped and bell-shaped 3d printed GDVNs.

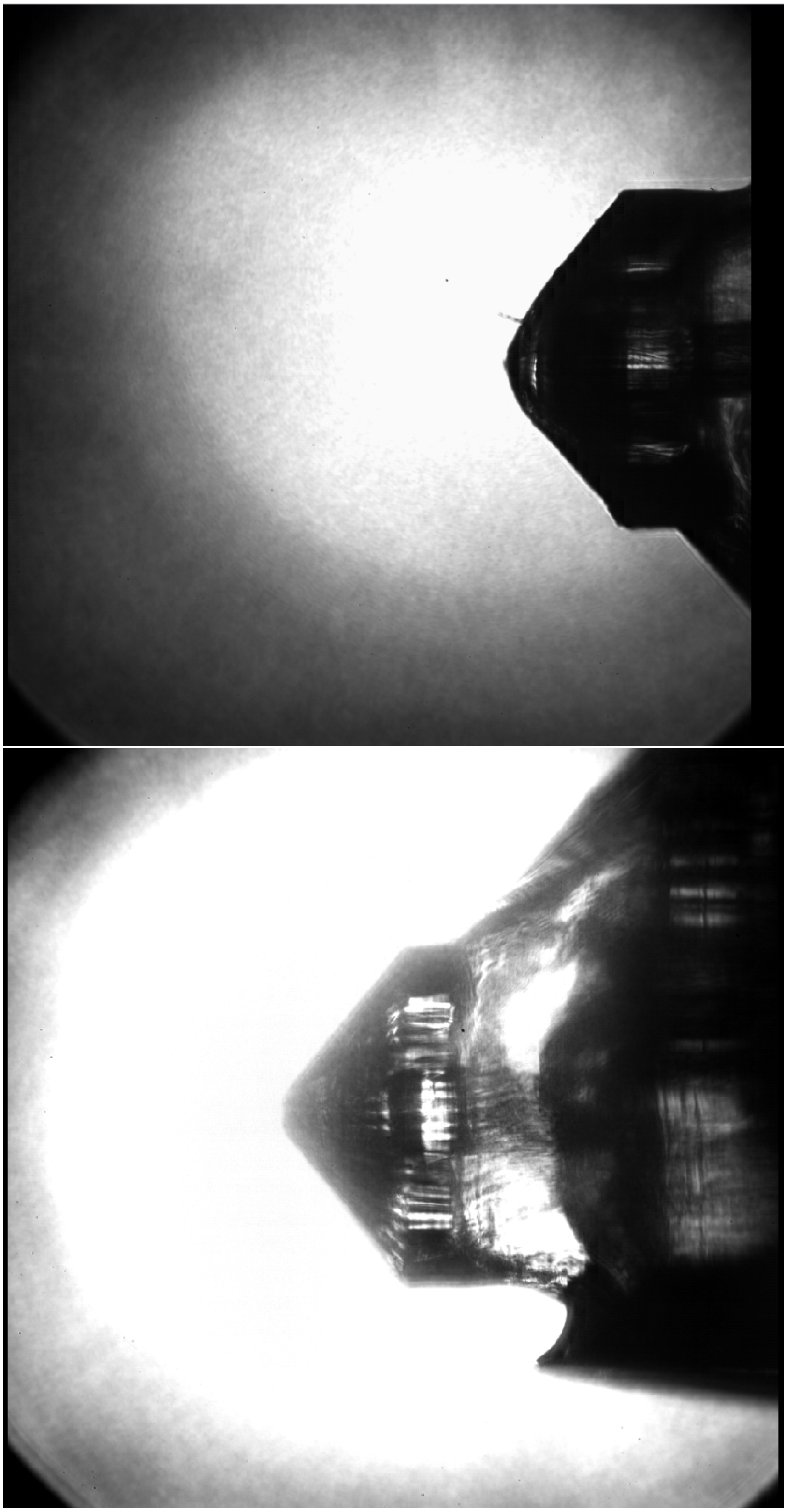

Figure 4.12: Picture of the 3d printed GDVN with bell-shaped gas flow field geometry (upper picture) and picture of the 3d printed GDVN with cone-shaped gas flow field geometry (lower picture).

Figure 4.13: Computational flow field for the GDVN with bell-shaped geometry for gas flow field. Blue surface is the surface of symmetry.

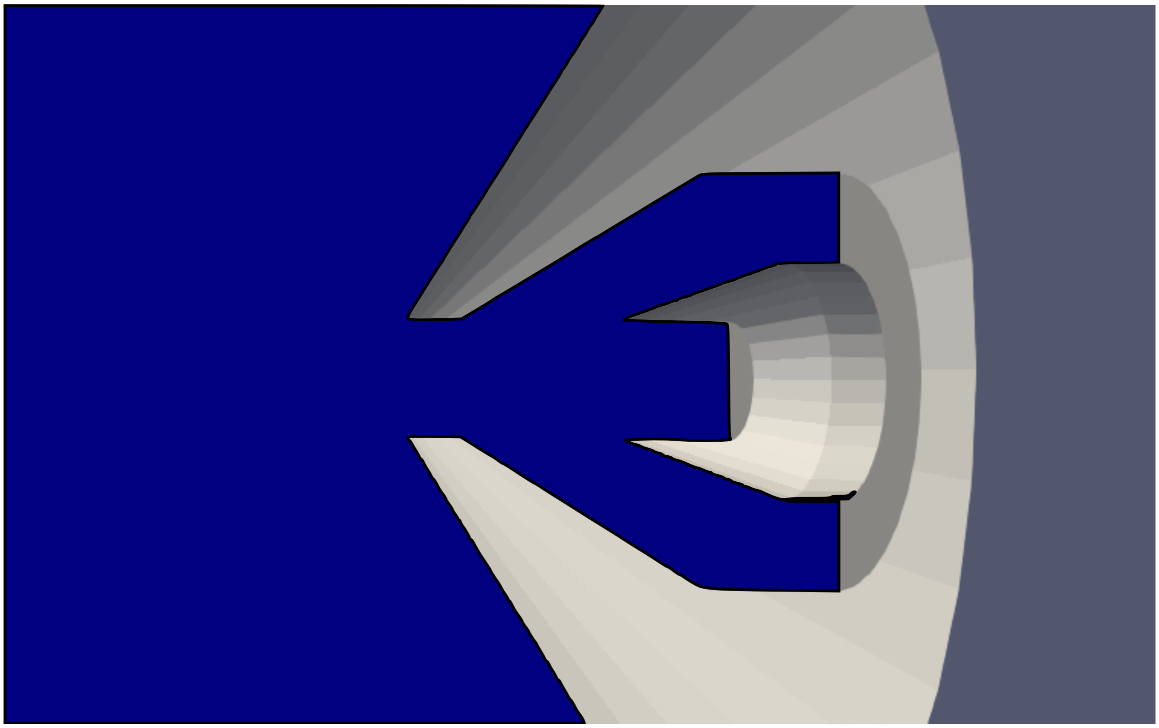

Figure 4.14: Computational flow field region for the GDVN with cone-shaped geometry for gas flow field.

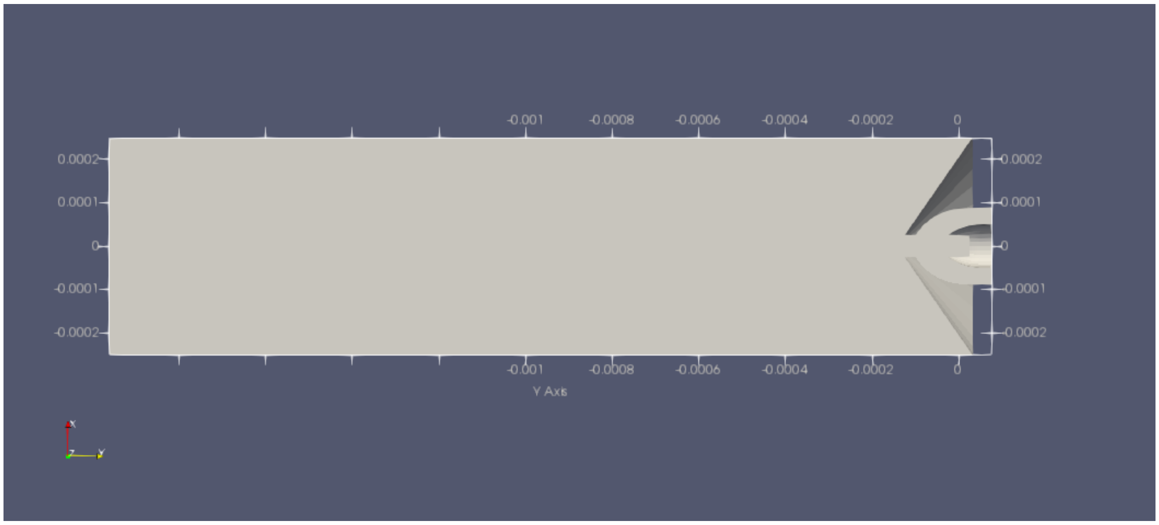

Figure 4.15: Complete flow field region for the bell-shaped nozzle numerical simulation.

Figure 4.16: A visualization of simple domain decomposition.

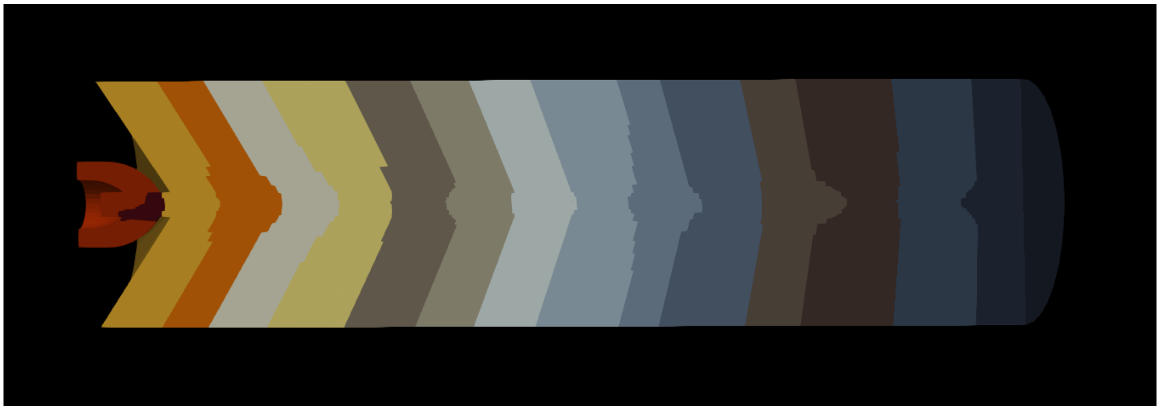

Figure 4.17: A Visualization of Scotch Domain Decomposition.

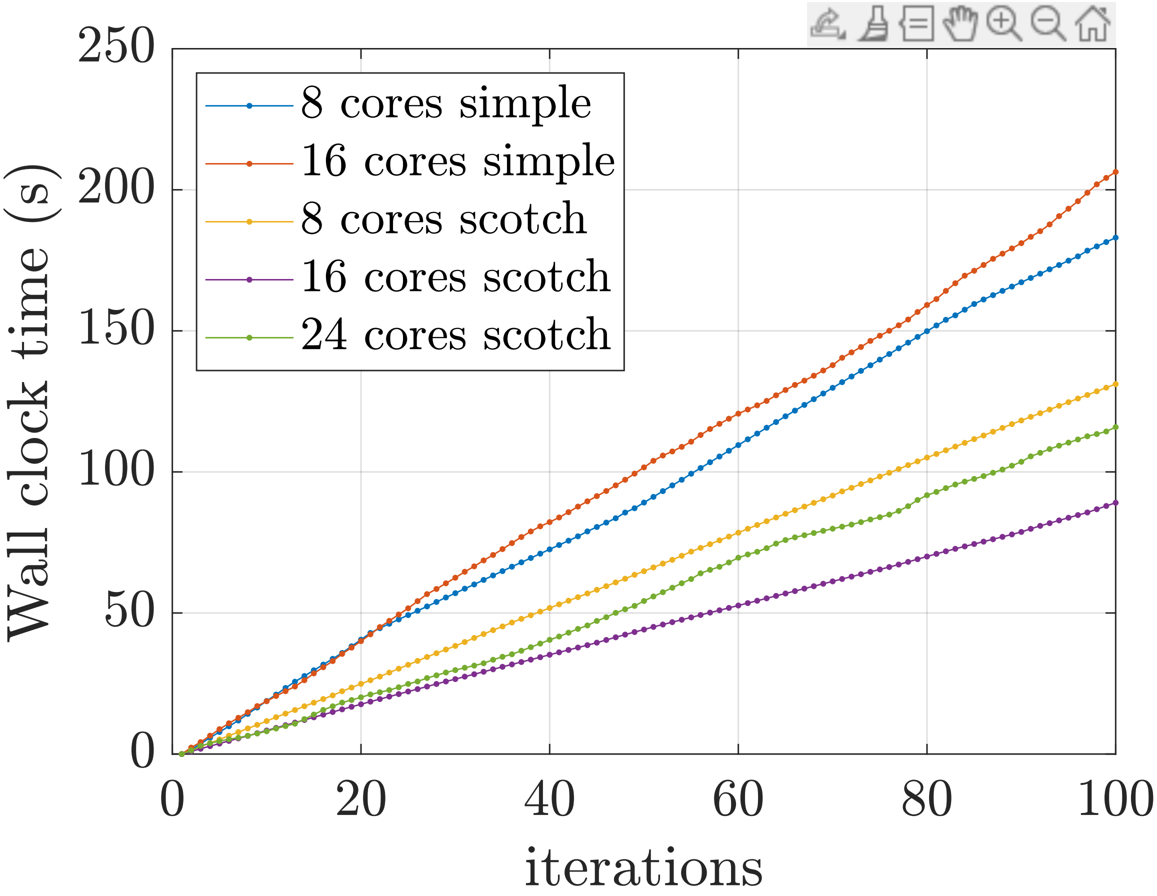

Figure 4.18: Speed variation of various methods for a various number of cores.

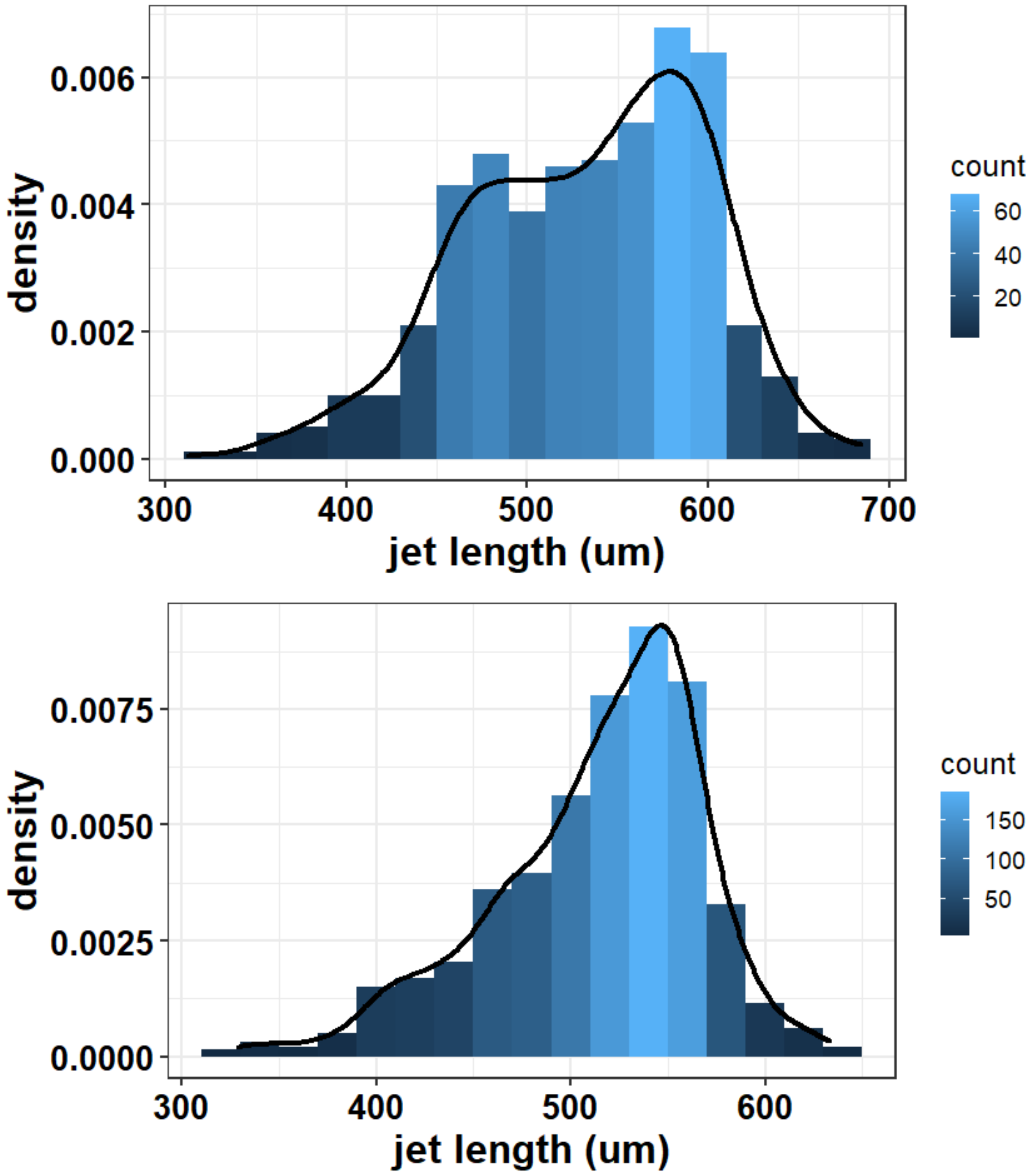

Figure 4.19: Experimental results of cone-shaped and bell-shaped nozzles.

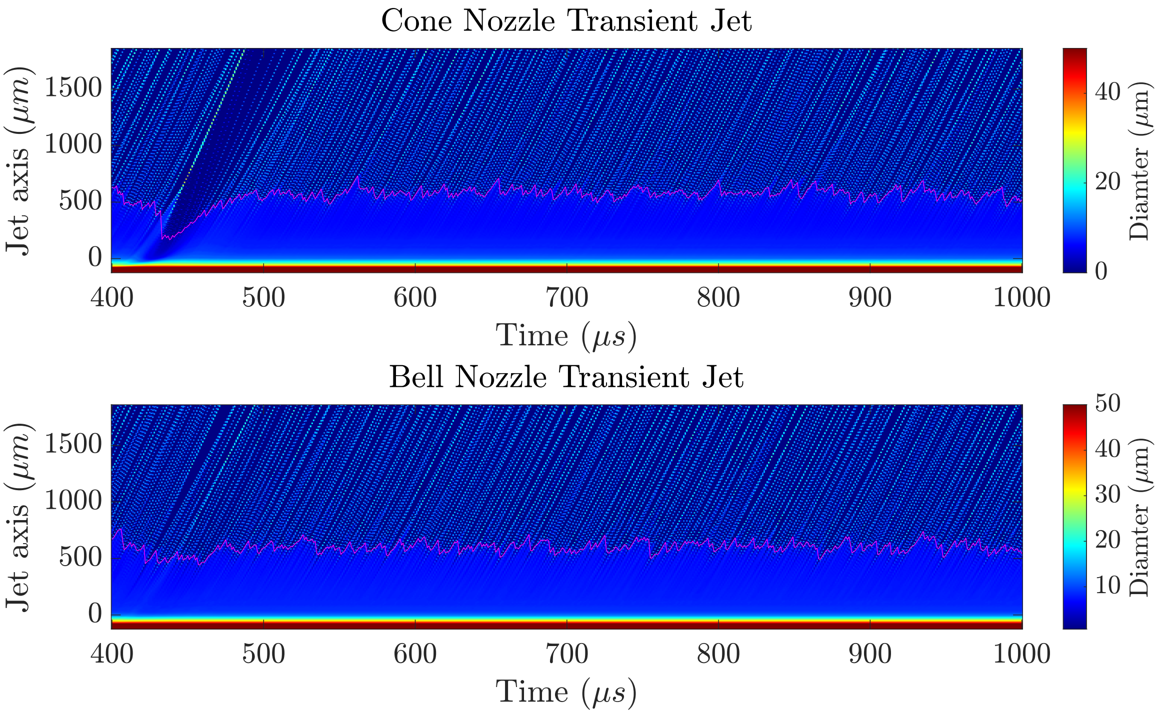

Figure 4.20: The jet length and diameter for given times. The temporal resolution is 1 μs.

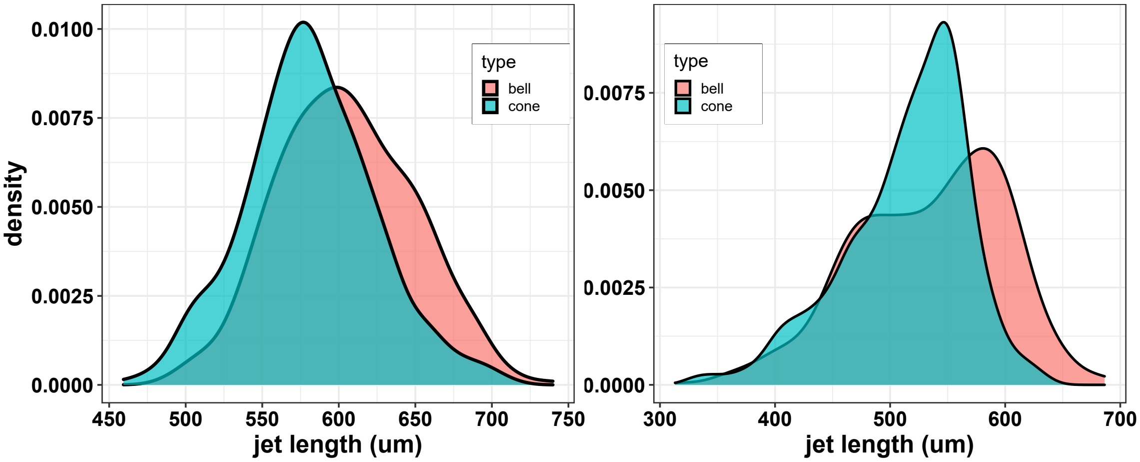

(a)

(b)

Figure 4.21: Numerical simulation results of cone-shaped and bell-shaped nozzles (a), and experimental results of cone-shaped and bell-shaped nozzles (b).

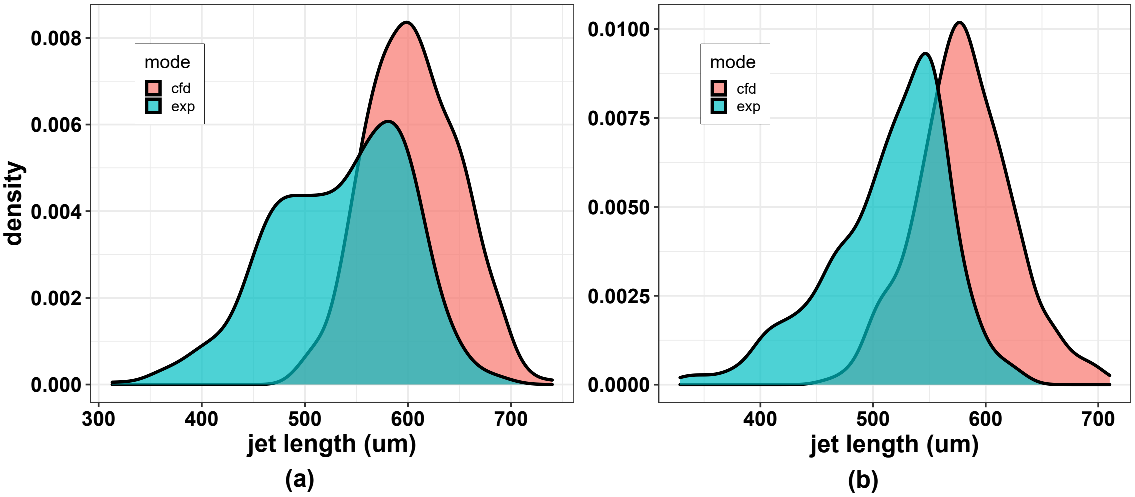

Figure 4.22: Experimental and CFD results of bell-shaped nozzles (a), and experimental and CFD results of cone-shaped nozzles (b).

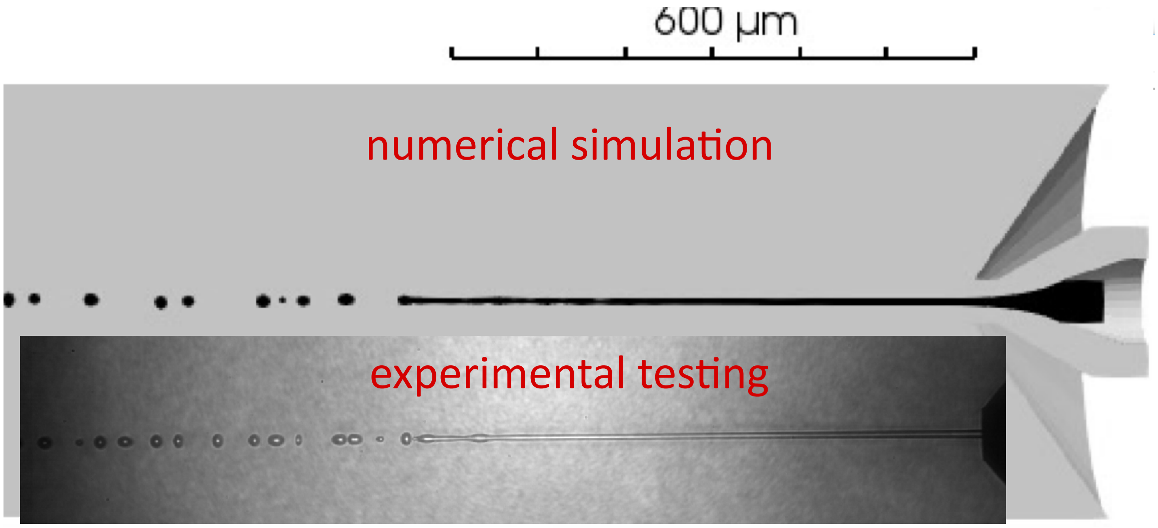

Figure 4.23: A picture from the numerical simulation and the experimental testing of a running jet from the cone-shaped GDVN design.

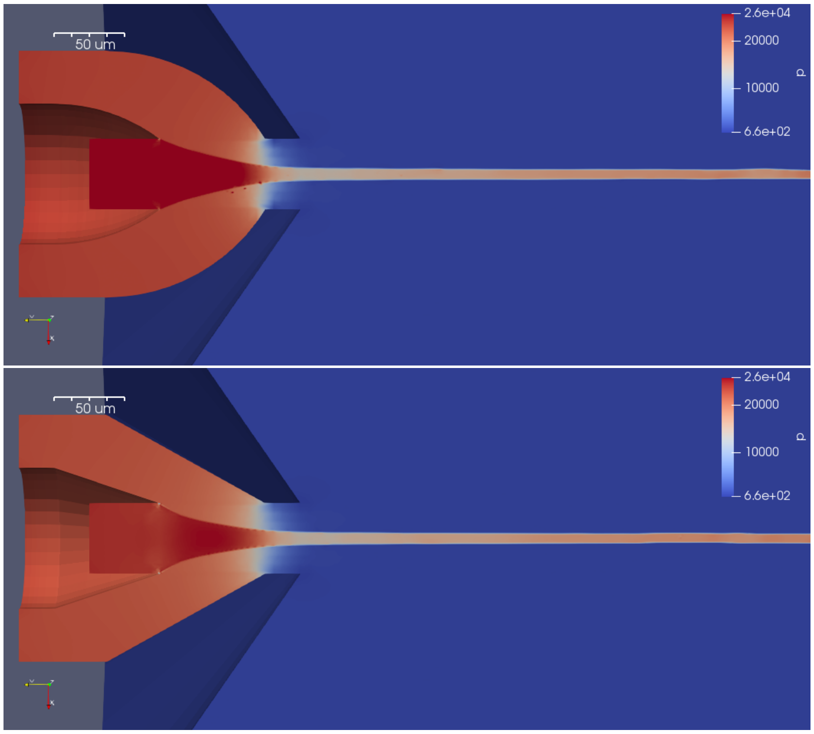

Figure 4.24: Pressure values in Pascal for the gas and liquid for the cone-shaped and the bell-shaped 3d simulation.

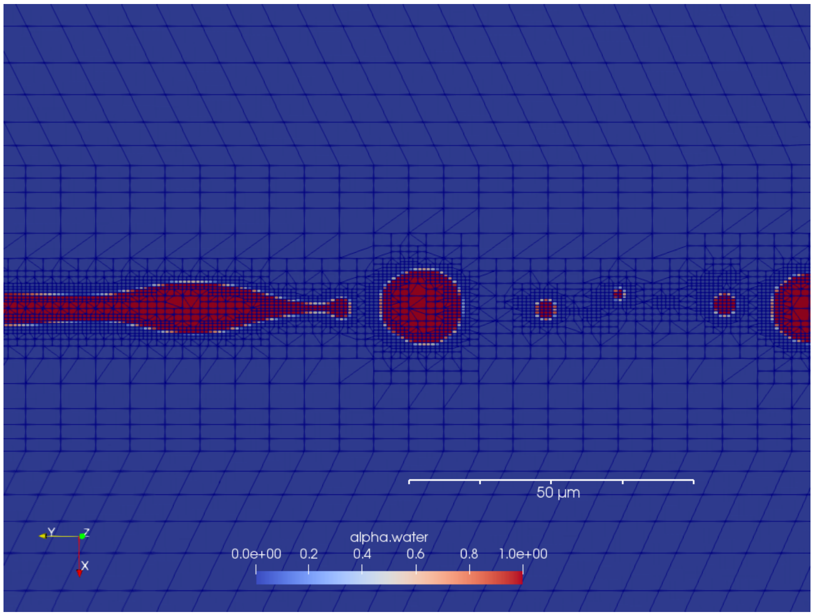

Figure 4.25: Three AMR levels for the cells in the vicinity of the liquid-gas interface for the bell-shaped nozzle design.

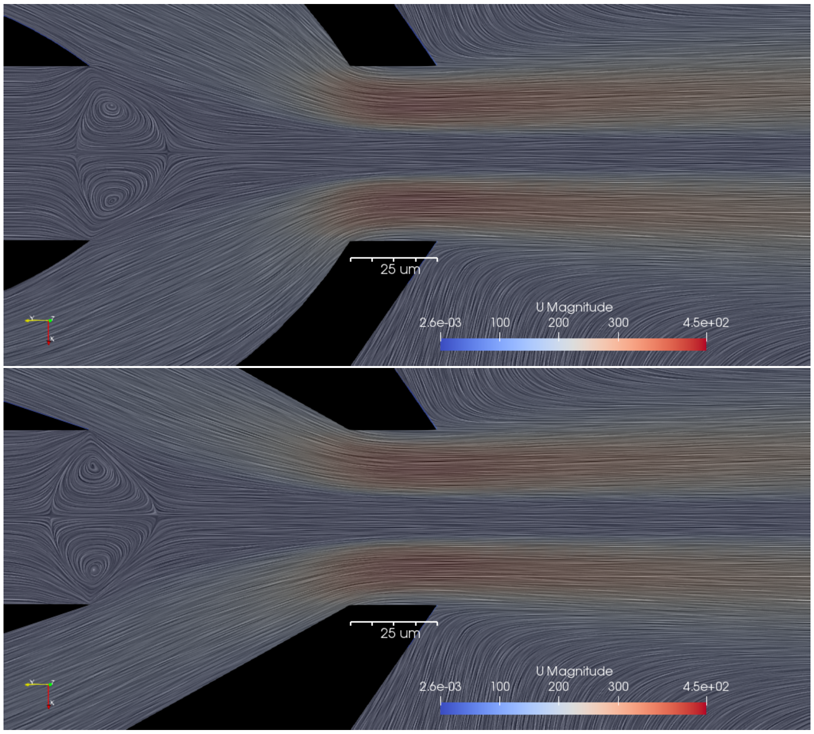

Figure 4.26: Streamlines of the gas flow and the liquid flow for the 3d simulation of the cone-shaped and the bell-shaped nozzle designs.

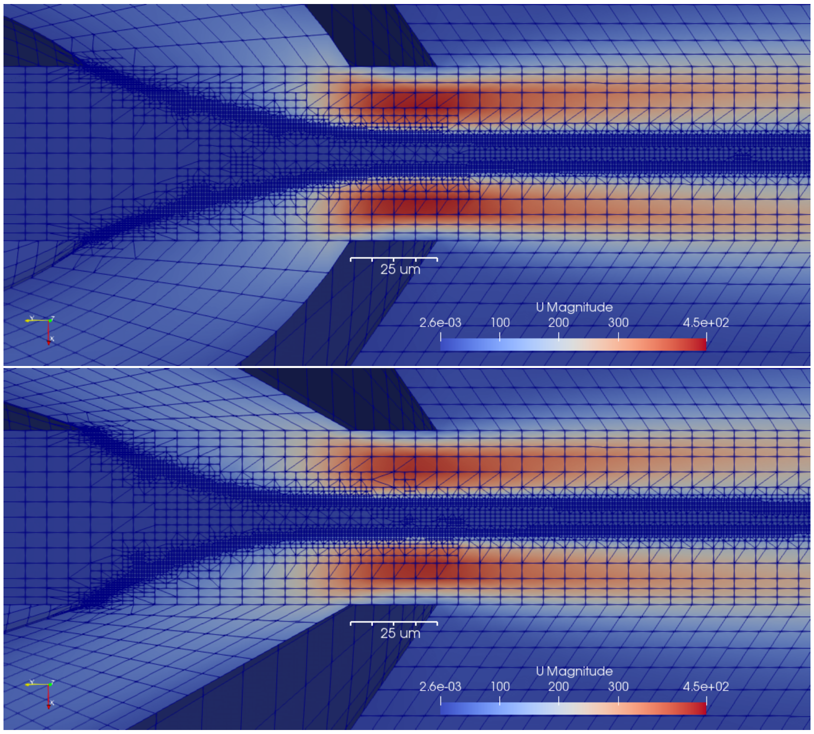

Figure 4.27: U component of the velocity magnitude in m/s. This component of the velocity magnitude is the component in the direction of jet propagation.

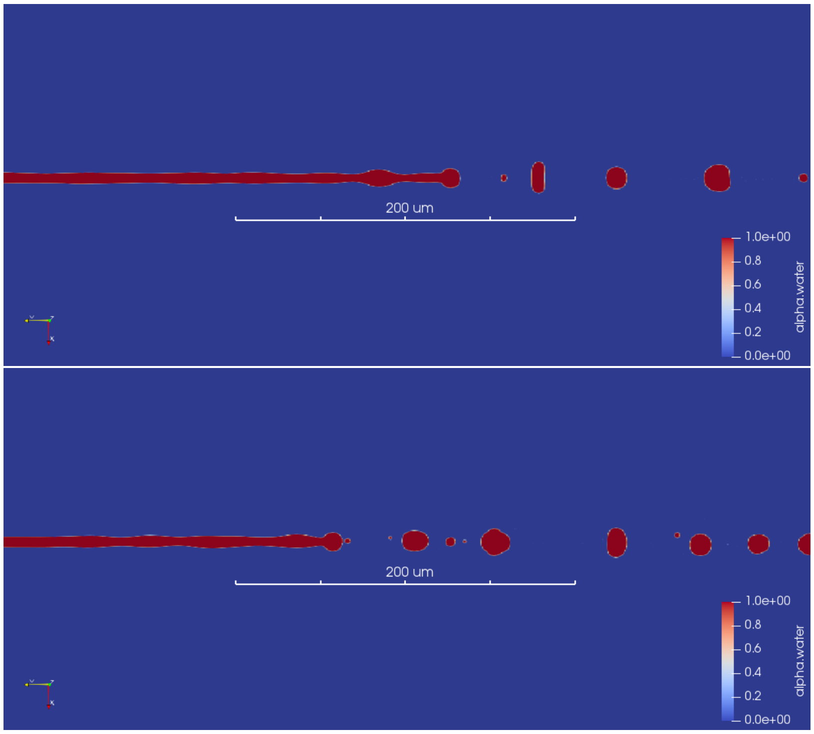

Figure 4.28: A cross-section of the jet and how it breaks up into droplets for the bell-shaped design (upper picture) and the cone-shaped design (lower picture).

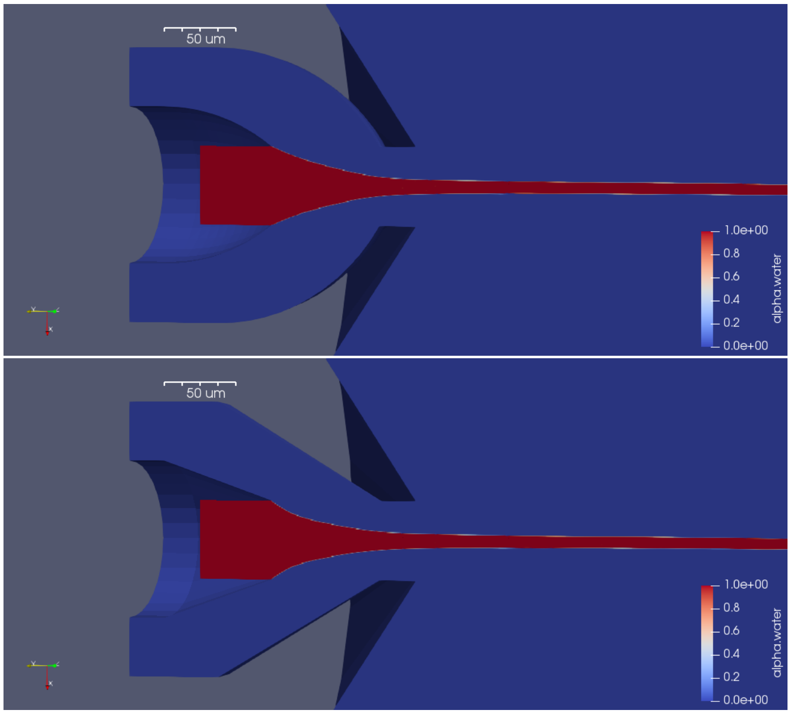

Figure 4.29: Jet regions in the cone-shaped and the bell-shaped design.

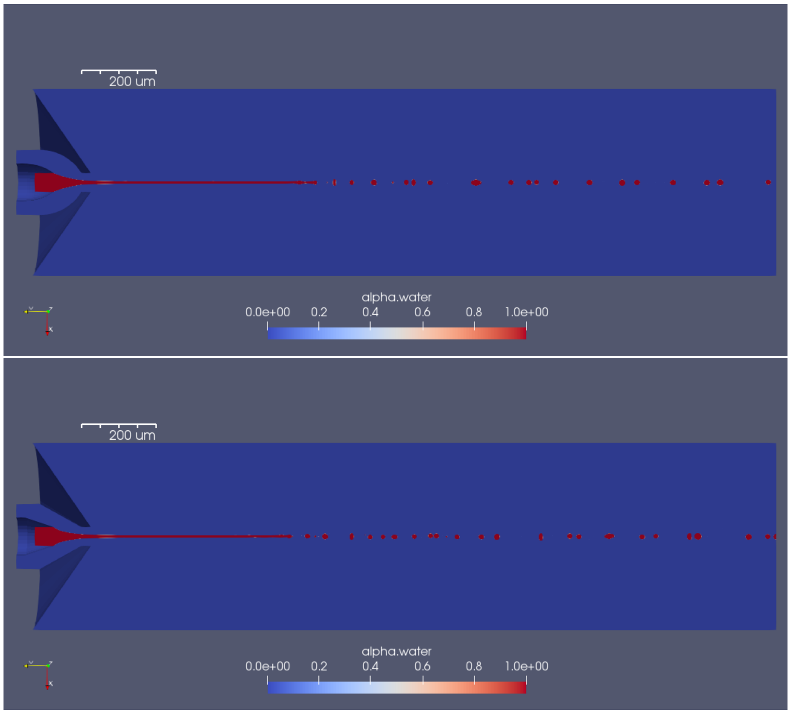

Figure 4.30: The jet regions for a running nozzle along with the droplets after the jet breakup for the cone-shaped (lower picture) and the bell-shaped (upper picture) designs.

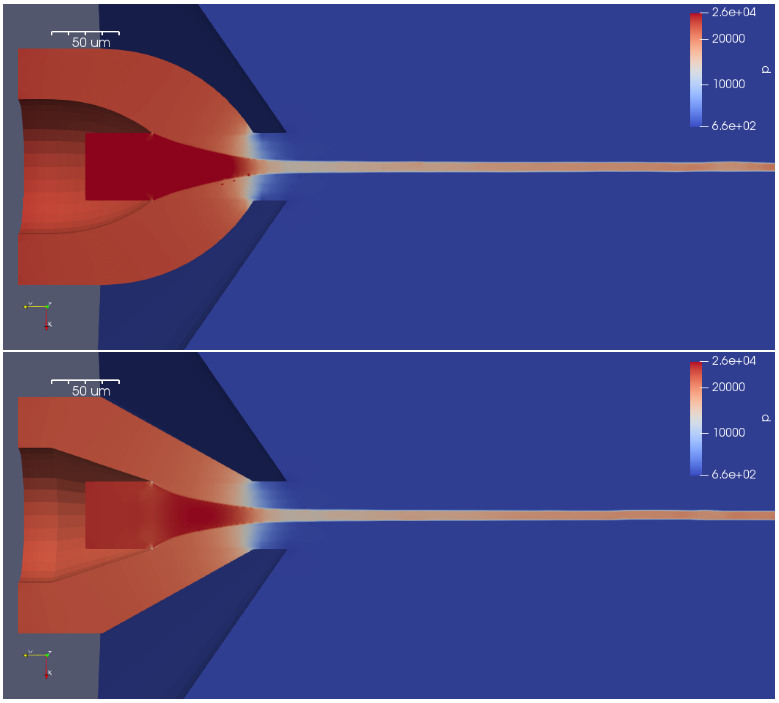

Figure 4.31: Contours of the pressure values (in Pascal) for the cone-shaped (lower picture) and the bell-shaped (upper picture) designs.

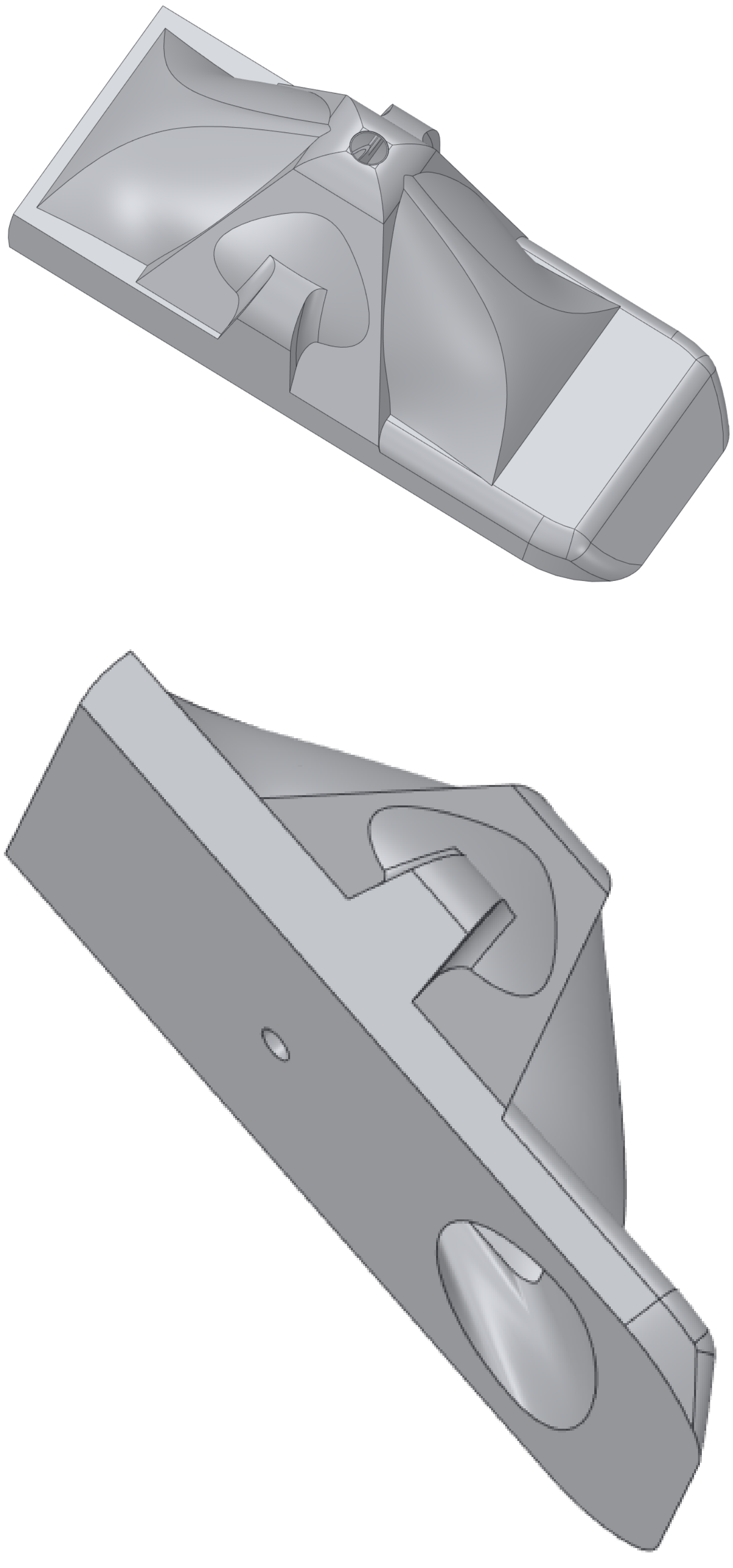

Figure 4.32: CAD (computer aided design) of the GDVN.

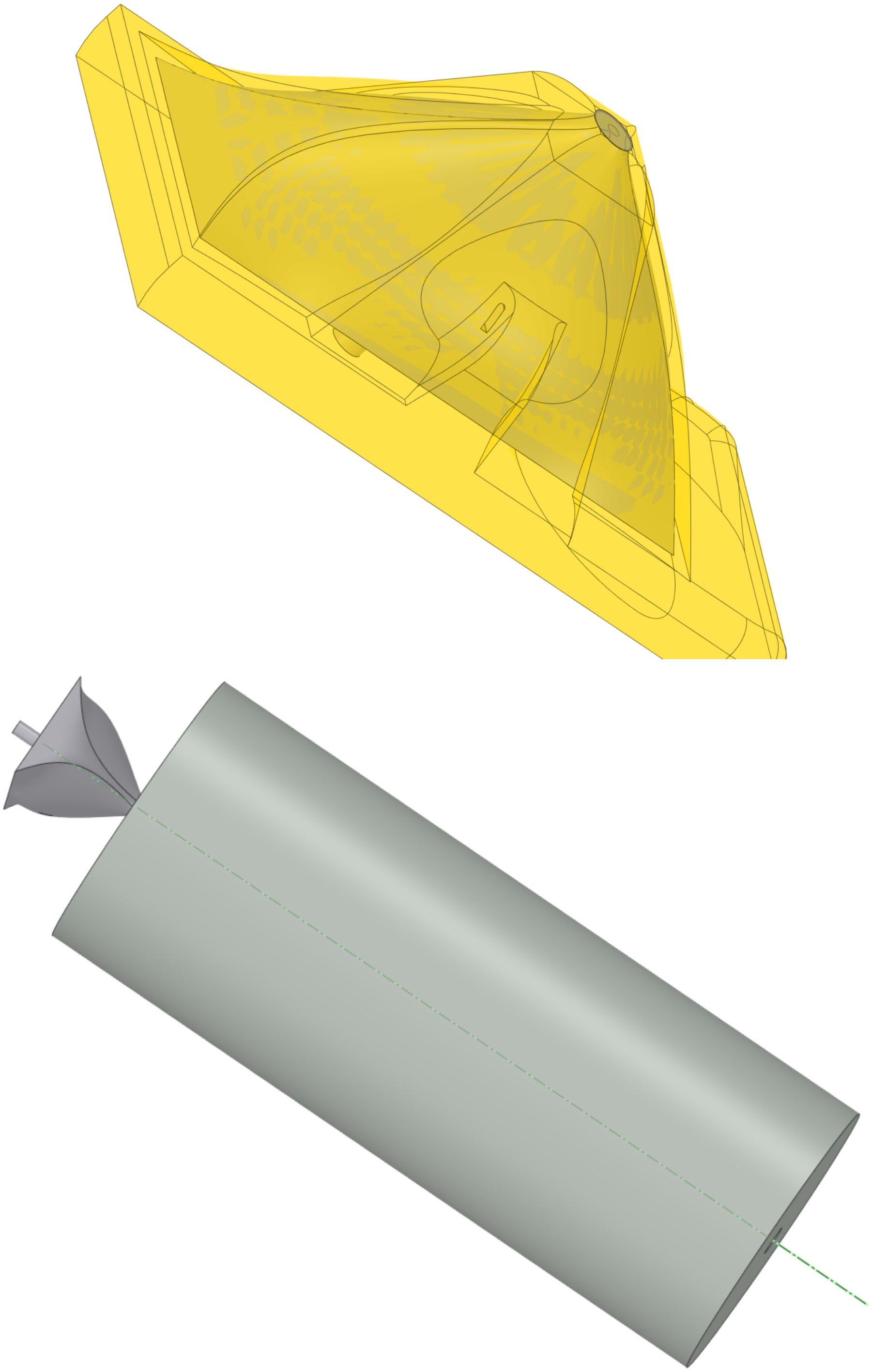

Figure 4.33: Three-dimensional flow region extracted from the CAD file (above picture) and afterward, adding a big cylinder to it to account for the flow region of the chamber.

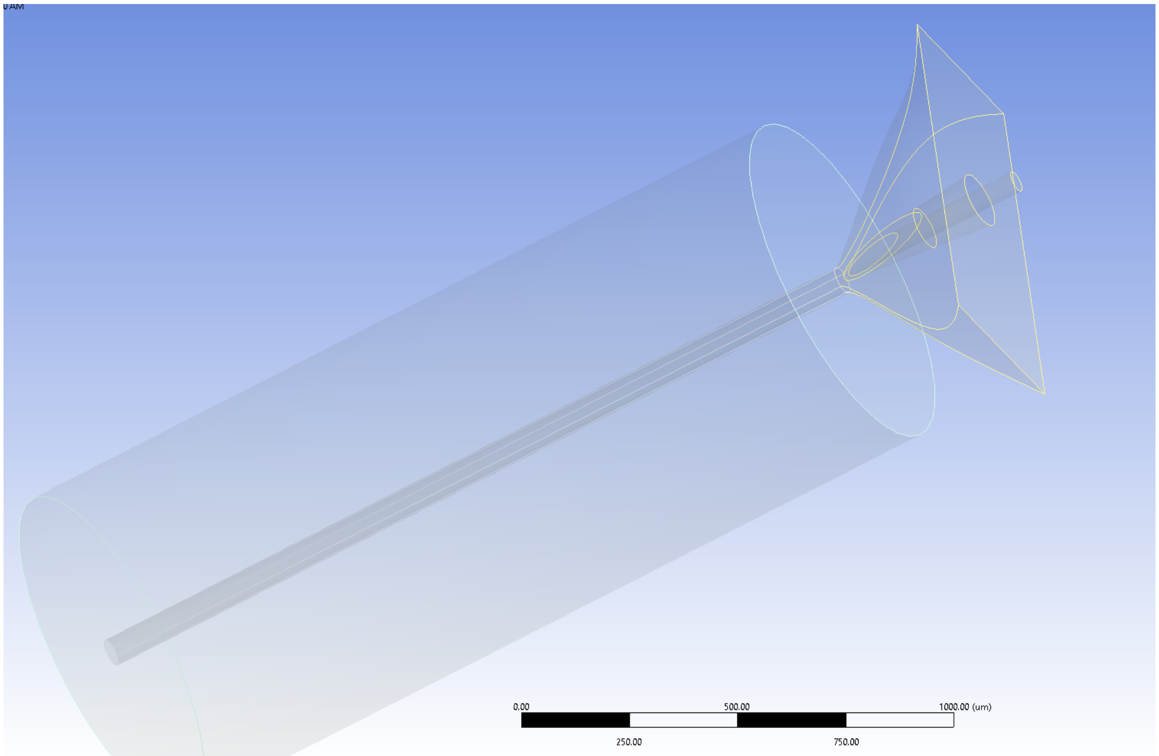

Figure 4.34: Another picture of the entire flow field region.

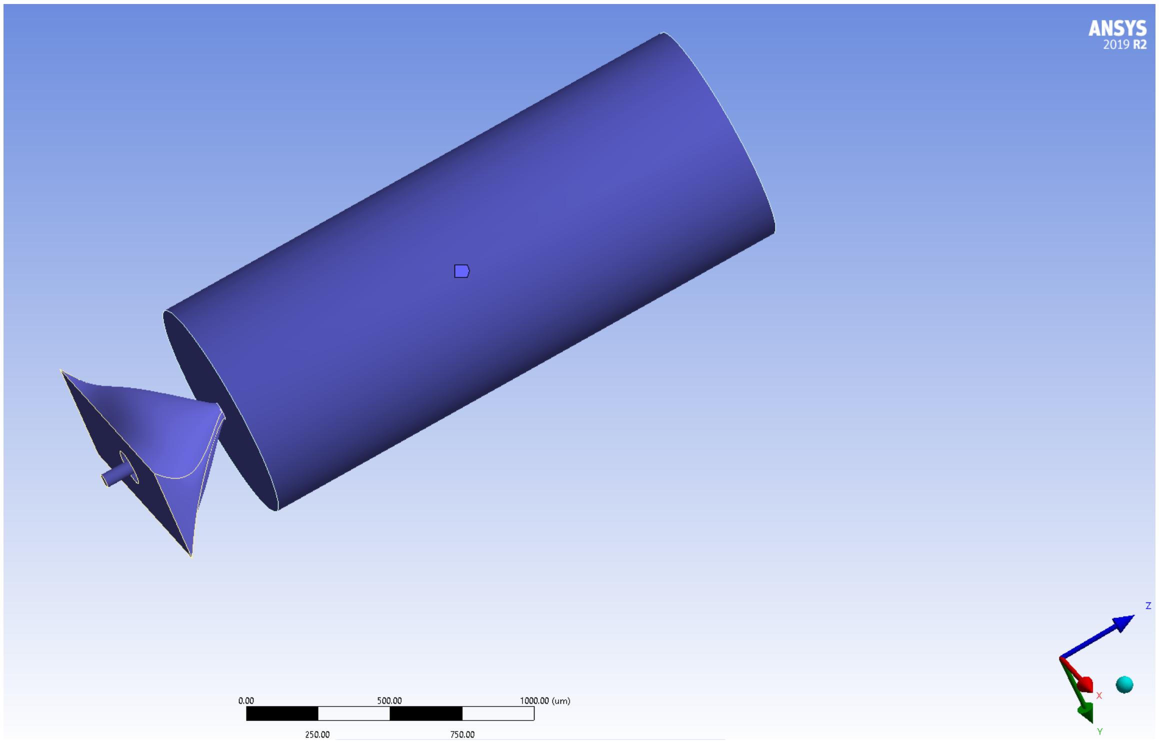

Figure 4.35: Complete flow region resulting from adding the flow region in the chamber to the region inside the nozzle.

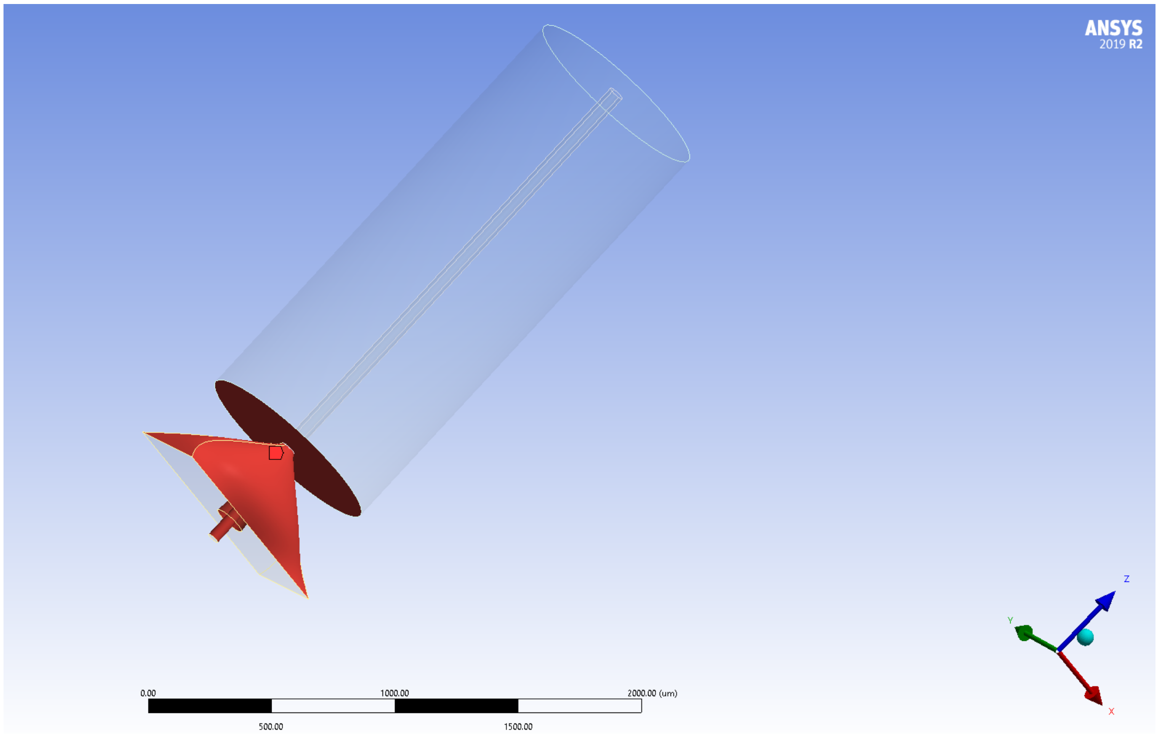

Figure 4.36: The boundary condition for walls.

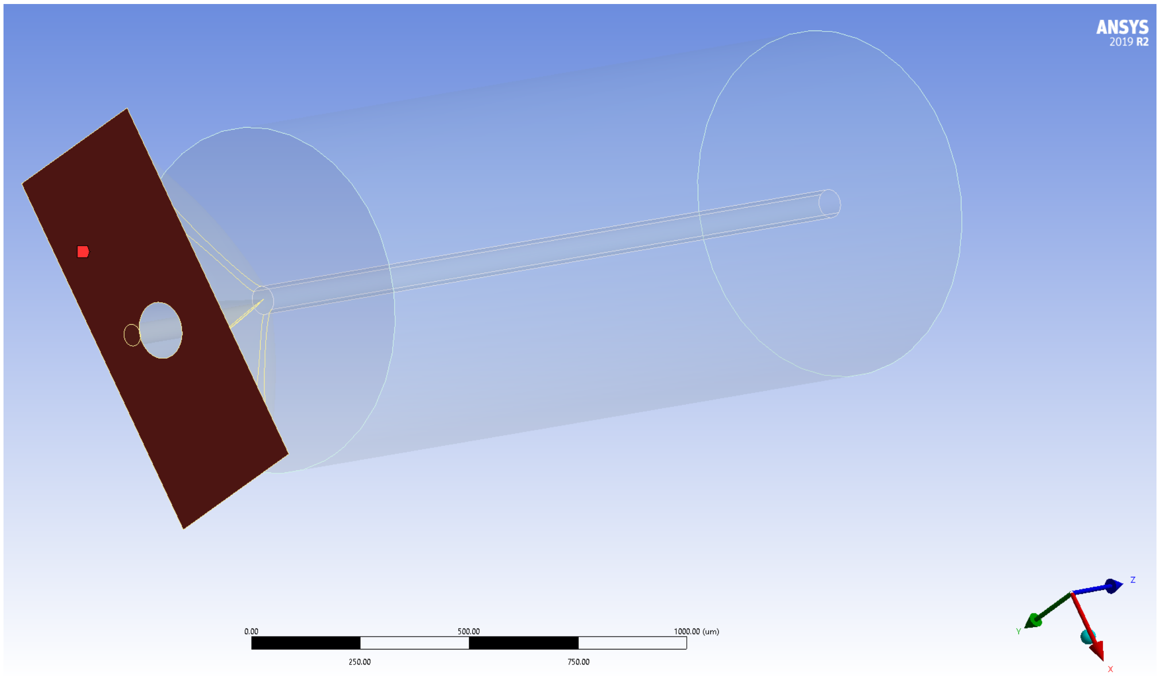

Figure 4.37: The boundary condition for sheath gas inlet.

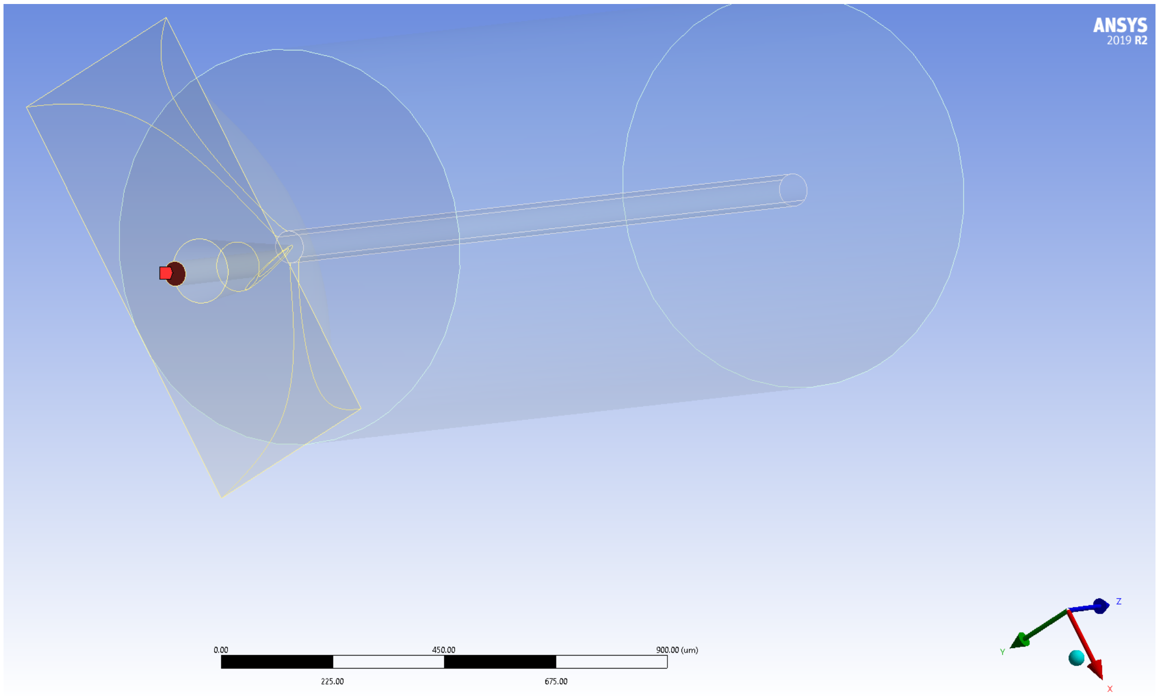

Figure 4.38: Boundary condition for water inlet.

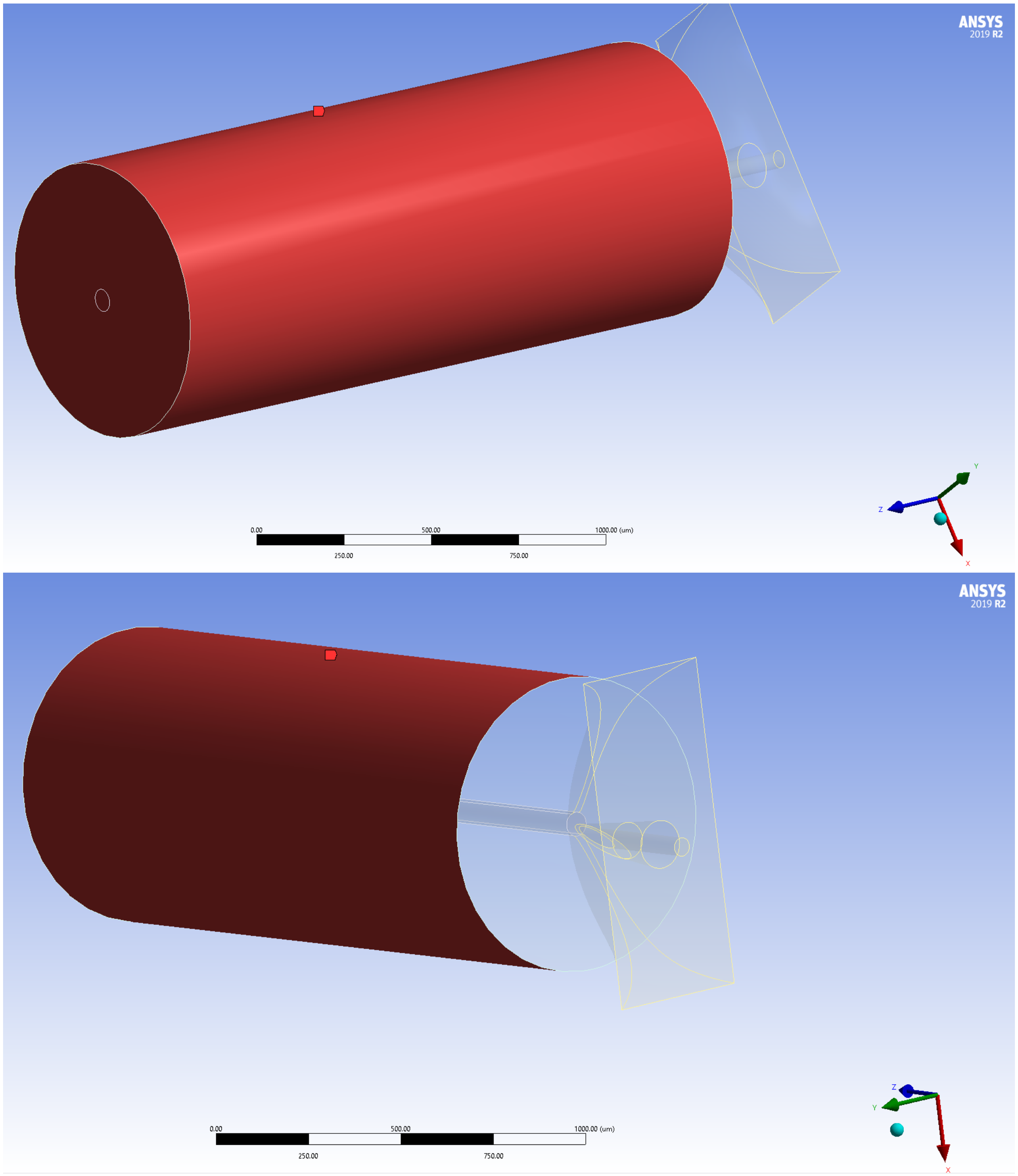

Figure 4.39: Boundary condition for pressure outlet.

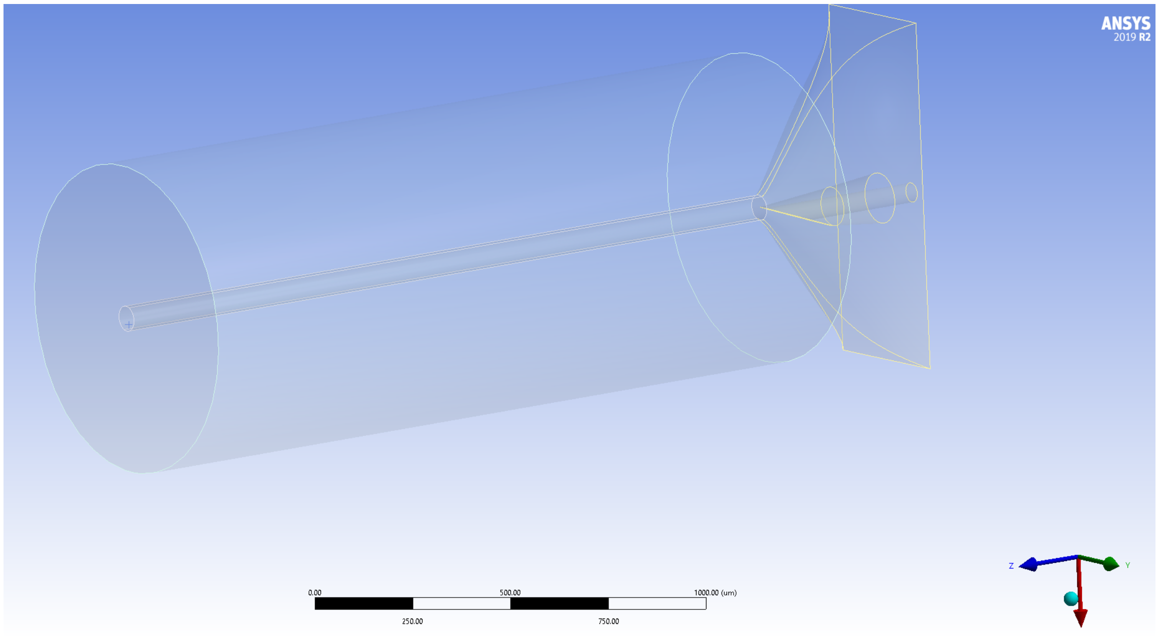

Figure 4.40: Body of influence for mesh refinement in the vicinity of the liquid jet and the droplets inside the chamber.

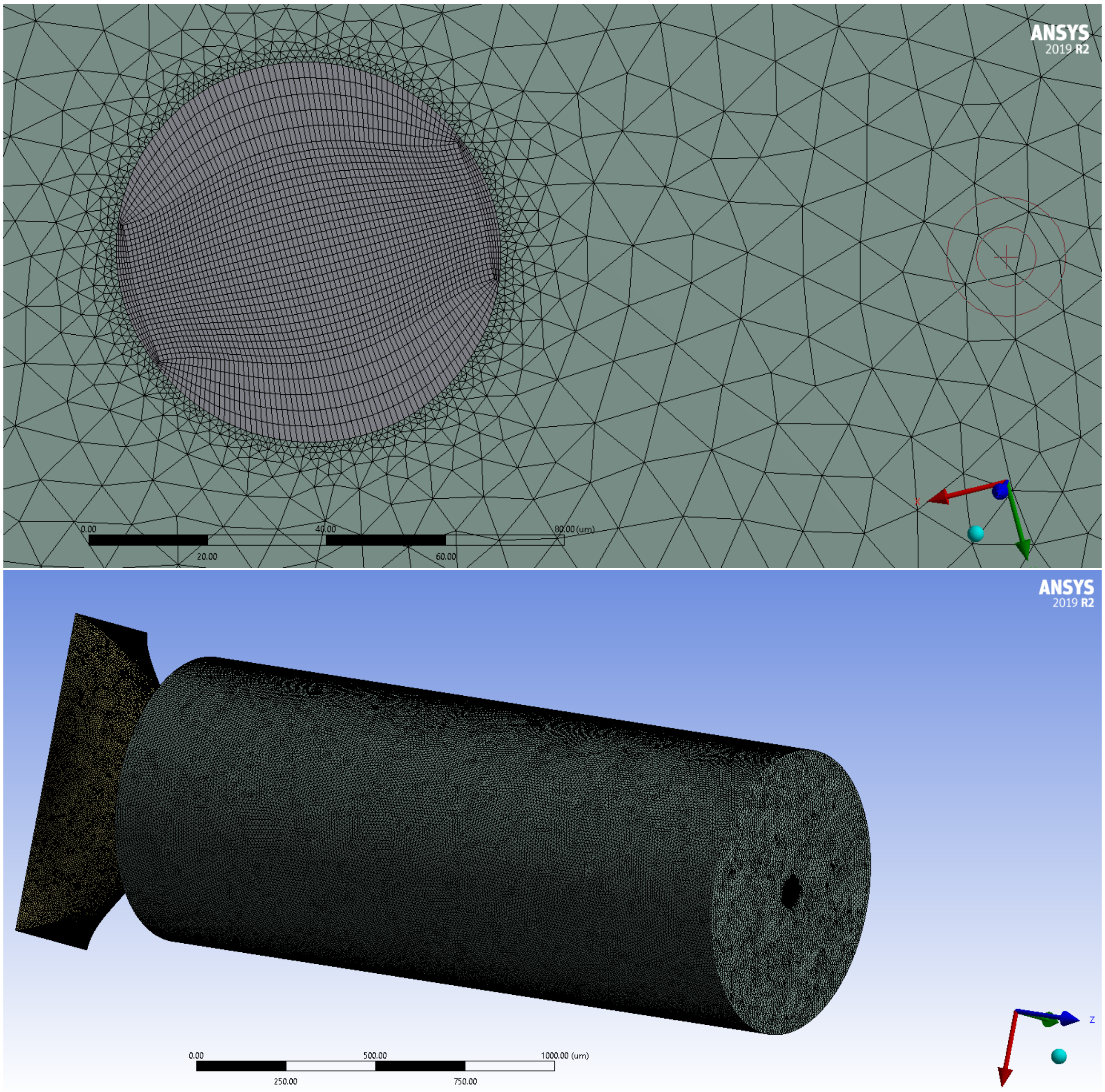

Figure 4.41: The meshing of the entire flow field.

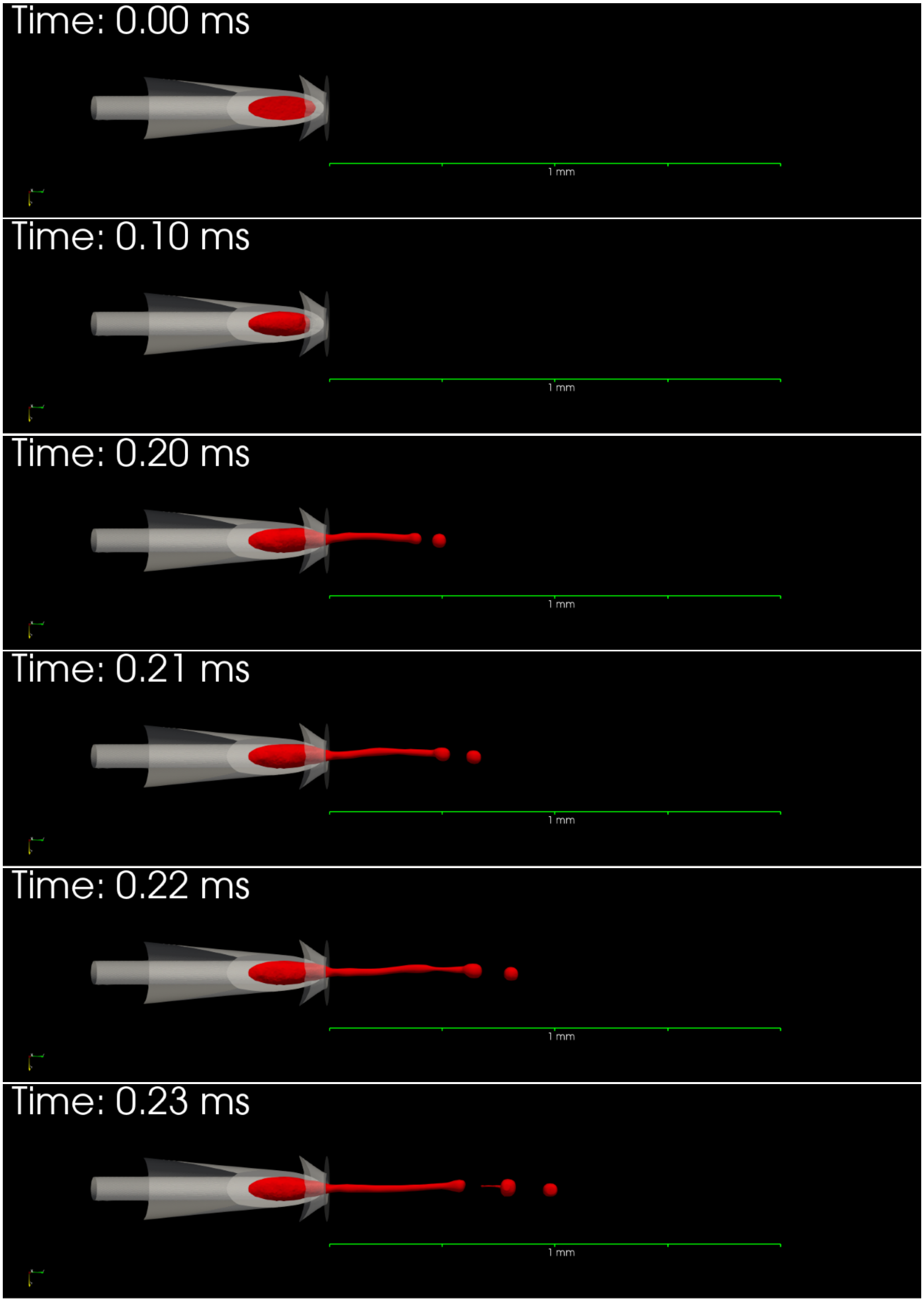

Figure 4.42: Liquid jet results at different time steps shown in red color for the 3D simulation described in section 4.6.

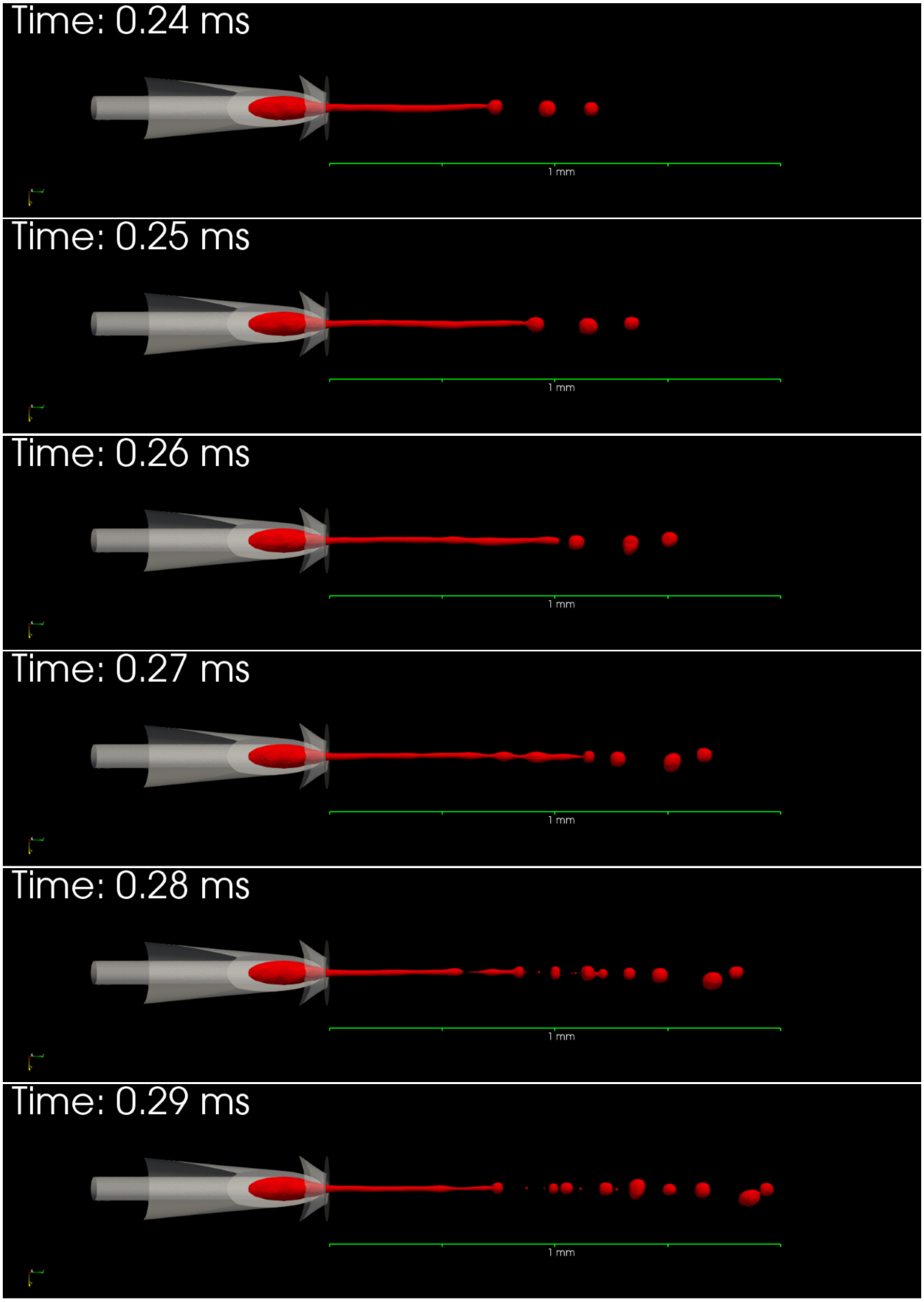

Figure 4.43: Liquid jet results at different time steps shown in red color for the 3D simulation described in section 4.6.

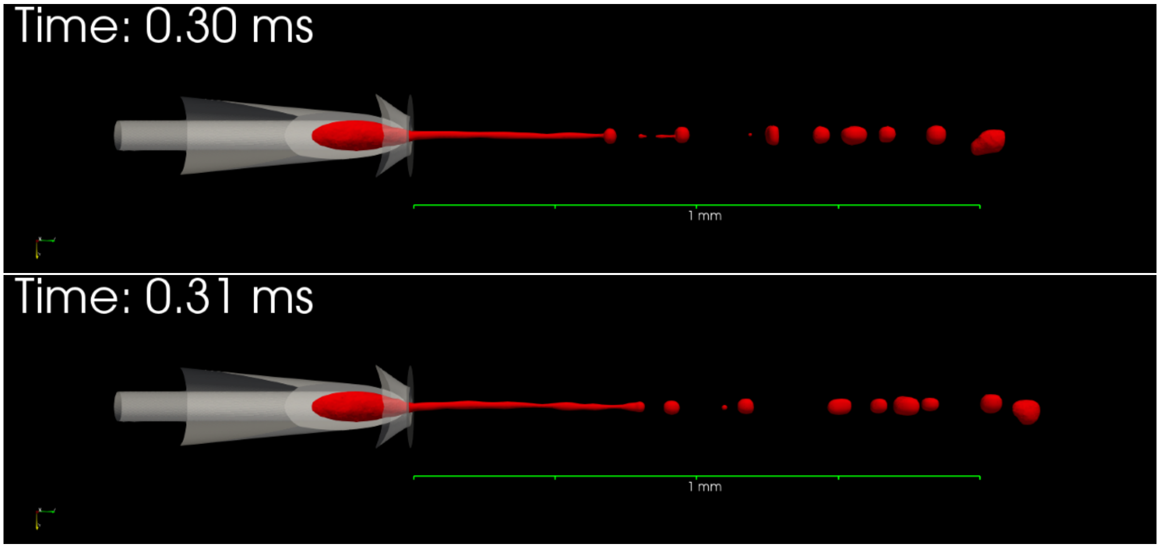

Figure 4.44: Liquid jet results at different time steps shown in red color for the 3D simulation described in section 4.6.

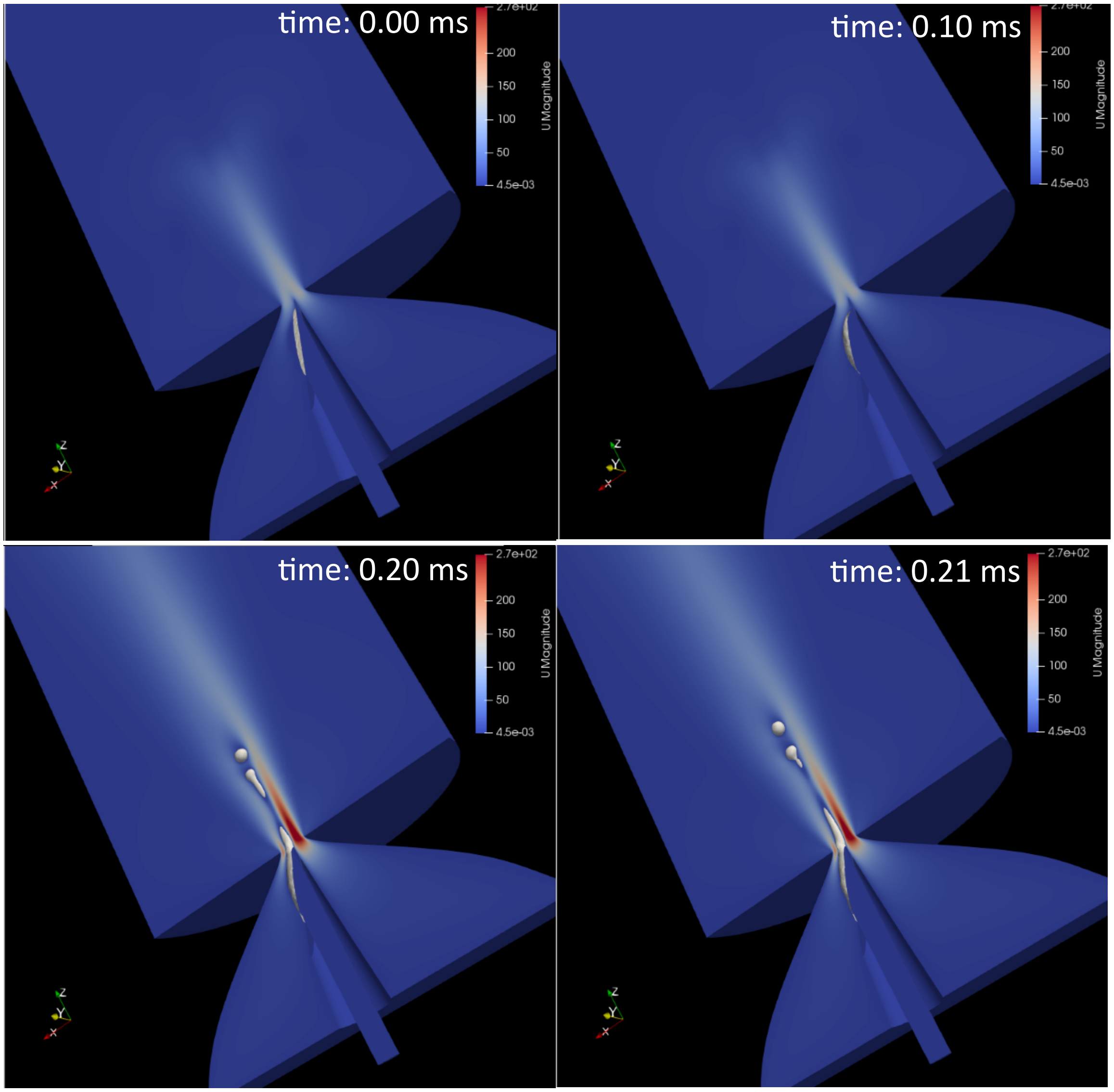

Figure 4.45: Liquid jet results at different time steps shown in red color for the 3D simulation described in section 4.6, colored by the component of velocity in the jet propagation direction.

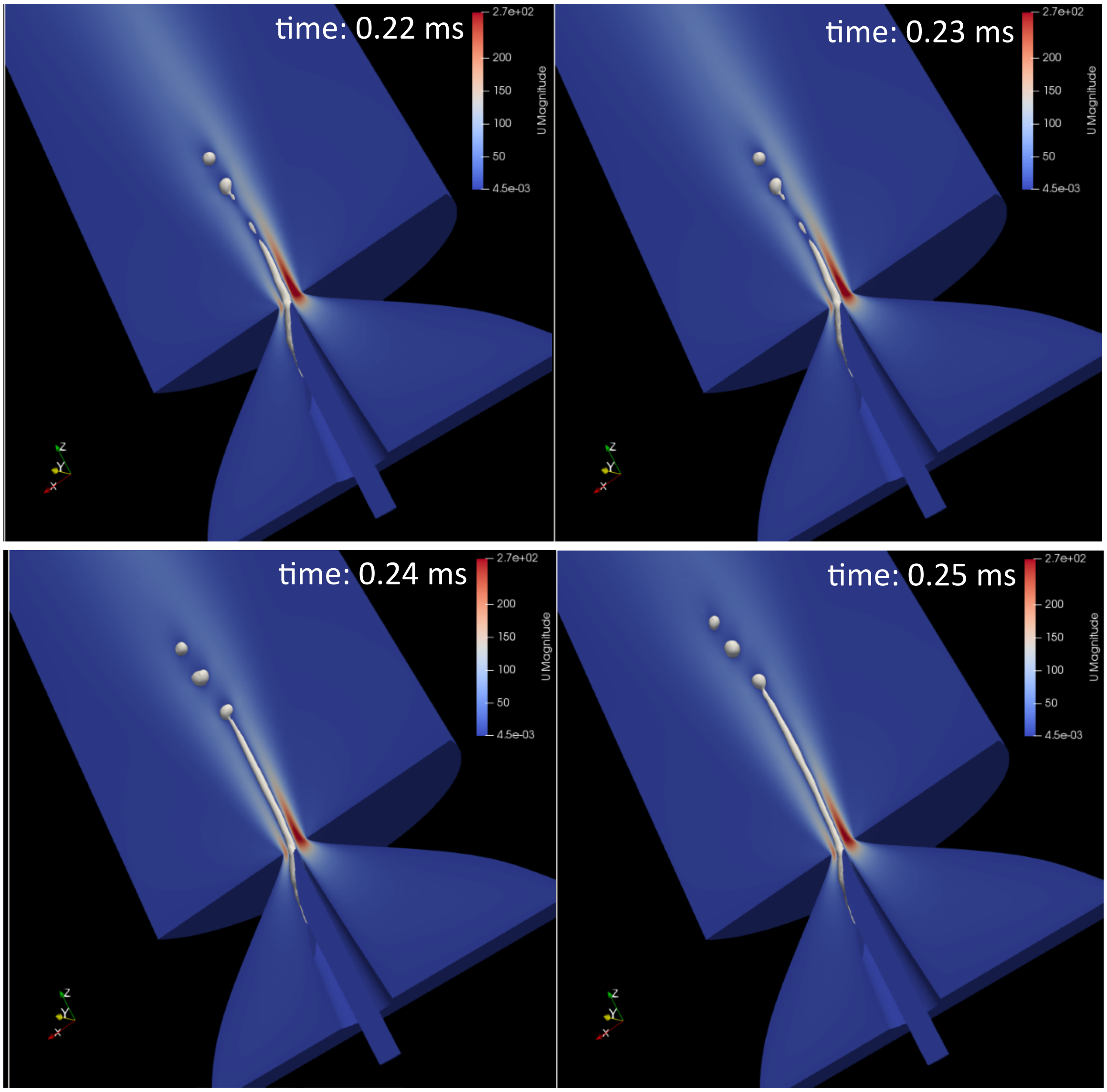

Figure 4.46: Liquid jet results at different time steps shown in red color for the 3D simulation described in section 4.6, colored by the component of velocity in the jet propagation direction.

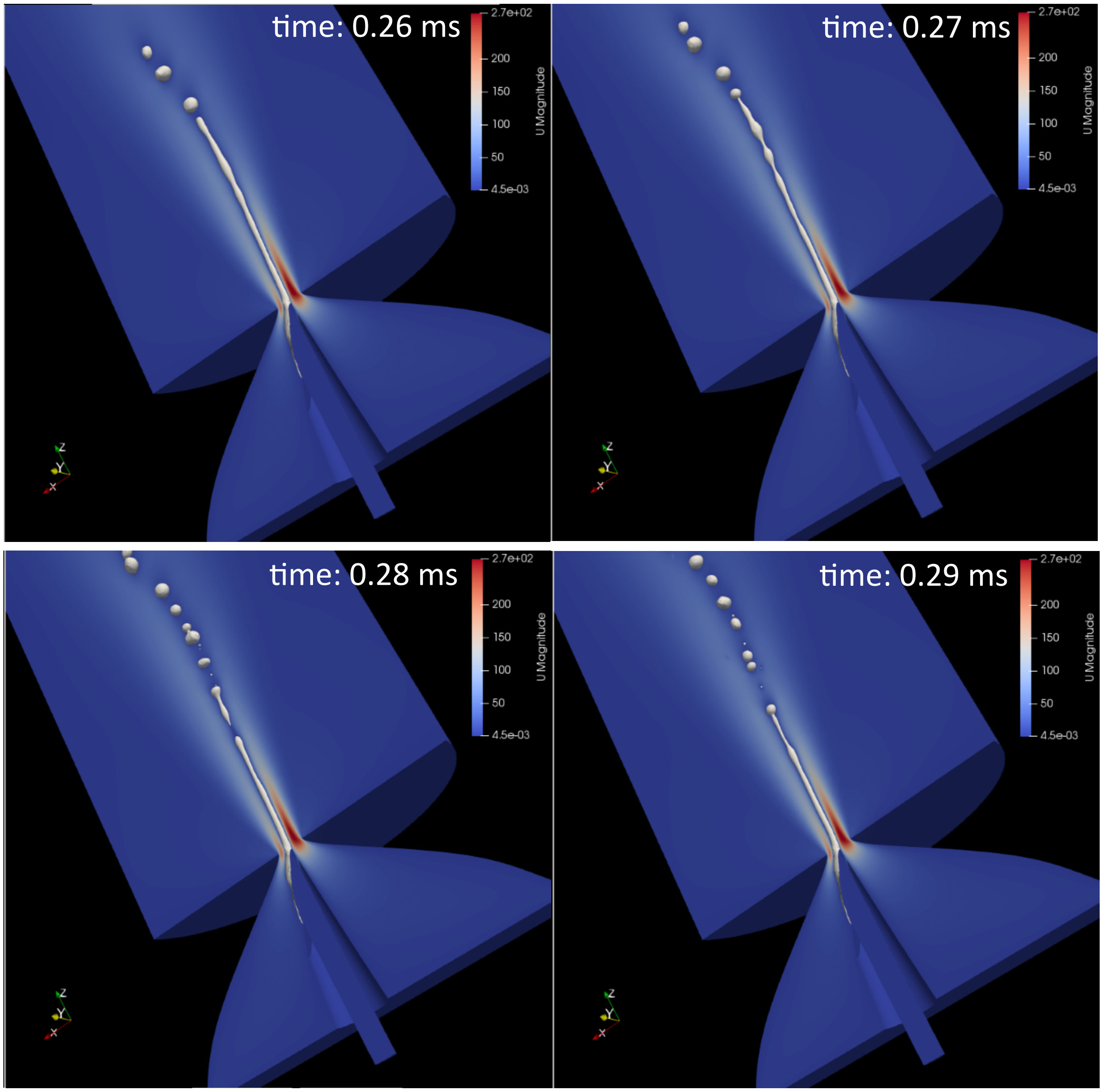

Figure 4.47: Liquid jet results at different time steps shown in red color for the 3D simulation described in section 4.6, colored by the component of velocity in the jet propagation direction.

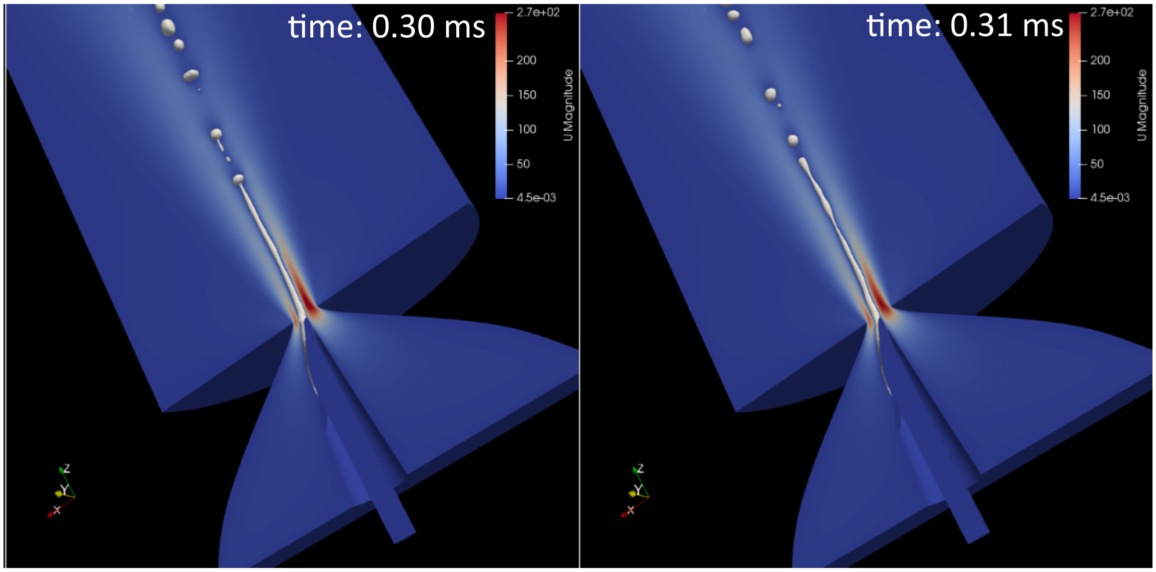

Figure 4.48: Liquid jet results at different time steps shown in red color for the 3D simulation described in section 4.6, colored by the component of velocity in the jet propagation direction.

Chapter 5

3D PRINTED GAS DYNAMIC VIRTUAL NOZZLES ALONG WITH LIQUID AND GAS FLOW RATE MANIPULATION SYSTEM TO SYNCHRONIZE DROPLETS WITH THE XFEL PULSES

5.1 Abstract

Continuous liquid microjets have been widely used in time-resolved solution scattering (TR-SS) experiments at X-Ray Free Electron Lasers (XFELs) to deliver samples to the intense focus of the x-ray beam. When conducting experiments at XFELs with pulse repetition rates on the order of 100 Hz, these continuous jets waste the vast majority of injected sample between shots, which is a major problem particularly in cases of irreversible reactions that do not allow for sample recycling. This is a major problem for expensive or difficult-to-produce samples and as such, triggering periodic droplets or jets under vacuum is a highly desired improvement for solution scattering experiments. Here we develop and test 3D-printed gas dynamic virtual nozzles (GDVNs) that are designed to produce periodic droplets that may be synchronized with XFEL pulses at 100 Hz.

5.2 Introduction

The invention of the Free electron Laser has allowed new avenues for structure determination of biological molecules. The destructive nature of these high-intensity X-ray laser pulses necessitates fast sample replenishment between pulses, which is easily accomplished with a liquid jet. Gas Dynamic Virtual Nozzles (GDVNs) produce microscopic flow-focused liquid jets and are widely used for injecting a stream of protein solution or protein nanocrystals into an X-ray Free Electron Laser (XFEL) for structural analysis.

Since the XFEL laser pulses are not continuous, sample contained in the portion of the jet that is not hit by laser in the continuous jet is wasted, as shown in figure 5.1. Here, we introduce a system consisting of 3D printed GDVNs along with a system to control the flow rates of gas flow rate and the liquid flow rate feeding the gas dynamic virtual nozzle to achieve periodic jets or droplets. The use of microdrops rather than continuous jets can simultaneously increase the scattering signal while reducing the liquid flow rate and thereby improve the overall measurement efficiency by orders of magnitude. We have ongoing efforts to develop variants of 3D-printed gas dynamic virtual nozzles (GDVN) that produce periodic droplets that may be synchronized with XFEL pulses at 100 Hz. An essential difference between these devices and existing off-the-shelf commercial devices is the ability to operate in a vacuum environment, which is highly desired for time-resolved XFEL-based solution scattering measurements in which the measurement of small difference signals demands a minimal amount of background gas scatter.

When conducting experiments at XFELs with pulse repetition rates on the order of 100 Hz, the existing GDVNs that provide continuous jets waste the vast majority of injected sample between shots, particularly in cases of irreversible reactions that do not allow for sample recycling. This is a major problem for expensive or difficult-to-produce samples and as such, triggering periodic droplets or jets under vacuum is a highly desired improvement for solution scattering experiments. There have been recent investigations to reduce sample consumption in the XFEL experiments by having a jet that includes droplets inside a sacrificed oil [29] [28]. In this approach, the droplets inside the liquid flow field are generated upstream of the GDVN. As a result, a jet is formed that has periodic content of samples to be synchronized with the XFEL laser pulses. This scheme for producing intermittent jets is particularly effective for XFELs that operate in burst modes, such as the European XFEL that generate short MHz pulse trains that repeat at 10 Hz. The production of spherical droplets without an oil-phase is more appropriate for solution scattering at reduced repetition rates (∼100 Hz rather than ∼MHz).

An immense volume of research has been dedicated to the triggering of microdrops. D.P. Deponte et al initially triggered periodic droplets from a GDVN in 2008 [27, 24]. However, the triggering frequency was in the range of 70kHZ-169kHz (near the Rayleigh instability). Their investigations resulted in significantly higher frequencies than the desired 100Hz droplet production frequency, but it could be inferred from their results that a broad range of droplet production frequencies should be possible. Multiple companies (such as PolyPico, Scienion and MicroFab) have developed off-the-shelf devices for triggering droplets. Unfortunately, they do not work in the vacuum as we desire.

Martien et al. were among the first groups who theoretically investigated the topic of the formation of several drops in a sequence, or dripping [55]. Afterwards, Ambravaneswaran et al. used a one-dimensional (1D) model based on a slender-jet approximation of the axisymmetric Navier-Stokes equations to probe the physics of dripping [5]. The previous studies led to the understanding that under specific operating conditions, GDVNs can achieve homogeneous droplets in the dripping mode [60]. Geometrical parameters can be adjusted in such a way to widen the range of operating conditions that result in periodic dripping. For this purpose, we need to overcome the nonlinearities that result in formation of different droplet sizes and satellite droplets due to nonlinearities in the breakup process [37].

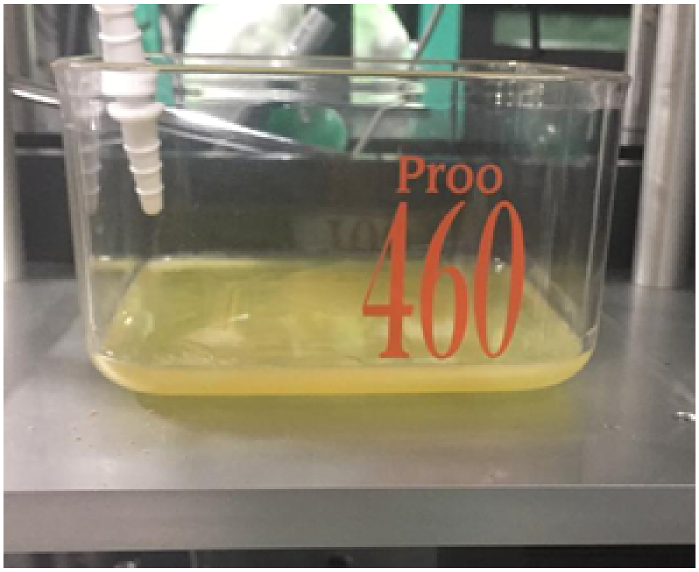

Figure 5.1: Example of wasted sample from a recent XFEL experiment.

5.3 Current Efforts and the Project Progress

Similar to a patent disclosed by Doak et al. [26] regarding periodic jets and droplets, in this project, 3D printed Gas Dynamics virtual Nozzles are to be used in the system. Figure 5.2 shows a single droplet being released from the nozzle tip of a GDVN. Since reproducibility of the performance is shown in the paper [61], reproducible production of periodic droplets is expected. Moreover, a complete image processing pipeline made it possible to characterize droplet and jet production frequencies, and as shown in figure 5.3, by adjusting the liquid flow rate and the gas flow rate for the specific design of a GDVN, frequency values analogous to the XFEL (X-Ray Free Electron Laser) pulse rate values or a multiple or a division of the XFEL pulse rate value can be achieved. This leads to considerable reduction of liquid sample consumption.

The frequency of the droplet and jet production is very sensitive to liquid and gas flow rates. The results of section showed that the droplet and the jet production frequency oscillate dominantly due to oscillations in the flow rates of the liquid and the sheath gas fed to the GDVN. Therefore, there needs to be a microfluidics system to help achieving steady liquid and gas flows with low flow rates. This can be achieved by several approaches. One approach is to feed the sheath gas and the liquid to the GDVN with very accurate flow rates with negligible oscillations that does not considerably affect the resulting droplet frequency, or the GDVN can operate with operating condition sets to produce droplets with frequencies that are a multiplication or a division of the XFEL frequency. Moreover, we can feed the GDVN in such a way that liquid or gas flow rate is supplied periodically to the GDVN, and that can be done by means of an Actuated Microfluidic Nanowell Device [1], piezoelectric actuation, surface acoustic waves or any form of valve system. A mechanical actuation mechanism will be necessary in order to stabilize the relative phase of the droplet production with the phase of the x-ray pulse arrival, as it is necessary to intercept the droplets with the x-ray pulses.

5.3.1 Results

Results are gathered showing estimated natural dripping frequencies for multiple liquid flow rates. Figure below shows that current GDVNs are able to achieve stable dripping modes at some operating condition regions with low liquid and gas flow rates, that was shown in figure 5.3.

An image analysis code is used to estimate the natural frequency of periodic droplets. The idea for the image analysis method is that when the droplet or jet comes out of the nozzle tip and enters the region of interest, the average intensity of the image starts to increase rapidly. A threshold is assigned to the average intensity of the image and the times the image intensity passes the threshold determines the frequency of droplet production.

Using an image analysis method, we gathered preliminary results showing estimated natural dripping frequencies for multiple liquid flow rates 5.3. Initial studies show that current GDVNs are able to achieve stable dripping modes at low liquid and gas flow rates.

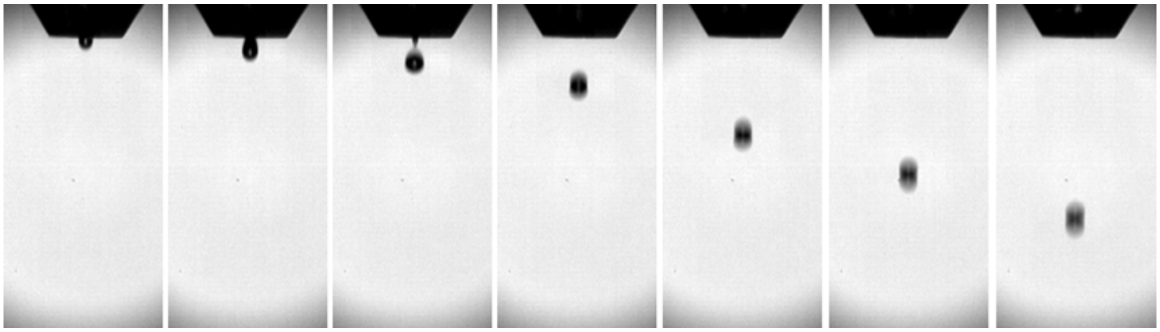

Figure 5.2: A single droplet being released from the nozzle tip.

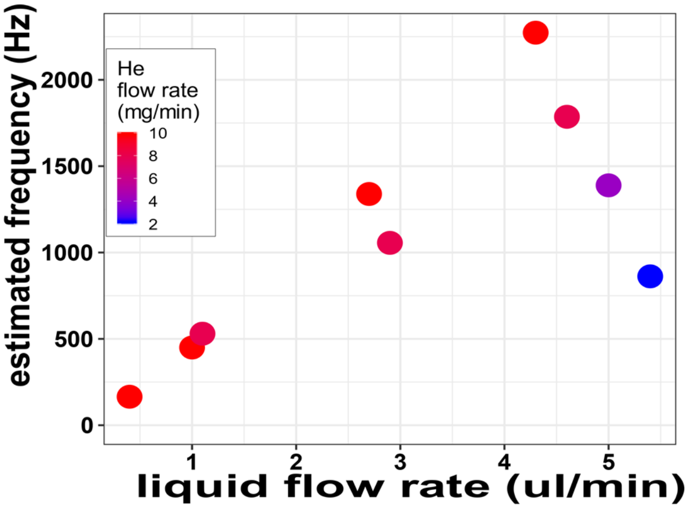

Figure 5.3: Natural droplet frequency from a 3D printed GDVN in dripping mode.

Chapter 6

MISCELLANEOUS PROJECTS

6.1 Array of Nozzles

Clogging of microfluidic devices while delivering protein microcrystals (with sizes of order 10 μm) during XFEL measurements is a long-standing problem that has caused countless nozzle replacements that cost a significant amount of money and time. In addition to the development of optimized GDVNs with large inner diameters, sample filtration, and good operational protocols, the development of printed nozzle arrays is an additional mechanism to minimize waste. In XFEL experiments, when a nozzle clogs, changing the nozzle in the vacuum chamber typically requires approximately 40 minutes when considering the time needed to install, establish a jet containing the sample solution, and re-align the x-rays to the new microjet. However, mounting an array of nozzles instead of a single nozzle in the XFEL chamber makes it possible to rapidly switch to the next nozzle by means of a simple microfluidic switch, without the need to interrupt the experiment. Figure 6.1 shows a printed monolithic array of nozzles. These nozzles were successfully used during solution scattering experiments at the SACLA XFEL in Japan in April 2019.

6.2 Integration of Nozzle Designs With Mixer Designs

Another integrated design is integration of the nozzle designs with the mixer designs to satisfy the requirements of XFEL's time-resolved crystallography experiments. 3D printed Mix-and-inject devices helped the XFEL community to achieve snapshots of chemical reactions in sub-milliseconds time points. Since different XFEL

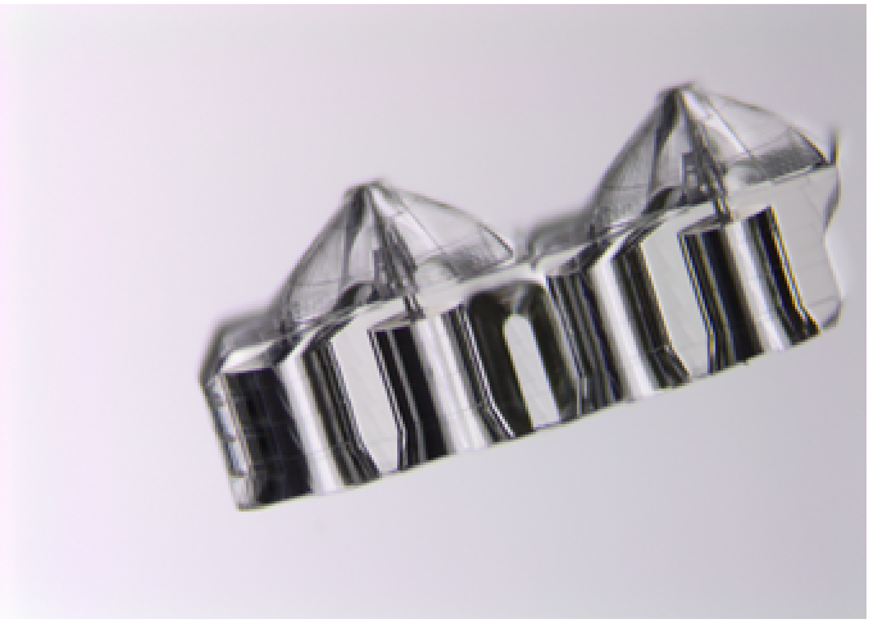

Figure 6.1: A 3D printed array of nozzles device.

experiments that involve mixing investigation have different requirements, for each XFEL experiment a unique mix and inject device is made to satisfy the special requirements of the experiment, such as time point. Design pictures of some variations of the integrated mix and injection devices are shown in figures 6.2.

After designing a mix and inject integrated device, in house tests are done to acquire jet characteristics such as jet velocity and jet length. The analyzed data help the XFEL scientists to estimate the time points with good accuracy.

6.3 Integration of Nozzle With T-junction

The purpose of the T-junction (intermittent jets of oil and sample) is to reduce sample consumption by interleaving sample within an intermittent sample jet that alternates with a sacrificial liquid, thereby delivering sample only at times when x-rays are incident on the jet [28]. A picture of a design of the T-junction with a nozzle design is showed in figure 6.3.

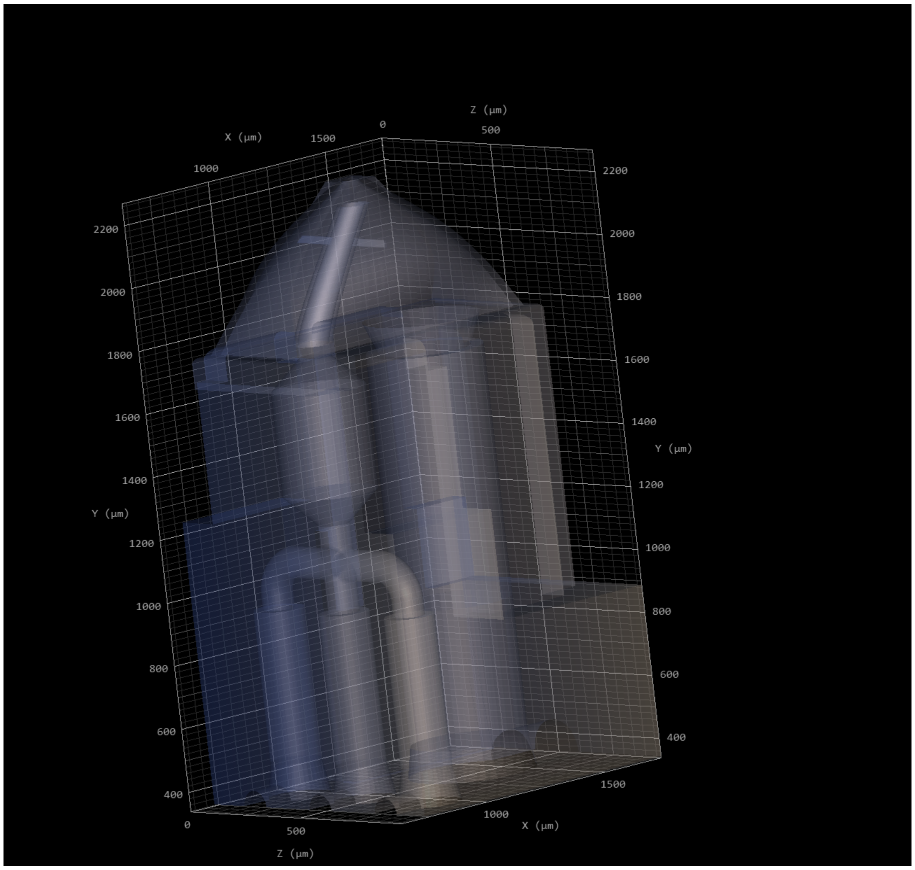

Figure 6.2: A picture of a design of a mix and inject device. In the picture, the left line is for the sacrificing oil, the middle line is for the sample, and the right line is for the sheath gas (collaborating with Dr. Alexandra Ros group; Austin Echelmeier, Jorvani Cruz).

6.4 Double Focusing Nozzles

Double focusing GDVNs (DFFN) are among the popular devices for XFEL experiments, and is used to have stable jet with lower sample flow rates [35],[65]. In double focusing GDVNs, focusing the inner liquid (sample) by liquid retards the sample jet breakup, since the capillary instability dominates the flow instead of shear instability that dominates the flow in the case that liquid is being focused by gas [35], [59]. Another advantage of a double focusing GDVN is that when the inner liquid is focused by another liquid, liquid viscosity causes a comparatively remarkable momentum dif-

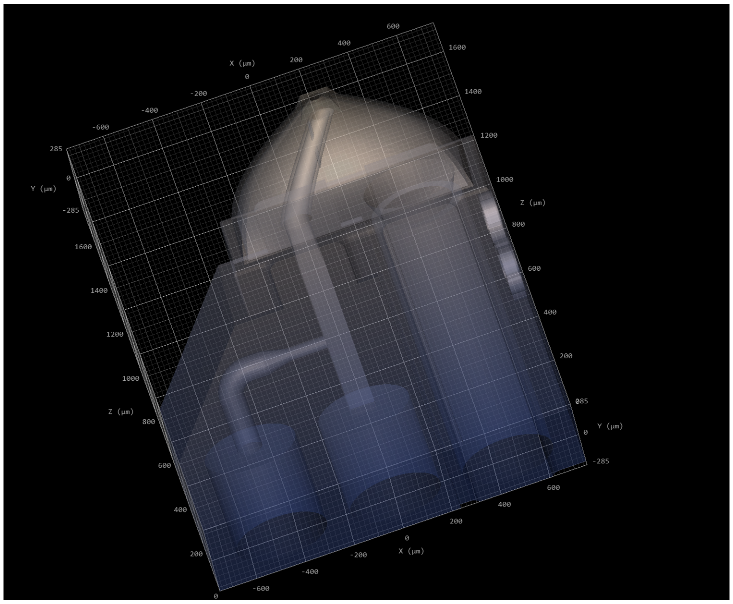

Figure 6.3: A picture of a design of the T-junction with a nozzle design (collaborating with Dr. Alexandra Ros group; Austin Echelmeier, Jorvani Cruz, Diandra Doppler).

fusion that smoothen quickly the downstream flow velocities of the inner liquid phase [35], [59]. Consequently with this method, the inner liquid (sample) can achieve jets of submicrometer sizes [35].

However, there are some drawbacks regarding these types of GDVNs that we mention some of them:

1. Eventually, the jet of the inner liquid (sample) breaks up into droplets due to the capillary perturbations growth, whereas the outer liquid jet stream still remains stable [35]. This means the inner jet length is comparatively very low.

2. There is a significant velocity gradient between near the interface of the medium liquid and the innermost liquid (sample). For example, In case the outer liquid is calculated by numerical simulation to have the velocity of more than 40 m/s, the innermost liquid (sample) nanojet is having the velocity of about 10 m/s, as we can see in the below figure from Calvo et al.'s paper [35].

Several 3D printed double focusing devices are developed. One of the designs is shown in figure 6.4 and the 3D printed devices developed based on this design are shown in figures 6.5 and **??**. Experimental testing results of testing of water in vacuum chamber are shown in figures 6.6 6.7 6.8 6.9.

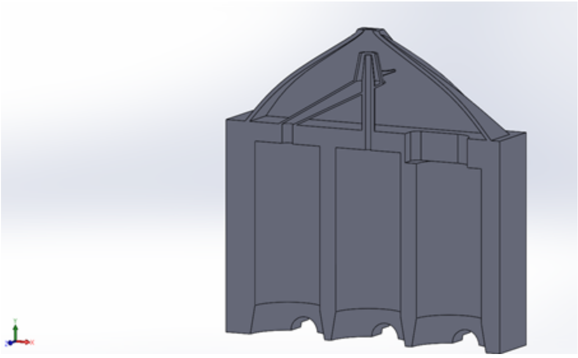

Figure 6.4: A picture of a design of the double focusing GDVN cut into half.

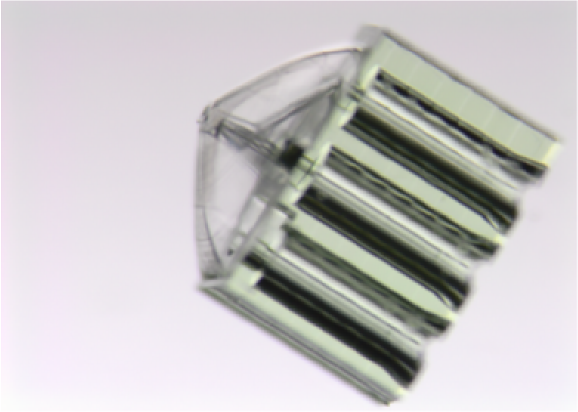

Figure 6.5: A picture of a 3D printed double focusing GDVN device.

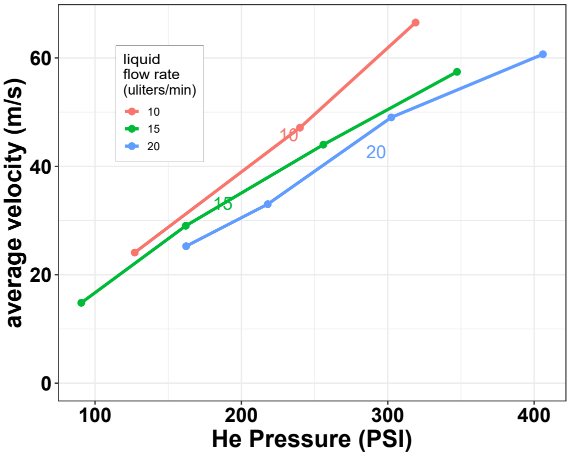

Figure 6.6: Average velocity versus upstream Helium gauge pressure for a DFFN GDVN liquid jet operating in vacuum chamber.

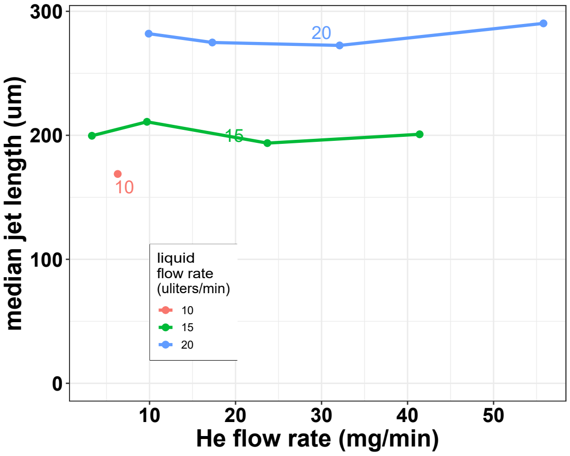

Figure 6.7: Median jet length versus upstream helium flow rate for a DFFN GDVN liquid jet operating in vacuum chamber.

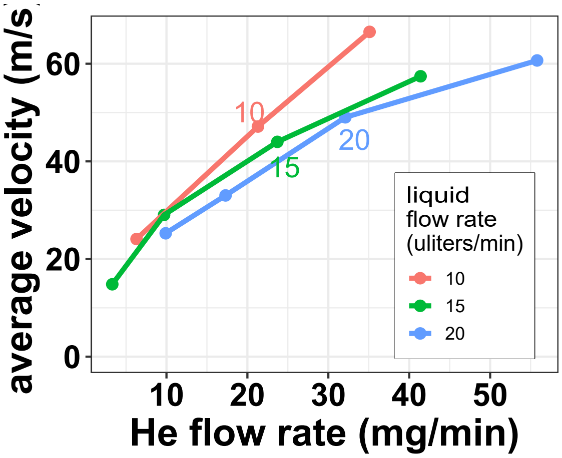

Figure 6.8: Average velocity versus Helium flow rate for a DFFN GDVN liquid jet operating in vacuum chamber.

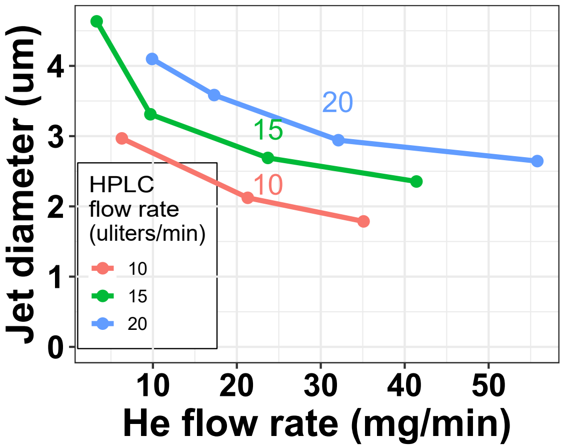

Figure 6.9: Jet diameter versus Helium flow rate for a DFFN GDVN liquid jet operating in vacuum chamber.

REFERENCES

[1] Bahige G Abdallah, Shatabdi Roy-Chowdhury, Raimund Fromme, Petra Fromme, and Alexandra Ros. Protein crystallization in an actuated microfluidic nanowell device. *Crystal growth & design*, 16(4):2074–2082, 2016.

[2] AJ Acero, N Rebollo-Muñoz, JM Montanero, AM Gañán-Calvo, and EJ Vega. A new flow focusing technique to produce very thin jets. *Journal of Micromechanics and Microengineering*, 23(6):065009, 2013.

[3] Ronald J Adrian. Particle-imaging techniques for experimental fluid mechanics. *Annual review of fluid mechanics*, 23(1):261–304, 1991.

[4] Ronald J Adrian and Jerry Westerweel. *Particle image velocimetry*. Number 30. Cambridge University Press, 2011.

[5] Bala Ambravaneswaran, Scott D Phillips, and Osman A Basaran. Theoretical analysis of a dripping faucet. *Physical review letters*, 85(25):5332, 2000.

[6] Shelley L Anna and Hans C Mayer. Microscale tipstreaming in a microfluidic flow focusing device. *Physics of Fluids*, 18(12):121512, 2006.

[7] Adil Ansari. A collation and analysis of two-dimensional unsplit conservative advection methods for volume of fluid at interfaces. Master's thesis, Arizona State University, 2019.

[8] I ANSYS. Ansys fluent user's guide, release 19.0. *Equation*, (6.68), 2018.

[9] I ANSYS. Ansys spaceclaim user's guide, release 19.0. *Equation*, (6.68), 2018.

[10] Dameli Assalauova, Young Yong Kim, Sergey Bobkov, Ruslan Khubbutdinov, Max Rose, Roberto Alvarez, Jakob Andreasson, Eugeniu Balaur, Alice Contreras, Hasan DeMirci, et al. An advanced workflow for single particle imaging with the limited data at an x-ray free-electron laser. *arXiv preprint arXiv:2006.08345*, 2020.

[11] Osman A Basaran. Small-scale free surface flows with breakup: Drop formation and emerging applications. *AIChE Journal*, 48(9):1842–1848, 2002.

[12] Carsten Baumgarten. *Mixture formation in internal combustion engines*. Springer Science & Business Media, 2006.

[13] Edin Berberovic. *Investigation of free-surface flow associated with drop impact: numerical simulations and theoretical modeling*. PhD thesis, Technische Universität, 2010.

[14] Cory Berkland, Emily Pollauf, Daniel W Pack, and Kyekyoon Kevin Kim. Uniform double-walled polymer microspheres of controllable shell thickness. *Journal of controlled release*, 96(1):101–111, 2004.

[15] KR Beyerlein, L Adriano, M Heymann, Richard Kirian, J Knoška, F Wilde, HN Chapman, and S Bajt. Ceramic micro-injection molded nozzles for serial femtosecond crystallography sample delivery. *Review of scientific instruments*, 86(12):125104, 2015.

[16] Subrahmanyan Chandrasekhar. Hydrodynamic and hydromagnetic stability. 1970.

[17] Henry N. Chapman. X-ray free-electron lasers for the structure and dynamics of macromolecules. *Annual Review of Biochemistry*, 88(1):annurev–biochem–013118–110744, 2019.

[18] Henry N Chapman, Petra Fromme, Anton Barty, Thomas A White, Richard A Kirian, Andrew Aquila, Mark S Hunter, Joachim Schulz, Daniel P DePonte, Uwe Weierstall, et al. Femtosecond x-ray protein nanocrystallography. *Nature*, 470(7332):73, 2011.

[19] Christophe Clanet and Juan C Lasheras. Transition from dripping to jetting. *Journal of fluid mechanics*, 383:307–326, 1999.

[20] Itai Cohen, Hui Li, James L Hougland, Milan Mrksich, and Sidney R Nagel. Using selective withdrawal to coat microparticles. *Science*, 292(5515):265–267, 2001.

[21] Richard Courant, Kurt Friedrichs, and Hans Lewy. On the partial difference equations of mathematical physics. *IBM journal of Research and Development*, 11(2):215–234, 1967.

[22] Brian H Cumpston, Sundaravel P Ananthavel, Stephen Barlow, Daniel L Dyer, Jeffrey E Ehrlich, Lael L Erskine, Ahmed A Heikal, Stephen M Kuebler, I-Y Sandy Lee, Dianne McCord-Maughon, et al. Two-photon polymerization initiators for three-dimensional optical data storage and microfabrication. *Nature*, 398(6722):51–54, 1999.

[23] Anil W Date. *Introduction to computational fluid dynamics*. Cambridge University Press, 2005.

[24] DP DePonte, Uwe Weierstall, Kevin Schmidt, J Warner, D Starodub, JCH Spence, and RB Doak. Gas dynamic virtual nozzle for generation of microscopic droplet streams. *Journal of Physics D: Applied Physics*, 41(19):195505, 2008.

[25] Suraj S Deshpande, Lakshman Anumolu, and Mario F Trujillo. Evaluating the performance of the two-phase flow solver interfoam. *Computational science & discovery*, 5(1):014016, 2012.

[26] Robert Bruce Doak, Robert Shoeman, Sabine Botha, and Ilme Schlichting. Method and device of producing an intermittent liquid jet, December 12 2017. US Patent 9,839,922.

[27] Robert Bruce Doak, John CH Spence, Uwe Weierstall, Daniel DePonte, Dmitri Starodub, and Jared Scott Warner. Gas dynamic virtual nozzle for generation of microscopic droplet streams, September 25 2012. US Patent 8,272,576.

[28] Austin Echelmeier, Daihyun Kim, Jorvani Cruz Villarreal, Jesse Coe, Sebastian Quintana, Gerrit Brehm, Ana Egatz-Gomez, Reza Nazari, Raymond G Sierra, Jason E Koglin, et al. 3d printed droplet generation devices for serial femtosecond crystallography enabled by surface coating. *Journal of Applied Crystallography*, 52(5), 2019.

[29] Austin Echelmeier, Jorvani Cruz Villarreal, Marc Messerschmidt, Daihyun Kim, Jesse D Coe, Darren Thifault, Sabine Botha, Ana Egatz-Gomez, Sahir Gandhi, Gerrit Brehm, et al. Segmented flow generator for serial crystallography at the european x-ray free electron laser. *Nature Communications*, 11(1):1–10, 2020.

[30] Jens Eggers and Emmanuel Villermaux. Physics of liquid jets. *Reports on progress in physics*, 71(3):036601, 2008.

[31] Alfonso M Gañán-Calvo. Generation of steady liquid microthreads and micron-sized monodisperse sprays in gas streams. *Physical Review Letters*, 80(2):285, 1998.

[32] Alfonso M Gañán-Calvo. Enhanced liquid atomization: From flow-focusing to flow-blurring. *Applied physics letters*, 86(21):214101, 2005.

[33] Alfonso M Gañán-Calvo, Daniel P DePonte, Miguel A Herrada, John CH Spence, Uwe Weierstall, and R Bruce Doak. Liquid capillary micro/nanojets in free-jet expansion. *Small*, 6(7):822–824, 2010.

[34] Alfonso M Gañán-Calvo et al. Jetting–dripping transition of a liquid jet in a lower viscosity co-flowing immiscible liquid: the minimum flow rate in flow focusing. *Journal of Fluid Mechanics*, 553:75–84, 2006.

[35] Alfonso M Gañán-Calvo, Román González-Prieto, Pascual Riesco-Chueca, Miguel A Herrada, and María Flores-Mosquera. Focusing capillary jets close to the continuum limit. *Nature Physics*, 3(10):737–742, 2007.

[36] Maria Göppert-Mayer. Über elementarakte mit zwei quantensprüngen. *Annalen der Physik*, 401(3):273–294, 1931.

[37] Simon L Goren and Stanislaw Wronski. The shape of low-speed capillary jets of newtonian liquids. *Journal of Fluid Mechanics*, 25(1):185–198, 1966.

[38] Thomas D Grant, Suchithranga M Perera, Leslie A Salas-Estrada, Andrey V Struts, Udeep Chawla, Xiaolin Xu, Steven D Fried, Nipuna Weerasinghe, D Mendez, R Alvarez, et al. Membrane protein dynamics revealed by x-ray scattering with a femtosecond free-electron laser. *Biophysical Journal*, 118(3):365a, 2020.

[39] Mingyan He, Jason S Kuo, and Daniel T Chiu. Electro-generation of single femtoliter-and picoliter-volume aqueous droplets in microfluidic systems. *Applied Physics Letters*, 87(3):031916, 2005.

[40] John Helmsen, Phillip Colella, and E Gerry Puckett. Non-convex profile evolution in two dimensions using volume of fluids. Technical report, Lawrence Berkeley Lab., CA (United States), 1997.

[41] Miguel A. Herrada, Conrado Ferrera, José M. Montanero, and Alfonso M. Gañán-Calvo. Absolute lateral instability in capillary coflowing jets. *Physics of Fluids*, 22(6):064104, Jun 2010.

[42] Patrick Huerre and Peter A Monkewitz. Local and global instabilities in spatially developing flows. *Annual review of fluid mechanics*, 22(1):473–537, 1990.

[43] Izumi Ishigami, Ariel Lewis-Ballester, Austin Echelmeier, Gerrit Brehm, Nadia A Zatsepin, Thomas D Grant, Jesse D Coe, Stella Lisova, Garrett Nelson, Shangji Zhang, et al. Snapshot of an oxygen intermediate in the catalytic reaction of cytochrome c oxidase. *Proceedings of the National Academy of Sciences*, 116(9):3572–3577, 2019.

[44] Hrvoje Jasak. Error analysis and estimation for the finite volume method with applications to fluid flows. 1996.

[45] W Kaiser and CGB Garrett. Two-photon excitation in ca f 2: Eu 2+. *Physical review letters*, 7(6):229, 1961.

[46] Joseph B Keller, SI Rubinow, and YO Tu. Spatial instability of a jet. *The physics of fluids*, 16(12):2052–2055, 1973.

[47] Juraj Knoška, Luigi Adriano, Salah Awel, Kenneth R Beyerlein, Oleksandr Yefanov, Dominik Oberthuer, Gisel E Peña Murillo, Nils Roth, Iosifina Sarrou, Pablo Villanueva-Perez, et al. Ultracompact 3d microfluidics for time-resolved structural biology. *Nature communications*, 11(1):1–12, 2020.

[48] Wingki Lee, Lynn M Walker, and Shelley L Anna. Role of geometry and fluid properties in droplet and thread formation processes in planar flow focusing. *Physics of Fluids*, 21(3):032103, 2009.

[49] SJ Leib and ME Goldstein. Convective and absolute instability of a viscous liquid jet. *The Physics of fluids*, 29(4):952–954, 1986.

[50] SJ Leib and ME Goldstein. The generation of capillary instabilities on a liquid jet. *Journal of fluid mechanics*, 168:479–500, 1986.

[51] Peng Liu, Paul J Ziemann, David B Kittelson, and Peter H McMurry. Generating particle beams of controlled dimensions and divergence: I. theory of particle motion in aerodynamic lenses and nozzle expansions. *Aerosol Science and Technology*, 22(3):293–313, 1995.

[52] Peng Liu, Paul J Ziemann, David B Kittelson, and Peter H McMurry. Generating particle beams of controlled dimensions and divergence: Ii. experimental evaluation of particle motion in aerodynamic lenses and nozzle expansions. *Aerosol Science and Technology*, 22(3):314–324, 1995.

[53] Ignacio G Loscertales, A Barrero, I Guerrero, R Cortijo, M Marquez, and AM Ganan-Calvo. Micro/nano encapsulation via electrified coaxial liquid jets. *Science*, 295(5560):1695–1698, 2002.

[54] Marc J Madou. *Manufacturing techniques for microfabrication and nanotechnology*. CRC press, 2011.

[55] P Martien, SC Pope, PL Scott, and RS Shaw. The chaotic behavior of the leaky faucet. *Physics Letters A*, 110(7-8):399–404, 1985.

[56] JM Martinez, X Chesneau, and B Zeghmati. A new curvature technique calculation for surface tension contribution in plic-vof method. *Computational Mechanics*, 37(2):182–193, 2006.

[57] A Martínez-Calvo, M Rubio-Rubio, and A Sevilla. The nonlinear states of viscous capillary jets confined in the axial direction. *Journal of Fluid Mechanics*, 834:335–358, 2018.

[58] JM Montanero, N Rebollo-Muñoz, MA Herrada, and AM Gañán-Calvo. Global stability of the focusing effect of fluid jet flows. *Physical Review E*, 83(3):036309, 2011.

[59] Kai Mu, Hang Ding, and Ting Si. Instability analysis of the cone–jet flow in liquid-driven flow focusing. *Microfluidics and Nanofluidics*, 22(12):138, 2018.

[60] Kai Mu, Ting Si, and Hang Ding. Nonlinear dynamics and manipulation of dripping in capillary flow focusing. *SCIENCE CHINA Physics, Mechanics & Astronomy*, 62(12):124713, 2019.

[61] Reza Nazari, Sahba Zaare, Roberto C Alvarez, Konstantinos Karpos, Trent Engelman, Caleb Madsen, Garrett Nelson, John CH Spence, Uwe Weierstall, Ronald J Adrian, et al. 3d printing of gas-dynamic virtual nozzles and optical characterization of high-speed microjets. *Optics Express*, 28(15):21749–21765, 2020.

[62] Garrett Nelson, Richard A Kirian, Uwe Weierstall, Nadia A Zatsepin, Tomáš Faragó, Tilo Baumbach, Fabian Wilde, Fabian BP Niesler, Benjamin Zimmer, Izumi Ishigami, M. Hikitia, S. Bajt, SR Yeh, DL Rousseau, HN Chapman, J.C. Spence, and Heyman M. Three-dimensional-printed gas dynamic virtual nozzles for x-ray laser sample delivery. *Optics express*, 24(11):11515–11530, 2016.

[63] Richard Neutze, Remco Wouts, David Van der Spoel, Edgar Weckert, and Janos Hajdu. Potential for biomolecular imaging with femtosecond x-ray pulses. *Nature*, 406(6797):752–757, 2000.

[64] William L Oberkampf and CJ Roy. Verification and validation in computational simulation. *AIAA Professional Development Short-course*, pages 6–7, 2004.

[65] Dominik Oberthuer, Juraj Knoška, Max O Wiedorn, Kenneth R Beyerlein, David A Bushnell, Elena G Kovaleva, Michael Heymann, Lars Gumprecht, Richard A Kirian, Anton Barty, et al. Double-flow focused liquid injector for efficient serial femtosecond crystallography. *Scientific reports*, 7:44628, 2017.

[66] Suhas Patankar. *Numerical heat transfer and fluid flow.* CRC press, 1980.

[67] Miłosz Pawlicki, Hazel A Collins, Robert G Denning, and Harry L Anderson. Two-photon absorption and the design of two-photon dyes. *Angewandte Chemie International Edition*, 48(18):3244–3266, 2009.

[68] Joseph Antoine Ferdinand Plateau. *Statique expérimentale et théorique des liquides soumis aux seules forces moléculaires*, volume 2. Gauthier-Villars, 1873.

[69] Radom Pongvuthithum, James Moran, and Tanakarn Sankui. A flow blurring nozzle design for combustion in a closed system. *Applied Thermal Engineering*, 131:587–594, 2018.

[70] Ali Ajdari Rad, Karim Faez, and Navid Qaragozlou. Fast circle detection using gradient pair vectors. In *Dicta*, pages 879–888, 2003.

[71] Lord Rayleigh. On the instability of jets. *Proceedings of the London mathematical society*, 1(1):4–13, 1878.

[72] TW Ridler and S Calvard. Picture thresholding using an iterative selection method. *IEEE trans syst Man Cybern*, 8(8):630–632, 1978.

[73] Johan Roenby, Henrik Bredmose, and Hrvoje Jasak. A computational method for sharp interface advection. *Royal Society open science*, 3(11):160405, 2016.

[74] Curtis T Rueden, Johannes Schindelin, Mark C Hiner, Barry E DeZonia, Alison E Walter, Ellen T Arena, and Kevin W Eliceiri. Imagej2: Imagej for the next generation of scientific image data. *BMC bioinformatics*, 18(1):529, 2017.

[75] Leslie A Salas-Estrada, Thomas D Grant, Suchithranga M Perera, Andrey V Struts, Udeep Chawla, Xiaolin Xu, Steven D Fried, Nipuna Weerasinghe, D Mendez, R Alvarez, et al. Rhodopsin's ultra-fast activation dynamics in bilayer and micelle environments. *Biophysical Journal*, 118(3):92a, 2020.

[76] Henning Scheufler and Johan Roenby. Accurate and efficient surface reconstruction from volume fraction data on general meshes. *Journal of computational physics*, 383:1–23, 2019.

[77] Johannes Schindelin, Ignacio Arganda-Carreras, Erwin Frise, Verena Kaynig, Mark Longair, Tobias Pietzsch, Stephan Preibisch, Curtis Rueden, Stephan Saalfeld, Benjamin Schmid, et al. Fiji: an open-source platform for biological-image analysis. *Nature methods*, 9(7):676, 2012.

[78] Caroline A Schneider, Wayne S Rasband, and Kevin W Eliceiri. Nih image to imagej: 25 years of image analysis. *Nature methods*, 9(7):671, 2012.

[79] Ting Si, Fang Li, Xie-Yuan Yin, and Xie-Zhen Yin. Modes in flow focusing and instability of coaxial liquid–gas jets. *Journal of Fluid Mechanics*, 629:1–23, 2009.

[80] John CH Spence and R Bruce Doak. Single molecule diffraction. *Physical review letters*, 92(19):198102, 2004.

[81] Claudiu A. Stan, Despina Milathianaki, Hartawan Laksmono, Raymond G. Sierra, Trevor A. McQueen, Marc Messerschmidt, Garth J. Williams, Jason E. Koglin, Thomas J. Lane, Matt J. Hayes, Serge A. H. Guillet, Mengning Liang, Andrew L. Aquila, Philip R. Willmott, Joseph S. Robinson, Karl L. Gumerlock, Sabine Botha, Karol Nass, Ilme Schlichting, Robert L. Shoeman, Howard A. Stone, and Sébastien Boutet. Liquid explosions induced by X-ray laser pulses. *Nature Physics*, 12(10):966–971, October 2016.

[82] Claudiu A Stan, Despina Milathianaki, Hartawan Laksmono, Raymond G Sierra, Trevor A McQueen, Marc Messerschmidt, Garth J Williams, Jason E Koglin, Thomas J Lane, Matt J Hayes, Matt J. Hayes, Serge A. H. Guillet, Mengning Liang, Andrew L. Aquila, Philip R. Willmott, Joseph S. Robinson, Karl L. Gumerlock, Sabine Botha, Karol Nass, Ilme Schlichting, Robert L. Shoeman, Howard A. Stone, and Sebastien Boutet. Liquid explosions induced by x-ray laser pulses. *Nature Physics*, 12(10):966, 2016.

[83] D Starodub, P Rez, G Hembree, M Howells, D Shapiro, HN Chapman, P Fromme, K Schmidt, U Weierstall, RB Doak, et al. Dose, exposure time and resolution in serial x-ray crystallography. *Journal of synchrotron radiation*, 15(1):62–73, 2008.

[84] Stanley R Sternberg. Biomedical image processing. *Computer*, (1):22–34, 1983.

[85] Vincenz Strouhal. Über eine besondere art der tonerregung. *Annalen der Physik*, 241(10):216–251, 1878.

[86] Mark Sussman. A second order coupled level set and volume-of-fluid method for computing growth and collapse of vapor bubbles. *Journal of Computational Physics*, 187(1):110–136, 2003.

[87] George P Sutton and Oscar Biblarz. *Rocket propulsion elements.* John Wiley & Sons, 2016.

[88] GI TAYLOR. Generation of ripples by wind blowing over a viscous fluid. reprinted in the scientific papers of sir geoffrey ingram taylor, vol. 3, 1963.

[89] Todd Thorsen, Richard W Roberts, Frances H Arnold, and Stephen R Quake. Dynamic pattern formation in a vesicle-generating microfluidic device. *Physical review letters*, 86(18):4163, 2001.

[90] Andrew S Utada, Alberto Fernandez-Nieves, Jose M Gordillo, and David A Weitz. Absolute instability of a liquid jet in a coflowing stream. *Physical review letters*, 100(1):014502, 2008.

[91] Andrew S Utada, Alberto Fernandez-Nieves, Howard A Stone, and David A Weitz. Dripping to jetting transitions in coflowing liquid streams. *Physical review letters*, 99(9):094502, 2007.

[92] Emilio J Vega, José M Montanero, Miguel A Herrada, and Alfonso M Gañán-Calvo. Global and local instability of flow focusing: The influence of the geometry. *Physics of Fluids*, 22(6):064105, 2010.

[93] Alex von Diezmann, Yoav Shechtman, and W. E. Moerner. Three-dimensional localization of single molecules for super-resolution imaging and single-particle tracking. *Chemical Reviews*, 117(11):7244–7275, Jun 2017.

[94] Uwe Weierstall. Liquid sample delivery techniques for serial femtosecond crystallography. *Philosophical Transactions of the Royal Society B: Biological Sciences*, 369(1647):20130337, 2014.

[95] Uwe Weierstall, RB Doak, JCH Spence, D Starodub, D Shapiro, P Kennedy, J Warner, GG Hembree, Petra Fromme, and HN Chapman. Droplet streams for serial crystallography of proteins. *Experiments in Fluids*, 44(5):675–689, 2008.

[96] Max O Wiedorn, Salah Awel, Andrew J Morgan, Kartik Ayyer, Yaroslav Gevorkov, Holger Fleckenstein, Nils Roth, Luigi Adriano, Richard Bean, Kenneth R Beyerlein, Joe Chen, Jesse Coe, Francisco Cruz-Mazo, Tomas Ekeberg, Rita Graceffa, Michael Heymann, Daniel A. Horke, Joraj Knoska, Valerio Mariani, Reza Nazari, Dominik Oberthur, Amit K. Samanta, Raymond G. Sierra, Claudia A. Stan, Oleksandr Yefanov, Dimitris Rompotis, Jonathan Correa, Benjamin Erk, Rolf Tresh, Joachim Schulz, Brenda G. Hogue, Alfonso M. Ganan-Calvo, Petra Fromme, Jochen Kupper, Andrei V. Rode, Sasa Bajt, Richard A. Kirian, and Henry N. Chapman. Rapid sample delivery for megahertz serial crystallography at x-ray fels. *IUCrJ*, 5(5), 2018.

[97] Max O Wiedorn, Dominik Oberthür, Richard Bean, Robin Schubert, Nadine Werner, Brian Abbey, Martin Aepfelbacher, Luigi Adriano, Aschkan Allahgholi, Nasser Al-Qudami, Jakob Andreasson, Steve Aplin, Salah Awel, Kartik Ayyer, Sasa Bajt, Imrich Barak, Sadia Bari, Johan Bielechi, Sabine Botha, Djelloul Boukhelef, Wolfgang Brehm, Sandor Brokhauser, Igor Cheviakov, Mathew A. Coleman, Francisco Cruz-Mazo, Cyril Danilevski, Connie Darmanin, R. Bruce Doak, Martin Domaracky, Katerina Dorner, Yang Du, Hans Fangohr, Holger Fleckenstein, Matthias Frank, Petra Fromme, Alfonso M. Ganan-Calvo, Yaroslav Gevrokov, Klaus Giewekemeyer, Helen Mary Ginn, Heinz Graafsma, Rita Graceffa, Dominic Greiffenberg, Lars Gumprecht, Peter Gottlicher, Janos Hajdu, Steffen Hauf, Michael Heymann, Susannah holmes, Daniel A. Horke, Mark S. Hunter, Siegfried Imlau, Alexander Kaukher, Yoonhee Kim, Alexander Klyuev, Joraj Knoska, Bostjan Kobe, Manuela Kuhn, Christopher

Kupitz, Jochen Kupper, Janine Maia Lahey-rudolph, torsten Laurus, Karoline Le Cong, Romain Letrun, P. Lourdu Xavier, Luis Maia, Filipe R.N.C. Maia, Valerio Mariani, Marc Messerschmidt, Markus Metz, David Mezza, Thomas Michelat, Grant Mills, Diana C.F. Monteiro, Andrew Morgan, Kerstin Muhlig, Anna Munke, Astrid Munnich, Julia Nette, Keith A. Nugent, Theresa Nuguid, Allen M. Orville, Suraj Pandey, Gisel Pena, Pable Villanueva-Perez, Jennifer Poehlsen, Gianpietro Previtali, Lars Redecke, Winnie Maria Riekehr, Holger Rohde, Adam Round, Tatiana Safenreiter, Iosifina Sarrou, Tokushi Sato, Marius Schmidt, Brend Schmidt, Robert Schonherr, Joachim Schulz, Jonas A. Sellberg, M. Marvin Seibert, Carolin Seuring, Megan L. Shelby, Robert L. Shoeman, Marcin Sikorski, Alessandro Silenzi, Claudiu A. Stan, Xintian Shi, Stephan Stern, Jola Sztuk-Dambietz, Janusz Szuba, Patrik Vagovic, Thomas Ve, Britta Weinhausen, Thomas A. White, Krzysztof Wrona, Chen Xu, Oleksandr Yevanof, Nadia Zatsepin, Jiaguo Zhang, Markus Perbandt, Adrian P. Mancuso, Christian Betzel, Henry Chapman, and Anton Barty. Megahertz serial crystallography. *Nature communications*, 9(1):4025, 2018.

[98] Martin Wörner. Numerical modeling of multiphase flows in microfluidics and micro process engineering: a review of methods and applications. *Microfluidics and nanofluidics*, 12(6):841–886, 2012.

[99] David L Youngs. Time-dependent multi-material flow with large fluid distortion. *Numerical methods for fluid dynamics*, 1982.

[100] Yuehua Yuan and T Randall Lee. Contact angle and wetting properties. In *Surface science techniques*, pages 3–34. Springer, 2013.

[101] Rizwan Zahoor, Saša Bajt, and Božidar Šarler. Influence of gas dynamic virtual nozzle geometry on micro-jet characteristics. *International Journal of Multiphase Flow*, 104:152–165, 2018.

[102] Rizwan Zahoor, Saša Bajt, and Božidar Šarler. Numerical investigation on influence of focusing gas type on liquid micro-jet characteristics. *International Journal of Hydromechatronics*, 1(2):222–237, 2018.

[103] Rizwan Zahoor, Grega Belšak, Saša Bajt, and Božidar Šarler. Simulation of liquid micro-jet in free expanding high-speed co-flowing gas streams. *Microfluidics and Nanofluidics*, 22(8):87, 2018.

[104] Rizwan Zahoor, Rok Regvar, Saša Bajt, and Božidar Šarler. A numerical study on the influence of liquid properties on gas-focused micro-jets. *Progress in Computational Fluid Dynamics, an International Journal*, 20(2):71–83, 2020.

[105] Xiaoguang Zhang and Osman A Basaran. Dynamics of drop formation from a capillary in the presence of an electric field. *Journal of Fluid Mechanics*, 326:239–263, 1996.

APPENDIX A

SUPPLEMENTARY INFORMATION

PUBLICATIONS

Some publications during my Ph.D. period which I have been in the author list are:

Nazari, R., Zaare, S., Alvarez, R. C., Karpos, K., Engelman, T., Madsen, C., ... Kirian, R. A. (2020). 3D printing of gas-dynamic virtual nozzles and optical characterization of high-speed microjets. Optics Express, 28(15), 21749-21765. ([61])

Wiedorn, M. O., Awel, S., Morgan, A. J., Ayyer, K., Gevorkov, Y., Fleckenstein, H., ... Chen, J. (2018). Rapid sample delivery for megahertz serial crystallography at X-ray FELs. IUCrJ, 5(5), 574-584. ([96])

Echelmeier, A., Kim, D., Cruz Villarreal, J., Coe, J., Quintana, S., Brehm, G., ... Batyuk, A. (2019). 3D printed droplet generation devices for serial femtosecond crystallography enabled by surface coating. Journal of Applied Crystallography, 52(5). ([28])

Assalauova, D., Kim, Y. Y., Bobkov, S., Khubbutdinov, R., Rose, M., Alvarez, R., ... Gelisio, L. (2020). An advanced workflow for single particle imaging with the limited data at an X-ray free-electron laser. arXiv preprint arXiv:2006.08345. ([10])

Grant, T. D., Perera, S. M., Salas-Estrada, L. A., Struts, A. V., Chawla, U., Xu, X., ... Karpos, K. (2020). Membrane Protein Dynamics Revealed by X-Ray Scattering with a Femtosecond Free-Electron Laser. Biophysical Journal, 118(3), 365a. ([38])

Salas-Estrada, L. A., Grant, T. D., Perera, S. M., Struts, A. V., Chawla, U., Xu, X., ... Karpos, K. (2020). Rhodopsin's Ultra-Fast Activation Dynamics in Bilayer and Micelle Environments. Biophysical Journal, 118(3), 92a. ([75])

BEAMTIMES

Listing of some of the XFEL experiments that our 3D printed devices have been directly or indirectly involved are shown in table A.1.

Dates	Facility	ID	PI	Experiment type	Notes
9/15/16	LCLS	N60	Brown	Solution scattering	Time-Resolved Wide-Angle X-Ray Scattering Investigation of Rhodopsin Activation.
3/20/17	EuXFEL	2042	Ros	Droplet source development	Droplet on Demand to Massively Reduce Sample Amount for Time-Resolved Serial Femtosecond crystallography
8/16/17	LCLS	LQ70	Ros	Droplet source development	Massively reduced sample consumption via microfluidic droplet generation for SFX and time resolved SFX with XFELs
11/16/17	EuXFEL	2116	Fromme	Crystallography	Unravel the primary reactions in Photosynthesis by use of the unique pulse train structure of the proteins
Run 17	LCLS	Mixed	Mixed	Mixed	LCLS sample injection group requests 20+ GDVNs (type 79 50 µm ID)
4/2/2018	LCLS	X269	Hunter	Solution scattering (CXS)	Systematic studies of fluctuation x-ray scattering at LCLS.
4/11/2018	LCLS	LR67	Qiao	Solution scattering (CXS)	Use of time-resolved correlated x-ray scattering to measure conformational changes induced in the G alpha subunit of the heterotrimeric G-protein by the chaperone protein Ric-8A

Table A.1 continued from previous page

Dates	Facility	ID	PI	Experiment type	Notes
4/18	SACLA		Brown	Solution scattering (CXS)	Time-Resolved Wide-Angle X-Ray Scattering Investigation of Rhodopsin Activation.
9/13/2018	LCLS	LU56	Zatsepin	Crystallography	Reza provided GDVNs (50, 75, 100 µm ID) for 5-10 micron crystals.
9/14/2018	LCLS	X341	Aquila	Single particle imaging	We supply nozzles to make the smallest drops possible. 4 12-hour shifts.
9/26/2018	LCLS	LT14	Martin	Solution scattering (CXS)	We supply standard GDVNs for solutions. Possibly high pH solutions. Jet stability is most important. 4 12-hour shifts.
10/17/2018	LCLS	LU18	Brown	Solution scattering	We supply standard GDVNs for solutions. Rhodopsin. 4 12-hour shifts.
10/26/2018	EuXFEL	2100	Brown	Solution scattering	We supply standard GDVNs for solutions. Rhodopsin. 4 12-hour shifts.
11/9/2018	LCLS	LU44	Rousseau	Mix and inject	Collaborating with Dr. Ros's group
12/14/2018	LCLS	LT43	Fromme	Crystallography	
2/28/19	EuXFEL		Fromme	Crystallography	
5/23/2019	EuXFEL	2145	Maia	Single particle imaging	Electrospray nozzles to be sent to Johan Bielecki.

Table A.1 continued from previous page

Dates	Facility	ID	PI	Experiment type	Notes
5/26/2019					
6/5/2019	EuXFEL	2146	Maia	Single particle imaging	
9/12/2019	EuXFEL	2326	Fromme	TR-SFX	
10/11/2019	SACLA	8039	Brown		Rhodopsin
8/24/2020	LCLS	P171	Schmidt		
8/28/2020	LCLS	P172	Fromme		
9/4/2020	LCLS	LV14	Ros		

Table A.1: Some of the XFEL Experiments of Which Reza Nazari Had contribution.

Figure A.1 shows a 3D printed nozzle operating in a XFEL experiment at SLAC national laboratory, Stanford, USA.

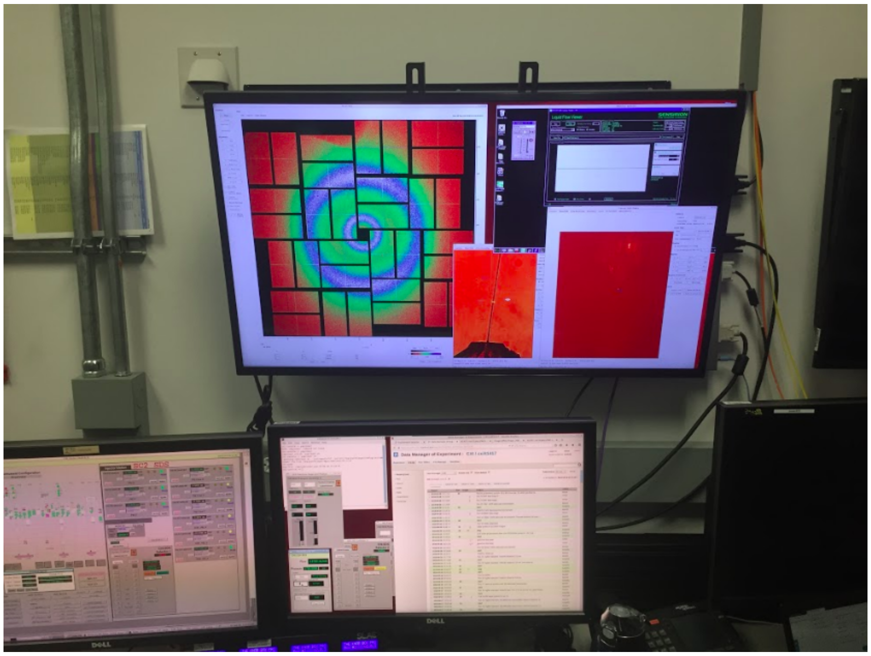

Figure A.1: A 3D Printed GDVN operating in an XFEL experiment at SLAC National Laboratory, Stanford, USA.

DIMENSIONLESS NUMBERS

REYNOLDS, WEBER AND CAPILLARY NUMBERS

Reynolds number can be defined as $Re* = \frac{\rho R U}{\mu}$, where U is average velocity, μ is viscosity and ρ is density. Capillary number is defined as $Ca = \frac{\mu U}{\sigma}$, where μ is kinematic viscosity and σ is surface tension. Finally, the Weber number is defined as $We = (Re*)(Ca) = \frac{\rho U^2 R}{\sigma}$ ([11]). Reynolds number demonstrates a comparative measure measurement of inertial forces to viscous forces. Capillary number demonstrates a comparative measurement of viscous forces to surface tension, and Weber number demonstrates a comparative measurement of inertial forces to surface tension.

ELECTRIC BOND NUMBER

Zhang et al. stated introduced another dimensionless number to characterize jets regimes, namely the electric Bond number $N = \frac{\epsilon E^2 R}{\sigma}$ in case the ambient fluid is an insulator or a dielectric of permittivity ϵ and the liquid is a perfect conductor ([105]). In the equation for the electric Bond number, R is the jet radius, σ is the surface tension and E denotes the electric field.

StrOUHAL NUMBER

In the formula A.1 ([85]), St is the Strouhal number, f is the vortex shedding frequency, L is the liquid jet diameter as the characteristic length of the flow, and U is the liquid jet velocity as the characteristic velocity.

$$St = \frac{fL}{U}([85]) \tag{A.1}$$

PECLET NUMBER

We define Peclet number as the ratio of a physical quantity advected by the flow to the rate of the same quantity diffused by an appropriate gradient. Therefore, we have ([66]):

$$Pe = \frac{\text{advective transport rate}}{\text{diffusive transport rate}}([66]) \tag{A.2}$$

AS a result, the Peclet formula for mass transfer becomes ([66]):

$$Pe_L = \frac{Lu}{D}([66]) \tag{A.3}$$

where u the local flow velocity, L is the characteristic length, D the diffusivity coefficient ([66]).

Capillary length (L_c) is a dimensionless number that quantifies the relative magnitude of surface tension and gravitational forces and is defined as ([100]):

$$L_c = \sqrt{\frac{\gamma}{\Delta\rho g}} \quad ([100]) \tag{A.4}$$

In formula A.4 for GDVNs, γ is the interfacial between the liquid and gas, $\Delta\rho$ is the density difference between liquid and gas, and g is the gravitational acceleration.

DILAS LASER PARAMETERS

DILAS laser parameters are 230 micro-Watts @10 kHz, 10 ns FWHM pulse length and 168 V driver voltage, as shown in figure7 A.2.

DRAWINGS OF THE DESIGNS

we can find the drawings corresponding to several designs in this section.

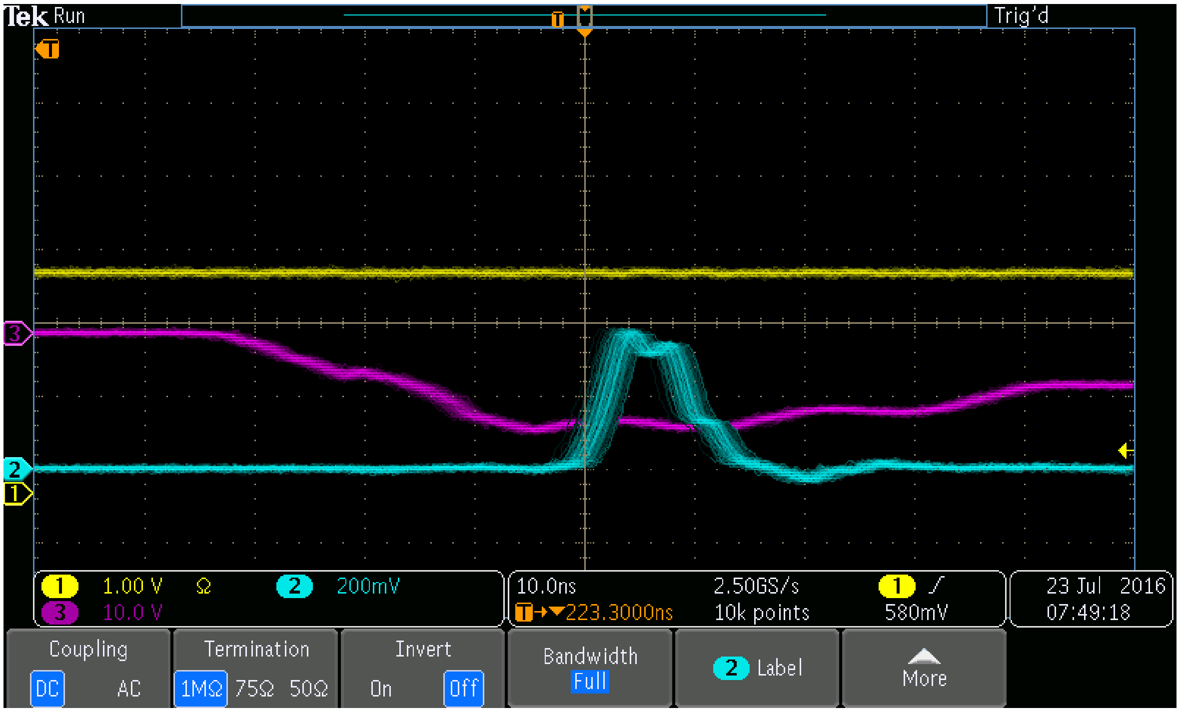

Coupling: DC AC
Termination: 1MΩ 75Ω 50Ω
Invert: On Off
Bandwidth: Full

Figure A.2: DILAS laser parameters.

DESIGNS OF GDVNS TO PRODUCE NANODROPS

To produce nanodrops, the GDVN should be able to produce a stable jet, even with very small liquid flow rates. Low liquid flow rates result in thin jets and consequently, the droplets resulting from jet breakup would be smaller. Design 42, and the successive design 53 A.4 are able to jet with very low liquid flow rates and are suitable to produce Nanodrops for SPI (single particle imaging) XFEL experiments. Devices from these designs were used in several XFEL experiments.

DESIGNS OF NOZZLES 50 μm LIQUID LINES

There are several nozzle designs with 50 μm liquid lines. Design details are shown in figures A.5, A.6, A.8, A.9 and A.10.

DESIGN OF NOZZLES WITH 75 μm LIQUID LINES

A design that fits 75 μm inner diameter and 360μm outer diameter liquid capillaries is shown in figure A.11.

DESIGN OF NOZZLES WITH 100 μm LIQUID LINES

Several GDVN designs having a 100 μm liquid lines has been developed. Figure A.12 shows that seven design geometrical parameters are being modified. Each design has a different set of geometrical parameters, shown in table A.

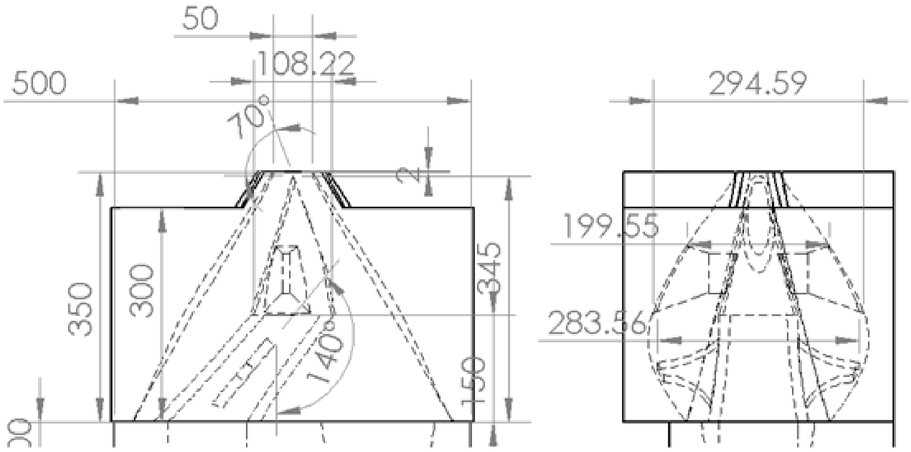

Figure A.3: Design Dimensions of the A42 Design (Design 42) in Micrometers.

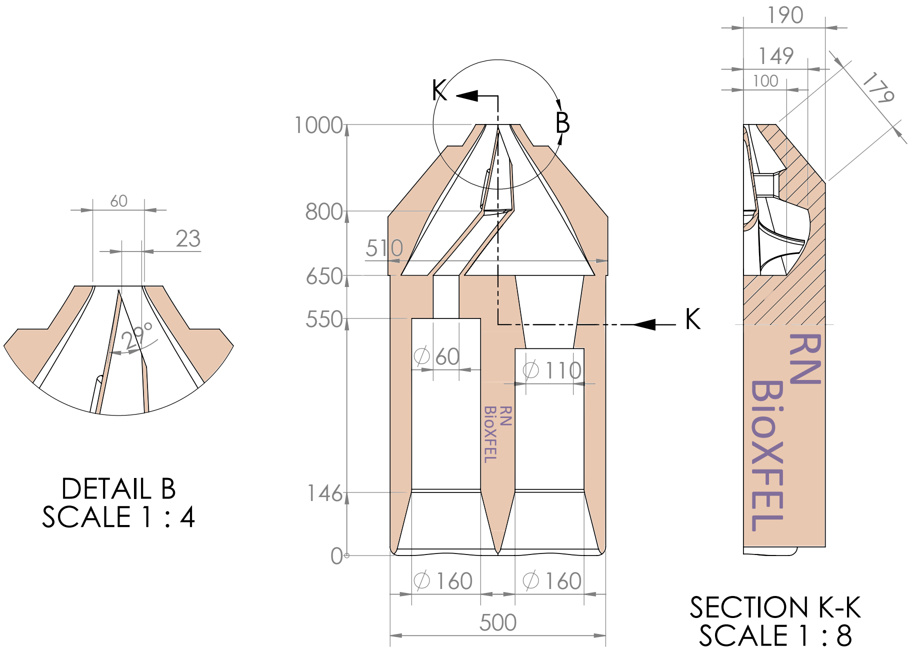

Figure A.4: Design dimensions of design 53 in micrometers.

DESIGN OF MONOLITHIC INTEGRATED MIXER AND NOZZLE (COLLABORATING WITH AUSTIN ECHELMEIER FROM DR. ALEXANDRA ROS GROUP)

The designs are usually custom-made to satisfy the requirements of the specific XFEL experiment, such as the experiment in paper by Ishigami et al. [43]. As an example, some details of one of the designs are shown in figure A.13.

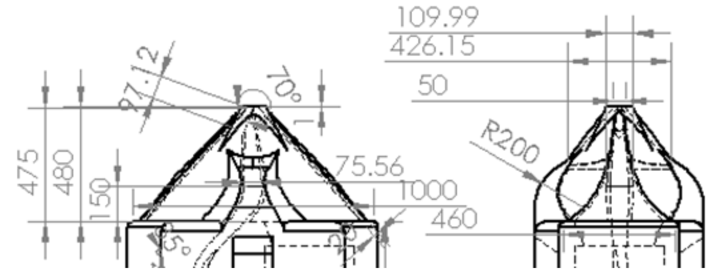

Figure A.5: Design Dimensions of the SC30I Design (Design 30) in Micrometers.

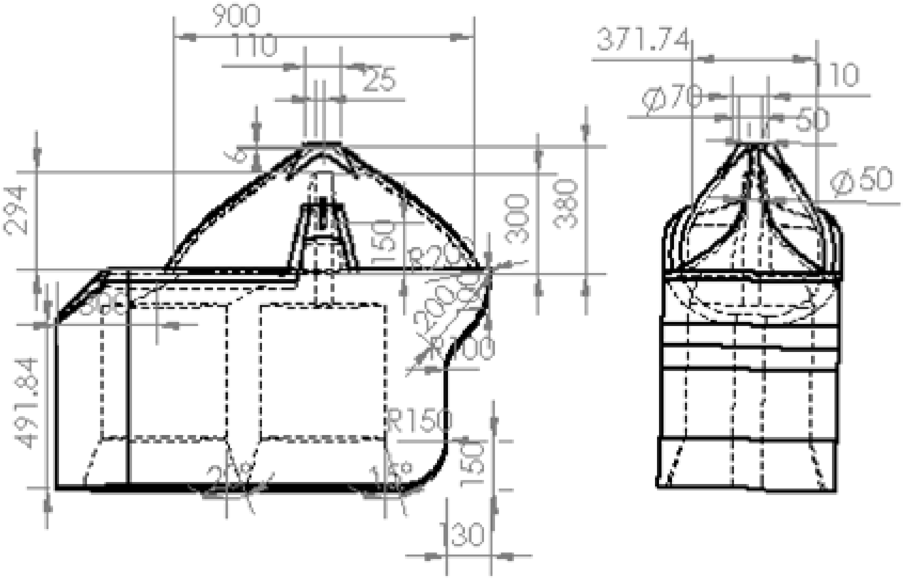

Figure A.6: The 56 design; two views of the design. Dimensions are in microns.

SETUP: DOUBLE-PULSED PIV IMAGING CONFIGURATION

This configuration is meant to allow the recording of double laser pulses, with each pulse recorded on separate frames. The pulses can be spaced by as little as 550 ns. This is what has been used to measure jet speeds.

The configuration goes as follows:

1. We use a simple (and cheap) signal generator as a "master clock". This typically runs at 100 Hz since we wish to gather random samples of jet speeds over time periods that are long in comparison to timescales jet phenomena.
    (a) Our cheap signal generator can be tricky to use.
2. The Photron fastcam is syncronized to the master clock, using the "sync in" BNC cable.

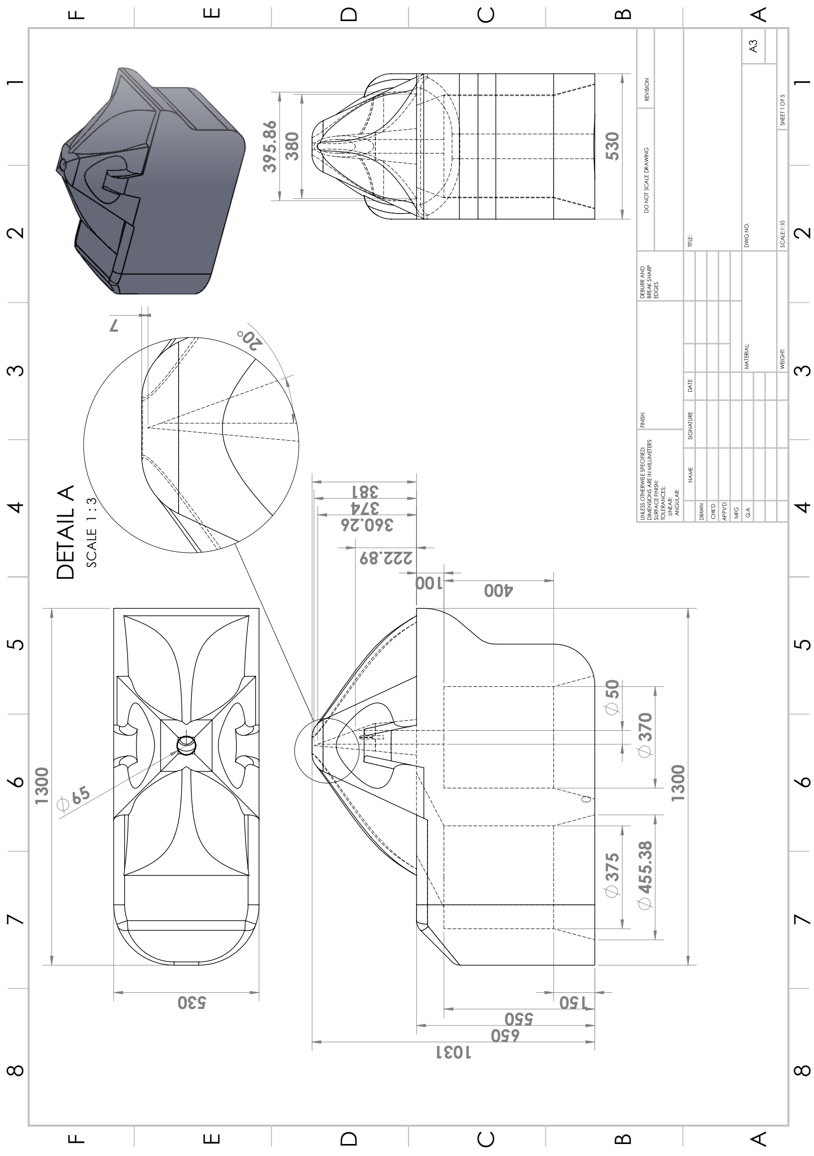

Figure A.7: Sheet 1 of the 79 design; 3rd angle projection drawing of the design.

   (a) Note that "synchronization" is functionally very different than "triggering". In synchronized mode, the fastcam uses an external clock and thus allows only one frame rate.

3. The master clock also triggers a delay generator (model DG645) that sends closely spaced pairs of trigger pulses to the laser (DILAS diode laser). Note that the delay generator must skip every second trigger from the master clock in order to ensure that there is no more than one laser flash per Fastcam frame.

   (a) In order to generate pairs of pulses from the delay generator, the "burst mode" must be enabled. The specific settings are:

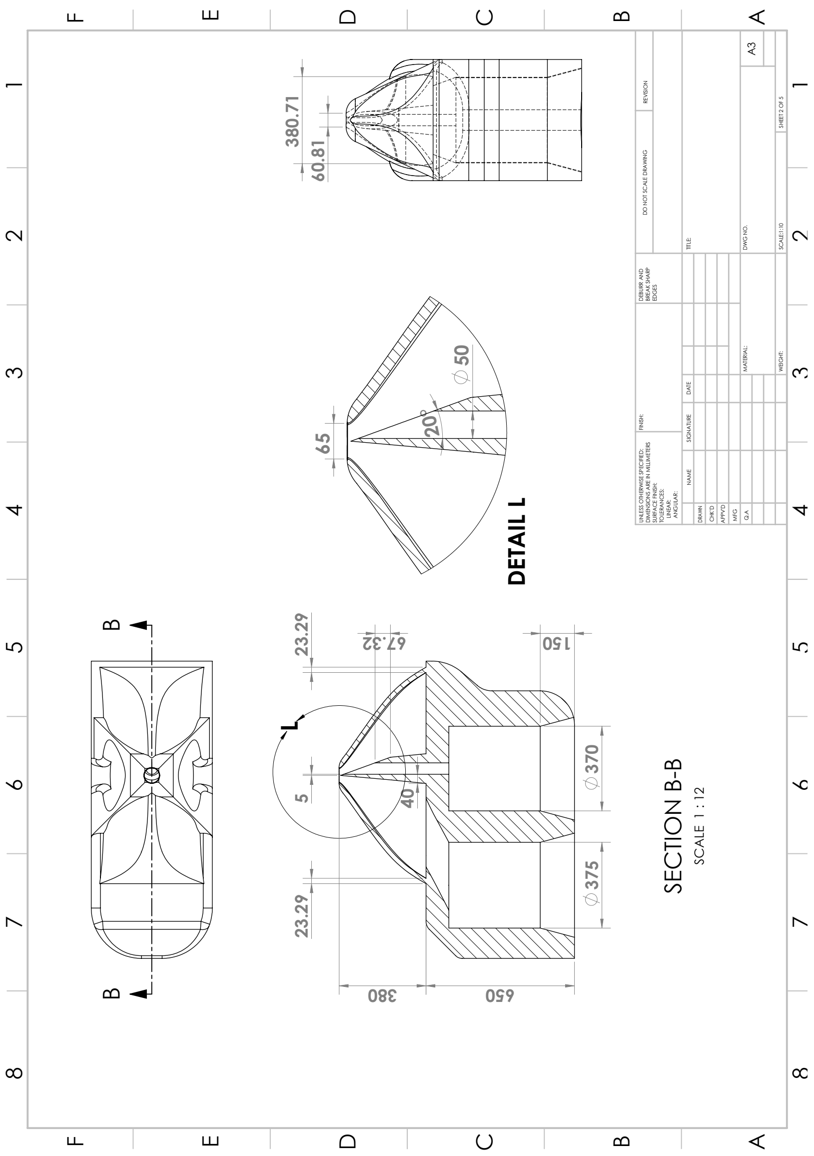

Figure A.8: Sheet 2 of the 79 design; 3rd angle projection drawing of the design.

   i. "Burst: on"
   ii. "t0 output on first" (not necessary, but possibly useful for triggering an oscilloscope. Makes one pulse per burst on the t0 output.)
   iii. "cnt 2" (generate two pulses)
   iv. "per 550 ns" (sets the time delay between burst pulses)

(b) In order to skip every second input trigger to the delay generator, "advanced triggering" must be enabled.

(c) In order to trigger the DILAS laser driver, it is usually necessary to set the output to "TTL".

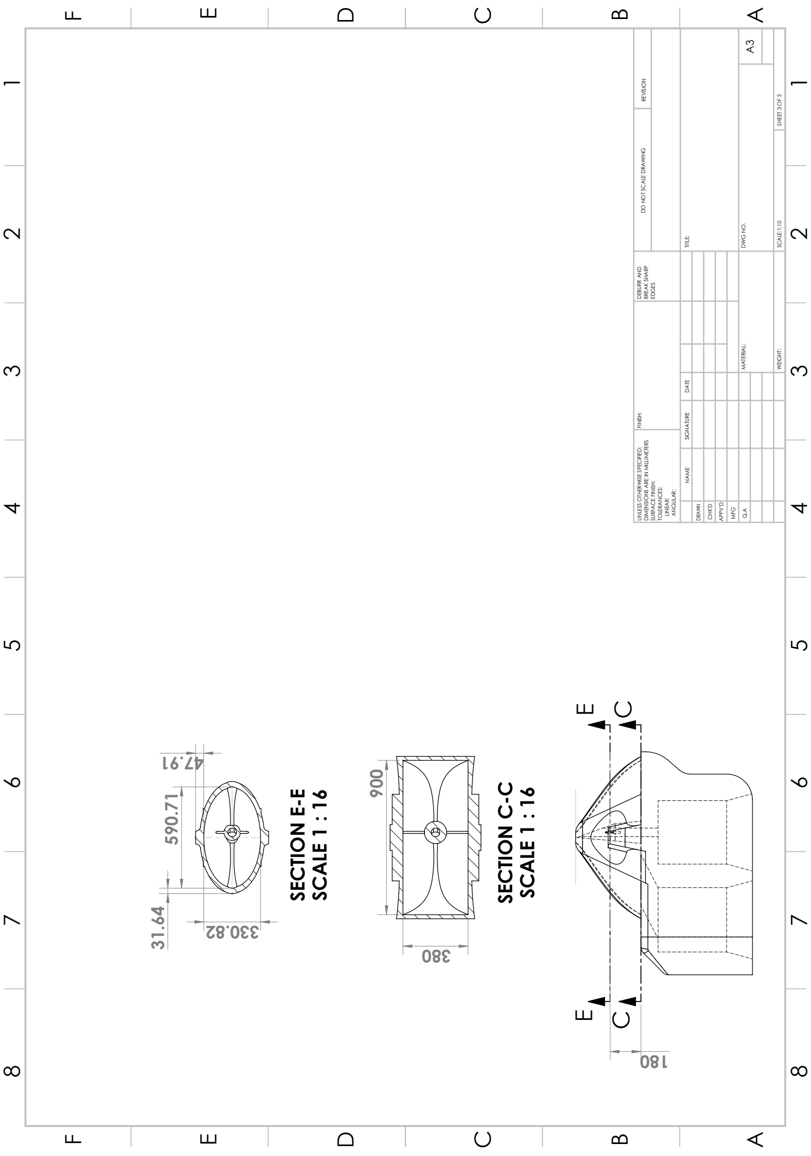

Figure A.9: Sheet 3 of the 79 design; some projections of the sections of the design.

   i. Select one of the output signal edges, then press "shift" and then "TTL"

4. The Fastcam PFV software has the following configurations:

   (a) In the Delay tab in Camera options:

      i. SINC IN is set to 400nsec (but we need to look at an oscilloscope to choose this setting properly, as shown in figures A.15.

      ii. TRIG OUT is set to 10 usec

      iii. SYNC OUT is set to 3usec 200nsec 1

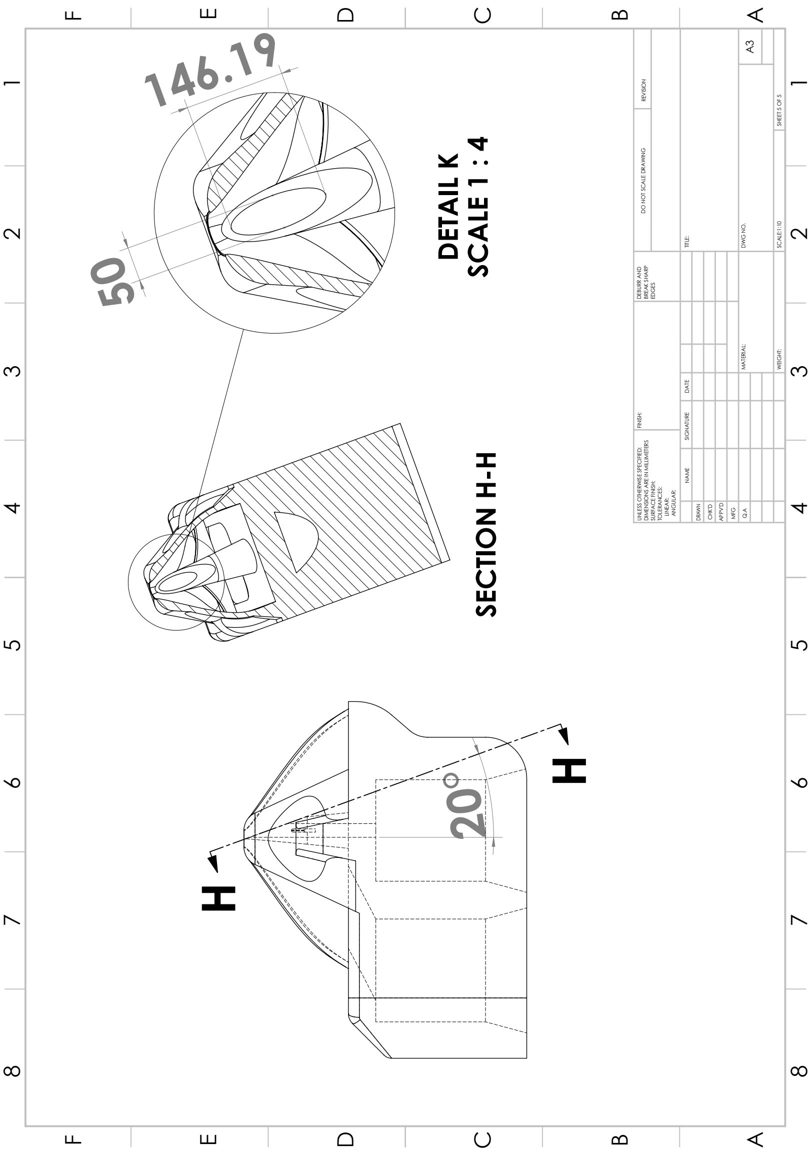

Figure A.10: Sheet 4 of the 79 design; some projections of the sections of the liquid capillaries of the design ([61]).

NOZZLE ASSEMBLY

This section explained the methods we came up with to assemble the 3D printed GDVNs. Konstantinos Karpos and Roberto Alvarez were trained to reproducibility assemble the nozzles. They contributed to writing the assembly procedure steps, that are being explained in this section (section A).

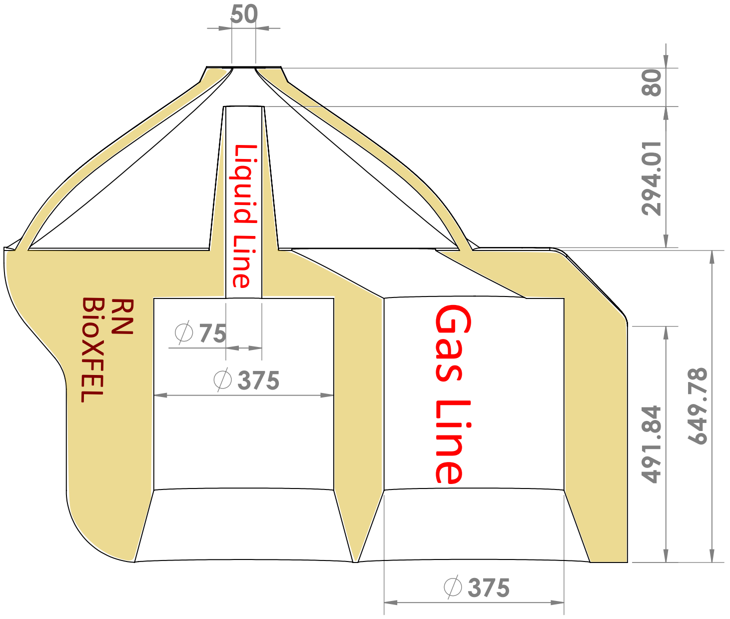

Figure A.11: The 175 design; The design for 75 μm liquid line. Dimensions are in microns.

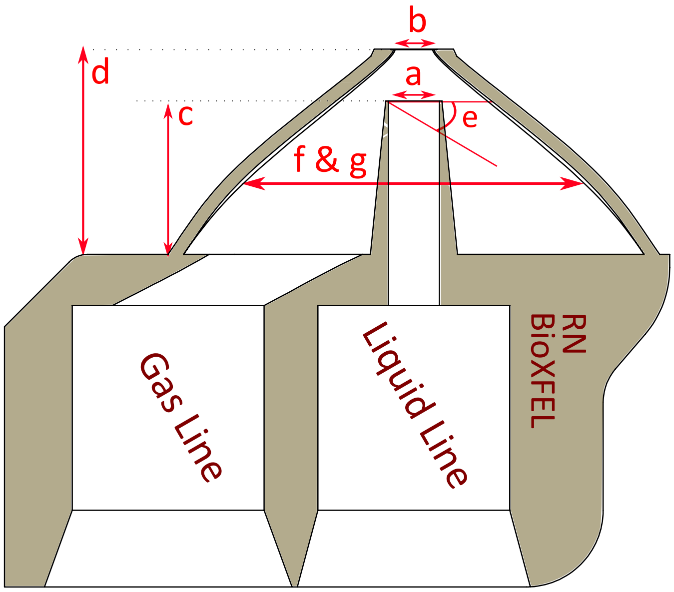

Figure A.12: Geometrical parameters of the 3D printed designs.

MATERIALS NEEDED

1. 2 - Capillaries cut to desired length

Design	a	b	c	d	e	f, g
61	100	60	300	400	0	331, 200
62	100	65	300	400	0	331, 200
63	100	80	300	400	0	331, 200
64	100	80	300	425	0	331, 200
66	100	100	300	425	0	331, 200
67	100	100	300	400	0	331, 200

Table A.2: Geometrical parameters of the designs with 100 μm inner diameter liquid line.

2. 2 - Double-Bubble Extra Fast Setting Epoxy (3-5 min worktime)
3. Idex metal sleeve, Part Number: U-145
4. 3D printed nozzle
5. Microscope
6. 2 - Disposable cups for mixing epoxy
7. 1 - Popsicle stick for mixing epoxy
8. Permanent marker (ex: black Sharpie)
9. Paper towel
10. 1 - Diamond capillary cutter
11. 1 - Heat shrink label (permasleeve)

ASSEMBLY PROCESS

1. Cut liquid capillary
    (a) Using the microscope and the diamond capillary cutter, carefully score the end that will be attached to the nozzle such that the break is as clean as possible. See figure A.16 1 for reference on good and bad cuts.
2. Cut gas capillary
    (a) To differentiate between gas and liquid:
        i. Wind up the gas capillary and using a black permanent marker, mark alternating stripes on the capillary as seen in figure A.17.
3. Align nozzle under microscope.
4. Using a small strip of PDMS or fine tipped tweezers, hold down the nozzle so it does not move when you insert the capillary, see figure A.17.

5. Put the gas capillary in first, then the liquid capillary (see figure A.18 for reference).
    (a) NOTE: The liquid capillary is the most important to get right. By putting the gas capillary first, you reduce the amount of movement in the liquid capillary, ensuring it is sitting in the correct orientation.
6. Mix the epoxy in a disposable cup using the popsicle stick.
    (a) Note that this is quick drying epoxy.
    (b) Put the used popsicle stick into the second disposable cup for reuse later.
7. Using a short piece of capillary, apply the epoxy to one side of the nozzle. Use the short capillary to move the epoxy around the interface of the capillary and nozzle, as shown in figure A.19.
    (a) NOTE: Using too much epoxy can cause issues with mounting the nozzle. Apply enough to secure the capillaries in place, but not too much that it becomes bulky.
8. Wait 10-15 minutes for the epoxy to fully cure.
    (a) NOTE: During this time, you can prepare the next nozzle for assembly.
9. While the nozzle is curing, put the label on the metal IDEX sleeve.
10. Once the epoxy has cured, slide the metal sleeve on the opposite end of the capillary (the side without the nozzle).
    (a) Note: Leave 1 or 2 mm of space between the nozzle and metal sleeve.
11. Using the second pack of epoxy, glue the metal sleeve to the capillary. See figure A.20 for an example.
    (a) NOTE: Add enough epoxy to each end such that it completely covers the holes. If there is not enough epoxy here, it might be problematic in a vacuum environment.
12. After 10-15 minutes of curing time, the nozzle is ready for immediate use.

NANOFAB 3D PRINTER OPERATIONS NOTES

The following guide is a step-by-step guide on how to use the labs NanoFab 3D printer. The notes were taken by Konstantinos Karpos in summer 2019 during a training session with Reza Nazari.

PRE-PRINTING NOTES

1. The IPA is located in the fume hood in room C29A in the Biodesign C building of the Arizona State University Tempe campus.
    (a) NOTE: Any chemicals taken from this fume hood (including IPA) must be returned after you are done using them
2. The IP-S photoresist is located in the sample fridge just down the hall from the printer room.
    (a) NOTE: Any chemicals taken from this fridge (including IP-S) must be returned after you are done using them. NOTE: The IP-S bottle is labeled "REZA" with the date it was opened.
    (b) NOTE: IP-S is light sensitive, do not remove the aluminum foil outside of the printer room

PRINTER PREPARATION

1. On the computer software, push "Exchange Holder".
    (a) NOTE: A pop-up will open informing you that the printer is safe to handle.
    (b) NOTE: Check the touch screen monitor to the left of the computer and confirm that the z-axis is set to its lower possible position, "Lower Z position reached" should be shown on the screen.
2. Use the buttons on the right side of the printer to rotate the objective holder such that the objective is near you.
3. Remove the objective.
    (a) NOTE: Rotate counterclockwise to loosen and clockwise to tighten
4. After removing the objective:
    (a) Attach the objective to its black base.
    (b) Remove the circular protection sponge
    (c) Cover the objective with its plastic cap
        i. NOTE: DO NOT transport the objective without the base and plastic cap attached!
5. Move the objective to the workbench and begin the cleaning procedure.
6. To clean the objective:
    (a) Remove the plastic top.
    (b) Spray the lens and the neighborhood of the lens with IPA.

  (c) Use chem-wipes to clean around the lens and remove any dirt/IP-S/etc.
  (d) Do not let the chem-wipe touch the glass, clean around the actual glass.
  (e) Reza Nazari recommends cleaning the objective with IPA 4 or 5 times.
    i. i. NOTE: Once cleaned, rotate the focus of the objective to the "TTT" position.
    ii. The 'focus' is the only rotating part on the objective.
  (f) Once clean, reattach the plastic top.
  (g) Reattach the objective to the printer.
    i. NOTE: The objective needs to be placed in position 1 on the printer.
    ii. NOTE: DO NOT over-tighten the objective! Once you feel it stop moving on the threads, DO NOT rotate it anymore!

IP-S LOADING

1. Clean the glass sample holders.
   (a) NOTE: Use the square glass plates only.
   (b) NOTE: Use gloves!
   (c) NOTE: DO NOT touch the center of the glass. Handle it by grabbing the sides of the glass only!
   (d) NOTE: Use IPA and a lint-free chem-wipe to clean the glass only!
2. Place on the 2 position on the black sample tray (it won't fit anywhere else).
3. Using the ohmmeter, confirm the conductive side of the glass plate is facing up.
   (a) a. NOTE: If it's not, DO NOT touch the center of the glass when handling the plate.
4. Place a thin strip of tape on two sides of the square plate so it stays in place.
5. Loading the photoresist:
   (a) CLOSE THE DOOR.
   (b) Dip the brush into the IP-S bottle, but remove all the excess by wiping it on the interior walls of the container.
      i. NOTE: DO NOT touch the brush!
      ii. NOTE: DO NOT touch the brush to the glass plate!
   (c) Place a small drop, about 1/4 of an inch in diameter, onto the center of the glass plate.
      i. NOTE: The photoresist needs to be EXACTLY centered on the glass plate. Get it as close as you can!

6. Place the brush back into the IP-S container and cover it with the aluminum foil.
7. Loading the sample tray into the printer:
    (a) Load the sample tray into the printer upside down.
        i. NOTE: The photoresist needs to be facing the objective, so turn the tray so the IP-S is facing the floor.
    (b) DO NOT apply pressure if the tray does not slide in! It will fit.
    (c) DO NOT let the photoresist touch the printer in any way!
        i. This is the hardest part. Slide it in at a slight angle, but do not apply too much pressure to the holder.
    (d) Push the sample tray all the way in until only the handle is visible.

STARTING THE PRINT JOB

1. Rotate the objective so that it is right underneath the photoresist, this may take a few clicks
2. On the touch screen monitor located on the computer desk:
    (a) Go to "HOME".
    (b) Push "Load position".
    (c) Once pushed, wait for the dialogue box stating that the printer reached its minimum z.
3. On the computer:
    (a) Make sure the correct sample tray is selected.
        i. A pop-up window should ask you to choose the sample tray, this should be the "DiLL" position.
        ii. There will be an image showing the square sample plates that are shown in figure **??**.
    (b) Push "OK".
    (c) Push "Approach sample".
    (d) Once pushed, wait for the code to read "interface found".
        i. NOTE: This is located on the main printer screen, it will be in the text box in the center.
4. Choosing the correct file:
    (a) Push "Load job".
    (b) Locate the correct file.

   i. If not locally found on the computer, copy the correct job files to the computer.

5. Push “Start Job“.

   (a) Wait for the print to start before leaving the room.

6. Change the sign on the door so it reads “Print in progress“.

OBTAINED PERMISSIONS

PERMISSION FOR THE OPTICS EXPRESS JOURNAL

Permission for the contents of Chapter 3 is obtained from Optics Express journal. Moreover, permission to use figure 2.2 is also obtained from AIP publishing publications.

Letter From Journal

Permission for Vega Figure for Instabilities

Permission to use figure 2.2 is in pictures of figures A.24, A.25 and A.26:

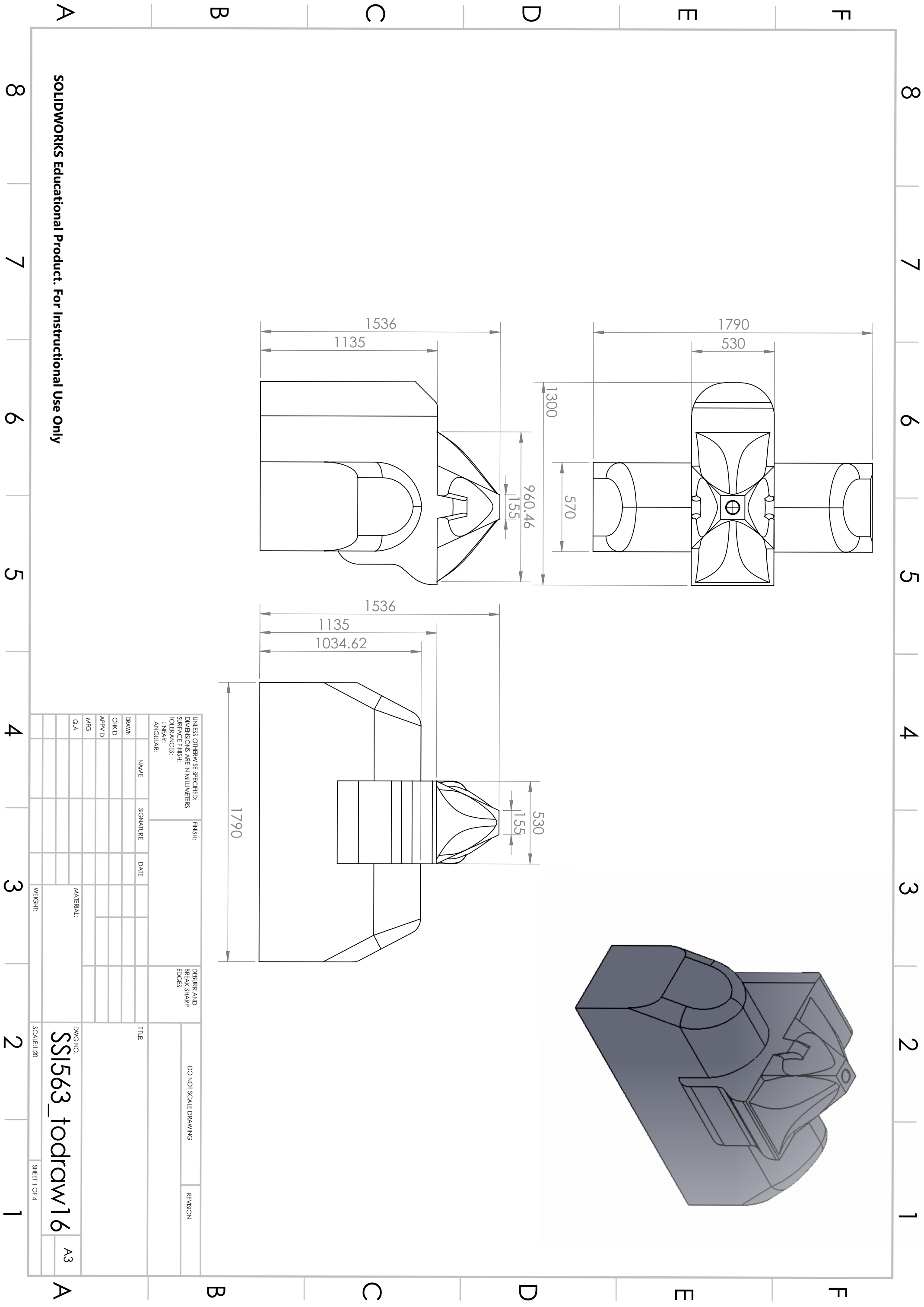

Figure A.13: Integration of a concentric mixer with a nozzle design (N63) (Collaborating with Dr. Alexandra Ros Group; Austin Echelmeier, Jorvani Cruz).

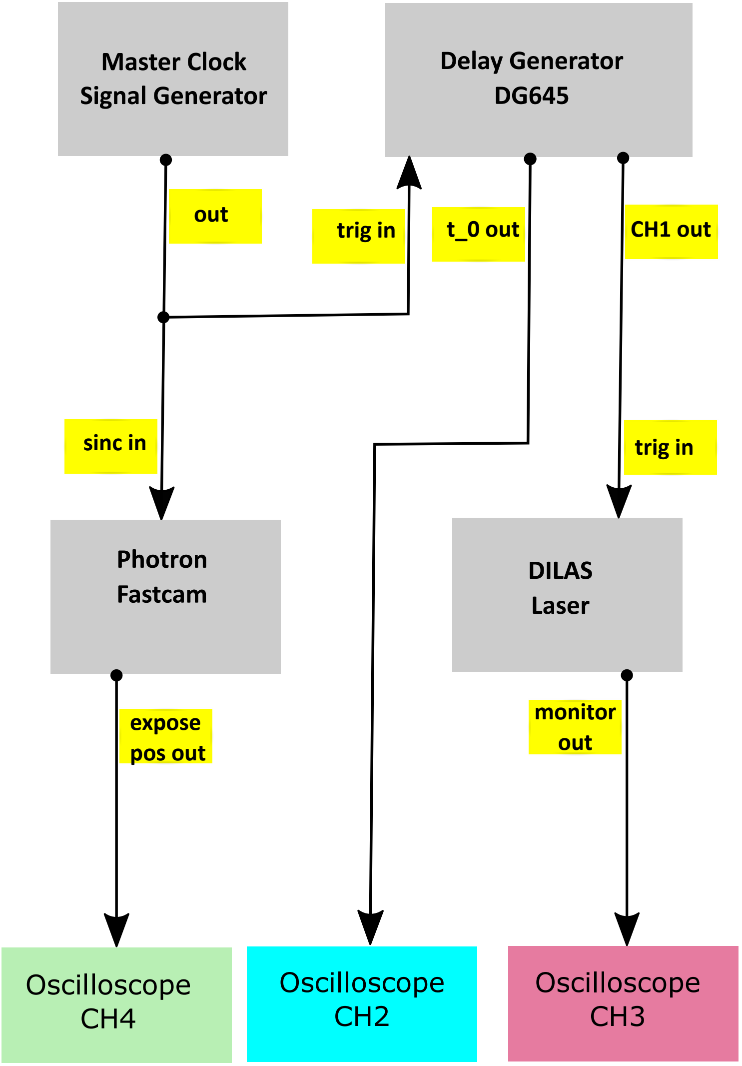

Figure A.14: Schematic of the dual image with dual pulse laser imaging station configuration.

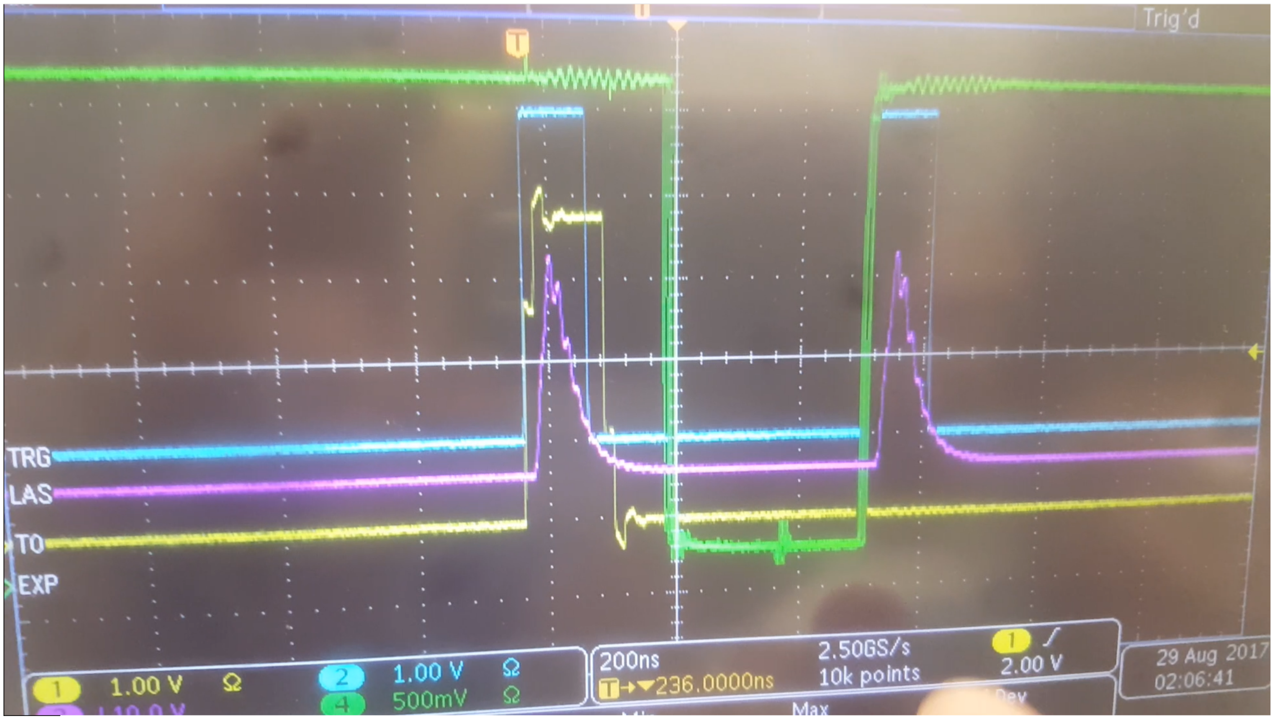

Figure A.15: Picture from the oscilloscope indicating that the master clock (Channel 1; yellow), the DG645 delay generator (Channel 2; light blue), the DILAS laser (Channel 3; purple) and the Photron Fastcam (channel 4; green), are all synchronized with respect to each other.

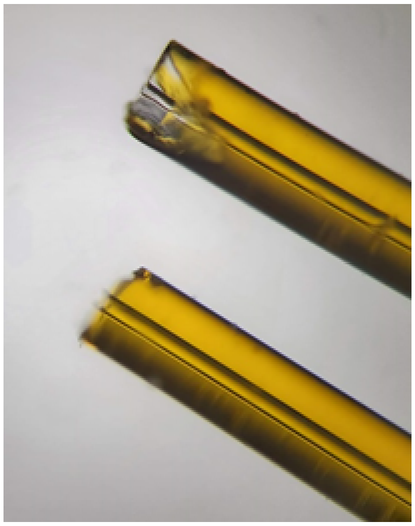

Figure A.16: Top: bad quality score, bottom: acceptable score.

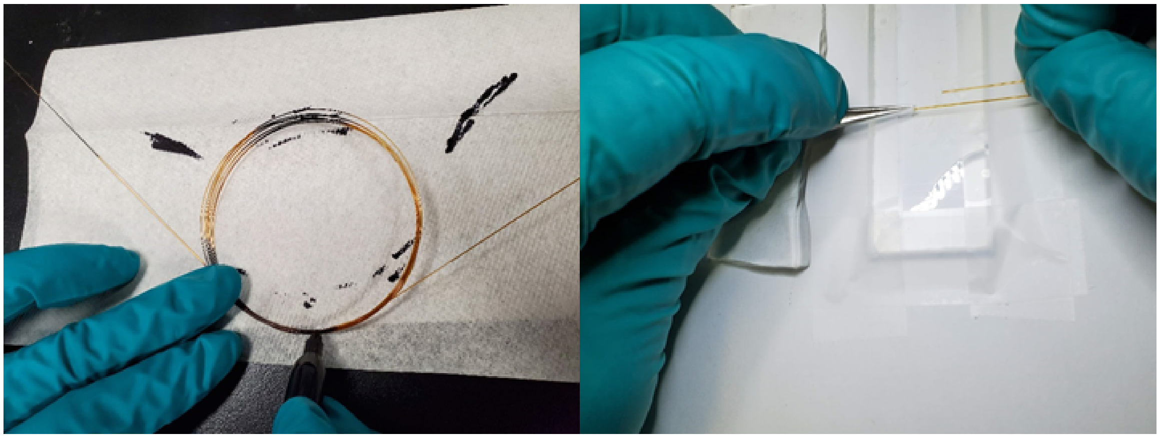

Figure A.17: (left) marking the gas capillary line using a black sharpie. (right): holding the nozzle with tweezers during capillary insertion.

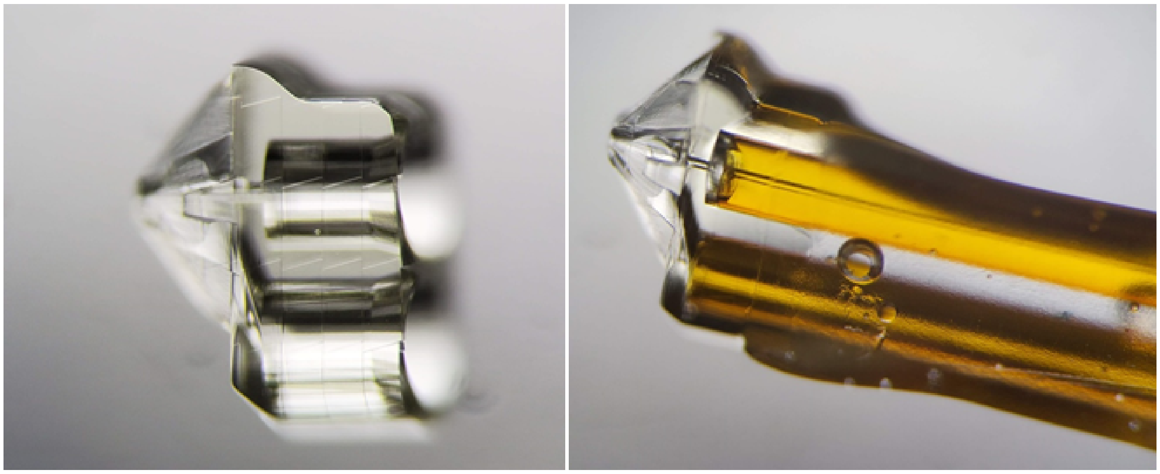

Figure A.18: (left): standalone nozzle, figure 3b (right): capillaries inserted into the nozzle. Top: liquid line, bottom: gas line.

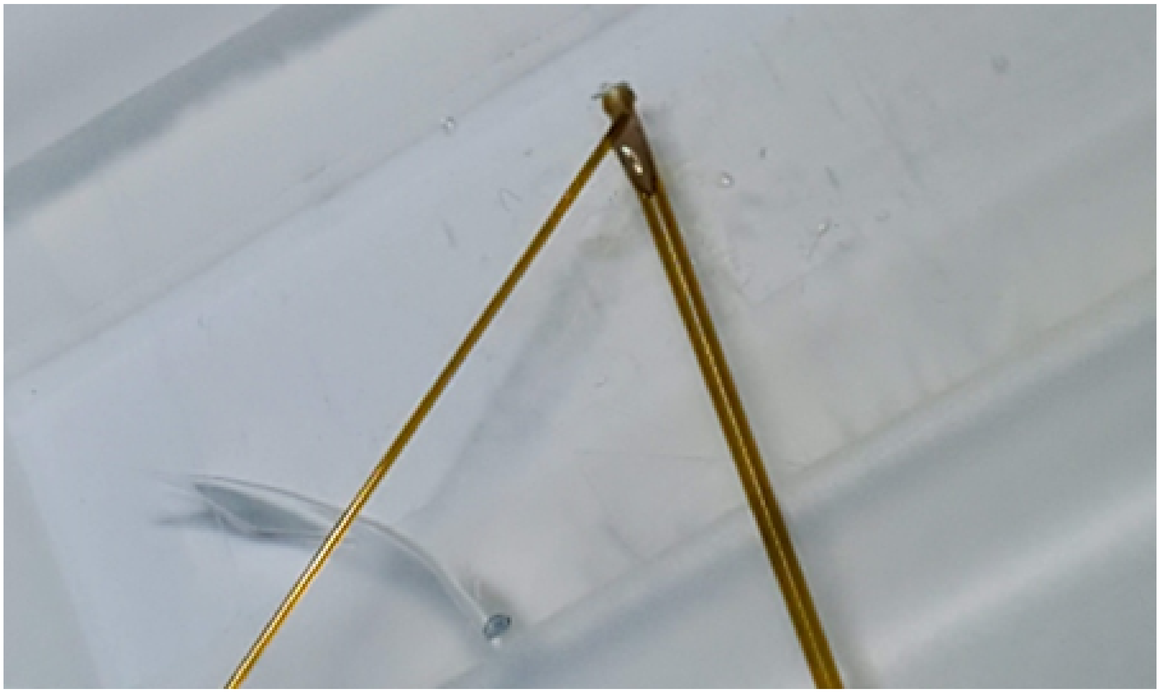

Figure A.19: Using a short/broken capillary to apply epoxy to nozzle head.

Figure A.20: (top): metal sleeve glued to nozzle/capillary, figure 5b (bottom): a visual on the approximate amount of glue needed at each end of the sleeve.

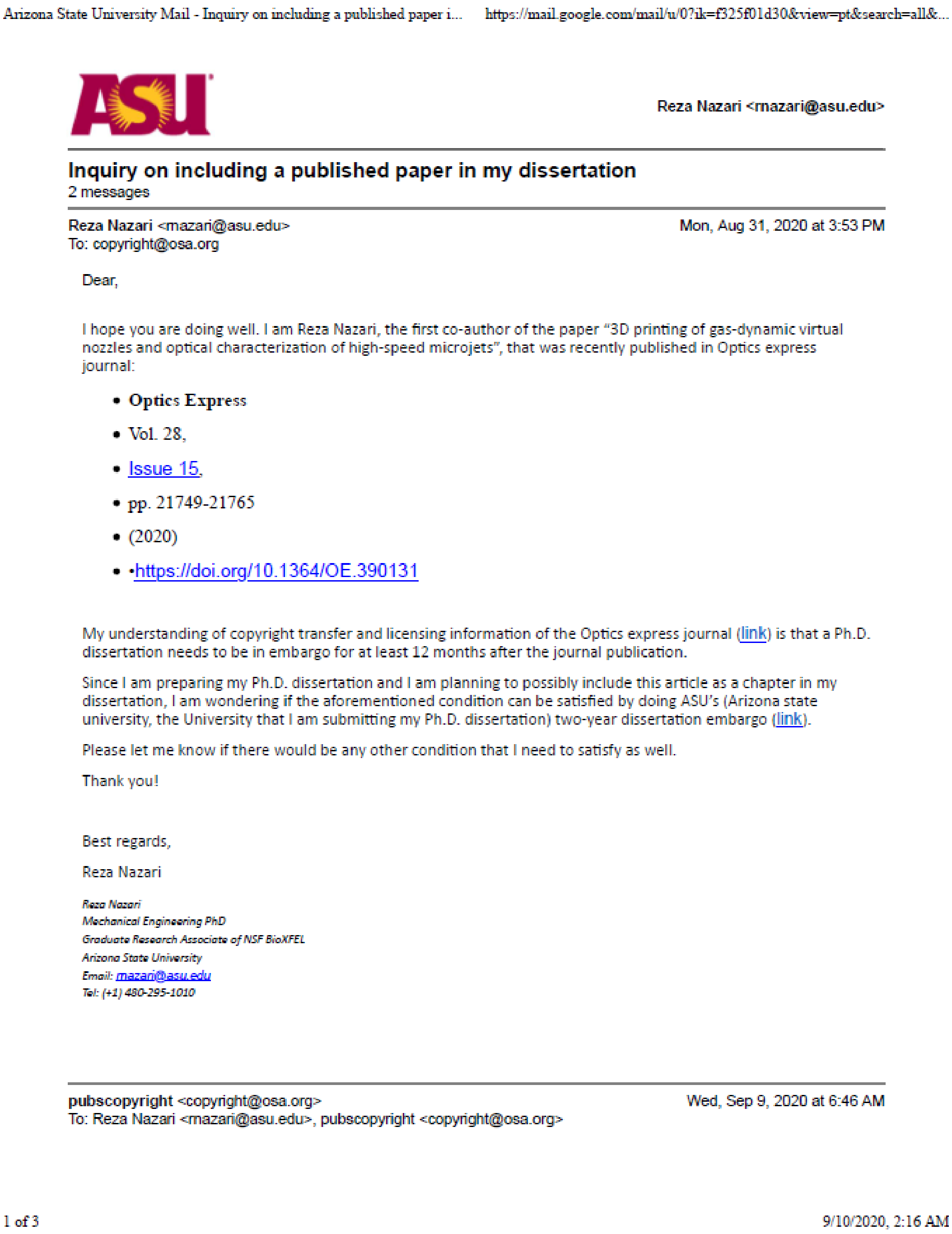

Arizona State University Mail - Inquiry on including a published paper i... https://mail.google.com/mail/u/0?ik=f325f01d30&view=pt&search=all&...

ASU

Reza Nazari <rnazari@asu.edu>

Inquiry on including a published paper in my dissertation

2 messages

Reza Nazari <rnazari@asu.edu> Mon, Aug 31, 2020 at 3:53 PM

To: copyright@osa.org

Dear,

I hope you are doing well. I am Reza Nazari, the first co-author of the paper "3D printing of gas-dynamic virtual nozzles and optical characterization of high-speed microjets", that was recently published in Optics express journal:

- **Optics Express**
- Vol. 28,
- Issue 15,
- pp. 21749-21765
- (2020)
- •https://doi.org/10.1364/OE.390131

My understanding of copyright transfer and licensing information of the Optics express journal (link) is that a Ph.D. dissertation needs to be in embargo for at least 12 months after the journal publication.

Since I am preparing my Ph.D. dissertation and I am planning to possibly include this article as a chapter in my dissertation, I am wondering if the aforementioned condition can be satisfied by doing ASU's (Arizona state university, the University that I am submitting my Ph.D. dissertation) two-year dissertation embargo (link).

Please let me know if there would be any other condition that I need to satisfy as well.

Thank you!

Best regards,

Reza Nazari

Reza Nazari
Mechanical Engineering PhD
Graduate Research Associate of NSF BioXFEL
Arizona State University
Email: rnazari@asu.edu
Tel: (+1) 480-295-1010

pubscopyright <copyright@osa.org> Wed, Sep 9, 2020 at 6:46 AM

To: Reza Nazari <rnazari@asu.edu>, pubscopyright <copyright@osa.org>

1 of 3 9/10/2020, 2:16 AM

Figure A.21: Permission from Optics Express Journal; part 1.

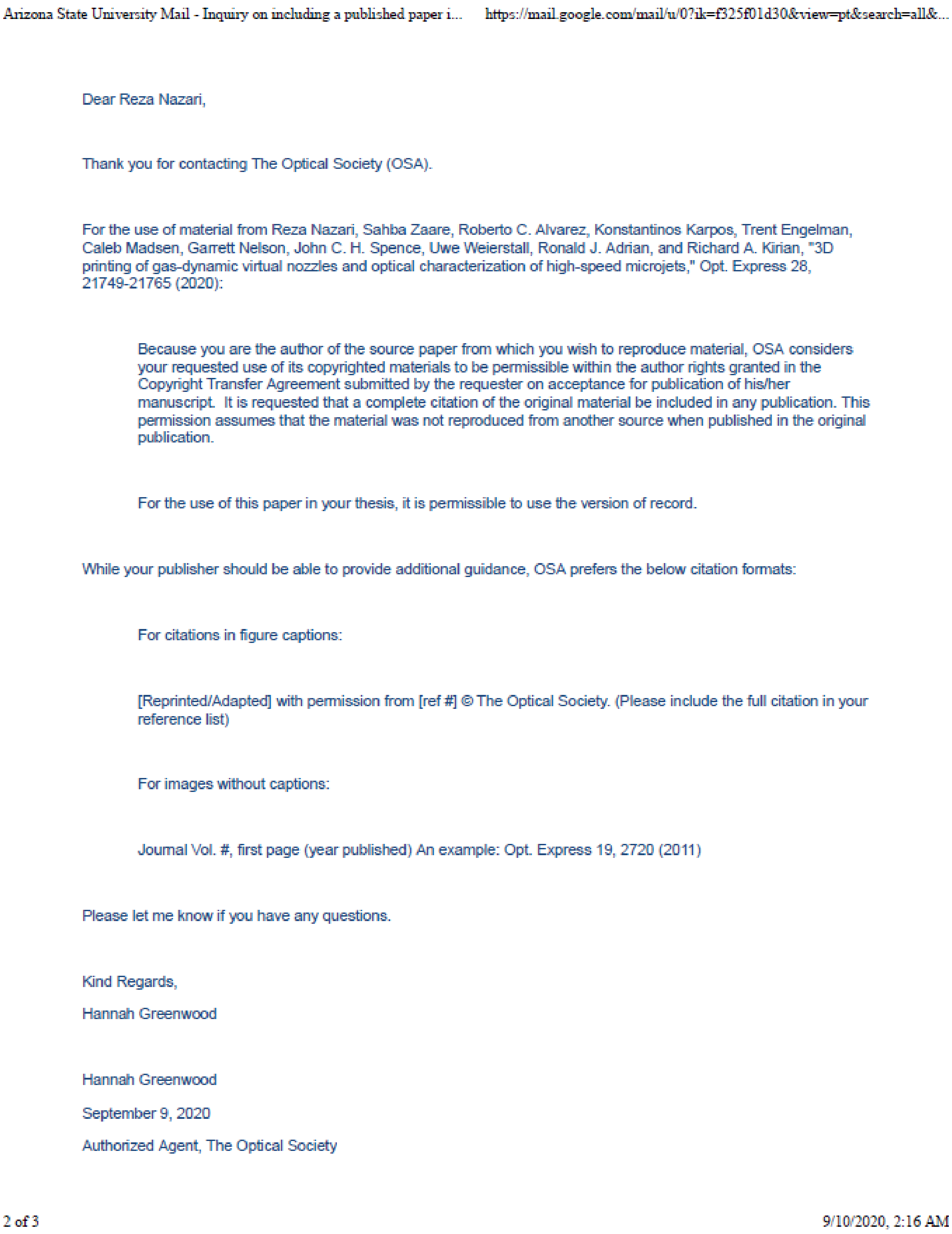

Arizona State University Mail - Inquiry on including a published paper i... https://mail.google.com/mail/u/0?ik=f325f01d30&view=pt&search=all&...

Dear Reza Nazari,

Thank you for contacting The Optical Society (OSA).

For the use of material from Reza Nazari, Sahba Zaare, Roberto C. Alvarez, Konstantinos Karpos, Trent Engelman, Caleb Madsen, Garrett Nelson, John C. H. Spence, Uwe Weierstall, Ronald J. Adrian, and Richard A. Kirian, "3D printing of gas-dynamic virtual nozzles and optical characterization of high-speed microjets," Opt. Express 28, 21749-21765 (2020):

> Because you are the author of the source paper from which you wish to reproduce material, OSA considers your requested use of its copyrighted materials to be permissible within the author rights granted in the Copyright Transfer Agreement submitted by the requester on acceptance for publication of his/her manuscript. It is requested that a complete citation of the original material be included in any publication. This permission assumes that the material was not reproduced from another source when published in the original publication.
>
> For the use of this paper in your thesis, it is permissible to use the version of record.

While your publisher should be able to provide additional guidance, OSA prefers the below citation formats:

> For citations in figure captions:
>
> [Reprinted/Adapted] with permission from [ref #] © The Optical Society. (Please include the full citation in your reference list)
>
> For images without captions:
>
> Journal Vol. #, first page (year published) An example: Opt. Express 19, 2720 (2011)

Please let me know if you have any questions.

Kind Regards,

Hannah Greenwood

Hannah Greenwood

September 9, 2020

Authorized Agent, The Optical Society

2 of 3 9/10/2020, 2:16 AM

Figure A.22: Permission from Optics Express Journal; part 2.

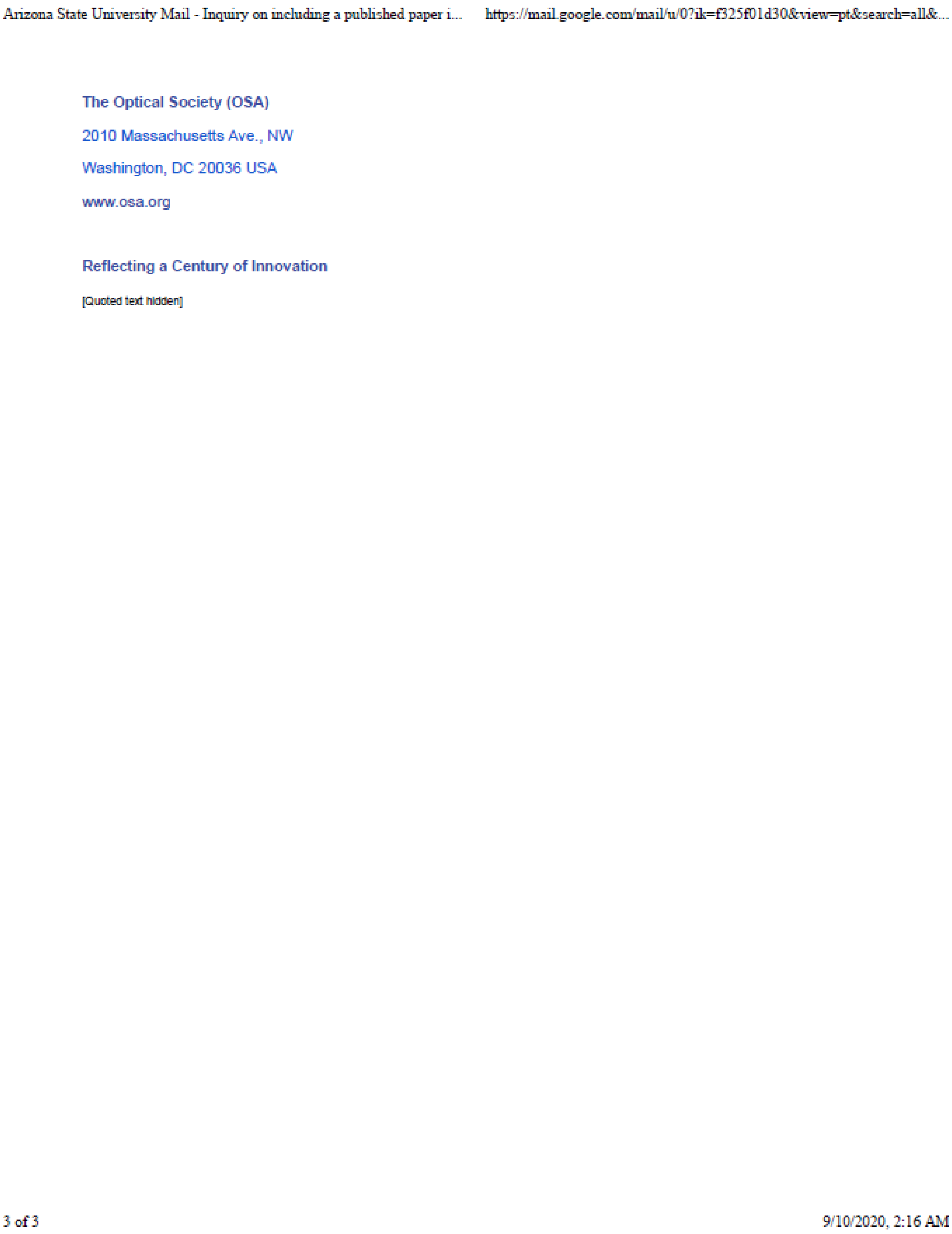

Arizona State University Mail - Inquiry on including a published paper i... https://mail.google.com/mail/u/0?ik=f325f01d30&view=pt&search=all&...

The Optical Society (OSA)
2010 Massachusetts Ave., NW
Washington, DC 20036 USA
www.osa.org

Reflecting a Century of Innovation

[Quoted text hidden]

3 of 3 9/10/2020, 2:16 AM

Figure A.23: Permission from Optics Express Journal; part 3.

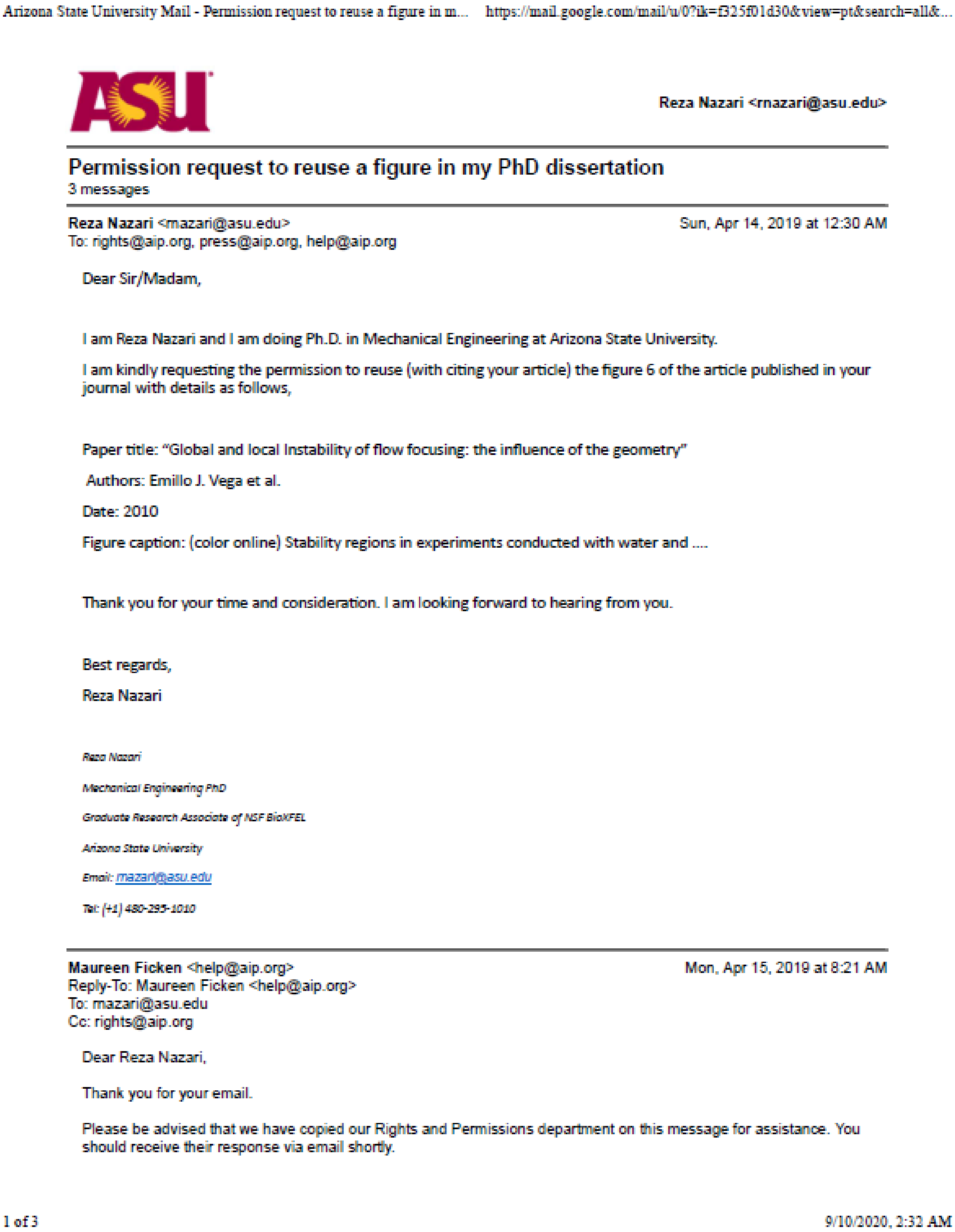

Arizona State University Mail - Permission request to reuse a figure in m... https://mail.google.com/mail/u/0?ik=f325f01d30&view=pt&search=all&...

Reza Nazari <rnazari@asu.edu>

Permission request to reuse a figure in my PhD dissertation
3 messages

Reza Nazari <rnazari@asu.edu> Sun, Apr 14, 2019 at 12:30 AM
To: rights@aip.org, press@aip.org, help@aip.org

Dear Sir/Madam,

I am Reza Nazari and I am doing Ph.D. in Mechanical Engineering at Arizona State University.

I am kindly requesting the permission to reuse (with citing your article) the figure 6 of the article published in your journal with details as follows,

Paper title: "Global and local Instability of flow focusing: the influence of the geometry"

Authors: Emillo J. Vega et al.

Date: 2010

Figure caption: (color online) Stability regions in experiments conducted with water and ....

Thank you for your time and consideration. I am looking forward to hearing from you.

Best regards,

Reza Nazari

Reza Nazari

Mechanical Engineering PhD

Graduate Research Associate of NSF BioXFEL

Arizona State University

Email: rnazari@asu.edu

Tel: (+1) 480-295-1010

Maureen Ficken <help@aip.org> Mon, Apr 15, 2019 at 8:21 AM
Reply-To: Maureen Ficken <help@aip.org>
To: rnazari@asu.edu
Cc: rights@aip.org

Dear Reza Nazari,

Thank you for your email.

Please be advised that we have copied our Rights and Permissions department on this message for assistance. You should receive their response via email shortly.

1 of 3 9/10/2020, 2:32 AM

Figure A.24: Permission from the AIP Publishing publications; part 1.

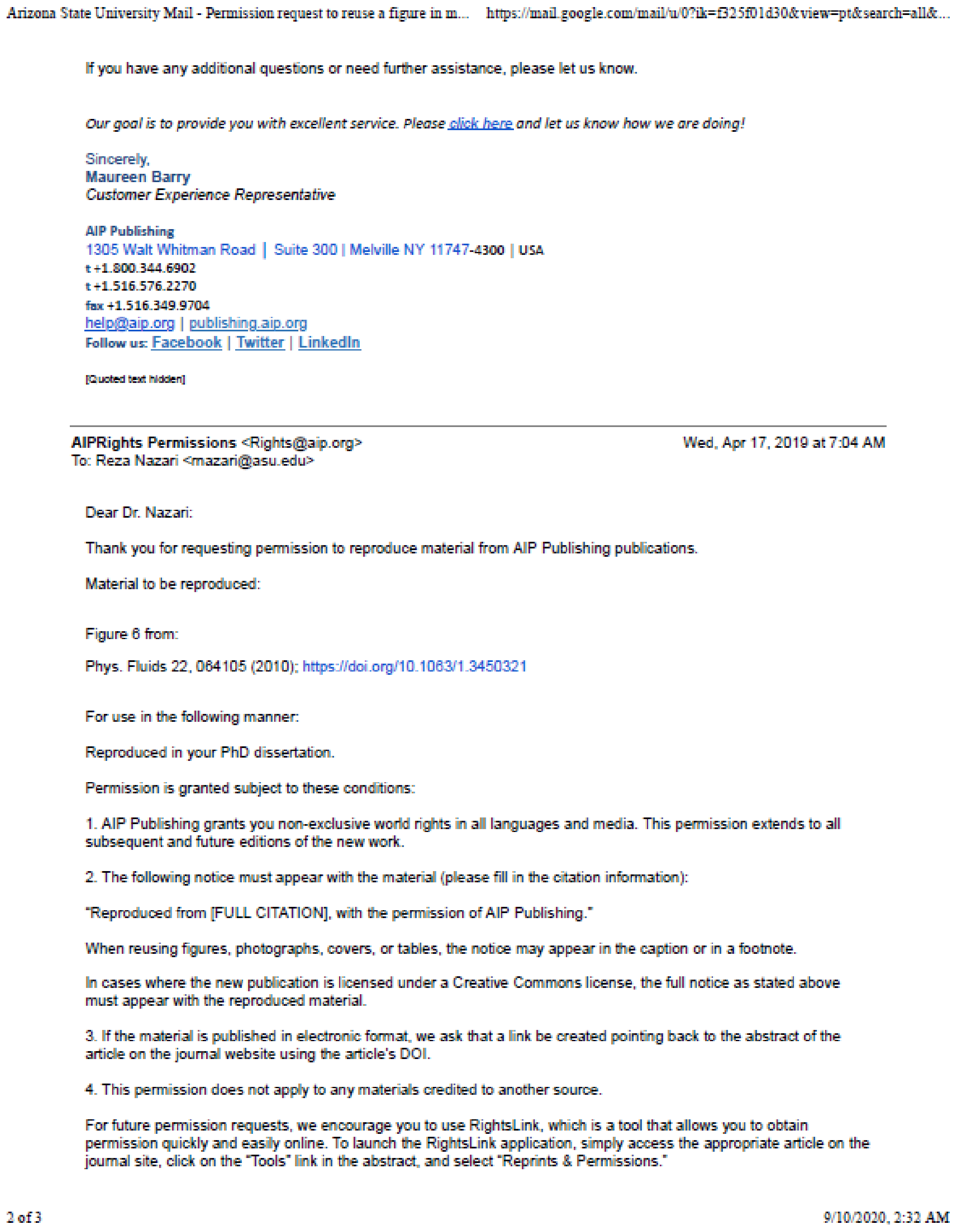

Arizona State University Mail - Permission request to reuse a figure in m... https://mail.google.com/mail/u/0?ik=f325f01d30&view=pt&search=all&...

If you have any additional questions or need further assistance, please let us know.

Our goal is to provide you with excellent service. Please click here and let us know how we are doing!

Sincerely,
Maureen Barry
Customer Experience Representative

AIP Publishing
1305 Walt Whitman Road | Suite 300 | Melville NY 11747-4300 | USA
t +1.800.344.6902
t +1.516.576.2270
fax +1.516.349.9704
help@aip.org | publishing.aip.org
Follow us: Facebook | Twitter | LinkedIn

[Quoted text hidden]

AIPRights Permissions <Rights@aip.org> Wed, Apr 17, 2019 at 7:04 AM
To: Reza Nazari <mazari@asu.edu>

Dear Dr. Nazari:

Thank you for requesting permission to reproduce material from AIP Publishing publications.

Material to be reproduced:

Figure 6 from:

Phys. Fluids 22, 064105 (2010); https://doi.org/10.1063/1.3450321

For use in the following manner:

Reproduced in your PhD dissertation.

Permission is granted subject to these conditions:

1. AIP Publishing grants you non-exclusive world rights in all languages and media. This permission extends to all subsequent and future editions of the new work.

2. The following notice must appear with the material (please fill in the citation information):

"Reproduced from [FULL CITATION], with the permission of AIP Publishing."

When reusing figures, photographs, covers, or tables, the notice may appear in the caption or in a footnote.

In cases where the new publication is licensed under a Creative Commons license, the full notice as stated above must appear with the reproduced material.

3. If the material is published in electronic format, we ask that a link be created pointing back to the abstract of the article on the journal website using the article's DOI.

4. This permission does not apply to any materials credited to another source.

For future permission requests, we encourage you to use RightsLink, which is a tool that allows you to obtain permission quickly and easily online. To launch the RightsLink application, simply access the appropriate article on the journal site, click on the "Tools" link in the abstract, and select "Reprints & Permissions."

2 of 3 9/10/2020, 2:32 AM

Figure A.25: Permission from the AIP Publishing publications; part 2.

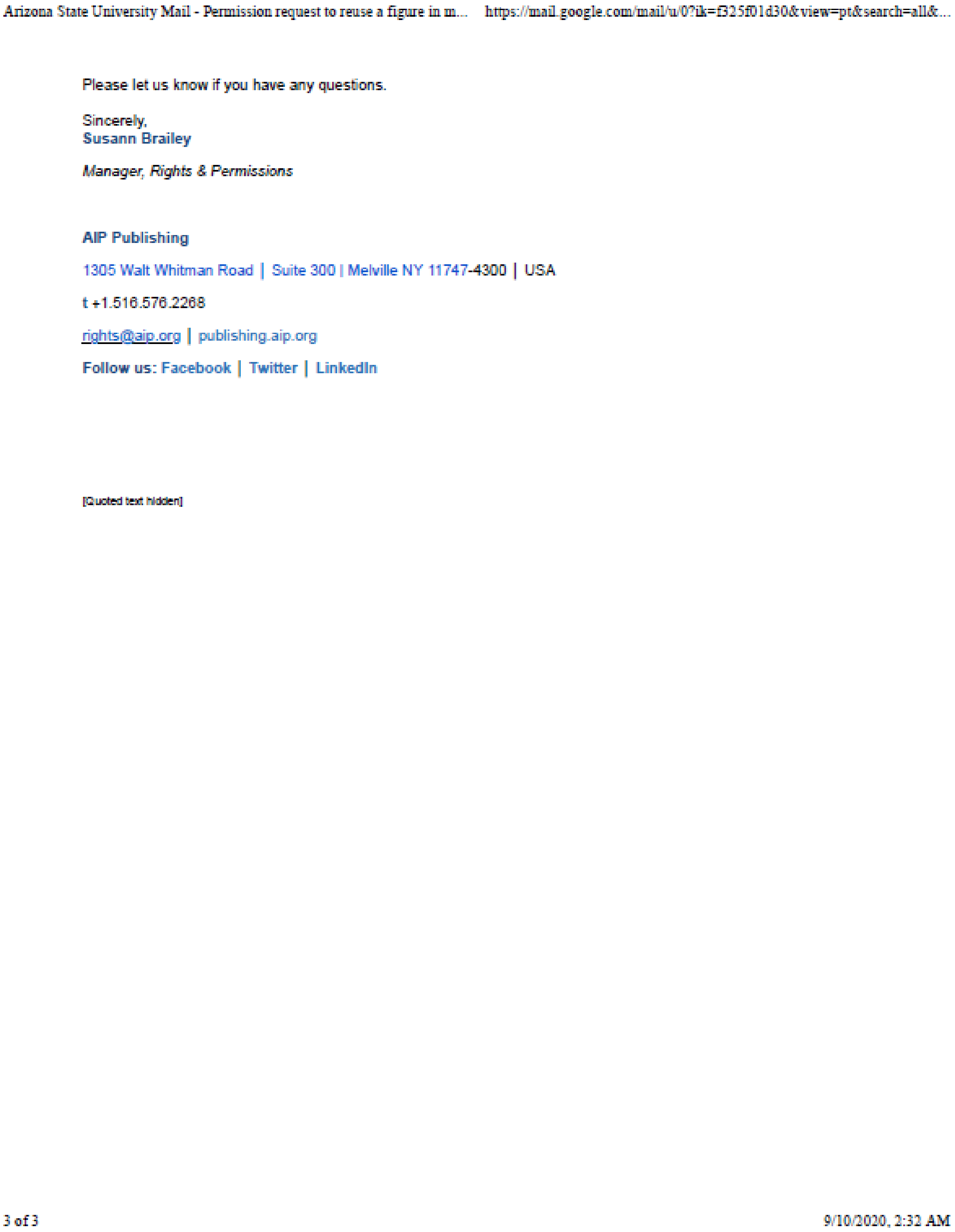

Arizona State University Mail - Permission request to reuse a figure in m... https://mail.google.com/mail/u/0?ik=f325f01d30&view=pt&search=all&...

Please let us know if you have any questions.

Sincerely,
Susann Brailey

Manager, Rights & Permissions

AIP Publishing

1305 Walt Whitman Road | Suite 300 | Melville NY 11747-4300 | USA

t +1.516.576.2268

rights@aip.org | publishing.aip.org

Follow us: Facebook | Twitter | LinkedIn

[Quoted text hidden]

3 of 3 9/10/2020, 2:32 AM

Figure A.26: Permission from the AIP Publishing publications; part 3.